



HAL
open science

Sources of the alkaline magmatism in the Turkish-Iranian Plateau: a link with the dynamic of stagnant lithospheres within the Mantle Transition Zone

Azam Soltanmohammadi

► **To cite this version:**

Azam Soltanmohammadi. Sources of the alkaline magmatism in the Turkish-Iranian Plateau: a link with the dynamic of stagnant lithospheres within the Mantle Transition Zone. Earth Sciences. Université Toulouse 3 Paul Sabatier (UT3 Paul Sabatier); Université Shahid Beheshti (Iran), 2018. English. NNT: . tel-01849123

HAL Id: tel-01849123

<https://theses.hal.science/tel-01849123>

Submitted on 25 Jul 2018

HAL is a multi-disciplinary open access archive for the deposit and dissemination of scientific research documents, whether they are published or not. The documents may come from teaching and research institutions in France or abroad, or from public or private research centers.

L'archive ouverte pluridisciplinaire **HAL**, est destinée au dépôt et à la diffusion de documents scientifiques de niveau recherche, publiés ou non, émanant des établissements d'enseignement et de recherche français ou étrangers, des laboratoires publics ou privés.



THÈSE

En vue de l'obtention du

DOCTORAT DE L'UNIVERSITÉ DE TOULOUSE

Délivré par :

Université Toulouse 3 Paul Sabatier (UT3 Paul Sabatier)
Cotutelle internationale avec l'Université Shahid Beheshti-Iran

Présentée et soutenue par :

Azam SOLTANMOHAMMADI

Le 06/02/2018

Titre :

Sources du magmatisme alcaline dans le plateau Turco-Iranien : un lien avec
la dynamique des lithosphères stagnantes dans la zone de transition du
manteau

École doctorale et discipline ou spécialité : Unité de recherche :

Géosciences Environnement Toulouse UM 97 UPS - UMR 5563 CNRS - UR 234 IRD

Directeurs de Thèse :

Dr. Georges Ceuleneer / Prof. Mohamad Rahgoshay
Dr. Michel Grégoire

Jury:

Georges Ceuleneer
Mohamad Rahgoshay
Michel Grégoire
Gianluca Bianchini
Claude Jaupart
Jean-Mard Lardeaux
Stéphane Guillot
Véronique Gardien
Michel Rabinowicz

Directeur de Recherche
Professeur
Directeur de Recherche
Professeur associé
Professeur
Professeur
Directeur de Recherche
Maître de Conférences
Professeur

Directeur de Thèse
Directeur de Thèse
Co-directeur de Thèse
Rapporteur
Rapporteur
Rapporteur
Président
Examinatrice
Invité

Sources of the alkaline magmatism in the Turkish-Iranian Plateau: a
link with the dynamic of stagnant lithospheres within the Mantle
Transition Zone

Résumé

Les laves alcalines continentales dérivent de magmas mantelliques, riches en éléments volatils, et se sont mises en place, soit dans un environnement orogénique, à proximité des zones de subduction, soit dans un environnement intracontinental éloigné de toute zone de subduction active. Leur genèse implique la fusion partielle des sources mantelliques soit à des profondeurs relativement faibles (<150 km), soit à plus grandes profondeurs (> 150 km) pouvant même atteindre le sommet de la zone de transition du manteau. Au niveau du plateau turco-iranien, les laves alcalines d'âge inférieur à 80 Ma présentent des signatures géochimiques pointant vers deux types de sources, c'est-à-dire des sources influencées par la subduction et d'autres intra-plaques (« OIB-like basalts »). Sur la base de la teneur en SiO₂ et de l'indice d'alcalinité, les laves peuvent être regroupées en trois types principaux, les groupes I, II et III. Les groupes I et II sont des laves potassiques/ultra-potassiques et alcalines sodiques avec des compositions chimiques soit influencés par la subduction soit de type OIB, alors que les laves du groupe III ont une composition transitoire entre les séries fortement potassiques calco-alcalines à alcalines dont la composition est influencée par les processus de subduction. En particulier, la chaîne de Salavat, située au nord-ouest de l'Iran, est caractérisée par des laves (coulées, «pillow-lavas») présentant une population abondante de macrocristaux de clinopyroxène zonés. La comparaison des variations de la composition chimiques de ces cristaux zonés avec les éléments majeurs et traces sur roche totale montre que les différentes populations de clinopyroxènes zonés sont représentatives des magmas du groupe I et / ou II. Notre synthèse des images les plus récentes de tomographie sismique montre la présence d'un grand ensemble de corps elliptiques à faible vitesse sismique, d'une taille d'environ 100 km, que nous avons appelés « poche de compaction », dispersés entre ~ 400 km et 100 km de profondeur. Un modèle est développé montrant que la faible vitesse sismique des « poche de compaction » résulte de la percolation et de la concentration dans ces grandes poches, de magmas riches en éléments volatils libérées à

environ 410 km de profondeur dans le «Big Mantle Wedge». Ces magmas riches en éléments volatils interagissent avec le manteau environnant à une température inférieure de ~ 100 à 200 ° C à celle de l'adiabat mantellique subcontinental habituel, ce qui entraîne finalement la précipitation de phases minérales hydratées et carbonatées à ~ 8 -6,5 GPa, la fusion partielle du manteau métasomatisé, entre 6,5 GPa et 4 GPa, et enfin la précipitation de phases minérales hydratées / carbonées en dessous de 4 GPa. L'extraction de ces magmas s'effectue par l'intermédiaire d'un essaim de dykes qui se déclenche lorsque le sommet du poche de compaction traverse successivement ces profondeurs critiques: ~ 240 km (8 GPa), ~ 165 km (5,5 GPa) et ~ 135 km (4,5 GPa). Il est montré que les trois groupes de laves (groupe I, II et III) peuvent être liés à ces trois événements successifs d'extraction à l'état fondu. Il est frappant de constater que la zonation des cristaux de clinopyroxène dans les laves de Salavat peut être représentative d'un magma du groupe I transporté par un dyke généré à 240 km de profondeur, qui se met en place près de la transition spinelle-grenat dans le manteau supérieur où il cristallise partiellement. Environ 0,3 Ma plus tard, lorsqu'un filon produit à 135 km de profondeur transportant un magma du groupe II traverse cette interface, il piège un assemblage partiellement cristallisé du magma du groupe I. Par la suite, ces deux magmas mélangés peuvent se mettre en place dans les niveaux superficiels froids de la croûte où ils se solidifient simultanément. Ceci explique pourquoi les cristaux zonés de clinopyroxènes sont en équilibre avec différents types de magmas alcalins.

Mots clés: laves alcalines continentales; phases hydratées / carbonatées; Zone de transition du manteau (MTZ); poche de compaction; manteau sub-continental adiabatic

ABSTRACT

Continental alkaline lavas are volatile-rich mantle derived magmas erupted either in orogenic setting, close to subduction zones, or in intracontinental setting far away from any active subduction zone. Their genesis involves partial melting of mantle sources either at shallow depths (< 150 km) or either at greater depths (> 150 km) down to the top of the Mantle Transition Zone. In the Turkish-Iranian Plateau, alkaline lavas younger than 80 Ma have geochemical signatures pointing to both types, i.e. subduction-influenced and intraplate (Oceanic Island Basalt-like). Based on SiO₂ content and alkalinity index, the lavas can be grouped into three main types, group I, II and III. Groups I and II are ultrapotassic-potassic and sodic alkaline lavas with subduction-influenced and Oceanic Island Basalt-like chemical patterns, respectively whereas group III lavas have a transient composition between high-K calc-alkaline to calc-alkaline series with subduction-influenced chemical patterns. Particularly the Salavat Range, located in NW Iran, is characterised by lavas (flow, pillow structures dykes) displaying an abundant population of zoned clinopyroxene macrocrysts. A combination of mineral chemistry of the zoning patterns with the bulk rock major and trace element features evidence that the different populations of zoned clinopyroxene are representative of melts of group I and/or II. Our synthesis of the most recent available seismic tomography images show the presence of a large set of elliptic, ~100 km size, low velocities bodies, we named “compaction pockets”, scattered from ~400 km up to ~ 100 km depth. A model is developed showing that the low velocity of the compaction pockets result from the percolation and concentration into large pockets of volatile-rich melt liberated at ~ 410 km depth in the “Big Mantle Wedge”. It is shown to result from interaction of volatile-rich melts with the surrounding mantle at a temperature ~100-200 °C lower than the usual sub-continental mantle adiabat, which eventually results in the precipitation of hydrated and carbonated mineral phases at ~8-6.5 GPa, partial melting of metasomatized mantle at 6.5 down to 4 GPa and finally in the

precipitation of hydrated/carbonated phases below 4 GPa. Melt extraction occurs via swarm of dykes triggered when the top of the compaction pocket successively crosses these critical depths: ~240 km (8GPa), ~165 km (5.5 GPa) and ~135 km (4.5 GPa). It is shown that the three groups of lavas (group I, II and III) may be linked to these three successive melt extraction events. Strikingly, the clinopyroxene zonings recorded in the Salavat Range lavas may be representative of group I melt transported by a dyke generated at 240 km depth which pond close to the spinel-garnet mantle transition and eventually partially crystalized there. About 0.3 Ma later, when a 135 km deep dyke transporting a group II melt crosses that last interface, it traps partially crystalized assemblage of group I melt. Thereafter, the couple of mantle-derived melts may pond in a cold horizon where they simultaneously solidify and can explain the formation of clinopyroxene zonings in equilibrium with different alkaline melts.

Key words: Continental alkaline lavas; hydrated/ carbonated phases; Mantle Transition Zone; compaction pockets; sub-continental mantle adiabat

Acknowledgement

First and foremost, special mention goes to my enthusiastic supervisors. My Ph.D has been an amazing experience and I thank Georges Ceuleneer, not only for his tremendous academic support, but also for his patience, motivation and giving me so many wonderful opportunities. Georges is the one of the smartest people I know. Similar, profound gratitude goes wholeheartedly to Michel Grégoire, who has been a truly dedicated supervisor for immense knowledge, thanks for his continuous support of my Ph.D study and related research. Georges and Michel have been supportive and have given me the freedom to pursue various aspects without objection. I will forever thankful to Mohamad Rahgoshy, my supervisor in Iran. Not only during staying in Iran Mohamad supported me to write Farsi version of my thesis, but also he has been helpful in providing advice many times during my geology course in Iran. I still think fondly of my time as an undergraduate student in his lab. Without his guidance, I had no opportunity to meet new research team in Toulouse.

Beside of my official supervisors, my sincere thanks goes Michel Rabinowicz, who so generously shared no less than ten years of his scientific career to help me to construct my Ph.D work. He showed me new perspective in science. His passion to be strong and, at the same time to enjoy working and loving science, was an example in my life. I hope I could be as lively, enthusiastic as Michel, and to someday be able to deep understanding science as well as he can.

I would like to thank the rest of my thesis committee: Prof. Jean-Mark Lardeaux, Prof. Claud Jaupart, and Dr. Gianluca Bianchini, Dr. Véronique Gardien, and Dr. Stéphane Guillot for their insightful comments and encouragement, but also for their questions which incited me to widen my research from various perspectives.

Completing this work would have been even more difficult without the support and friendship provided by the members of Géosciences Environment Toulouse (GET), Observatoire Midi-Pyrénées (OMP), Paul Sabatier University and Shahid Beheshti University (Iran). I would like to extend thanks to the many people who so generously contributed to the work presented in this thesis. I appreciated to Muriel Gerbault at GET, especially for sharing her knowledge of rheology of lithosphere mantle and advises of Mohsen Moazen at Tabriz University in Iran, to select regional case study in Iran. My sincere thanks also goes to Mathieu Benoit, Philippe de Parseval, Sophie Gouy, Frederic Candodap and Fabienne de Parseval who provided me an opportunity access to the laboratories and research facilities in Toulouse. Without their precious support, it would not be possible to conduct geochemical part of my

work. I am hugely appreciative to Anne-Marie Cousin for her passion as professional work to draw figures to illustrate wonderfully my work. I thank Anne-Marie also for the stimulating discussions, and for all the fun we had in the last four years.

A good support system is important to solve many complicated administrative processes for foreigner. I thanks to Laurence Marlats, general secretary of GET, Carine Baritaud secretary of director. I also thank Etienne Ruellan present director of GET, Geneviève Soucail head of doctoral school and Marie-Claude Cathala secretary of doctoral school.

I gratefully acknowledge the funding sources that made my Ph.D work possible. I was funded by French Embassy in Teheran as bourses du gouvernement français (BGF) fellowship. Delphine Texier, responsible for service Europe-International office in OMP is helpful person, who have been pretty supportive during my staying in GET. Delphine made lot of effort to joint program between Paul Sabatier University and Shahid Beheshti University (Iran) to work well, and my Ph.D also has been supported by international office in Paul Sabatier University. I also thank people who were not in France but helped me; Mrs. Zohreh Mirbaha, responsible of granted student in French embassy in Tehran, also all member of legal advisor of previous president in shahid Beheshti University to make effort joint program start. I also founded by centre national de la recherche scientifique (CNRS).

My time at Toulouse was mad enjoyable in large part due to the many friends that became a part of my life: Anne, Anne-Marie, Christiane (Kikie), Elisabeth, Maria, Michèle, Myriam, Natacha. I would like to give special thanks to them; particularly Anne Briais who hosted me during my staying in Toulouse, thanks you Anne for sharing lot of good moments with me and make my life in Toulouse as I am at home. To my officemate, Myriam Zoulida for all attentive supports during entire period for writing my thesis.

Last but not the least, I would like to thank my family: my parents, my sister, my sister-in law and my brothers, for almost unbelievable support. My parents are the most important people in my world and I dedicate this thesis to them.

Thanks

Azam Soltanmohammadi

Toulouse, February 2018

“Science is the poetry of reality”

Richard Dawkins

Table of contents

CHAPTER I: INTRODUCTION	1
1.1 INTRODUCTION.....	3
CHAPTER II: PETROLOGY AND GEOCHEMISTRY OF POTASSIC IGNEOUS ROCKS OF THE SALAVAT RANGE, NW IRAN; CHARACTERISTICS OF THE PARENT MELT(S) AND PETROGENESIS.....	13
2.1 INTRODUCTION.....	13
2.2 GEOLOGICAL BACKGROUND	14
2.2.1 Regional geology.....	14
2.2.2 Field relation of alkaline rocks.....	16
2.3 SAMPLE PREPARATION AND ANALYTICAL TECHNIQUES	25
2.3.1 ICP-AES	25
2.3.2 Inductively coupled plasma mass spectrometry (ICP-MS).....	26
2.3.4 Thermal Ionization Mass Spectrometer (TIMS)	26
2.3.5 Element Mapping	27
2.3.6 Laser-ablation coupled plasma mass spectrometry (LA-ICP-MS) analysis	27
2.4 RESULTS	28
2.4.1 Petrography.....	28
2.4.2 Mineral chemistry.....	37
2.4.3 Elemental variations of zoned clinopyroxene.....	53
2.4.4 Whole rock geochemistry	62
2.5 DISCUSSION	80
2.5.1 Role of continental crust.....	80
2.5.2 Presence of several mantle-derived melts; evidence from macrocrystal compositions	86
2.5.3 Nature of involved alkaline melts.....	93
2.6 CONCLUSIONS.....	105
CHAPTER III: TRANSPORT OF VOLATILE-RICH MELT FROM THE MTZ BY COMPACTION WAVES: IMPLICATION FOR MANTLE METASOMATISM AND THE ORIGIN OF ALKALINE LAVAS IN THE TURKISH-IRANIAN PLATEAU	110
3.1 INTRODUCTION.....	112
3.2 GENERAL GEOLOGY OF TURKISH-IRANIAN PLATEAU (TIP)	112
3.3 SURFACE MAGMATISM IN CORRELATION WITH TOMOGRAPHY AND GPS DATA IN THE TIP.....	114
3.3.1 Central Anatolia.....	115
3.3.2 The East Pontides- the East Anatolia.....	118
3.3.3 The Lesser Caucasus- NW Iran.....	123
3.3.4 Alborz.....	127
3.3.5 Central-East Iranian microcontinent (CEIM).....	128
3.3.6 The Urmieh- Dokhtar Magmatic (UDM) zone	131
3.4 GEOCHEMISTRY	132
3.4.1 Chemical classification of lavas	132
3.4.2 Salient conclusions of the geochemical synthesis.....	138
3.5 UPPER MANTLE TOMOGRAPHY BENEATH THE TIP, AND IDENTIFICATION OF COMPACTION POCKETS....	142
3.6 HOW COMPACTION POCKETS DEVELOP FROM VOLATILE-RICH MELTS CARRIED BY “ COLD WET DIAPIRS”	146
3.6.1 A model of compaction waves for rising mantle melts	150
3.6.2 Application of propagating compaction waves and melt distribution inside cold diapirs below the TIP	155

3.6.3 How melts are extracted from ascending compaction pockets from 8 GPa up to 4 GPa (~240 km up 120 km depths).....	157
3.7 LINK BETWEEN VOLATILE-RICH MELT PERCOLATION INSIDE “ COMPACTION POCKETS” AND CONTINENTAL ALKALINE MAGMATISM IN THE TIP	160
3.7.1 Extraction of volatile-rich melt at 8 GPa and origin of group Ia lavas.....	160
3.7.2 The generation of OIB-like melt from 6.5 to 5 GPa and the origin of group IIa lavas	163
3.7.3 The generation of OIB-like melt from 5 to 4 GPa and the origin of group IIb lavas	166
3.7.4 Application of the model to explain the generation of the classified lavas	167
3.8 CONCLUSION.....	173
CHAPTER IV: CONCLUSIONS & PERSPECTIVES	176
4.1 CONCLUSION.....	178
BIBLIOGRAPHY	189
APPENDIX.....	223

List of figures :

Figure 1.1 Large-scale distribution of alkaline magmatism in the Mediterranean region.....	6
Figure 1.2 diagrams showing the distribution of different types of magmatism versus time (a) and location in the TIP (b).	9
Figure 1.3 Schematic figure showing a subduction zone with the main upper mantle structures (modified after Green et al., 2010).	10
Figure 2.1 Simplified geological map from East Anatolia to NW Iran.....	15
Figure 2.2 a) Geological map of Lahrud province showing distribution of Cenozoic magmatism in the Salavat Range (modified after Babakhani et al., 1990).....	17
Figure 2.3 Field photographs outcrops of tephrite and lamrophyre dykes.....	19
Figure 2.4 Field photographs. Tephrite dykes occur as multi directions linear structures crosscutting breccia host lavas with chilled margins.....	21
Figure 2.5 Field photographs of analcime-bearing lavas in the eastern of Salavat Range.....	22
Figure 2.6 Field photographs of hornblende andesite and intrusions.....	24
Figure 2.7 Photomicrographs of host lavas..	30
Figure 2.8 Photomicrographs of kersantite and minette lamrophyres.....	31
Figure 2.9 Photomicrographs of tephrite dykes and analcimate lavas and breccias.	33
Figure 2.10 Photomicrographs of hornblende andesite.....	36
Figure 2.11 Major elements compositions versus Mg# for clinopyroxene of host lavas.	38
Figure 2.12 Chemical classification (Mg-Ca-Fe mol%) triangular diagrams for Clinopyroxene (after Morimoto et al., 1988).....	40
Figure 2.13 Major elements compositions versus Mg# for clinopyroxene of lamrophyres.....	41
Figure 2.14 Mg-Fe-Al classification triangular diagram for mica in lamrophyres from the Salavat Range. The compositional fields for lamrophyre and lamproites are after Sheppard and Taylor (1992) and Rock (1991).	42
Figure 2.15 Major element variations of Al ₂ O ₃ versus TiO ₂ (a) and Mg# (b) for phlogopite in lamrophyres from the Salavat Range	43
Figure 2.16 Mg# versus Si classification diagram for calcic amphiboles (after leake et al., 1997)..	45
Figure 2.17 Plots of MnO, NiO and CaO versus Fo for olivine in lavas and intrusions from the Salavat Range. Fields for mantle xenoliths from the TIP, potassic rocks from the West Medditerranean - NW Iran based on data from Su et al., 2014 and Shafaii Moghadam et al., 2014, respectively.	46
Figure 2.18 Major elements compositions versus Mg# for clinopyroxene of tephrite dikes.	48
Figure 2.19 Compositional fields of clinopyroxene from different rocks from the Salavat Range..	50
Figure 2.20 Major elements compositions versus Mg# for clinopyroxene of intrusions from the Salava Range. The field for clinopyroxene in the intrusions in the NW Iran	52
Figure 2.21 Core to rim major element variation in Type-I clinopyroxene phenocrysts.	54

Figure 2.22 Major element distribution maps of the four type of zonation in the clinopyroxene.....	55
Figure 2.23 Core to rim major element variation in Type-I (a) and Type-II clinopyroxenes (b) in the tephrite dykes.	56
Figure 2.24 Core to rim major element variation in Type-III clinopyroxenes in kersantite lamprophyres.....	57
Figure 2.25 Core to rim (a) and rim-to-rim (b) major element variation in Type-IV clinopyroxenes in tephrite and kersantite..	58
Figure 2.26 Chondrite-normalized (Ch) and primitive mantle-normalized (PM) trace element patterns and REE patterns of classified clinopyroxenes (Ch and PM values after Sun and McDonough, 1989)..	61
Figure 2.27 (a) Total alkali vs silica diagram (Le Maitre, 2002), (b) K ₂ O vs Na ₂ O diagram, (c) K ₂ O/Na ₂ O vs MgO diagram for classification of the investigated rocks from the Salavat Rang..	64
Figure 2.28 a) CaO vs Al ₂ O ₃ diagram (Foley et al., 1987) b) Al ₂ O ₃ vs TiO ₂ classification diagram for LM-lavas from the Salavat Range.....	66
Figure 2.29 Diagrams of alkali oxides (K ₂ O+Na ₂ O, K ₂ O) vs SiO ₂ (a and b), Sr/Y vs MgO (c), Sr/Y vs SiO ₂ (d), Sr/Y vs Y (e) and La/Yb vs Yb (f) showing that the adakitic geochemical signature of Ps-rocks overlaps with field of adakites from the TIP..	69
Figure 2.30 Whole rock trace element and REE patterns normalised to chondrite and primitive mantle (McDonough and Sun, 1989), for investigated rocks.....	71
Figure 2.31 ¹⁴³ Nd/ ¹⁴⁴ Nd versus ⁸⁷ Sr/ ⁸⁶ Sr isotopic diagram.....	73
Figure 2.32 Variation diagrams for selected major oxides (wt.%) from investigated rocks. Plots of a) CaO, b) SiO ₂ , c) TiO ₂ d) Al ₂ O ₃ , e) Fe ₂ O ₃ f) Na ₂ O, g) K ₂ O, h) P ₂ O ₅ vs MgO (wt.%)..	77
Figure 2.33 Variation diagrams for selected trace elements (ppm) vs MgO (wt.%) for investigated rocks.	78
Figure 2.34 a) ⁸⁷ Sr/ ⁸⁶ Sr vs SiO ₂ , b) ¹⁴³ Nd/ ¹⁴⁴ Nd vs MgO, c) ⁸⁷ Sr/ ⁸⁶ Sr Th, d) ⁸⁷ Sr/ ⁸⁶ Sr vs Rb/Sr, e) (Nb/La) _N vs SiO ₂ and f) (Nb/La) _N vs MgO diagrams for investigated rocks.....	79
Figure 2.35 Diagram illustrating that chondrite-normalized (Sun and McDonough, 1989) REE patterns of Ps-rocks differ from fractional crystallization (FC).....	85
Figure 2.36 Mg# in clinopyroxene (cpx) vs Mg# in rock diagram..	89
Figure 2.37 a) Primitive mantle trace element and b) chondrite-normalized REE patterns (Sun and McDonough, 1989) for alkaline lavas from the TIP.	92
Figure 2.38 Bulk rock Sr-Nd isotope ratios vs alkali (K ₂ O and Na ₂ O) major elements (wt.%) for HM-lavas and pillow lavas of LM-lavas.....	94
Figure 2.39. a) variation of Ce/Pb vs ¹⁴³ Nd/ ¹⁴⁴ Nd and b-c) Nb/U and Th/Nb vs ⁸⁷ Sr/ ⁸⁶ Sr to identify the change of bulk rock composition of HM-lavas and LM-lavas (pillow lavas).....	96
Figure 2.40. Ti (a.p.f.u) vs Al (a.p.f.u) of clinopyroxene for potassic and ultrapotassic lavas..	97

Figure 2.41. CaO (wt.%) vs MgO (wt.%) diagram for clinopyroxene (cpx) of HM-lavas from the Salavat Range.....	98
Figure 2.42. Chondrite normalized (Sun and McDonough, 1989) REE diagram showing melt in equilibrium with colorless clinopyroxene from Type-I (a), Type -II (b), and green colored clinopyroxene from type-III (c) and -IV (d) zoned macrocrysts..	100
Figure 2.43 $^{143}\text{Nd}/^{144}\text{Nd}$ vs $^{87}\text{Sr}/^{86}\text{Sr}$ diagram illustrating the mixing of different compositions to explain the observed isotopic ratios of the investigated rocks..	104
Figure 3.1.(a) Regional tectonic setting of TIP with main tectonic divisions in relation to the Arabian and Eurasian plates. (b) Schematic map showing the distribution of the continental magmatism (adapted from the Middle East geological map (Aghanabati, 1986).....	117
Figure 3.2. Map views through S- wave tomographic model velocity at 60 km (a) and 150 km (b) depth adapted after Fichtner et al., 2013..	118
Figure 3.3. (a) The map represents a 150 km deep horizontal section of the P-wave anomalies field of the TIP along with the neighbouring Eurasia and Arabia lands.....	122
Figure 3.4. A and B vertical S-waves velocity anomaly cross-sections joining the Zagros to the Great Caucasus, following the C-D line from figure 3b, indicate present of low velocity anomalies beneath TIP.....	126
Figure 3.5. a) Bouguer anomaly, b) S-waves velocity anomaly c) density distribution that optimizes the relationship between S-waves anomaly and Bouguer anomaly across Central-East Iranian blocks joining Zagros to Kopet Dagh.....	130
Figure 3.6. Geochemical variation diagrams for the purpose of lavas classification. Diagram showing classification of studied lavas into sodic, transitional from sodic to potassic, potassic and ultrapotassic series.....	134
Figure 3.7. $^{143}\text{Nd}/^{144}\text{Nd}$ versus $^{87}\text{Sr}/^{86}\text{Sr}$ diagram for each group of lavas compared with the mantle components.....	137
Figure 3.8. Primitive mantle-and chondrite –normalized (Sun & McDonough, 1989) multi-element distribution patterns of lavas..	140
Figure 3.9. Middle East large-scale tomography model (P-wave anomalies) by Nafi Toksöz <i>et al.</i> (2008) (a) at 700 km and (b) at 500 km, respectively..	143
Figure 3.10. Display of S- receiver function along a North-South profile between 30 and 39 °E of Central Anatolia (Fig. 3.2c), from Kind et al., (2015), with modifications.....	144
Figure 3.11. Pressure-temperature diagram to illustrate a) the solidus of different mantle components resulting from melting experiments, including mantle adiabatic temperature (after Katsura <i>et al.</i> , 2010).....	149
Figure 3.12. Gregoire et al., (2006)' compaction experiment..	153

Figure 3.13. Obtained from Gregoire et al. 2006: (a) the dimensionless melt concentration (ϕ') by volume (dashed line), and the excess pressure ρ' vertical profile (continuous line) taken at time 27 along the left lateral face of the model of figure 3.12..	154
Figure 3.14. (a) N-MORB normalaized (Sun & McDonough, 1989) and (b) GLOSS normalaized (Plank & Langmuir, 1998)..	162
Figure 3.15. a) Ce/Pb versus Ce for classified lavas considered in this study. Symbols are same as in figure 3.8.b) Effect of Variable CO2 on hybrid peridotite derived melt at 3 GPa and alkali or silica content of primary melts.....	165
Figure 3.16. (a and b) Schematic cartoons proposed for the development and ascent evolution of Compaction pockets from low velocity layer at the top of the MTZ..	170

Chapter I: Introduction

1.1 INTRODUCTION

Alkaline igneous rocks, sodic or potassic, are issued from volatile-rich mantle derived melts. They occur in a variety of tectonic settings including oceanic and continental hotspots, continental shields and, to a lesser extent, in orogenic belts (Morgan, 1971; Streckeisen 1979; Foley *et al.*, 1987; Fitton & Upton, 1987; Wilson, 1989; Rock 1991; Mitchell & Bergman, 1991). Continental alkaline magmas is not volumetrically widespread, but its exotic mineral assemblages and bulk rock characteristics draw attention of an increasing number of studies. They are interpreted as mantle derived partial melts which alkalis (K and Na), and silica vary in a wide range (*nepheline-* to *quartz-* normative). Although, the main geochemical characteristics of alkaline magma are well documented, e.g. high concentration of alkalis (Na, K), LILE, LREE/HREE and isotope ratios corresponding to the mantle range, many questions related to their genesis and mantle source characteristics remain discussed. As it is difficult to explain alkaline magmas characteristics with common mantle sources (e.g. Wyllie, 1980; Rock, 1991; Foley *et al.*, 1992; Mitchell, 1995; Mitchell & Bergman, 1991), it generally have been accepted that they derive from metasomatized mantle sources, especially to account for their volatile-rich components (C-O-H) (Ulmer & Sweeney, 2002; Brey *et al.*, 2008; Girnis *et al.*, 2011; Grassi *et al.*, 2012; Novella & Frost 2014; Ghosh *et al.*, 2014; Condamine & Médard, 2014; Förster *et al.*, 2016). Generally speaking, their geochemical fingerprints and elemental concentrations are explained by i) a low degree of melting (Wyllie, 1980; Pilet *et al.*, 2008; Davis & Hirschmann, 2013) ii) an uncommon mantle source with or without continental components in the source (e.g. Murphy *et al.*, 2002; Willbold & Strack, 2006, Rapp *et al.*, 2008; Grassi *et al.*, 2012), iii) metasomatic reactions and diffusive exchange with surrounding mantle during migration (e.g. Khazan & Fialko, 2005).

Occurrence of alkaline rocks is not necessarily linked to a deep-seated mantle plume (e.g. Murphy *et al.*, 2002; Lustrino & Wilson, 2007; Kuritani *et al.*, 2013). In continental settings, non-plume related alkaline rocks are found either in a marginal setting, close to subduction zones (e.g. less than 500 km off trenches), or in an intracontinental setting far away from any active subduction zone (e.g. up to 5000 km). Petrological and experimental studies show that the mantle sources of the alkaline igneous rocks originate either at shallow depths (i.e. less than 150 km) (Hirschmann *et al.*, 1998; Conceicao & Green, 2004; Fumagali & Poli, 2008; Tumiati *et al.*, 2013; Codamine & Medard, 2014; Forster *et al.*, 2016; Condamine *et al.*, 2016) or at greater depths: i.e. from 150 km down to the top of the Mantle Transition Zone (MTZ) (Ulmer & Sweeney, 2002; Rapp *et al.*, 2008; Grassi *et al.*, 2012, Litasov *et al.*, 2013; Novella & Frost, 2014). In all cases, the parental melts of alkaline rocks derive from heterogeneous mantle sources. Heterogeneity in the mantle source can result from the modification of the mantle during processes removing or adding chemical components such as subducted sediments or other enriched materials (Hawkesworth *et al.*, 1993; Willbold & Strack, 2006; Anderson, 2006; Jackson & Dasgupta, 2008). For instance, alkaline rocks observed close to subduction zones mainly result from syn- and post- collisional processes. The scenarios proposed to explain the formation and origin of such alkaline rocks include: i) partial melting of metasomatized mantle along the slab-mantle wedge interface (Foley, 1994; O'Brein *et al.*, 1995; Ulmer, 2001; Tumiati *et al.*, 2013); ii) upwelling and underplating of enriched mantle beneath the lithosphere (Hole *et al.*, 1991; Özdemir & Guec 2014; Prelević *et al.*, 2015); iii) re-melting of previously underplated magma or metasomatized lithosphere (Bonin *et al.*, 1998; Avanzinelli *et al.*, 2009); (iv) finally a combination of those scenarios (e.g. Prelević *et al.*, 2008, 2010). Alkaline rocks from the Andes, Alps, Zagros, Himalaya and Tibet, result from such convergence related processes (e.g. Gao *et al.*, 2007; Keskin *et al.*, 2008; Prelević *et al.*, 2008).

Within the Mediterranean and surrounding regions, outcrops of alkaline lavas are widespread (Wilson & Bianchini, 1999; Lustrino & Wilson, 2007; Lustrino *et al.*, 2011). Although they appear close to subduction zones, their mantle sources have geochemical fingerprints of both subduction-related and intracontinental magmatism (i.e. subduction unrelated) processes (Fig 1.1). In the Eastern Mediterranean, the Turkish-Iranian Plateau (TIP) occupies a significant median portion of the Alpine-Himalayan orogenic belt, limited North and South by the Northern and Southern branches of the Tethys ocean sutures (Şengör & Kidd, 1979; Stampfli, *et al.*, 2002, 2013; Berra & Angiolini, 2014). The TIP is characterised by widespread and long standing continental magmatism (up to 500 km in extent) since Mesozoic times (last 200 Ma). This igneous activity is classically divided into four periods marked in the geological subdivisions: Central- East Anatolia, East Pontides, Lesser Caucasus- south Armenia-NW Iran, Alborz, the Urmieh- Dokhtar Magmatic zone, Central Iran, East Iran (Lut Block) (chapter 3 Fig .3.1). *Period 1* (Jurassic to Cretaceous) is characterized by abundant calc-alkaline igneous rocks (Khalaj *et al.*, 2007; Hassanzadeh & Wernicke, 2016). *Period 2* (Late Cretaceous to Palaeocene) have experienced widespread tholeiitic volcanism related to the opening of oceanic basins (e.g. Khalatbari Jafari *et al.*, 2016), intra-continental intrusions (i.e. A type granitoides, Boztug *et al.*, 2007, Karsli *et al.*, 2012a) and continental alkaline volcanism (Aghazadeh *et al.*, 2015; Doroozi *et al.*, 2015). *Period 3* (Early to Middle Cenozoic) called the magmatic “flare up”, consists of widespread high-K calc-alkaline to transient alkaline lavas and related subvolcanic intrusions (Vincent *et al.*, 2005; Boztug & Jonckheere, 2007; Ardjmanzadeh *et al.*, 2011; Verdel *et al.*, 2011; Asiabanha & Foden, 2012, Karsli *et al.*, 2012b; Pang *et al.*, 2013; Moritz *et al.*, 2016; Beydokhti *et al.*, 2015; Ahmadian, *et al.*, 2016); finally, *period 4*, since the Late Cenozoic, is characterized by alkaline lavas (Pearce *et al.*, 1990; Wilson, *et al.*, 1997; Aydin *et al.*, 2008; Liotard *et al.*, 2008; Lustrino *et al.*, 2010; Mirnejad *et*

al., 2010; Saadat *et al.*, 2010; Saadat & Stern, 2012; Allen *et al.*, 2013; Pang *et al.*, 2013; Shafaii Moghadam *et al.*, 2014; Aghazadeh *et al.*, 2015; Kheirkhah *et al.*, 2015; Prelević *et al.*, 2015).

The long-lived subduction history of the Tethys beneath the plateau is a natural argument to link these four magmatic periods to classical subduction related processes. However, although *period 1* is dominated by uniformed classical calc-alkaline intrusions and known as continental arc magmatism (Hassanzadeh & Wernicke, 2016 and reference there in), the consequences of subduction and mantle wedge processes remains controversial during Late Cretaceous to Oligo-Miocene (corresponding *period 2 and 3*). Many studies evoke melt generation within extensional settings (e.g. intra arc or back arc basin e.g. Vincent *et al.*, 2005). However, geochemical diversity of magmatism with both subduction-related (HFSE depletions) and intraplate magmatism (OIB-like patterns) make their interpretations confusing. The proposed source is the shallow depth subcontinental mantle lithosphere with or without

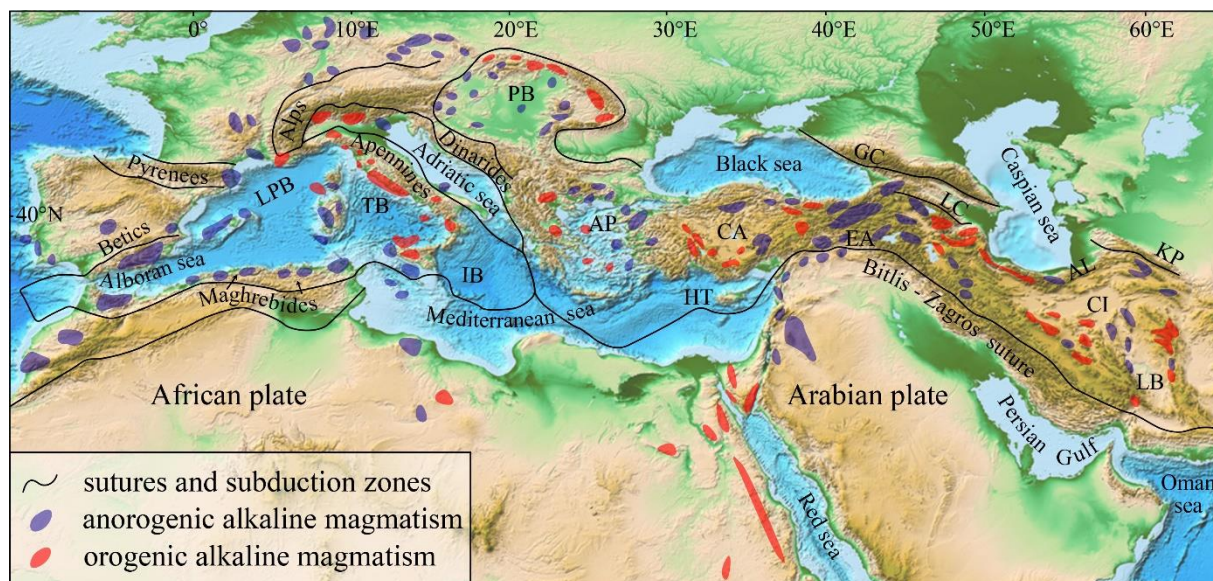


Figure 1.1 Large-scale distribution of alkaline magmatism in the Mediterranean region. Red and blue areas highlight alkaline magmatism with anorogenic and orogenic geochemical signature, respectively. Western Mediterranean and Eastern Mediterranean regions indicated and abbreviated after Lustrino and Wilson, 2007 and this study, respectively. Geological boundaries and distribution of main tectonic unites taken from the tectonic map of the Middle East, Geological Survey of Iran, (Aghanabati, 1986).

influence of continental crust for subduction related magmatism (e.g., Castro *et al.*, 2013; Verdel. *et al.*, 2011). Other studies propose that they are fingerprints of intraplate magmatism resulting from the interaction of continental lithosphere with the asthenosphere (Pearce *et al.*, 1990; Özdemir & Güleç, 2014; Prelević *et al.*, 2015). To explain such geochemical diversity, the presence of oceanic subducted slab and influence of subduction processes during Late Cretaceous to Middle Eocene are suggested and explained as resulting from various geometry of the subducting slab (e.g. slab window, break-off, flattening). Witnesses of such processes and various geometry are not directly documented in the geological record. In more details, the origin of melts is explained by either (i) cold and hydrated plumes rooted at slab-mantle wedge interfaces (Castro *et al.*, 2013), (ii) hydrated mantle located at the top of a flat slab (Verdel. *et al.*, 2011) and (iii) the rise of a hot asthenosphere flow during slab break-off (Keskin *et al.*, 2008; Agard *et al.*, 2011) or slab tearing (Jolivet *et al.*, 2009, 2013). Finally, post-subduction and post-collisional crustal thickening lead to delamination and/or partial melting of the metasomatized mantle lithosphere and ultimately to the emplacement of hot mantle up to the base of the crust (Şengör *et al.*, 2003; Keskin *et al.*, 2008; Özacar *et al.*, 2008; Francois *et al.*, 2014). The latter scenario provides a frame for the Late Cenozoic and recent magmatism in the TIP, and to the 2 km plateau uplift. However, such type of slab-mantle wedge scenario can explain melt compositions in a given regional setting but its use to explain formation of alkaline rocks at different periods of time and/or tectonic contexts. For example similar geochemical fingerprints than those observed during *period 4* (post collision magmatism) are also found during magmatic phases prior to the final collisional time (30 Ma) (e.g. Aghazadeh *et al.*, 2015; Gülmez *et al.*, 2016).

In a chronological perspective, the interpretation of the origin of the Eocene-Oligocene alkaline magmatism is the most controversial issue in the plateau, because it occurs before the post-collisional ages. *This motivated my case study of the “Salavat Range”, which is one of the*

most famous alkaline magmatism outcrops in NW Iran (chapter 2. Fig 2.1). Igneous rocks from potassic and sodic alkaline series, of high potassium calc-alkaline affinities are mostly exposed as volcanic, sub-volcanic and plutonic rocks emplaced during Early to Late Cenozoic (Alberti *et al.*, 1976; Babakhani *et al.*, 1990). In chapter 2, I present fieldwork and analyses carried out on alkaline rocks from the Salavat Range (sections 2.2 and 2.3). This work is the first report on the discovery of important lithologies (e.g lamprophyres), and on their composition (mineral chemistry and whole rocks major, trace elements and Nd-Sr isotopes). The geochemical characteristics of alkaline rocks from the Salavat Range are transitional between potassic and sodic series. They put in evidence the mixing process between mantle-derived melts. I focus in chapter 2, on *the determination of the characteristics and origin of alkaline melts source(s) of the Salavat Ranges rocks*. The major, trace element and isotopic composition of Eocene alkaline rocks demonstrate that they originate from similar mantle sources than those of the younger alkaline magmas (≤ 11 Ma) which clearly emplaced in a post-collisional setting (30 Ma). To avoid confusions with pre- or post-collisional magmatism, in chapter 3, we consider the occurrence of alkaline magmatism during time range from the Late Cretaceous (~80 Ma) to present-day, i.e a period clearly covering the initial collision time in the plateau (see Şengör & Yilmaz, 1981; McQuarrie & van Hinsbergen, 2013). Then, alkaline magmatism is classified in terms of SiO₂ content and alkalinity indexes. I distinguish three categories of rocks: i) alkaline potassic (group I), ii) alkaline sodic (group II) and iii) calc-alkaline (group III) series. Interestingly, the rocks do not show any systematic changes in term of geochemistry (e.g. fluid immobile elements) neither by time or locations. On the contrary, they show a scattered pattern of fluid immobile elements (Fig. 1.2). All these observations confirm that there is no clear geochemical fingerprints of the alkaline magmatism with the evolution of the subduction process and the subsequent continental collision. They lead me to consider, the whole available data set of the TIP to determine the main geochemical fingerprints and melt characteristics of

the rocks in the plateau. In the same chapter, I determine the link between the distribution and composition of the alkaline lavas and various geophysical and tectonic observations (GPS data, seismic tomography, gravity and structural geology).

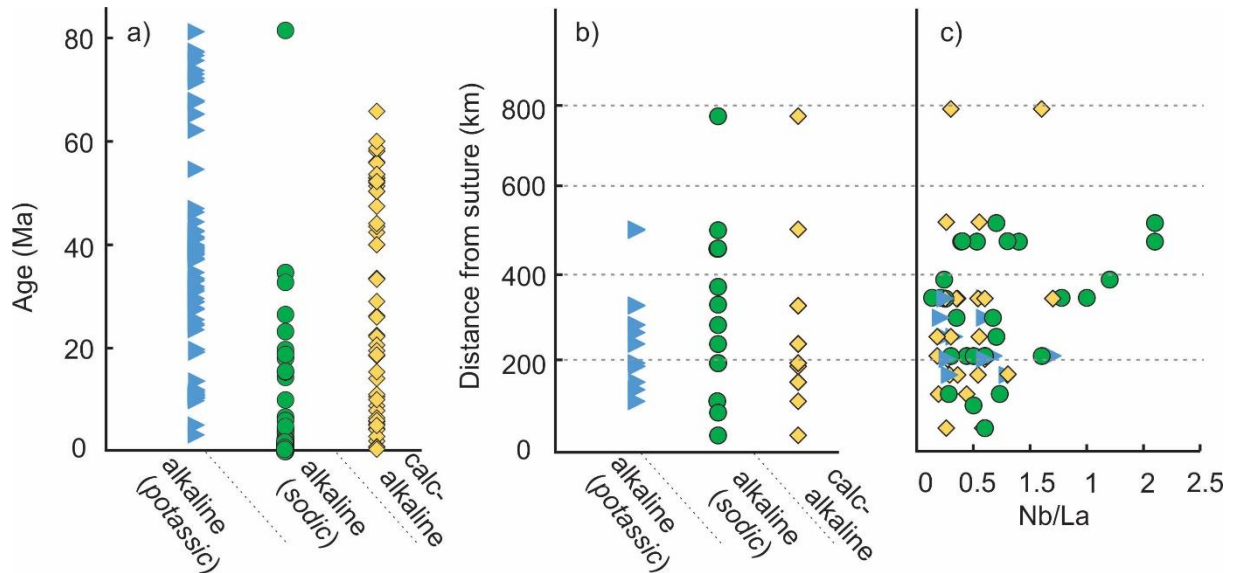


Figure 1.2 diagrams showing the distribution of different types of magmatism versus time (a) and location in the TIP (b). In figure c, plot of elemental ratio (Nb/La) indicative of slab derived-fluid/melts versus location of the classified rocks.

Due to the lack of a consistent model to explain the sources of alkaline lavas in the plateau, I seek for an alternative one, which is specifically linked to the geophysical observations, deciphered below the lithosphere of the TIP. As mentioned before, all previous scenarios for the melting mantle processes consider that the sources of alkaline lavas from the plateau are shallower than 150 km. The situation radically differs when we take into account intracontinental magmatism located at large distances from subductions. In this case it has been interpreted in the frame of the “Big Mantle Wedge” concept (BMW, Ohtani & Zhao, 2009; Zhao *et al.*, 2009; Kameyama & Nishioka, 2012) which considers several tens to a few hundred million years of thermal and chemical evolution of the MTZ (Mantle Transition Zone, c.a. 660

km depth), where subducted slabs accumulate (e.g. Fukao *et al.*, 2001). Segregation of slabs and decarbonation-dehydration at the top of the MTZ, induced by the phase change from wadsleyite to olivine, develops a 20 km thick C-O-H rich partially molten mantle layer (Komabayashi & Omori, 2006; Motoki & Ballmer, 2015; Myhill *et al.*, 2017), which subsequently diapirically rises to the surface (Morra *et al.*, 2015; Safonova *et al.*, 2015; Litasov *et al.*, 2013) (Fig. 1.3).

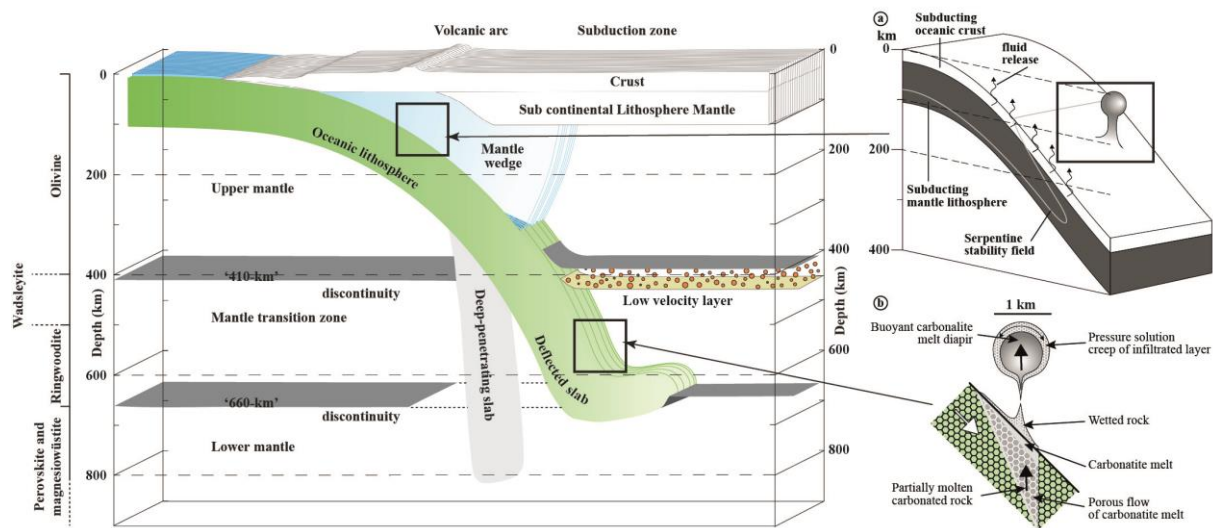


Figure 1.3 Schematic figure showing a subduction zone with the main upper mantle structures (modified after Green *et al.*, 2010). In addition, two models of diapirs located in the shallow mantle (Gerya *et al.*, 2006) and at greater depths (Litasov *et al.*, 2013) are illustrated.

Tomography images reveal frequently low velocity bodies located in the upper mantle below the TIP. A synthesis of recently published tomography models allowed me to propose a 3D image of the upper mantle in chapter 3 showing ~ 100 km wide, elliptic low velocity bodies scattered from ~400 to 100 depth. In the other hand, throughout the TIP, the closing and opening of several branches of the Tethys have possibly led to the accumulation, differentiation and heating of subducted blocks within the MTZ, building complex tectonic and magmatic signals that superimpose on active subduction and collision zones along the Alpine-Himalaya belt. Low

velocity anomalies in the upper mantle beneath the TIP and long lived-subduction of Tethys open a question: *is there any relationship between low velocity anomalies in the TIP and the “BMW” model diapirs?* Finally in chapter 3 I discuss which parameters led to develop diapirs similar to the “BMW” but relatively close to a subduction zone. The model assumes two important restrictive conditions: (i) the whole mantle below the lithosphere is 200° colder than the oceanic adiabat; (ii) there is no mantle plume below the TIP originating either in the MTZ or of the lower mantle. In the conclusion (chapter 4), I propose that both conditions apply to the TIP and that the alkaline magmas are extracted from three sets of dyke swarms originated at 240 km, 165 km, 135 km depths, respectively. Future works should lead to a generalization of the model, i.e. how it needs to be modified when this couple of restrictive conditions are no more present.

Chapter II: Petrology and Geochemistry of Potassic Igneous Rocks of the Salavat Range, NW Iran; characteristics of the parent melt(s) and petrogenesis

2.1 INTRODUCTION

Alkaline magmatism in the Salavat Range is representative of Eocene magmatism from the NW Iran. In this chapter, detailed relationships between the various lithologies of this region are studied. Previous studies of similar alkaline rocks from the NW Iran were mainly interpreted on the basis of bulk-rock major, trace elements geochemistry, and Sr and Nd isotopes. They proposed that those rocks originated from uncommon metasomatized mantle sources located at lithospheric depths or as result of processes occurring in the descending slab-mantle wedge interface (Castro *et al.*, 2013; Pang *et al.*, 2013; Aghazadeh *et al.*, 2015). However, none of those interpretations were based on detailed mineral chemistry and its impact on bulk rocks chemistry. In this study, we describe different lithologies from the Salavat Range, some of them never mentioned in the geological reports on the regions (e.g. lamprophyres). Additionally, I present geochemical arguments showing that the alkaline rocks from the Salavat Range are not the product of a primary melt originated from a single process of partial melting of metasomatized lithosphere mantle. In this study, I use early-crystallized minerals (e.g. clinopyroxenes) as petrogenetic indicators to distinguish between various involved melts, and their effect to the lateral composition of the bulk rocks. I describe for the first time in the Salavat Range, complex major and trace elements zoning in clinopyroxene. Moreover, trace element patterns in zoned minerals led me to interpret melt characteristics and evolution during petrogenetic processes. The results show that, the involved melts are not similar to classical calc-alkaline series (arc-type) although the rocks dated ~47 Ma are known to belong to a flare-up period of subduction below the Iranian plateau (e.g. Verdel *et al.*, 2011). In the following, I present the general geology of the region as well as field description, mineral data, and bulk rocks characteristics of different investigated lithologies from the Salavat Range. Later the

geochemistry of the involved melts and their similarities with the magmatism from the TIP is discussed.

2.2 GEOLOGICAL BACKGROUND

2.2.1 Regional geology

East Anatolia-NW Iran is the largest region in the Turkish-Iranian Plateau (TIP) covered by Cenozoic-Quaternary magmatism. During the last 90 Ma, the multi-phases magmatic activity in the northwest of Iran formed a semi-rounded magmatic plateau (Fig 2.1). To the North, this plateau is separated by a sedimentary folded zone from the Kura basin and the Lesser Caucasus, whereas towards South, it is limited by the Tabriz fault. The Tabriz fault characterized by a NW-SE orientation separates older magmatism events located North of the fault in the Sabalan block from younger ones to the South in the Sahand block. In the former, magmatism is mainly marked by Cenozoic high-K calc alkaline and alkaline intrusive and extrusive magmatism (Alberti *et al.*, 1976; Alberti *et al.*, 1980; Aghazadeh *et al.*, 2010; 2015), and finally by the Plio-Quaternary Sabalan volcanoes (Ghulamghash *et al.*, 2016). To the South, in the Sahand block, magmatism is younger, since Oligo-Miocene magmatism mainly occurred as lavas and pyroclastic eruptions, and finally during Quaternary the magmatism was centered to the Sahand volcano or elongated along the Tabriz fault (Jahangiri *et al.*, 2007; Ahmadzadeh *et al.*, 2010; Pang *et al.*, 2013; Shafaii Moghadam *et al.*, 2014).

In the northern part of the Sabalan volcano, the magmato sedimentary sequences crop out over an area of about 1500 km² called the “*Salavat Range*”, and known as the most voluminous linear structure, flows and intrusion in NW Iran (Babakhani *et al.*, 1990). Structurally, the Salavat Range is separated from the Moghan sedimentary plain by the Allhayarlou-Huwai folded zone to the North (Fig 2.2). The Moghan plain consists of Early Cretaceous-Neogene

volcano-sedimentary succession (6300 km²). It extends from the south of the Kura basin in the Caucasus Mountains (North of block) to the Talesh Mountain in the west of the block (Fotuhi

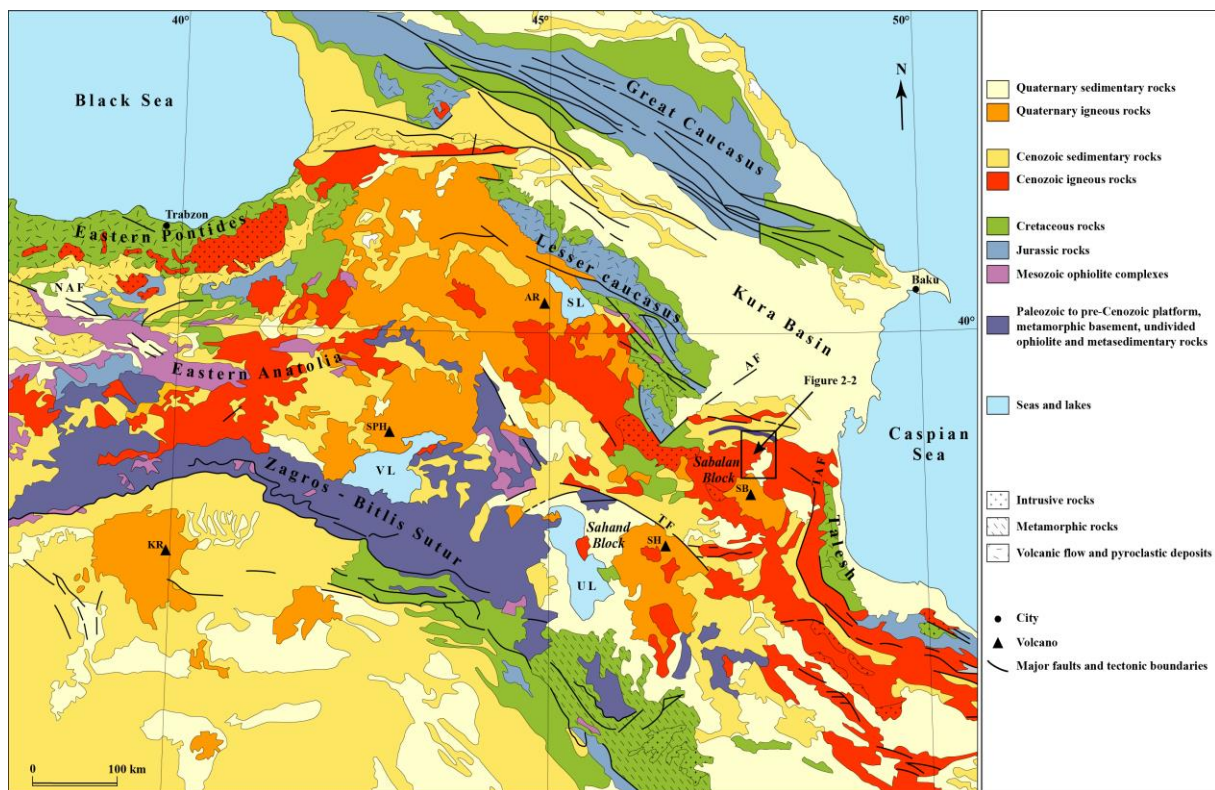


Figure 2.1 Simplified geological map from East Anatolia to NW Iran, showing an extensive Cenozoic-Quaternary magmatism limited by the famous sutures of the Lesser Caucasus and the Zagros-Bitlis, to the North and South, respectively (modified from geological map of the Middle East, Geological Survey of Iran, (Aghanabati, 1986). The rectangle highlights the location of the Figure.2.2 focusing on the Salavat Range in the Sabalan block. Geological key features: NAF: North Anatolian Fault; AF: Aras Fault, TF: Tabriz Fault; KR: Karakudagh volcano; SPH: Suphan Volcano; SH: Sahand volcano; SB: Sabalan Volcano; AR: Ararat volcano. VL: Van Lake; SL: Sevan Lake, UL: Urmieh Lake.

1973, Brunet *et al.*, 2009). Early to Late Cretaceous volcano-sedimentary deposits are the oldest part of the Moghan succession, which are covered by younger Paleogene deposits, e.g. “*Mikop series*” (Willim *et al.*, 1961; Vincent *et al.*, 2005). Finally, the whole of the volcano-sedimentary deposits were folded as anticlines and synclines during Miocene (Brunet *et al.*, 2009, Babakhani *et al.*, 1990). The Allah yarlou-Hovai folded zone consists of East-West magmato-sedimentary assemblages, running along a set of faults just in the south of the Moghan volcano sedimentary succession (Fig 2.2). Regionally the rocks constituting this zone represent the Pre-Cretaceous country rocks of the Salavat Range. They consist of serpentine peridotite, dunite, gabbro and

diabase, which underwent greenschist facies metamorphism and are associated with gneiss, amphibolite, metabasalt and marble. However, controversial definition of ophiolite were used to describe these outcrops (Babakhani *et al.*, 1990; Sudi Ajirlu & Moazen, 2014). These so-called ophiolites are discontinuously covered by Late Jurassic- Cretaceous sediments (Didon & Germain, 1976; Babakhani *et al.*, 1990).

To the east of the Sabalan block, occur an equivalent of the Moghan succession described by Vincent *et al.* (2005) in the Talesh Mountain (Fig 2.1), where in addition to the sedimentary deposits, the volcanic activity is stratigraphy interlayered with the sediments. In the Talesh Mountain major eruptions occurred during middle Eocene “*Peshtasar*” lavas (Vincent *et al.*, 2005), reported as high K calc-alkaline to potassic alkaline rocks. To the south of Talesh Mountain, in western Alborz, Eocene magmatism is mainly reported as lavas and pyroclastic deposits whose thickness dramatically increases southward. In the south of the Caspian Sea, in the middle-west of Alborz, it reaches its maximum thickness (see Asiabanha & Foden, 2012). To the southwest of the western Talesh, the Eocene magmatism occurs as alkaline intrusions with shoshonitic (potassic) affinity, and with a semi arc geometry continue to the Sabalan block (Castro *et al.*, 2013; Nabatian *et al.*, 2014).

2.2.2 Field relation of alkaline rocks

Nearly half of the Sabalan block is covered by Cenozoic lava flows exposed as the main part of the “Salavat Range”. This magmatic unit has a slightly dipping slope to the south ($\sim 10^\circ$) and is 35 km long; it consists of magmatic lithologies as pyroclastic deposits and lavas flows, swarm of dykes (Fig 2.2). In addition, volcanic activities in some outcrops is associated with sub- volcanic and plutonic rocks. Later, Plio-Quaternary lavas covered whole of the southern part of the Salavat Range (Alberti, 1980; Ghalamghash *et al.*, 2016). The main field characteristics of the Cenozoic rocks are described below.

2.2.2.1 Host basalts

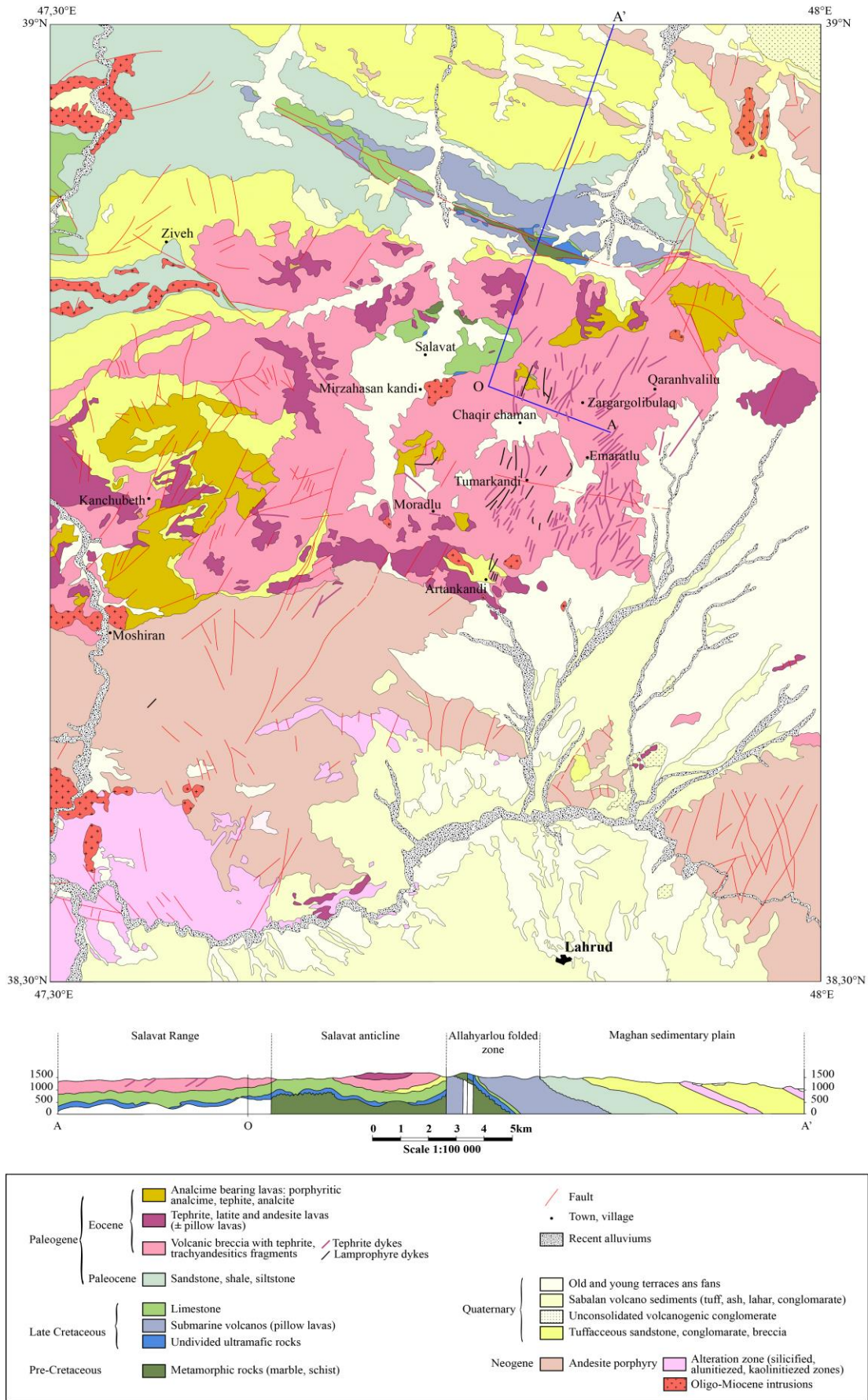
They crop out as i) Ha; highly altered lavas or volcanic breccias (Figs. 2.3c, d, Fig. 2.4 d), or ii) Hb, fresh pillow lavas (Fig. 2.3e). In the altered breccia, volcanic fragments with basaltic composition range from 50 to 200 mm in diameters. Fresh lavas have pillow structures. The shape of pillow lavas are varying from spherical to ellipsoidal in cross sections. Most pillows have a “mega pillow” structure (1-5 m) and few ones have a “normal size” (< 1m). Evidence of alteration occurred only in amygdoidal vesicles filled with secondary minerals (e.g. calcite, zeolites).

2.2.2.2 Dykes

They represent unique linear magmatic structures in the Salavat Range, which are uncommon in the whole of the TIP. They cross cut the host lavas as multi nets of dykes with different orientations and lithologies (Figs 2.3 a,b and c, Fig.2.4a). In many cases, there are straight chilled margins between dykes and host lavas or between two dykes with varied orientations. Dykes cluster around the central and eastern part of the Salavat Range, and suddenly disappear to the west and southern sides. They are crystalline with porphyritic texture, and heterogeneous in their mineral assemblages. Based on abundance of minerals, they divided into three groups with more frequent analcime- and mica- bearing basalts, and less common dykes exposed as hornblende- bearing andesite. Based on petrography, I classified as tephrite, lamprophyre, and hornblende andesite, respectively.

Figure 2.2 a) Geological map of Lahrud province showing distribution of Cenozoic magmatism in the Salavat Range (modified after Babakhani et al., 1990). b) Cross section (A-A') between Moghan sedimentary plain to the North and magmatic plateau from the centre of the Salavat Range showing structural-stratigraphy relationships between Cretaceous and later magmatism and sedimentary basins in the region. See figure 2.1 for location of the map.

Chapter II : Petrology & geochemistry...



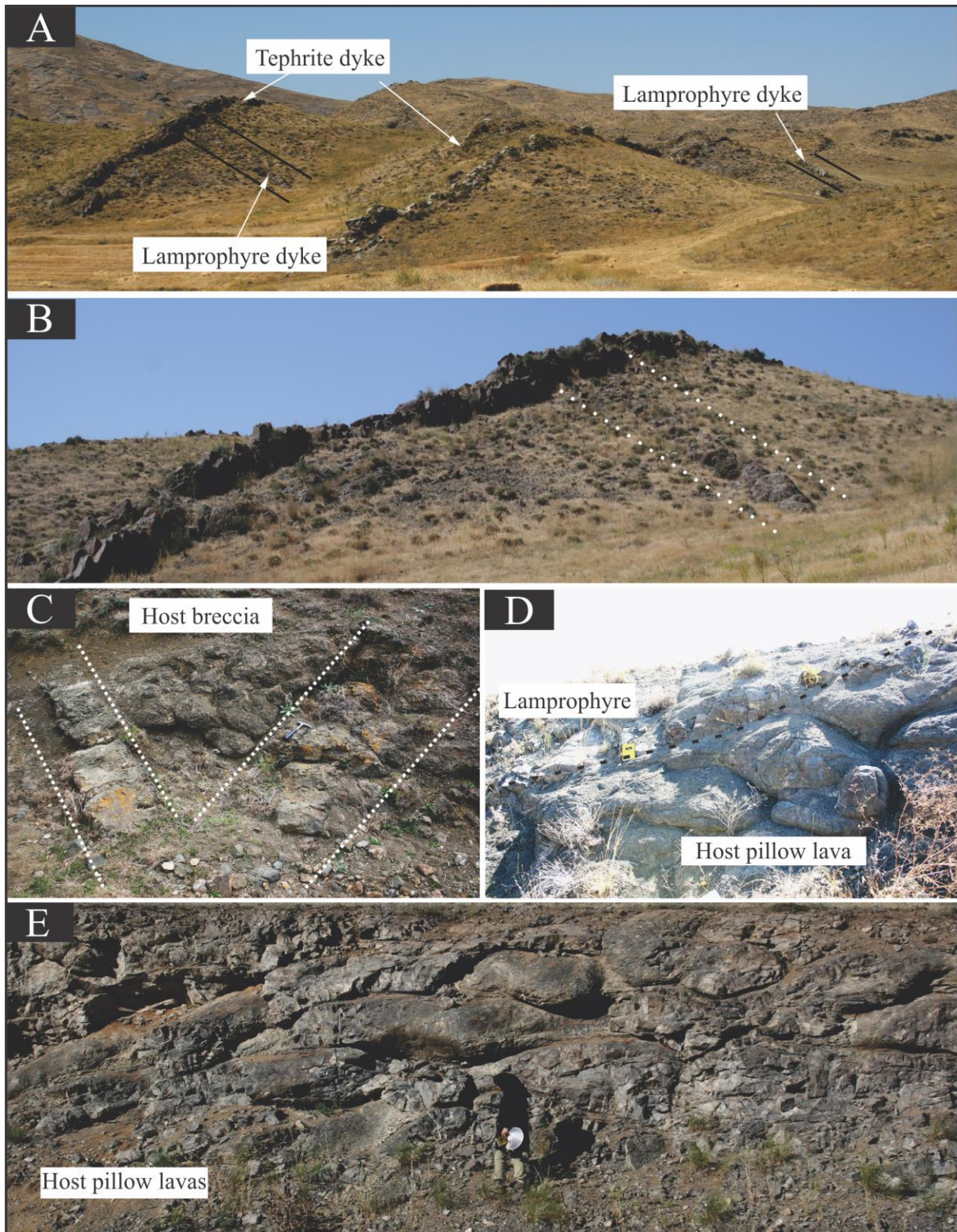


Figure 2.3 Field photographs. (A-D) outcrops of tephrite and lamprophyre dykes with different orientations cross-cutting the host breccia and pillow lavas (Ha) in the Salavat Range. (E) The pillow structure (Hb) vary in size and shape, they distinguished from those of host lavas (Ha) cross-cut by dykes (see text).

Tephrite dykes frequently cross cut lamprophyre dykes with high-angle contact and are well distinguished from lamprophyres by horizontal columnar joints structures (Figs 2.4 b and e). K/Ar whole rock geochronology on tephrite dykes gave ages ranging from 42.7 to 38.4 Ma (Alberti *et al.*, 1976). Tephrite dykes cut both lamprophyre and host lavas, but the cross-cutting relationships of dykes with those host pillow lavas (Hb) is not clear on the field.

2.2.2.3 Other lavas

The abundance of subaerial analcime-bearing lavas and pyroclastic eruptions is noteworthy in the Salavat Range, and it is known in Sabalan block for its outcrops of well-shaped crystals of analcime (e.g. Comin-Chiaramonti *et al.*, 1979). Similarly to Tephrite dykes, columnar joint structure are also observed in these lavas as radial and perpendicular columnar joint (Fig 2.5b). Stratigraphic relationships show this magmatic phase is younger than host lavas and dykes. However, the lavas covered by Oligo-Miocene clastic sandstone and conglomerate sediment (Fig 2.5a), in the lower part of sequences, contain similar clasts and consist of analcime-bearing lithologies (Fig 2.5c). Similarly in North of the Sabalan block, Late Cretaceous-Early Miocene basaltic flow and tuffaceous sandstone are covered by Oligo-Miocene sediments (e.g. Fotohi, 1973; Babakhani *et al.*, 1990; Jafarzadeh *et al.*, 2014). They are mostly composed of siliciclastic sandstone, conglomerate and shale, known as “Zivah” formations (see Jafarzadeh *et al.*, 2014) which crop out in Caucasus Mountain southward to the Allah yarlou-Hovai folded zone. In addition, similarly to analcime-bearing to analcimate lavas and pyroclastic they extend around 100 km along faults in the southern border of the Sabalan block (known as Bozkush Mountain: 3306 m). These lavas bounded by Cretaceous sedimentary sequence of the Talesh Mountain, which based on stratigraphy, are marked as Eocene or Oligocene volcanic eruptions in the geological reports (Lotfi, 1976; Lescuyer, 1978; Emami, 1992). However, the precise age of analcime-bearing lavas in the Salavat range remains unknown; the best we can say is that they belong to the Eocene –Oligocene period.

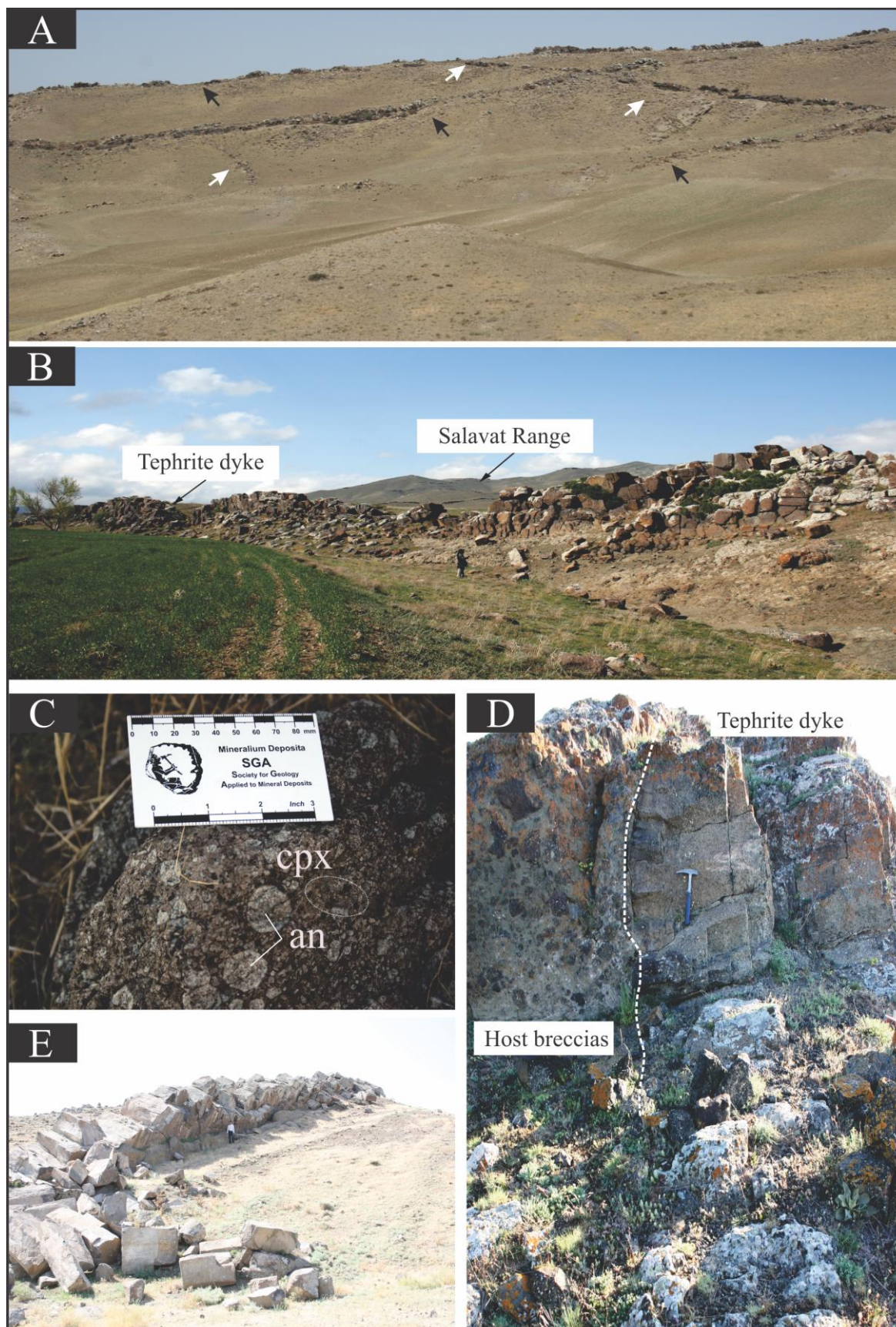


Figure 2.4 Field photographs. Tephrite dykes occur as multi directions linear structures crosscutting breccia host lavas with chilled margins (a and b). Dykes display horizontal columnar joint structure (a and e). Tephrite are highly porphyritic with analcime and clinopyroxene phenocrysts (c).

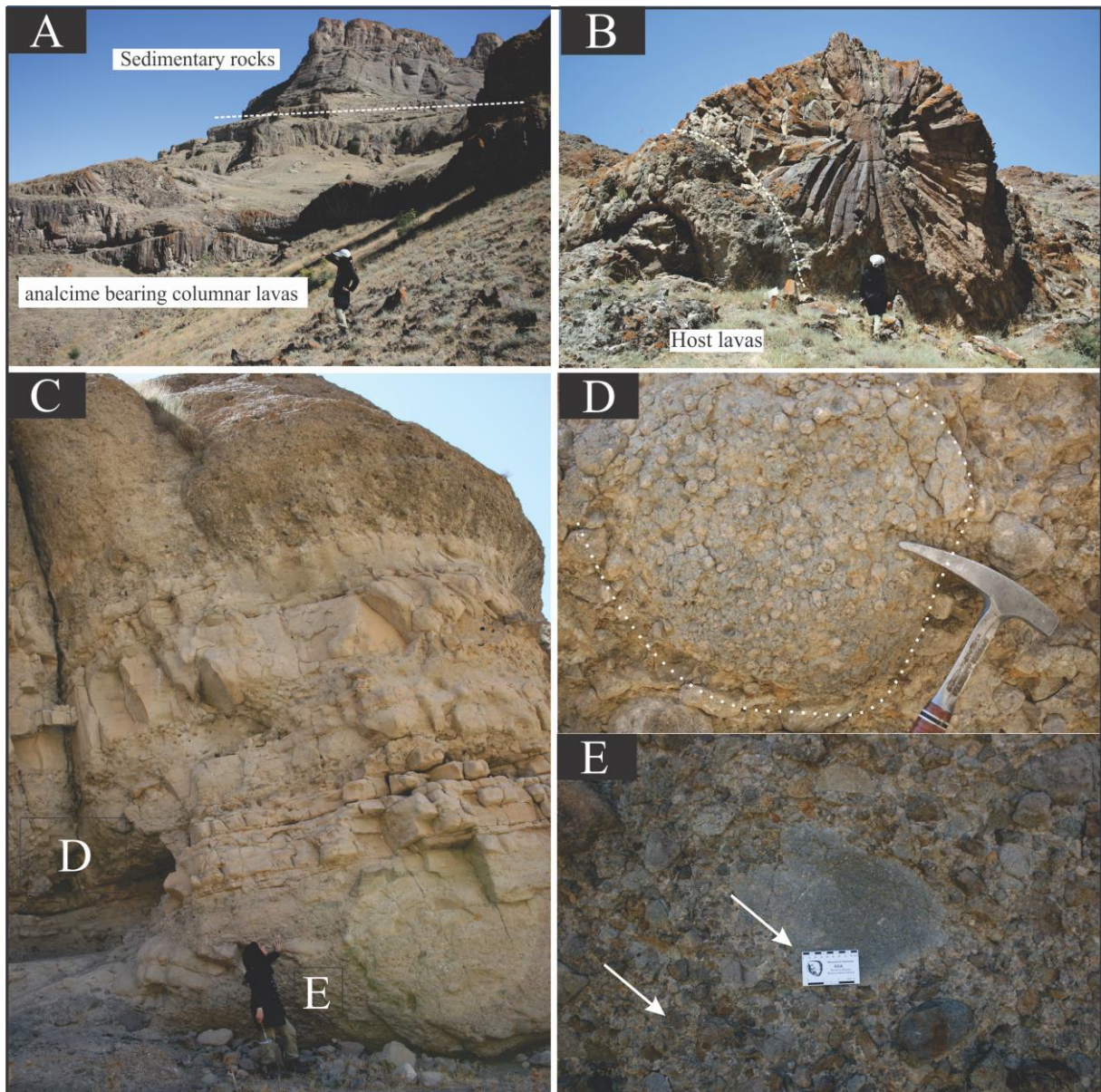


Figure 2. 5 Field photographs of analcime-bearing lavas in the eastern of Salavat Range. They display columnar joint structure (a and b). The lavas are covered by Oligo-Miocene sedimentary rocks (a). At the base of sequence, they consist of volcanic fragments including rock-forming minerals similar to those of analcime-bearing lavas (c, d and e).

2.2.2.3.1 Hornblende andesite

Close to the Salavat anticline, in the center of study area (Fig 2.2) there is an isolated volcanic outcrop consisting of highly porphyritic hornblende andesite containing few angular crustal xenoliths with sharp contact (Fig. 2.6b). In addition, they contain xenoliths with

assemblages of similar minerals than their andesitic host (Fig 2.6a). These lavas have no contact with isolated plutonic rocks around; they are significantly different from tephrites and lamprophyres in terms of mineral assemblages. The stratigraphic relationships of these lavas with other lithologies are difficult to specify (e.g. dykes).

2.2.2.4 Plutonic rocks

They are reported in the whole Sabalan block (around 800 km²). According to QAPF classification (Streckeisen, 1967) they include gabbros, monzogabbros, diorites and syenites. Zircon U-Pb ages of plutonic rocks from the whole of the Sabalan block range from 40.8 to 9.8 Ma (Ashrafi, 2009, Aghazadeh *et al.*, 2010; Alberti *et al.*, 1976). In the southern part of the Salavat Range, intrusion of gabbros, monzonites and granites dated at 28 Ma. Finally, syenite intrusions emplaced as last plutonic phases at around 24-26 Ma (Aghazadeh *et al.*, 2010, 2011). In the Salavat Range, plutons are mainly exposed in the Moradlou, Salavat, Hassan kandi villages (Fig.2.2) as gabbro, monzogabbro, diorite, and alkali feldspar syenite. They occur principally as large bodies and as micro dykes cross cutting host lavas or earlier plutonic rock (Fig. 2.6). In the study area, no clear contact between plutonic intrusions and tephrite and lamprophyre dykes are observed, however, Aghazadeh *et al.* (2010) reported lamprophyre dykes at 23 Ma crossing monzonites intrusions in the south of the Salavat Range. In most outcrops, plutons have uniform medium to coarse-grained granular texture with mafic-intermediate compositions, cross cut by more evolved compositions. For example, olivine monzogabbro plutons in the ArtanKandi (see Fig.2.2) crop out as isolated rounded body, toward inner part its composition changes to alkali feldspar syenite (Fig 2.6c).

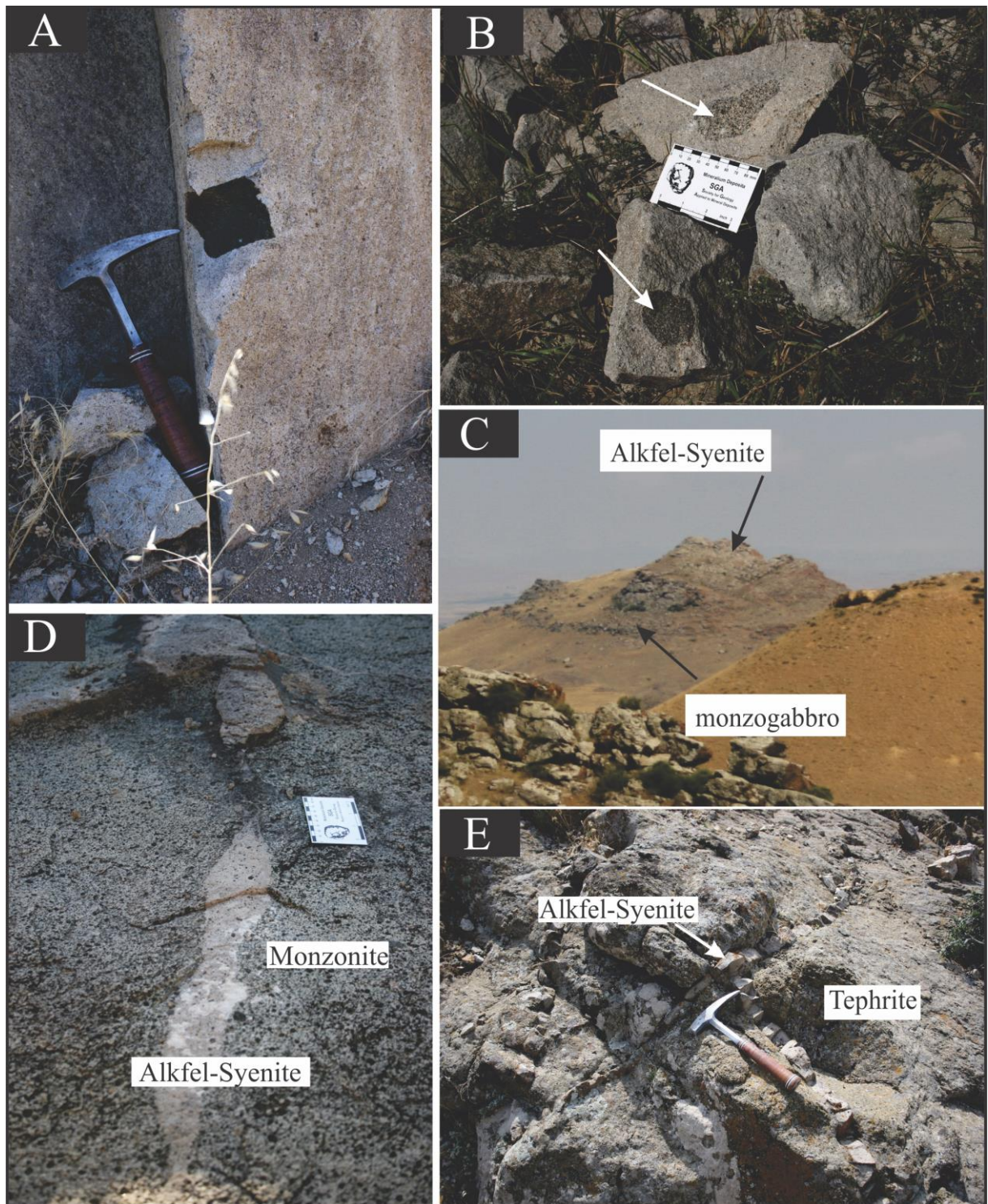


Figure 2.6 Field photographs of hornblende andesite and intrusions. A) crustal xenoliths and b) amphibole-rich cumulative xenoliths in hornblende andesites. C) A zoned intrusive body in the Artankandi showing a felsic alkali feldspar syenite surrounded by a mafic intrusion (monzogabbro). D) and e) similar felsic lithology observed in the Mirzahasan Kandi, as microdykes (Alkali feldspar syenites) cross-cutting monzonite body or tephrite lavas.

In addition, similar heterogeneous lithologies occur in a large monzonite body in the Mirzahasan kandi village, which is cross cutted by alkali feldspar syenite micro dykes (Fig. 2.6d).

2.3 SAMPLE PREPARATION AND ANALYTICAL TECHNIQUES

Sampling was carried out within the 1/100,000e geological map of Lahrud along stratigraphy profiles cross cutting the Salavat range. I sampled mainly Cenozoic magmatic rocks, a total of 150 representative fresh samples from the main outcrops in Gharnh valilou, Zargargoli boulaq, Chaqir chaman, Emaratlou, Toumarkandi, Salavat, Moradlu, Mirzahasan kandi, Artankandi (Fig 2.2). After petrographic observation, these lithologies were identified as: lamprophyre, tephrite, analcime-bearing tephrite, phonolite, analcimite, hornblende andesite, gabbro, monzonite and alkali feldspar syenite.

2.3.1 ICP-AES

The major element bulk rocks compositions of 44 samples were analyzed at the ALS geochemical laboratory, Sevilla, Spain. A prepared sample (0.200 g) was added to lithium metaborate/lithium tetraborate flux (0.90 g), mixed well and fused in a furnace at 1000°C. The resulting melt was then cooled and dissolved in 100 ml of 4% nitric acid 2% hydrochloric acid. This solution was then analyzed by ICP-AES and the results corrected for spectral inter-element interferences. Oxide concentration was calculated from the determined elemental concentration. The total oxide content was also determined from the ICP analyses concentrations and loss on Ignition (L.O.I.) values. A prepared sample (1.0 g) was placed in an oven at 1000°C for one hour, cooled and then weighed. The percent loss on ignition was calculated from the difference in weight.

2.3.2 Inductively coupled plasma mass spectrometry (ICP-MS)

100 mg of investigated whole-rock powders and rock reference materials (BEN, DRN), were weighted into Savillex Teflon vials then dissolved in ultrapure concentrated HF-HNO₃ 1/1 ml at 85° C for 48h, dried and then dissolved/evaporated in 1ml HNO₃ at 80° C for 12 hours. Dried samples were diluted into 7ml 6N HCl. An aliquot of this solution was weighted and spiked with Tm, dried and then diluted into 30 ml HNO₃ 0.37N before analysis. All processes for the sample solutions were carried out in the clean room of Geosciences Environment Toulouse (GET). The trace element contents of the sample solutions were analyzed by using the ICP-MS 7500ce Agilent from GET. A blank solution was prepared and systematically subtracted to the sample signal. Concentrations were calculated following the Barrat et al. (1996) procedure.

2.3.4 Thermal Ionization Mass Spectrometer (TIMS)

Sixteen samples selected following the same procedure as for trace elements. After weighting 50 mg of powder (according to the amount of Sr and Nd present in the sample and measured by ICPMS), the solid residue was taken up with 1 ml 2N HNO₃, and centrifuged (5mn). The sample solution was loaded into 0.3 ml Sr-Spec column stacked on 0.3 ml TRU-spec column. Each column was previously washed before used. The Sr and REE fractions were extracted using HNO₃ 0.05N and H₂O respectively, after matrix removal. Then REE fraction was dried, dissolved in 0.25N HCl and loaded in 300 mg Ln-Spec column for Nd elution (Pin *et al.*, 1997). Sr and Nd fractions were dried before filament loading. Nd and Sr fractions were analyzed by using the Finnigan MAT 261 from GET. Sr was loaded on W filament covered with Ta activator and run in static mode. Nd was loaded on Re filament and run in static mode using double Re configuration. International standards are run on a daily basis in order to check

for measurement accuracy. The mean value for NBS 987 is $^{87}\text{Sr}/^{86}\text{Sr}$: 0.710255 +/-35 and for La Jolla $^{143}\text{Nd}/^{144}\text{Nd}$: 0.511856 +/-20. Typical blanks are 300 mg for Sr and 20 mg for Nd.

2.3.5 Element Mapping

The electron microprobe allows quantitative analysis with accuracy of about $\pm 1\%$ for major elements, while detection limits ranging from 20 to 1000 ppm can be attained for minor and trace elements. The spatial resolution is approximately 1 μm . Element distribution line scans and 2-dimensional 'maps' were produced at the "Centre de Microcaractérisation Raimond Castaing", UMS-CNRS 3623, Paul Sabatier University, Toulouse. The Electron Microprobe used in this study is a CAMECA SXFive with one energy dispersive and 5 wavelength dispersive spectrometers, capable of automated quantitative analysis and elemental map for Mg, Si, Ti, Cr, Fe, Ca, and Al.

2.3.6 Laser-ablation coupled plasma mass spectrometry (LA-ICP-MS) analysis

Trace element concentrations in minerals were determined by laser ablation inductively coupled plasma mass spectrometry, using a NWR213 Laser Ablation system coupled to a Thermo ELEMENT XR ICP-MS system at GET (CNRS-CNES-IRD-Paul Sabatier University). Calibration and quantification techniques for LA-ICP-MS involve combinations of internal standardization and external reference materials because of the transient nature of the LA-ICP-MS signals. (e.g. Longerich *et al.*, 1997). The silicate certified reference materials (CRMs) included in this study was obtained from the National Institute of Standard and Technology (NIST). The reference materials used as external standards are synthetic calcium-sodium aluminosilicate glasses with concentration of approximately 400 ppm (NIST 610) and 40 ppm

(NIST 612) for a wide range of trace elements. Ca values determined by electron microprobe was used an internal standard for clinopyroxene analyses. Target crystals free from mineral inclusions and exsolutions were analysed on petrographic thin section 100 microns thick in order to keep the textural relationships. The ablation was carried out in a He atmosphere. The laser-spot diameter was 50 μm , energy of laser ablation 10 Hz, and fluence of 12 Jcm^{-2} (energy density). Scanning rate of 30 mm/s was used. Details of the analytical method have been described by Morishita et al. (2005).

2.4 RESULTS

2.4.1 Petrography

About 200 thin sections from all Cenozoic lithologies were examined. They were classified according to the IUGS classification scheme (Le Maitre, 2002) and to Mitchell & Bergman, (1991) and Woolley et al. (1996) scheme for exotic alkaline rocks. Field occurrence and petrography concurred to classify rocks into basaltic andesite lavas, lamprophyre (kersantite and minette) and tephrite dykes, analcime-bearing phonolite, analcimite lavas and hornblende andesite lavas and intrusions as microgabbro, monzogabbro, monzonite and alkali feldspar syenite.

2.4.1.1 Lavas

2.4.1.1.1 Andesitic basalt (host)

All lavas are porphyritic in texture with microlitic to hyalomicrolitic groundmass. However, in breccia, a heterogeneous magmatic texture due to mingling is observed (Fig. 2.7a). The phenocrysts assemblages is dominated by zoned euhedral clinopyroxene and plagioclase

varying in size from 2 mm to < 1 mm and 1mm to < ~0.3 mm, respectively. Microlithic clinopyroxene, plagioclase and Fe-Ti oxides set in a fine-grained groundmass. Carbonate and analcime are secondary minerals filling vesicles and ranging from 0.1 to 1 mm in size. Clinopyroxene phenocrysts are mostly grass colored, oscillatory-zoned, and rarely form colorless, non-zoned crystals. Samples with mingling texture, including globules of microlithic feldspar, contain few non-zoned clinopyroxene with Fe-Ti oxides set in the altered glass. However, evidence of mingling is never observed in fresh lavas with pillow structures (Figs. 2.7 c-d). In these lavas phenocrysts are strongly oscillatory zoned and occur in a hyaline groundmass marked by quenched clinopyroxene and “*swallow-tailed*” plagioclase (Fig. 2.7d).

2.4.1.1.2 Lamprophyre

Lamprophyre with euhedral phenocrysts of various size (3 mm to <1 mm) display typical panidiomorphic porphyritic textures (Fig. 2.8). Based on the petrography and classification scheme for lamprophyres (e.g. Mitchell & Bergman, 1991, Rock, 1991), they divided into Kersantite and Minette.

Kersantites; clinopyroxene and phlogopite as the most abundant mafic phases occasionally associated to amphibole and plagioclase are the main minerals in the studied kersantites (Figs. 2.8a-c). The groundmass consists of microcrystalline clinopyroxene, phlogopite and varying modes of feldspar and glass. Abundance of plagioclase dramatically decreases when the mode of mafic minerals (e.g cpx or phlogopite) increases. Fe-Ti oxides and apatite with variable grain size occur as both microphenocrysts and in the groundmass. Clinopyroxene displays a strong zoning. They are typically grass colored oscillatory-zoned grains; however, some clinopyroxene have optical zoning with colorless (Fig. 2.8b).

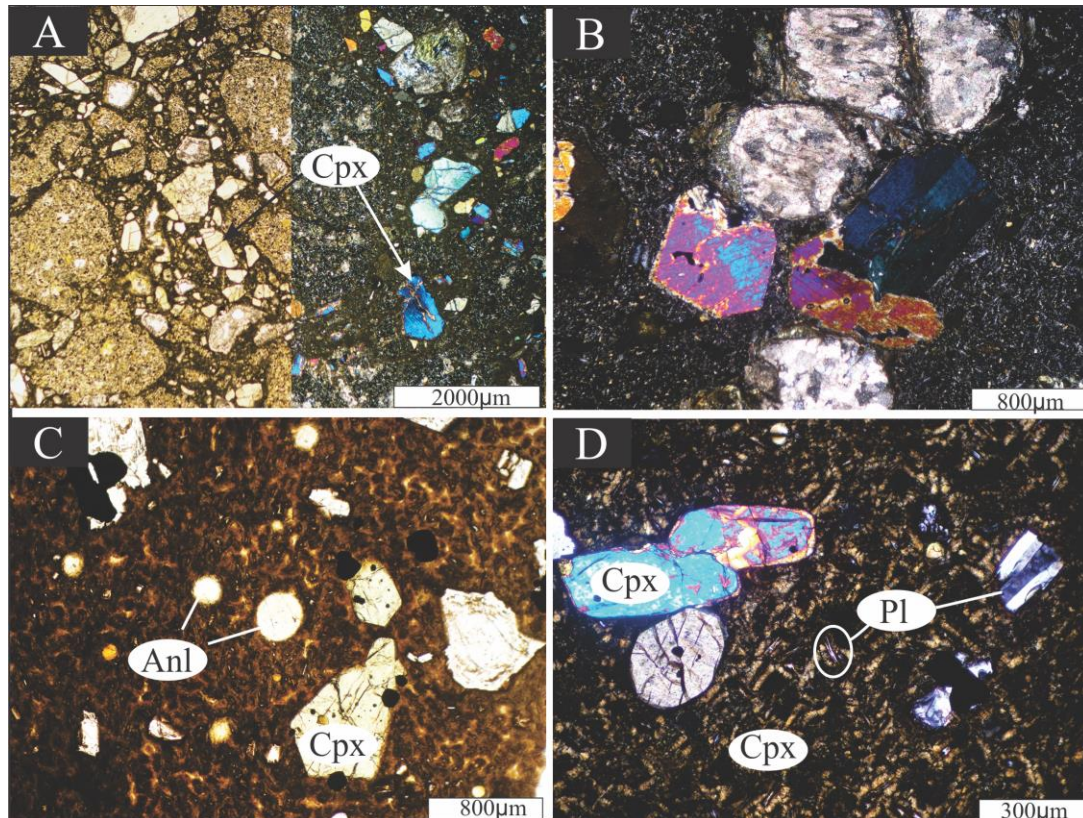


Figure 2.7 Photomicrographs of host lavas. A-B) heterogeneous magmatic texture consisting of zoned clinopyroxene (cpx) phenocrysts. C-D) clinopyroxene phenocrysts in lavas with pillow structures, arrows point to vesicles filled by analcime (anl) and circle points to swallow-tailed plagioclase (pl) in the groundmass.

Sometimes some colorless areas appear within the core of crystal and are mantled by green areas. In all cases transition between colors are abrupt with irregular boundary. Phlogopite frequently form euhedral to subhedral crystals (Fig. 2.8a) showing no evidence of strain (kink-band, undulose extinction), optical zoning. They mainly oriented in the magmatic flow. The brown-green euhedral to subhedral amphibole are zoned and contained inclusions of clinopyroxene and Fe-Ti oxides. Occasionally, oscillatory zoned phenocrysts of plagioclase (up to 1.5 mm in diameter) were observed; they are anhedral semi rounded crystals with corrosion textures.

Minettes similarly to kersantite in term of major phenocrysts consist mostly of clinopyroxene and phlogopite. However, amphibole or plagioclase are absent in the minette.

Sanidine is the sole feldspar in these rocks and restricted to the groundmass. In addition, clinopyroxene, phlogopite, Fe-Ti oxides and apatite appear in the groundmass, whereas

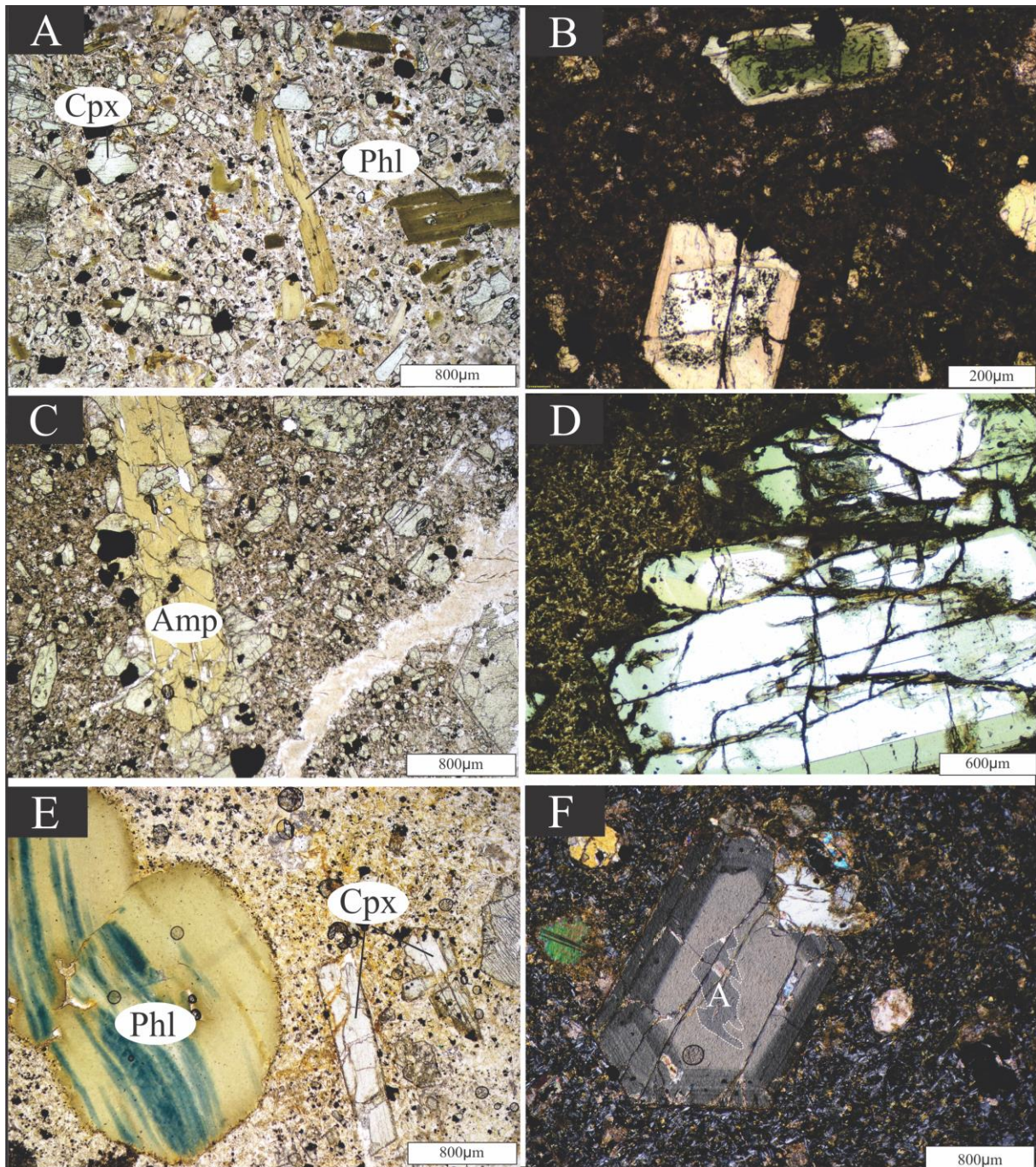


Figure 2.8 Photomicrographs of kersantite (A-C) and minette (D-F) lamprophyres. A) Typical phaneritic porphyritic texture with clinopyroxene (cpx) and phlogopite (phl) lath phenocrysts. B) Zoned colorless and green colored clinopyroxenes occur as macrocrysts in the same samples (M-113). C) Amphibole (amp) phenocrysts including cpx. D-F) oscillatory zoned macrocrysts of clinopyroxenes with colorless zone and corroded edge (A) mantled by green colored zone. E) Resorbed phlogopite evidences the disequilibrium with surrounding groundmass.

accessory minerals (e.g. apatite and Fe-Ti oxides) also occur as prismatic, needle-like microphenocrysts or as inclusion in phenocrysts. Moreover, there are assemblages of K-feldspar, calcite and secondary hydrous aluminosilicate minerals, pink in color, filling amygdaloidal vesicles. Clinopyroxene similar to the ones in kersantites present the same oscillatory zoning than grass green phenocrysts whereas clinopyroxenes with colorless cores appear as megacrysts, similar to the ones in kersantite; they present an abrupt optical zoning from colorless core to grass green overgrowth (Figs. 2.8d-f). Clinopyroxene with green cores are absent in minettes. Phlogopite appears mainly as macrocrysts and shows disequilibrium texture with groundmass highlighted by fine-grained Fe-Ti oxides occurring along the phlogopite rim (Fig. 2.8e). However, biotite appears as tabular lath shaped microphenocryst in equilibrium with the groundmass. They are similar to those occurring in kersantites.

2.4.1.1.3 Tephrite

Most samples can be classified as tephrites and more rarely as phonotephrites. They are highly porphyritic with phenocrysts of 1-2 mm in size. They are characterized by phenocrysts of clinopyroxene, analcite, and rare olivine and plagioclase with accessory minerals (e.g. apatite and Fe-Ti oxides) (Figs. 2.9a-d). Colorless clinopyroxene cores occur in tephrite such as in lamprophyres; they have similar petrographic features than those identify for kersantite and megaphenocryst in minette (colorless core and pale grass green rim). In addition, colorless areas appear in clinopyroxene as bright bands in between grass green oscillatory-zoned parts (Figs. 2.9a-b). Analcime is the second dominant mineral and the only feldspathoid similarly to all studied rocks from the Salavat Range. They form subhedral polyhedral phenocryst, occasionally enveloped by clinopyroxenes whereas in groundmass, analcime frequently appears as irregular patches. Olivine is rarely observed (< 2-3 %), generally as microphenocrysts. In rare phenocrysts, they are subhedral with embayment edge mantled by

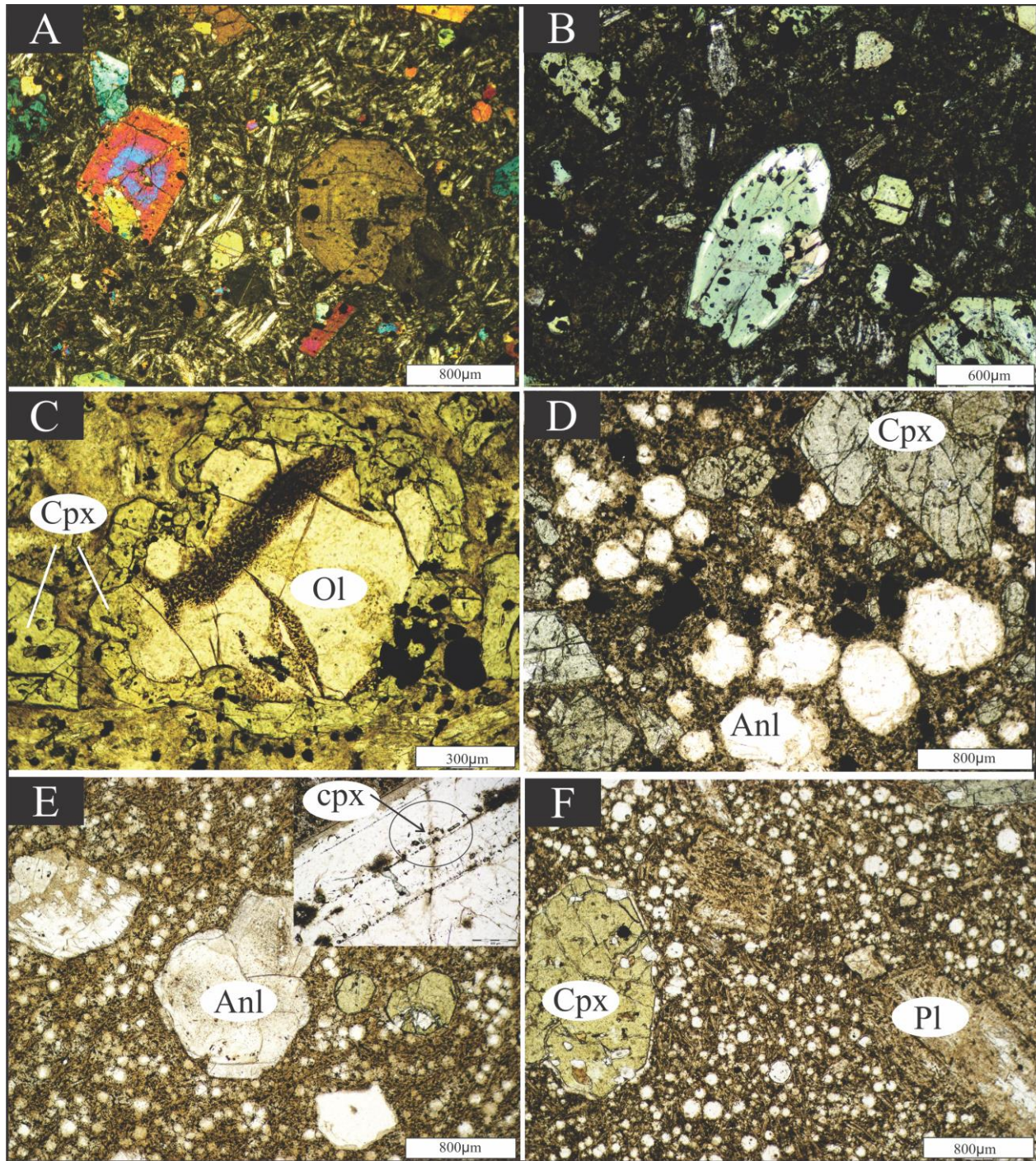


Figure 2.9 Photomicrographs of tephrite dykes (A-D) and analcimite lavas and breccias (E-F). A-B) green-colored zoned clinopyroxene (cpx) with colorless bright band. C) Olivine (ol) macrocrysts mantled by clinopyroxene. D) Occurrence of analcime as phenocrysts and microphenocrysts. E-F) Porphyritic texture of analcimite (anl) consists of clinopyroxene and analcime. Arrow points to clinopyroxene and apatite hosted in the crystal growth zone of analcime.

clinopyroxene (Fig. 2.9c). Microcrystalline groundmass is mostly composed by similar minerals as the phenocrysts; plagioclase and more rarely K-feldspar are common as microlitic laths associated to apatite, Fe-Ti oxide, and rarely needles of biotite.

2.4.1.1.4 Anacimite and analcime-bearing phonolite

Based on petrography, analcime-bearing lavas and breccias are classified as phonolite to phonotephrite, or analcimite. They have porphyritic to hyalomicroporphyritic or glomeroporphyritic textures. They consist of clinopyroxene+ plagioclase+ sanidine+ analcime+ Fe-Ti oxide+apatite (Figs. 2.9e-f). Clinopyroxene is the only mafic mineral in these lavas. Similarly to tephrite, euhedral clinopyroxene are green colored and highly oscillatory zoned. Colorless clinopyroxene does not occur in these lavas. The abundance of clinopyroxene and Fe-Ti oxides dramatically drops from phonotephrite to phonolite and analcimite. Analcime appears as characteristic well developed six-sided crystals ranging in size from 1 mm to 2 for phenocrysts, ~0.4 mm for microphenocrysts, and less than 0.2 mm for microliths. Plagioclase occurring as euhedral phenocryst displays sieve texture with oscillatory zoning in phonotephrite, while it is absent in analcimite. Analcime and alkali feldspar are the main component of groundmass. Accessory mineral (e.g apatite) and/or major minerals (e.g. Cpx, Feldspar) appear as inclusions in analcime (Fig. 2.9e). Zeolite, clay minerals, and calcite are common secondary minerals.

2.4.1.1.5 Hornblende andesite

Andesites from the Salavat range are all highly porphyritic (~ 30 % phenocrysts) with crystalline groundmass. The primary phenocrysts are large (up to 2.5 mm in size), zoned plagioclase and amphibole with rare biotite (Fig. 2.10). In addition to complex zoning witnesses for unstable magmatic conditions (P-T-X) occur. Indeed amphibole are partly or completely

altered to opaque-rich rim. Disequilibrium textures also appear in plagioclase as sieved texture. Occasionally an overgrowth rim of alkali feldspar surrounds complex zoned plagioclase. Plagioclase, amphibole, rare biotite and Fe-Ti oxides phenocrysts set in finer groundmass of dominantly feldspar with minor amphibole (Fig. 2.10a). Cumulate and crustal xenoliths, frequently occur in andesite samples. A cumulate xenolith contain abundant feldspar and amphibole and rare Fe-Ti oxides similar to their phenocryst counterparts (Fig. 2.10b). Clinopyroxene does not occur in andesite samples, but they occur rarely in some cumulate xenoliths consisting of clinopyroxene, biotite, amphibole and Fe-Ti oxides (Fig. 2.10c). The latter mineral assemblage are obviously different from mineral assemblages from the host lava.

2.4.1.2 Plutonic rocks

Plutonic rocks are microgabbro, monzogabbro, monzonite, and alkali feldspar syenite.

2.4.1.2.1 Microgabbro

They are holocrystalline. Clinopyroxene and plagioclase are the dominant phases. Clinopyroxene is subhedral to euhedral, pale green and, with the angular networks of plagioclase lath intergrowth contribute to the ophitic or subophitic texture of these rocks. Clinopyroxene is weakly zoned, whereas plagioclase is not. Most of them are twinned. Other phases include accessory Fe-Ti oxides, rare apatite with secondary minerals; carbonate, chlorite, and amphibole.

2.4.1.2.2 Olivine monzogabbro

They are also holocrystalline. Mineral assemblages consist of olivine, clinopyroxene, alkali feldspar, plagioclase, biotite, apatite, and opaque minerals. They form hypidiomorph,

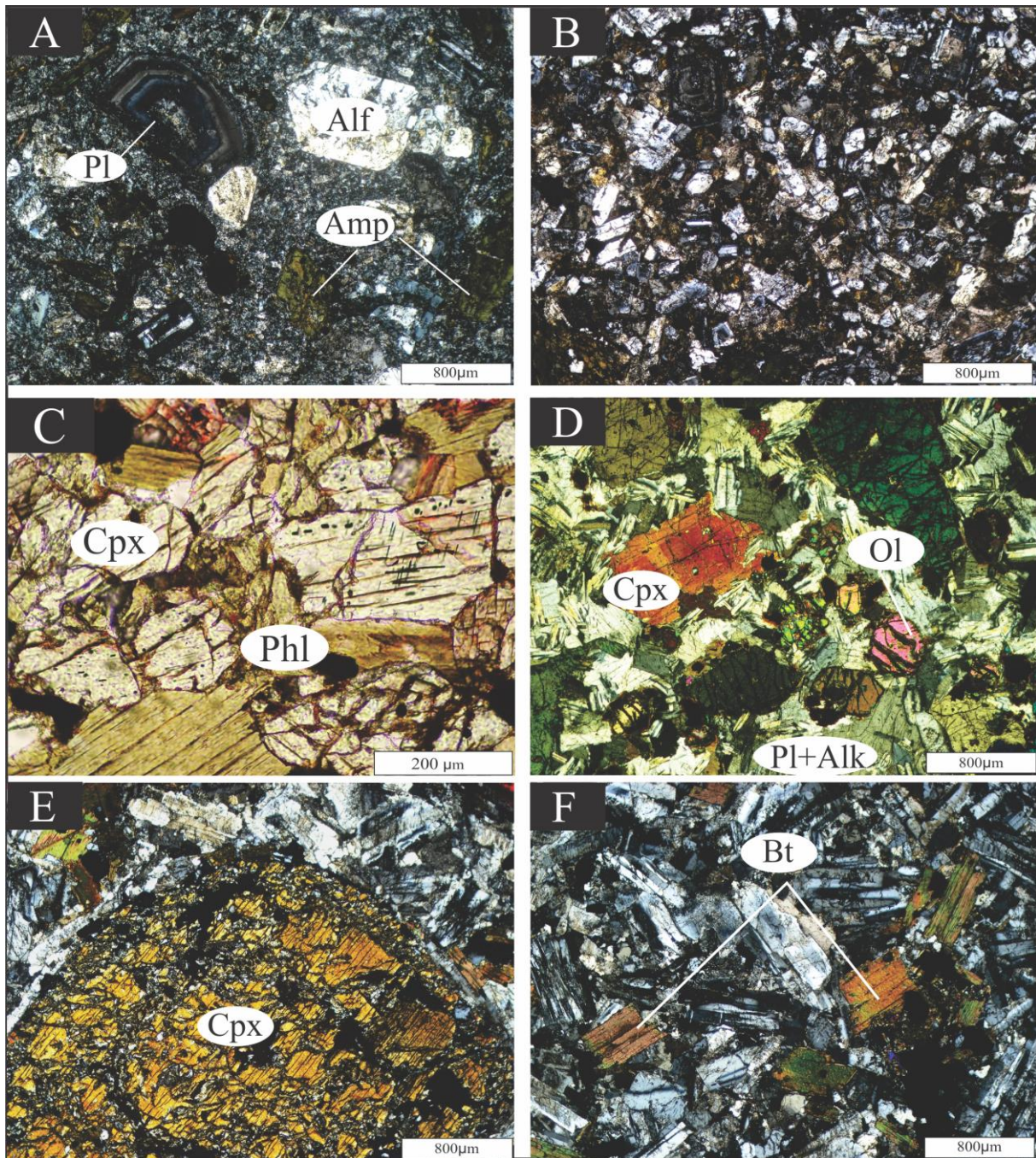


Figure 2.10 Photomicrographs of hornblende andesite (A), associated cumulates (B), xenoliths (C) and intrusions (D-F). A) Zoned plagioclase (pl) and amphibole (amp) phenocrysts. B) cumulates with similar mineral assemblage than the hornblende andesite host, C) xenoliths consisting of clinopyroxene (cpx) and phlogopite (phl). D) Olivine (ol) and zoned clinopyroxene represent the main mafic minerals in the monzogabbro. E) clinopyroxene in monzonite D) biotite (bt) and feldspar laths in alkali feldspar syenite.

coarse-grained textures. Olivine and clinopyroxene constitute the mafic mineral assemblage (Fig. 2.10d); olivine occurs as minor, undeformed, magmatic, anhedral to subhedral crystals. It

is frequently altered to secondary iddingsite and occasionally to serpentine. Green clinopyroxene with average size of up to 2cm and patchy core shows slight zoning. The laths of feldspars form poikilitic textures.

2.4.1.2.3 Monzonites

Their medium to coarse-grained component are commonly plagioclase and alkali feldspar with subordinate amount of clinopyroxene and biotite. Apatite and opaque minerals are present as accessory phases. They are very similar to olivine monzogabbros, but clinopyroxene is mainly surrounded by alkali K-feldspar laths and reaches a few centimeters in size (Fig.2.10e).

2.4.1.2.4 Alk feldspar syenites

They display coarse grained granular to porphyritic texture with medium grained crystalline groundmass in microsyenite. Main constituents are essentially subhedral to euhedral lath of alkali feldspars and more rarely of plagioclase. Mafic minerals are insignificant. Indeed only minor biotite and rare amphibole and clinopyroxene occur as anhedral minerals (Fig. 2.10f). Quartz is entirely absent. Zircon, Titanite, Fe-Ti oxides are accessory minerals (less 3%).

2.4.2 Mineral chemistry

2.4.2.1 Host lavas

2.4.2.1.1 Clinopyroxene

All analysed clinopyroxenes from the host lavas are plotted on Mg# versus major oxides (CaO, Al₂O₃, TiO₂, and Na₂O) diagrams (Fig. 2.11). Clinopyroxene are characterized by Mg# > 0.7, CaO ~24 – 22 wt%, low TiO₂ (< 1.5 wt%), Cr₂O₃ < 0.15 wt%, and varied Al₂O₃ (2-7 wt%).

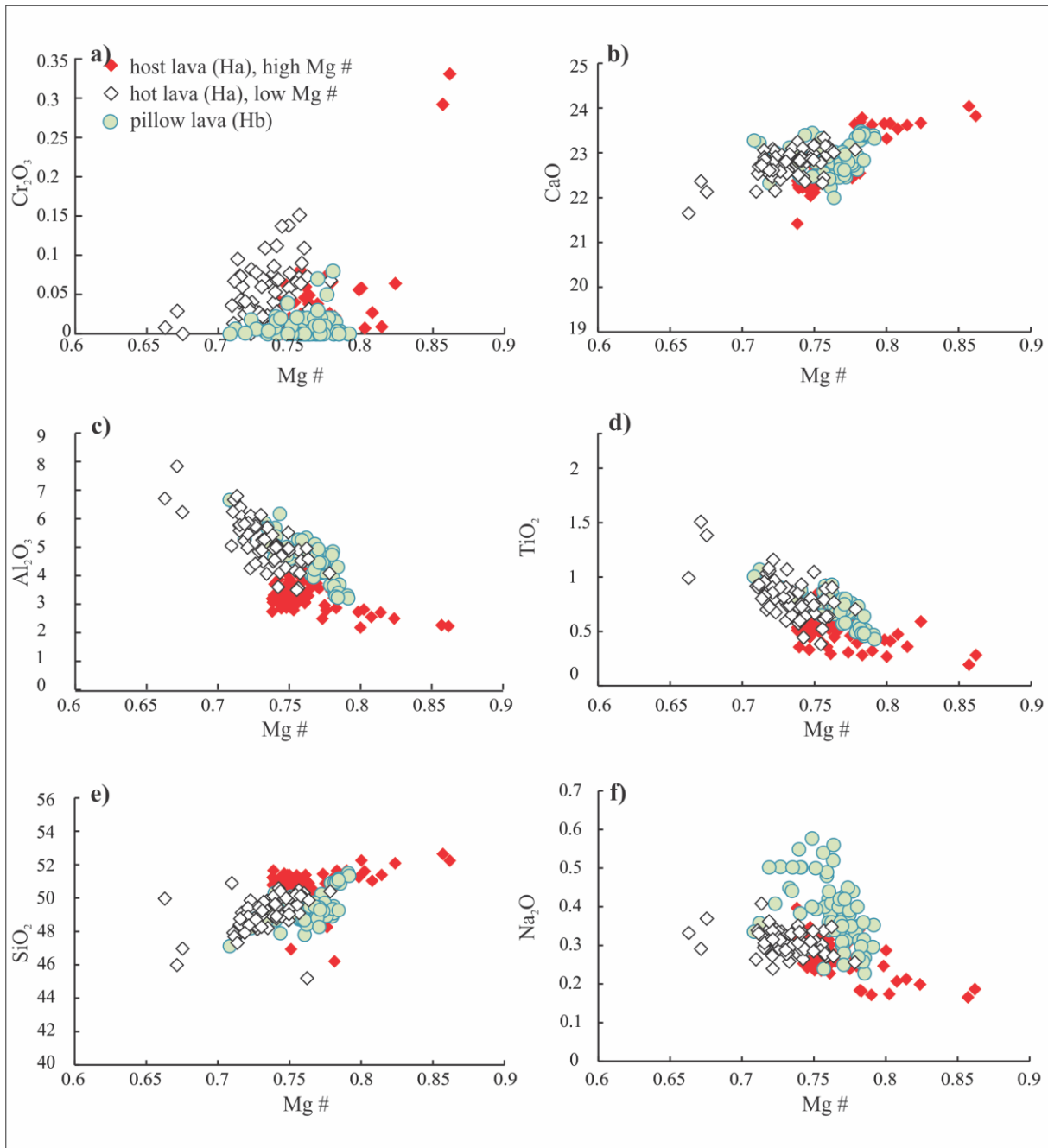


Figure 2.11 Major elements compositions versus Mg# for clinopyroxene of host lavas.

The overall trend follows very common trajectories that may be interpreted as fractional crystallization trends with TiO₂, Al₂O₃ and Na₂O increasing with decreasing Mg#. These trends are regular with the exception of slight drops or peaks in some oxides (e.g. SiO₂, Al₂O₃, Na₂O and Cr₂O₃) around Mg# 0.75. Henceforth, considering this point and slight change at ~Mg#

0.75 lead us to group the samples in the two categories i) high Mg# (>0.75), and ii) low Mg# (< 0.75). It is to highlight that those trends are not essentially following core to rim of crystals. Interestingly, high Mg # trend overlaps with colorless clinopyroxene (samples with mingling texture), whereas low Mg# are green clinopyroxenes (oscillatory zoned clinopyroxenes). Clinopyroxenes with high # Mg plot in the diopside field of the nomenclature of Morimoto et al. (1988), whereas those with low # Mg and oscillatory zoned clinopyroxene plot towards fassaite composition (Fig. 2.12c).

2.4.2.1.2 Plagioclase

Representative compositions of plagioclase in host basalt are presented in table 2 appendix. According to ternary plot of An-Ab-Or, feldspars are generally plagioclase with labradorite composition (Ab_{26.6-35.5} An_{59.1-69.9} Or_{3.3-5.2}), they have Na₂O ranging from 3.02 to 3.9 wt.% and FeO from 0.9 to 1.02 wt.%.

2.4.2.2 Lamprophyres

2.4.2.2.1 Clinopyroxene

As mentioned above, clinopyroxenes from both group of kersantite and minette display complex zoning features. They scatter in composition from diopside to fassaite (Fig. 2.12b). Moreover they plot in the field of worldwide lamproites and lamprophyres (Fig. 2.12). They are characterized by a heterogeneous composition in terms of major element compositions which highlights the large ranges from colorless to green colored clinopyroxenes with wide range of Mg# (0.9-0.85 and 0.80-0.65, respectively) and relatively low Cr content (Cr₂O₃<0.5). Elemental content of colorless clinopyroxene characterized by high Mg#, are generally restricted to a limited range with low values of TiO₂ and Al₂O₃ (< 0.4 and < 2 wt.%, respectively and Fig. 2.13). They are therefore characterized by Al₂O₃ > TiO₂, a specific feature of potassic

rocks, different from worldwide lamproites showing $Al_2O_3 < TiO_2$ (Rock, 1991). Whereas green-colored clinopyroxenes present generally a wider range with respect to the variations of the Mg# which is lower than the one of colorless clinopyroxenes (e.g. TiO_2 ; 0.2-1.4 wt.%; Al_2O_3 ; 2-8 wt.%). In general, all elemental trends in figure 2.13 are attributable to fractional crystallization. However, a significant compositional gap at $\sim Mg\# 0.8$ is diagnostic of additional processes controlling the elemental concentrations.

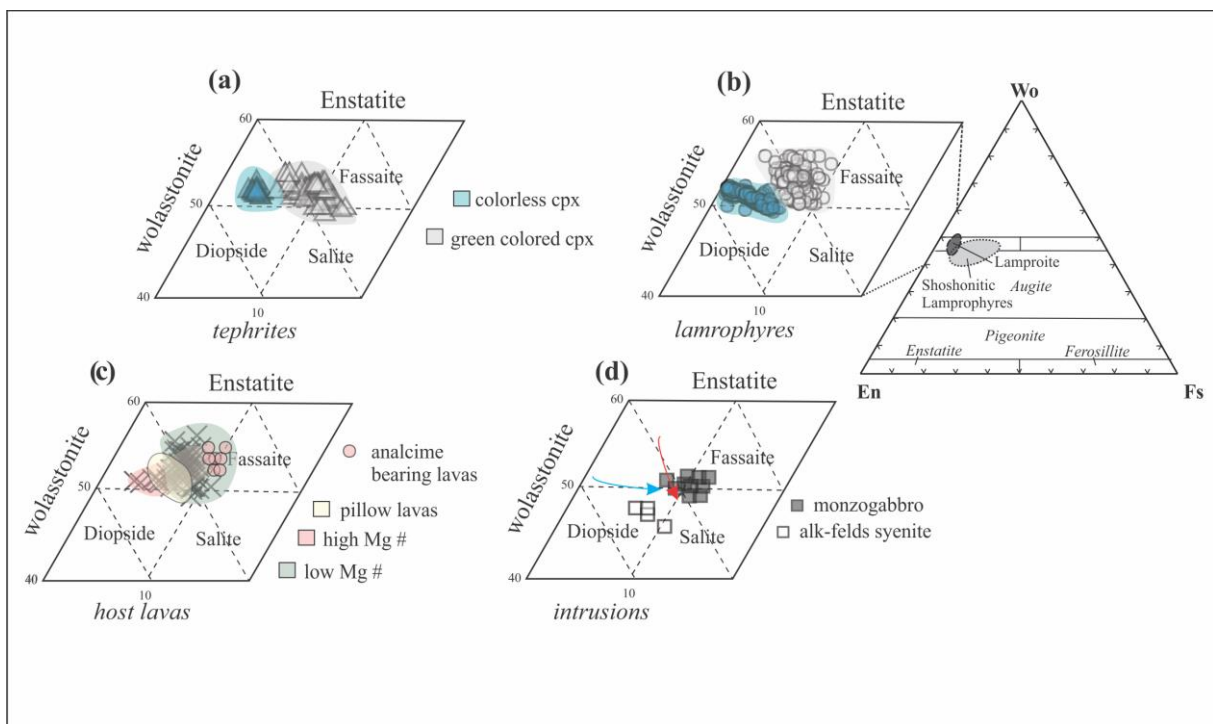


Figure 2.12 Chemical classification (Mg-Ca-Fe mol%) triangular diagrams for Clinopyroxene (after Morimoto et al., 1988), compositional fields from lamproite and lamprophyres are after Rock, 1991. a) clinopyroxene (cpx) from tephrite; b) cpx from lamprophyres; c) cpx from host lavas and analcime-bearing lavas and breccias; d) cpx from intrusions. The symbols and explanations for each group of lavas identify core and rim composition of phenocrysts and microcrysts in the groundmass.

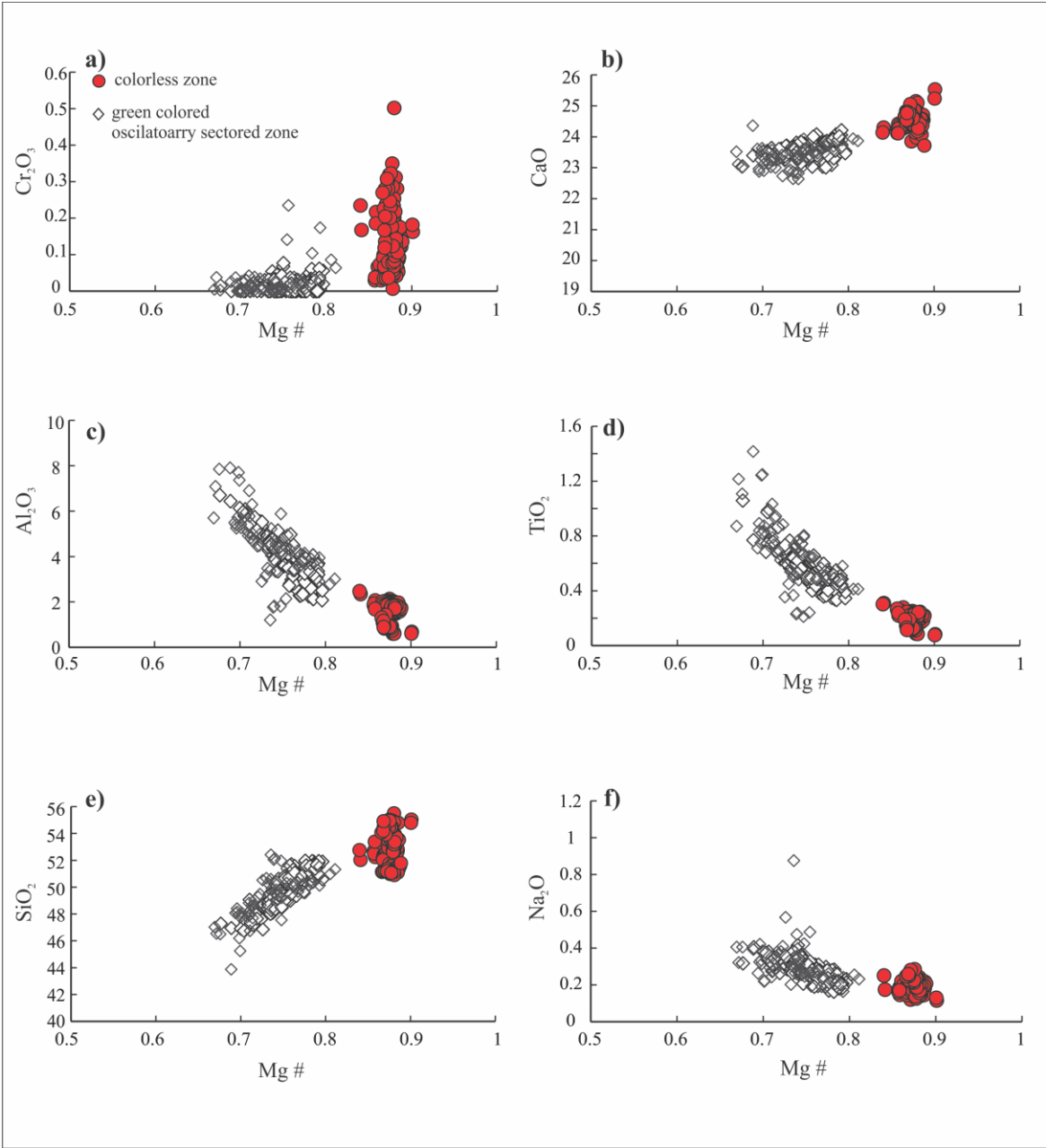


Figure 2.13 Major elements compositions versus Mg# for clinopyroxene of lamprophyres.

2.4.2.2.2 Biotite

Representative analyses of biotite occurring as phenocrysts and in groundmass in kersantite and minette lamprophyres are presented in table 3 appendix. They are all phlogopites with higher # Mg ($Mg/Mg+Fe^{+2}$; 0.73-0.82), Cr_2O_3 (0.06-0.6), lower TiO_2 (0.95-2.24) and Al_2O_3 (14.7-15.2) in minettes than in kersantite ($Mg\#$ 0.63-0.79; Cr_2O_3 0-0.2; TiO_2 1.33-3.9; Al_2O_3 14.1-16.07); in fact rarely phlogopites in kersantites (e.g. M-113) have composition close to those in minette. In both groups of lamprophyres. In all samples, there is no striking difference in composition between core and rim. Based on Mg-Fe-Al diagram (after Sheppard & Taylor, 1992), all analysed phlogopites plot in the field of phlogopite from shoshonitic lamprophyres and ultramafic lamprophyres, which are higher in Al than lamproites (Fig. 2.14).

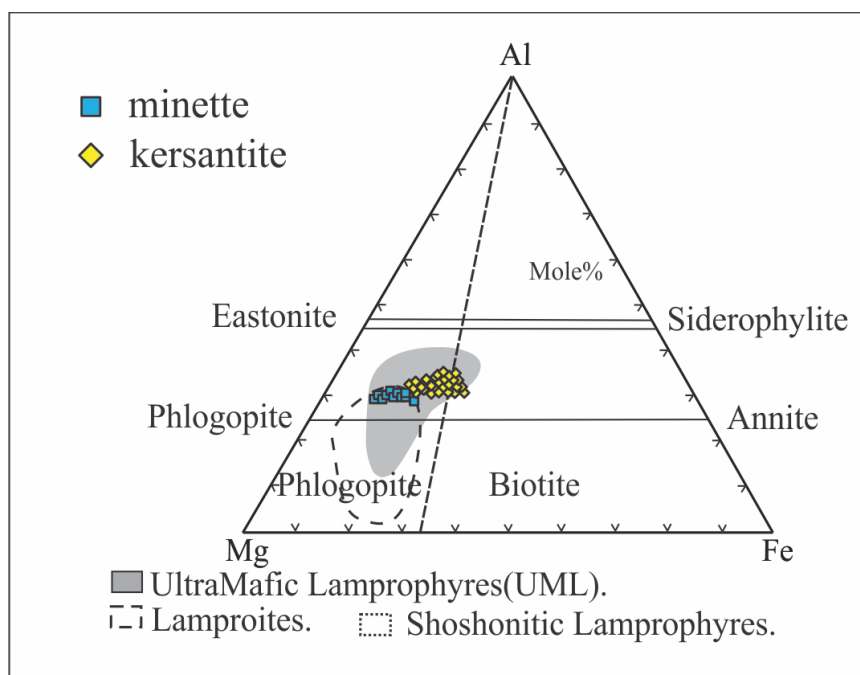


Figure 2.14 Mg-Fe-Al classification triangular diagram for mica in lamprophyres from the Salavat Range. The compositional fields for lamprophyre and lamproites are after Sheppard and Taylor (1992) and Rock (1991).

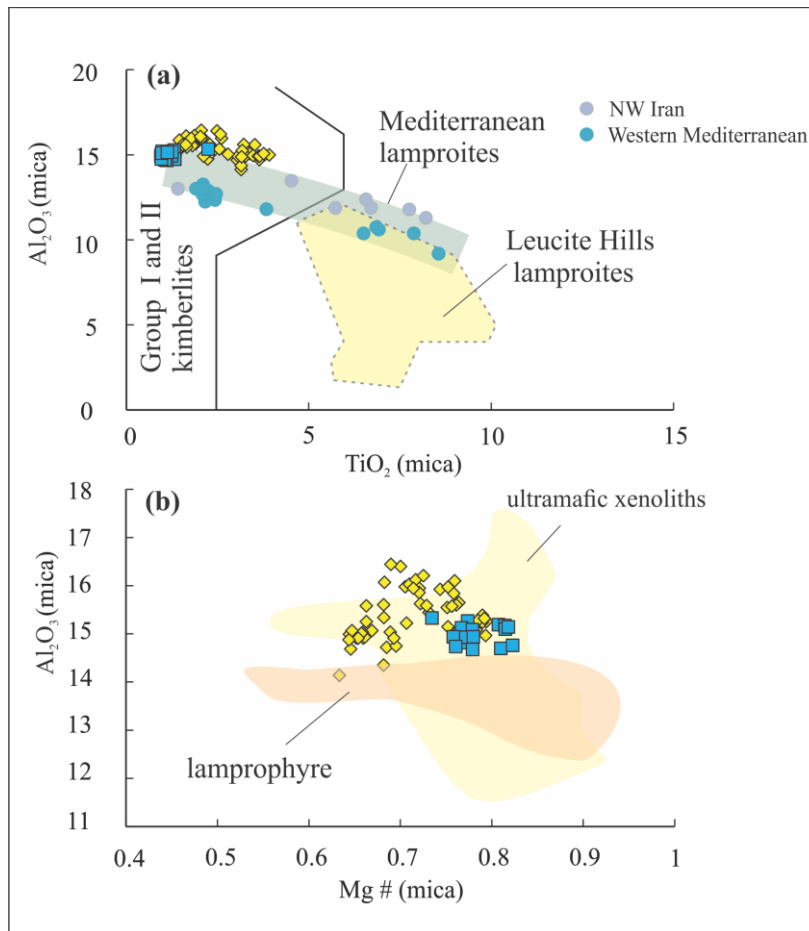


Figure 2.15 Major element variations of Al_2O_3 versus TiO_2 (a) and Mg# (b) for phlogopite in lamprophyres from the Salavat Range compared in particular with micas from kimberlite and Leucite Hills lamproites taken from Mitchell (1995) and Mitchell and Bergman (1991). Fields of micas from other regions are based on data from Mediterranean and NW Iran lamproites (Fritschle *et al.*, 2013; Shafaii Moghadam *et al.*, 2014), lamprophyre and ultramafic xenoliths (from Bucholz *et al.*, 2014 and reference therein).

The Al_2O_3 , Na_2O , FeO or TiO_2 diagrams adapted for the general field of exotic melts defined by natural samples and experimental studies (Fig. 2.15). Analysed phlogopites from the present study with high Al_2O_3 >14 wt.% and moderately low TiO_2 <3.9 wt.% extend in region where biotite crystallized from lamprophyre magma (e.g. minette) and appear different from classical worldwide lamproitic melts characterised by lower Al_2O_3 (< 12 wt%) and higher TiO_2 (> 4 wt%) (Rock, 1991), accordingly TiO_2 content are lower than those in counterparts from lamproite-like lavas from NW Iran (e.g. 4.8 wt.% , Shafaii Moghadam *et al.*, 2014).

2.4.2.2.3 Amphibole

Representative data of amphibole are listed in table 4 appendix. According to classification proposed by Leake et al. (1997), the average value showing high CaO (11.7-12.4 wt%), Mg# ranging from 0.61 to 0.66, and Si < 6.5 belong to calcite amphibole, and especially corresponds to magnesio-hastingsite. They are characterized by TiO₂ varying from 1.96 to 2.6 wt.%, which are similar to magmatic amphibole and calc-alkaline lamprophyre (Rock, 1991), however their composition is close to those of lamprophyre from NW of Iran and cumulates (Fig. 2.16a). In zoned crystals, they have slightly lower Al₂O₃ (12.5-13.6 wt.%), whereas FeO content decreases from core to rim (from 13.3-12.4 wt.% to 11.4-11.9 wt.%), BaO and Cr₂O₃ are low and are <0.1 wt.% and <0.01 wt.%, respectively.

2.4.2.2.4 Feldspar

Studied lamprophyres contain feldspar essentially as microliths in the groundmass, and more rarely as phenocrysts. In the kersantites, phenocrysts are bytownite in composition. In the zoned plagioclase, they range between Ab_{7.4-15.5} An_{83.4-92.1} Or_{0.2-1}. The compositions of those occurring in groundmass are similar to those of the rim of phenocrysts (Ab_{7.4-26.06} An_{60.6-81.5} Or_{0.36-5.6}). Only few crystals of Na-sanidine to Ca-sanidine (Ab_{1.7-4.5} An_{31.35-40.44} Or_{55.02-66.9}) were detected as microphenocrysts. In minette, microlithic sanidine (Ab_{36.7-41.39} An_{3.2-6.7} Or_{52.7-} relatively high abundances of Na₂O (3.36-4.7 wt%) and FeO (0.34-0.55 wt%).^{59,3}) are restricted

to the groundmass . Sanidine is characterized by TiO₂ (0.01-0.13 wt%), and these values are higher than in lamproites (Mitchell & Bergman, 1991).

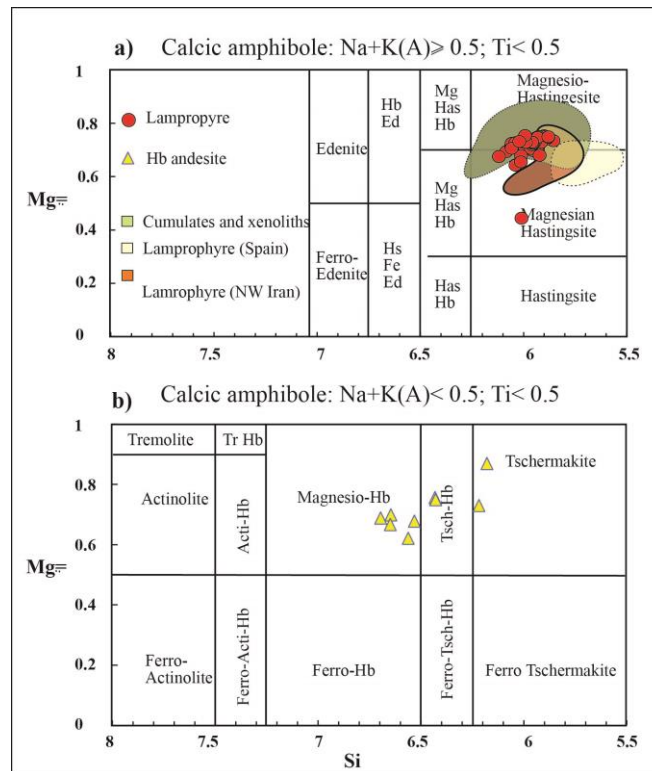


Figure 2.16 Mg# versus Si classification diagram for calcic amphiboles (after leake *et al.*, 1997). Fields for amphiboles from cumulates and xenoliths are from Shaw 2004 and Shaw and Eyzaguirre, 2000, amphiboles of lamprophyres from Spain and NW Iran from Orejana *e al.*, 2007 and Aghazadeh *et al.*, 2015, respectively. Hb; hornblende; Ed edenite, Mg Has; magnesio-hastingsite, Acti; actinolite, Tr; Tremolite.

2.4.2.3 Tephrite

2.4.2.3.1 Olivine

The olivines display moderate Fo (50-71) [(Fo= 100× Mg/(Mg+Fe), cation ratio)]. The olivine phenocrysts are characterized by higher MgO (32.7-35.6 wt%), lower CaO (0.15-0.41 wt%), and MnO (0.58-0.79 wt%) than those of microphenocrysts with MgO: 22.7-26.5 wt%, CaO: 0.40-0.52 wt% and MnO: 1.2-1.4 wt%(table 5 appendix). All samples plot away from the

field of olivine from mantle xenoliths carried by alkaline lavas from the plateau, and are similar to those of the alkaline potassic lavas from Mediterranean region (Fig. 2.17).

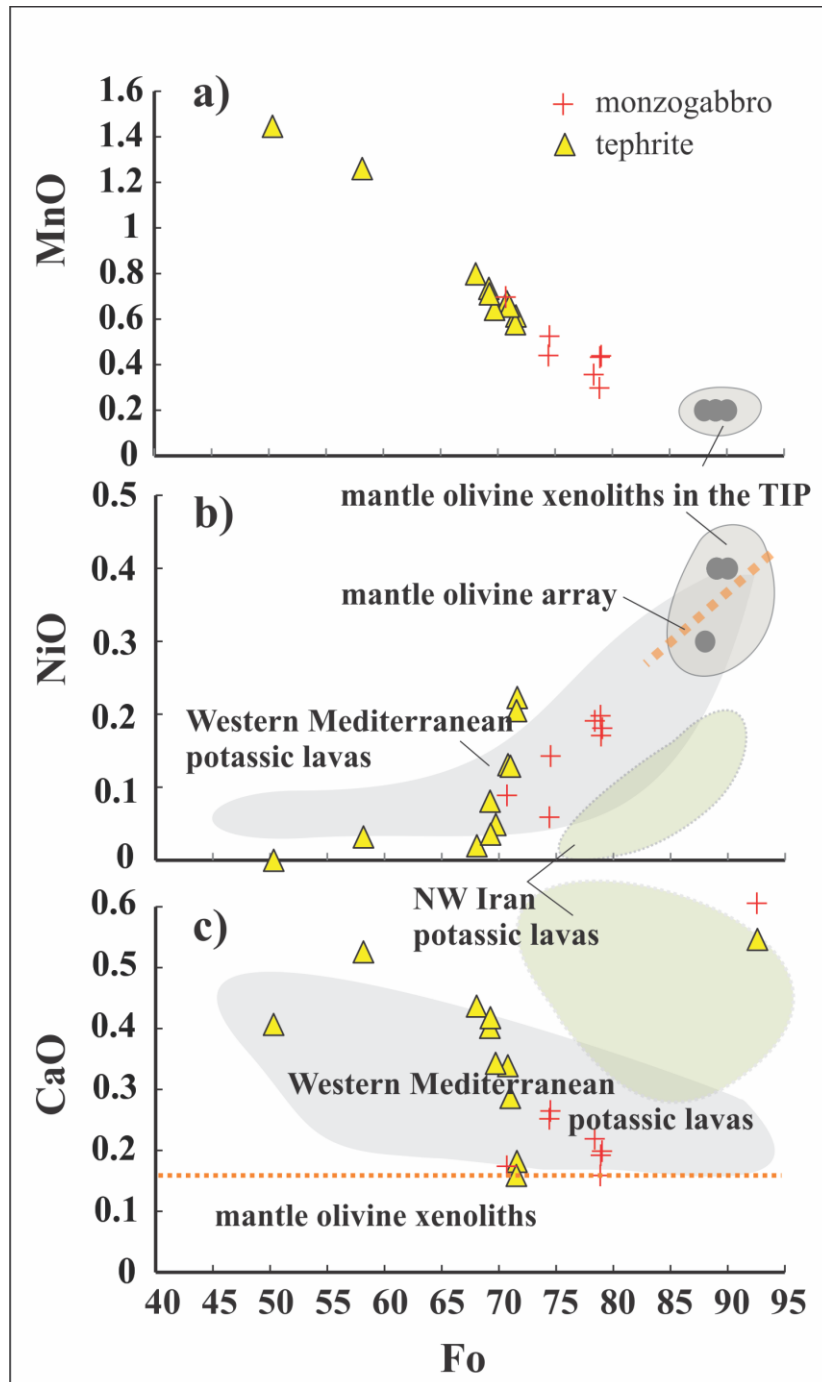


Figure 2.17 Plots of MnO, NiO and CaO versus Fo for olivine in lavas and intrusions from the Salavat Range. Fields for mantle xenoliths from the TIP, potassic rocks from the West Mediterranean - NW Iran based on data from Su et al. (2014) and Shafaii Moghadam et al. (2014), respectively.

2.4.2.3.2 Clinopyroxene

Clinopyroxene is the most abundant phenocryst type in tephrite dykes. Based on major elements, as in lamprophyres, they show heterogeneous compositions. Core-rim variations are observed in most of them. They show moderate normal zoning, except in samples with bright colorless bands where the zoning is inverse and then convert to normal oscillatory zoning towards the rims. Similar to lamprophyres, colorless clinopyroxenes have high Mg# (0.75-0.88) Na₂O (0.2-0.6 wt%) and Cr₂O₃ (< 0.9 wt%) and TiO₂ (<0.6 wt%) (Fig. 2.18), plotting in the field of Cr-diopside xenoliths from alkaline volcanic rocks (Fig. 2.19). They are mantled by green clinopyroxene with lower Mg# (0.65-0.8) and similar to most phenocrysts with only oscillatory sector zoning and/or clinopyroxene microphenocryst or occurring in the groundmass. Generally, they have a highest range of TiO₂ (0.5-2 wt%), Al₂O₃ (1.7-9.1 wt%) and Na₂O (0.16-1 wt%). According to classification of Morimoto et al. (1988), all clinopyroxenes plot above 50% of Wo and range in composition from colorless diopside to green fassaite (Fig. 2.12a).

2.4.2.3.3 Analcime

Abundant analcime occurs as microphenocrysts or in the groundmass of tephrite dykes. They are SiO₂-rich (~58.3 wt%), and contain up to 21.43 wt% Al₂O₃, 0.13 wt% of K₂O and 0.13 wt% of CaO, which have a similar composition to L-type (pseudomorph after leucite) and P-types (magmatic) analcimes (SiO₂; 55.2 wt% and 56.3 wt%; Al₂O₃; 21 wt%, and 22.1 wt%, respectively). However, CaO content in studied analcime is closer to value in L-type (0.09 wt%) than in P-type (0.26 wt.%) (see Luhr & Kyser, 1989).

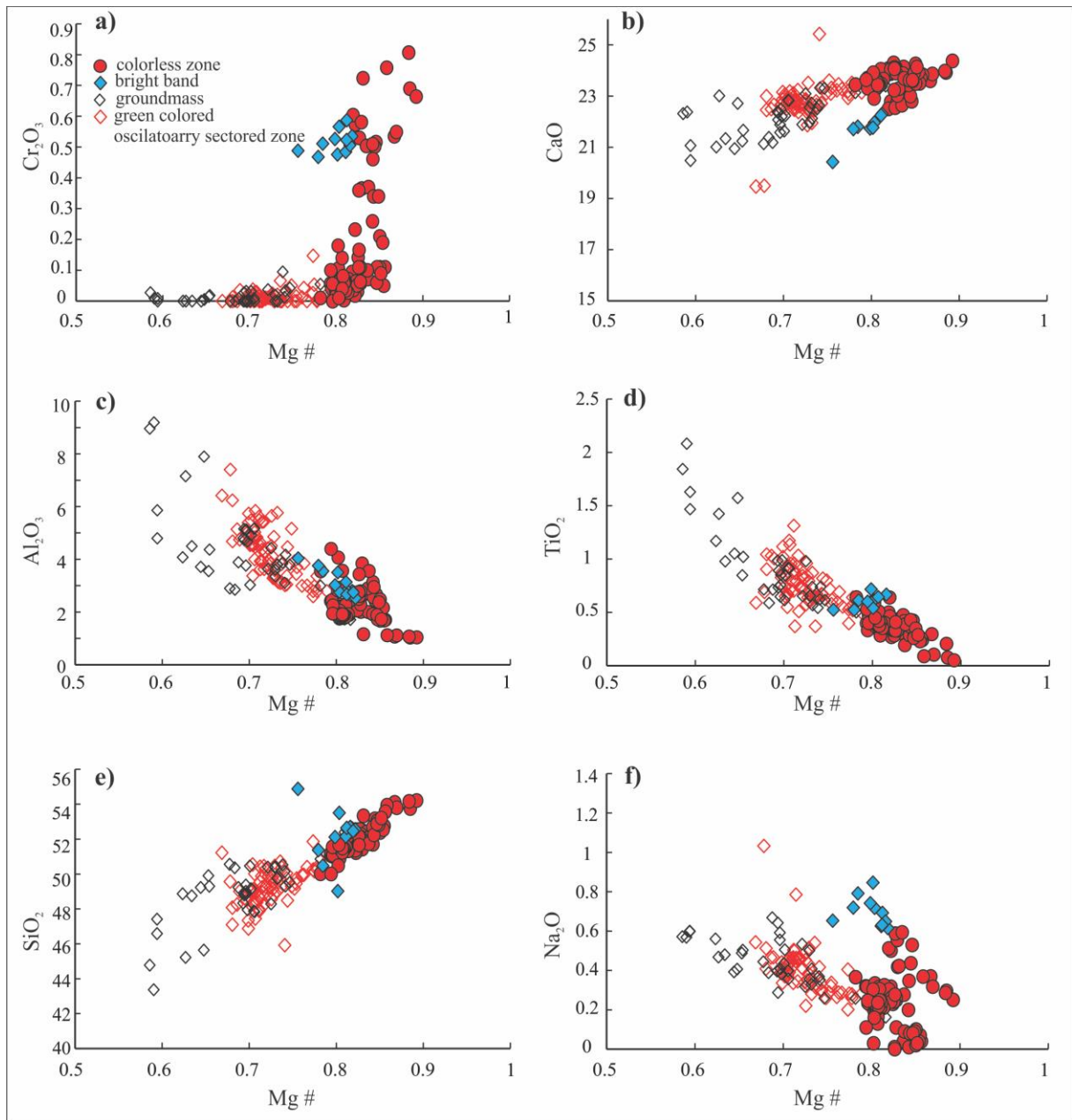


Figure 2.18 Major elements compositions versus Mg# for clinopyroxene of tephrite dikes.

2.4.2.3.4 Biotite

Only few laths of biotite occur in the groundmass. They represent evolved compositions with low Mg# 0.28-0.40, high TiO₂: 4.1-5.3 wt%, Al₂O₃: 13-13.1 wt% and FeO: 23.04-26.17 wt%.

2.4.2.3.5 Feldspar

Representative data are listed in table 2 appendix. They vary in composition from plagioclase labradorite (An_{50.6-70.8} Ab_{27.1-42.08}Or_{2.01-9.7}), to sanidine and more rarely orthoclase (An_{2.1-5.9} Ab_{9.5-37}Or_{58.6-95.36}).

2.4.2.3.6 Fe-Ti oxides

Representative composition of Fe-Ti oxides in tephrite are given in table 6 appendix. They are magnetite in composition (FeO: 29.34-30.5 wt%, Fe₂O₃, 47.5-50.5 wt%, TiO₂: 5.8-6 wt%).

2.4.2.4 Analcim bearing lavas

2.4.2.4.1 Clinopyroxene

Clinopyroxene can be classified as fassaite (Wo_{51.87-56.19} En_{32.2-37.8} Fs_{7.4-11.6}) with low Mg # (0.61-0.68), high TiO₂ (1.17-2.14 wt%), Al₂O₃ (6.5-9.4 wt%), Na₂O₃ (0.5-1.2 wt%), and low SiO₂ (43.9-47.6 wt%). They represent evolved composition compared to clinopyroxenes in lamprophyre and tephrite (Fig. 2.19).

2.4.2.4.2 Analcime

Euhedral to subhedral phenocrysts and microphenocrysts of analcime generally have similar composition than those in tephrite dykes. They contain Al₂O₃; 21.27-22.57 wt%, Na₂O; 12.13-13.21 wt%, and CaO; ~0.1 wt% and are similar to L-type analcime (table 8 appendix).

2.4.2.4.3 Feldspar

Plagioclase composition are mainly bytownite (An_{71.04-76.1} Ab_{22.8-27.4} Or_{0.7-1.5}) and rarely andesine (An_{47.2} Ab_{49.8} Or_{2.8}).

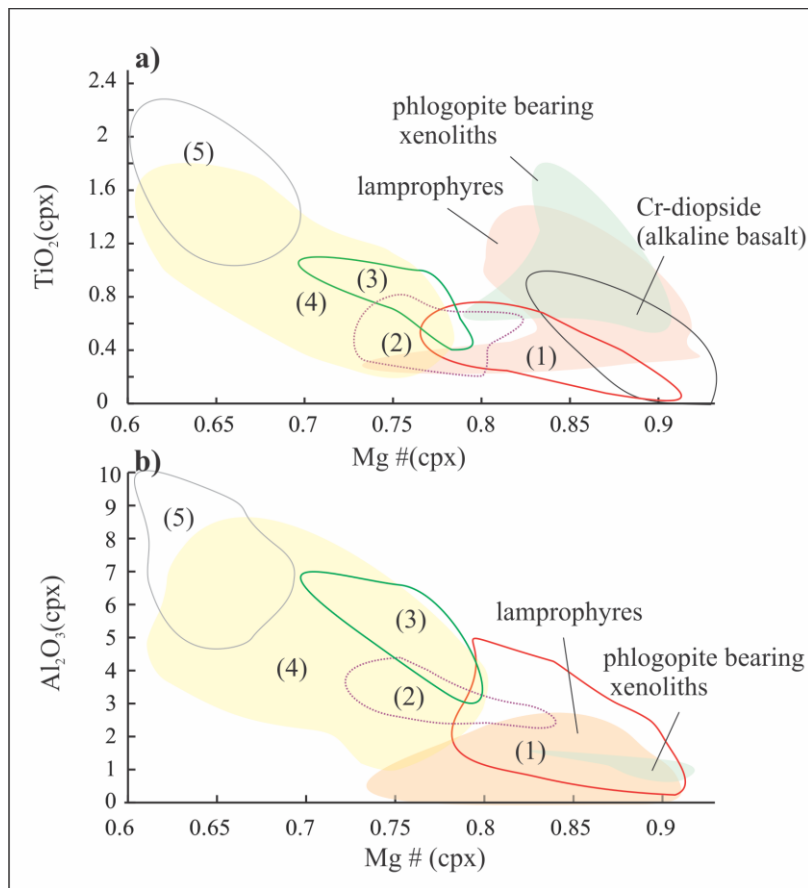


Figure 2.19 Compositional fields of clinopyroxene from different rocks from the Salavat Range. 1) colorless clinopyroxene in lamprophyre, tephrite and host lavas (Ha), 2); bright band colorless clinopyroxene in tephrite, 3); green clinopyroxene in lamprophyres and pillow lavas 4); oscillatory sector zoned clinopyroxene phenocryst, rim of colorless clinopyroxene microphenocryst and microcryst in the groundmass, 5); clinopyroxene phenocrysts from the analcinite and analcime-bearing lavas. Fields for Cr-diopside in alkaline rocks are from Wass, 1979 and for lamprophyres and phlogopite-bearing xenoliths from references given by Bucholz et al. (2014).

2.4.2.5 Hornblende andesite

2.4.2.5.1 Amphiboles

According to Leake et al., (1997), the amphiboles are hornblende (Fig. 2.16b), with low Al# [$Al\# = Al^{vi}/(Al^{vi} + Al^{iv}) \leq 0.21$] which is similar to those in calc alkaline magma. They are moderately rich in MgO (11.2-14.9 wt%), FeO (11.4-17.1 wt%), CaO (11.5-12.3 wt%) and Al₂O₃ (7.7-13.1 wt%) with minor TiO₂ (1.14-1.77 wt%), Na₂O (1.36-2.09 wt%), and K₂O (0.6-1.38 wt%).

2.4.2.5.2 Feldspars

They are mainly sanidine ($Ab_{23.2-29.6} An_{0.8-1.5} Or_{64.4-71.1}$) with K_2O ; 10.7-11.8 wt% and FeO ~0.1-0.2 wt%.

2.4.2.6 Intrusions

2.4.2.6.1 Olivine

Olivine Fo in monzogabbros range from Fo 70.68 to 78.9 (table 5 appendix). Compared to tephrite dykes; they have higher MgO, SiO_2 , lower NiO, MnO, CaO, FeO, CaO, while CaO (0.15-0.26 wt%). They have normal zoning with decreasing Fo values and NiO contents, and increasing CaO and MnO from core to rim. Toward the rim, their composition overlap with composition of olivine from tephrite dykes and plotting in the field of potassic rock in the Mediterranean (Fig. 2.17).

2.4.2.6.2 Clinopyroxene

Representative chemical compositions are listed in table 1 appendix. Monzogabbro and alkali feldspar syenite have significant difference in their modal compositions apart that of clinopyroxene (5.7-1%) but they display similar chemical compositions. However, in monzogabbro clinopyroxene composition plots in between Salite and fassaite line, whereas in alkali feldspar syenite, they have composition ranging from diopside to salite (Fig. 2.12d). Interestingly, in terms of major elements, clinopyroxene from alkali feldspars syenite have composition very close to those of rims of clinopyroxenes from the monzogabbros (Fig. 2.20). In fact, slightly lower MgO and higher FeO towards rim in these rocks indicate a reverse zoning trend. In figure 2.20 the composition of clinopyroxene in mafic and felsic intrusions from the Salavat range are compared to those of the alkaline intrusions occurring in the NW of Iran and

Alborz. They mainly display the same range for MgO (~13.5-15 wt.%), CaO (20-22 wt.%), and have very similar Al₂O₃ (2.2-5.1 wt.%) and TiO₂ (0.7-1.3 wt.%) contents than those of the gabbro from the NW of Iran.

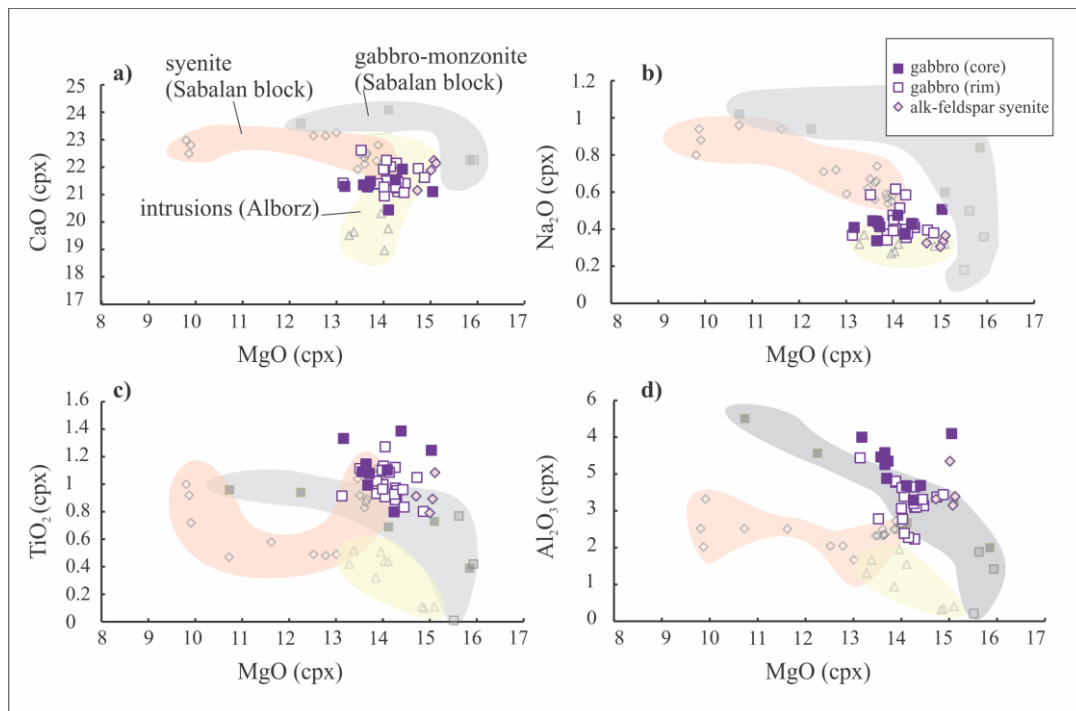


Figure 2.20 Major elements compositions versus Mg# for clinopyroxene of intrusions from the Salava Range. The field for clinopyroxene in the intrusions in the NW Iran and Alborz based on data from Aghazadeh et al., 2010, Ashrafi et al., 2014. Nabatian et al., 2014.

2.4.2.6.3 Feldspar

Potassium feldspar is common in mafic and felsic intrusions, reaching up to 75% in volume in alkaline feldspar syenite. Their composition (Or_{45.65-49.33} Ab_{45.63- 50.64} An_{3.69-4.87}) corresponds to sanidine and Na- sanidine. Plagioclase is relatively abundant in monzogabbros and monzonites and rare in alkaline feldspar syenites. Their chemical compositions are labradorite and oligoclase in monzogabbro and monzonite, respectively.

2.4.3 Elemental variations of zoned clinopyroxene

Representative major and trace element compositions of the zoned crystals are presented in table 7 of the appendix. The optical complex zoning patterns are associated to a drastic compositional zoning in major elements. The zoning is defined by alternations of colorless and green zones in a single crystal of clinopyroxene. The coexisting colorless and green colored clinopyroxenes is a common feature of the studied samples, particularly in of the host basalt (Ha), lamprophyre and tephrite dykes, whereas in host basalts (Hb) and analcime-bearing lavas, only green colored clinopyroxene occurs. To provide a relatively comprehensive picture of the growth history of early-crystallized crystals, 2D mapping and profile (core-rim) spot analysis of colorless and green colored clinopyroxenes was carried out. In addition, laser ablation analyses were performed in zoned crystals to evaluate if trace element content also vary in relation to optical zoning and to estimate the theoretical composition of melt(s) in equilibrium with those different clinopyroxenes. As we see in figures 2.21-26 analyses perfectly highlight the different compositions of colorless and green colored crystals in term of major and trace elements. In the following, we focus on the different zoning features in term of their major and trace element patterns.

2.4.3.1 Major elements

2.4.3.1.1 Type I

The first type corresponds to normal zoning found in minette, kersantite and tephrite dykes. It is characterized by colorless clinopyroxenes in core with highly magnesian and relatively uniform Cr₂O₃ and low Al₂O₃ and TiO₂ concentrations mantled by green colored clinopyroxenes characterized by low MgO, Cr₂O₃, high Al₂O₃, TiO₂ and moderate Na₂O contents. Variation trends in core composition (colorless) and rim (oscillatory sector zone)

of this type of zoning could be linked to common fractional crystallization processes. However, the core to rim zoning is marked by an abrupt compositional change at $Mg\# \sim < 0.8$ which corresponds to the gap in major element trends (Fig. 2.21) and to the corroded borders in the 2D maps (Fig. 2.22).

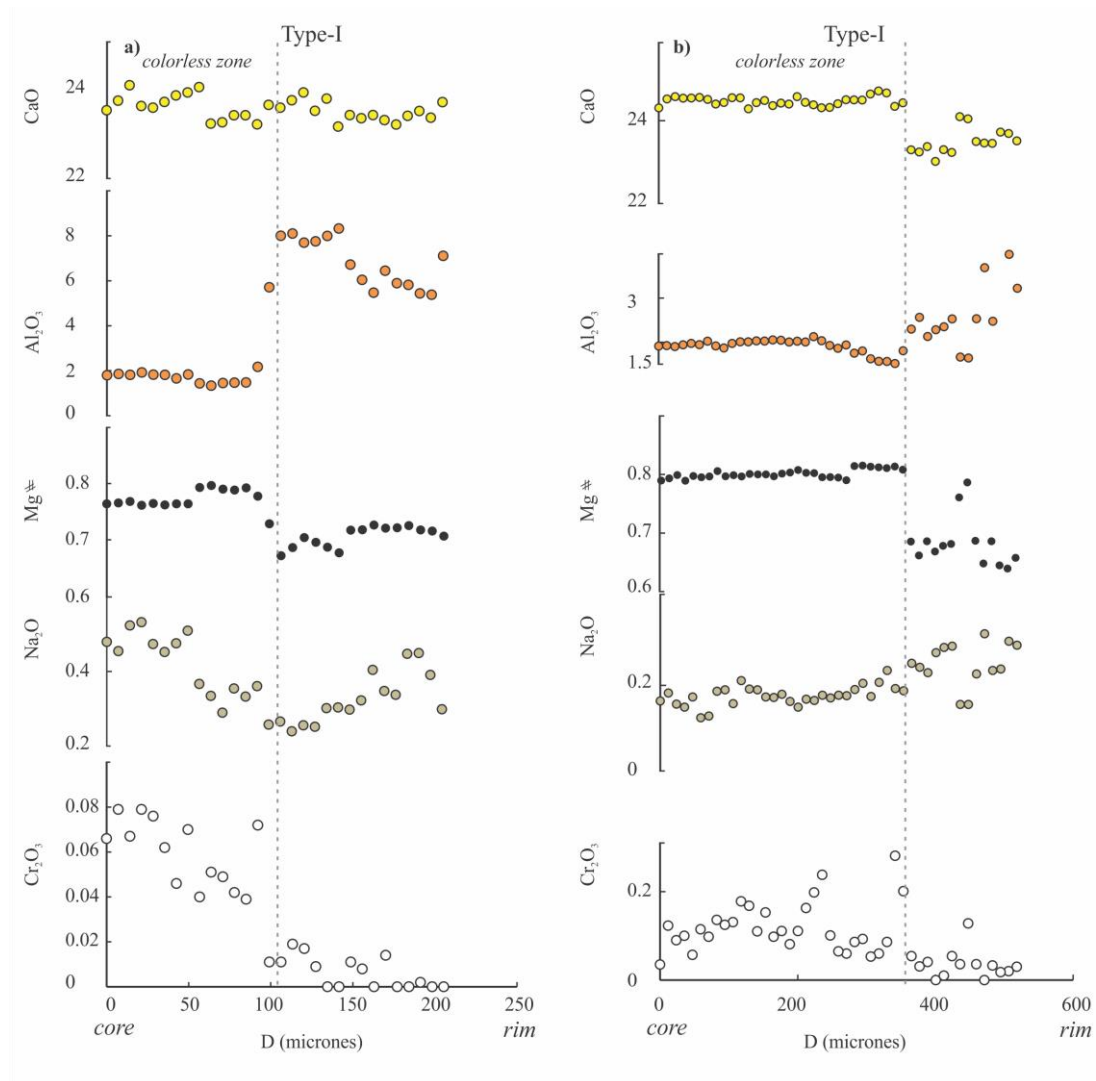


Figure 2.21 Core to rim major element variation in Type-I clinopyroxene phenocrysts from the kersantite (a) and minette (b). The vertical dotted lines separate the chemical zoning part according to the optico-chemical changes.

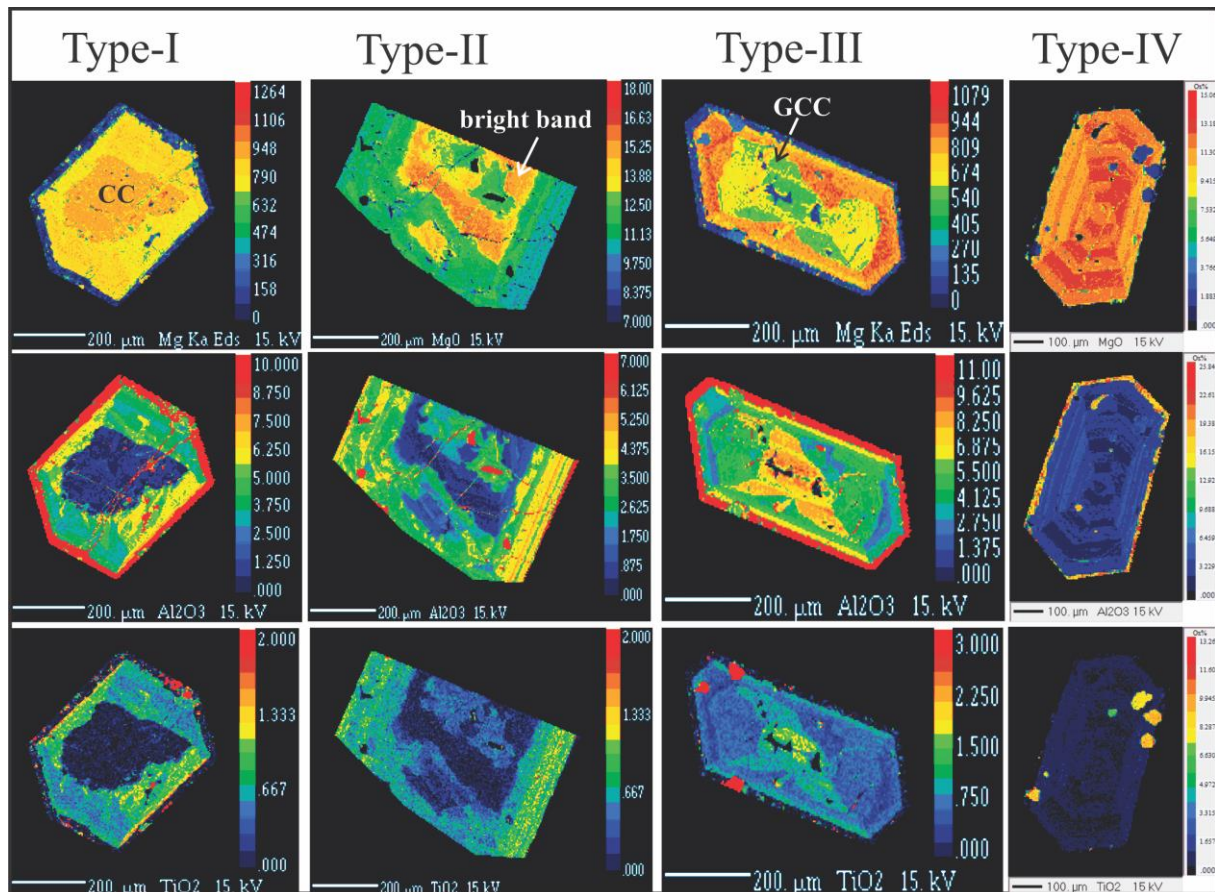


Figure 2.22 Major element distribution maps of the four type of zonation in the clinopyroxene. The major element distribution indicates that the various colorless (CC) and green colored (GCC) zones overlap with disequilibrium texture. The arrows highlight the separated zones according to the observed chemical changes.

2.4.3.1.2 Type II

This type common in kersantite and tephrite dykes consists of the classical oscillatory zoning patterns showing a heterogeneous composition in term of Mg#, Al₂O₃, TiO₂, Cr₂O₃, and Na₂O (Fig. 2.23). They can be distinguished by bright bands from other types of oscillatory zoning patterns in clinopyroxene (e.g. type IV or V, see following). In fact, in overall the core to rim major element composition of this pattern shows a complex oscillatory trend with a general tendency to a normal trend. It is worth noting that i) the trends are marked by abrupt

drops in Al_2O_3 , TiO_2 and Na_2O at increasing # Mg or Cr_2O_3 and ii) they are characterized by high MgO, Cr_2O_3 and Al_2O_3 contents in core of crystals with higher Na_2O than the rims (Fig. 2.23b). The abrupt compositional peaks/drops correspond to the optical bright bands which have similar MgO, Na_2O and Al_2O_3 contents than the core of clinopyroxene with type I zoning pattern (Fig. 2.23a). There is no obvious optical properties to distinguish colorless bands with high Na_2O from those with low ones.

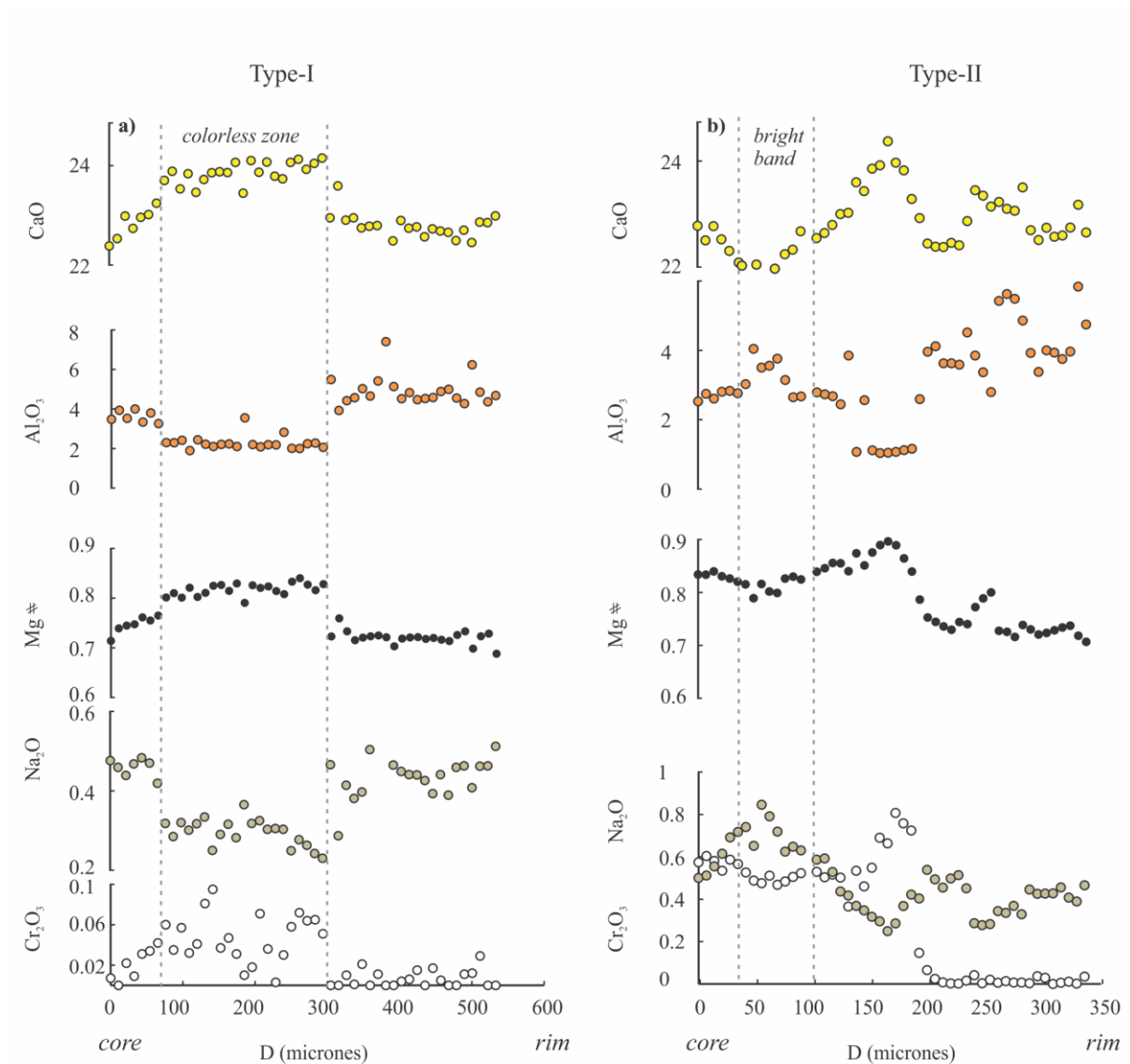


Figure 2.23 Core to rim major element variation in Type-I (a) and Type-II clinopyroxenes (b) in the tephrite dykes. The vertical dotted lines separate the chemical zoning part according to the optico-chemical changes

2.4.3.1.3 Type III

It displays green colored clinopyroxene cores mantled by colorless clinopyroxenes, occurring in kersantite lamprophyres. The optical differences from core to rim are mirrored by differences in chemical compositions. The green core follows a distinct trend in major element variation diagrams which emphasizes their lower Mg# with high Al_2O_3 and TiO_2 similar to rim of type-I (Fig. 2.19). Considering the melt evolution by considering of Na_2O , Al_2O_3 (TiO_2 not shown), and Cr_2O_3 with Mg#, it appears that the crystals characterized by this type of zoning record a reverse zoning (Fig. 2.24). In addition, the main observation of crystal profiles and analysis of 2D maps evidence at a first order result a magmatic origin for the green core clinopyroxenes reflected by the compositional oscillatory zoning (Figs. 2.22 and 2.24).

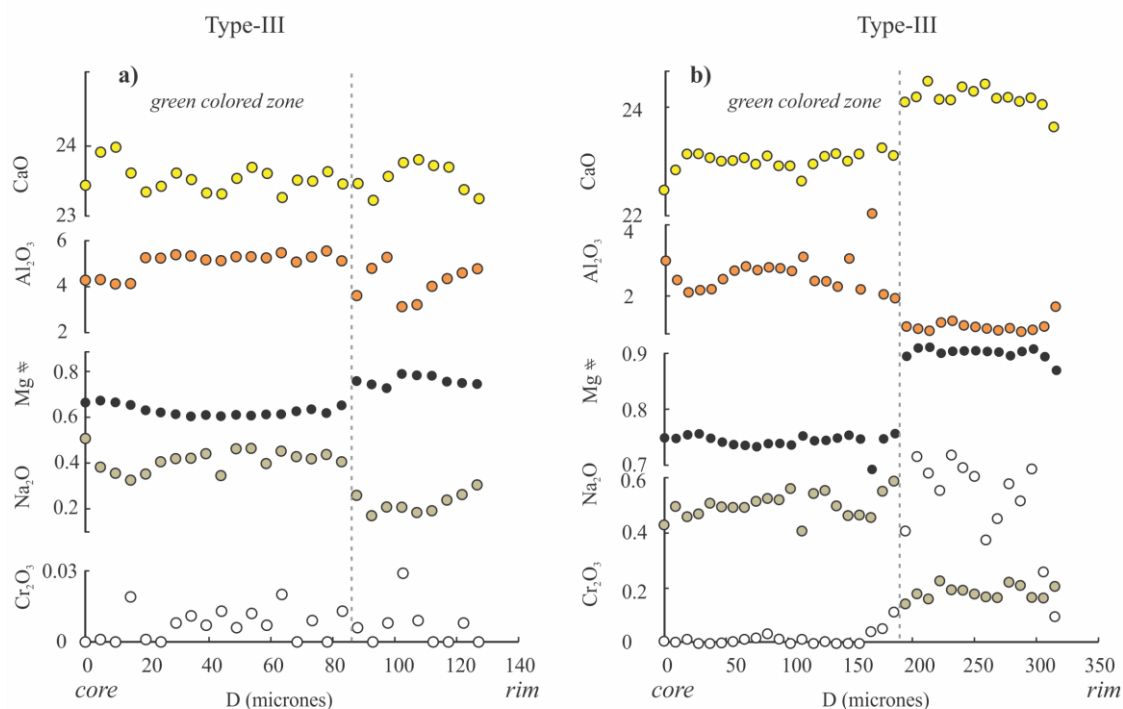


Figure 2.24 Core to rim major element variation in Type-III clinopyroxenes in kersantite lamprophyres. Core (low Mg#) to rim (high Mg#) zoning in these clinopyroxenes represent reverse zoning. The vertical dotted lines separate the chemical zoning part according to the optico-chemical changes.

2.4.3.1.4 Type IV

It is the most abundant type of zoning pattern in all samples, with sectored and oscillatory zoned crystals. However occasionally they also appear only as oscillatory zoned grains (e.g. pillow lavas). Accordingly, clinopyroxene patterns in term of major elements can be divided into two series; a) pillow lavas with relatively high Na_2O (> 0.4) content and a limited range of $\text{Mg}\#$ (~ 0.75 Fig. 2.19), b) oscillatory-sectored clinopyroxenes with lower Na_2O (< 0.4) and a wider range of $\text{Mg}\#$ (0.8-0.6) (e.g. Fig. 2.25). It is interesting to mention that the type IV-a is similar to the green core clinopyroxene of type III.

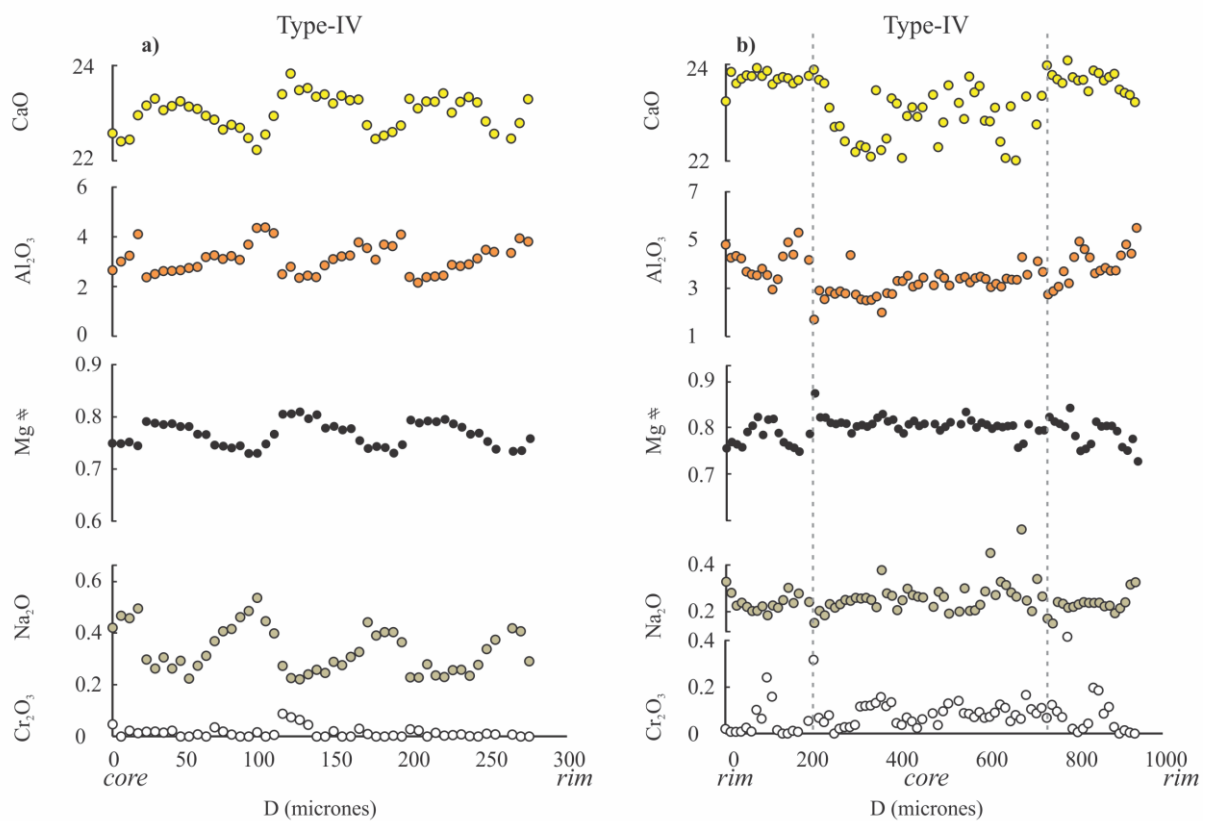


Figure 2.25 Core to rim (a) and rim-to-rim (b) major element variation in Type-IV clinopyroxenes in tephrite and kersantite. The vertical dotted lines separate the chemical zoning part according to the optico-chemical changes.

2.4.3.2 Trace element chemistry

Trace element data from colorless and green colored clinopyroxenes of different rock types (tephrite, kersantite and minette) were plotted on chondrite and primitive mantle-normalized diagrams (Fig. 2.26). They show relatively large irregular variations in trace elements concentrations. They show varied La and Yb values and significant Nb-Ta and Hf-Zr variations. Moreover, no correlation between Mg# and those elements are observed. Based on variable trace element concentrations they could be classified into four types.

2.4.3.3.2.1 Type I

They correspond to colorless core clinopyroxene from type I-zoning. They have negative Ba, Ta, Zr, and Hf anomalies but no Pb anomalies (Fig. 2.26a). They have nearly paralleled REE patterns with similar convex upward shape, relatively flat for HREE and lack of Eu anomalies, in agreement with their co-genetic origine (Fig. 2.26b). Commonly clinopyroxenes with similar LREE-depleted patterns are interpreted as xenocrysts derived from shallow lithospheric mantle (e.g. Jankovics *et al.*, 2016) but the observed magmatic features avoid considering such mantle origin in our case (see above).

2.4.3.3.2.2 Type II

They correspond to colorless bands from the type II zoning (Fig. 2.22). Similarly to type-I they are depleted in Ba, Ta, Zr and Hf, with contents significantly below those of the primitive mantle (e.g. Ba and Rb). They have distinctive pattern with slightly high LREE content and more steeper HREE shape in comparison to type I (Fig. 2.26d). Additionally, they are characterized by higher concentration of other incompatible elements compare to type I (Sr, La, Nd, Zr and Hf), slight negative Pb anomalies, and Nb and Ta decoupling (Fig. 2.26c).

2.4.3.3.2.3 Type III

They consist of green colored clinopyroxene of Type-III and Type IV-a zonings. Similarly to the major elements, in term of trace elements they have similar parallel trends together with slight gradual increase of elemental concentrations. Similarly to type II, most of samples are characterized by significant low Rb and Ba below values of primitive mantle, and also the Nb and Ta decoupling. However, they display higher normalized values for Nd and Sm and lower drops in Hf and Zr. REE are 10-70 times more enriched than in primitive mantle (Fig. 2.26f). They display REE pattern with similar slopes but sometimes a slight higher fractionation of LREE/HREE with $(La/Yb)_N$ ranging from 1.5 to 2.9 (Fig. 2.26 e-f).

2.4.3.3.2.4 Type IV

They mainly correspond to the type IV-b zoning, their $(La/Yb)_N$ ranges from 1.5 to 4.7 and their La content is ~10-75 times higher than that of chondrite (Fig. 2.26h). This type is mostly intermediate between the most depleted and enriched types (type I and III, respectively), but sometimes overlap with the most enriched patterns (type III). The main characteristics of other types such as a significant Rb and Ba depletion (below primitive mantle values), Nb and Ta decoupling and slight drops in Pb and/or Zr-Hf pair are highlighted in primitive mantle normalized diagram (Fig. 2.26g).

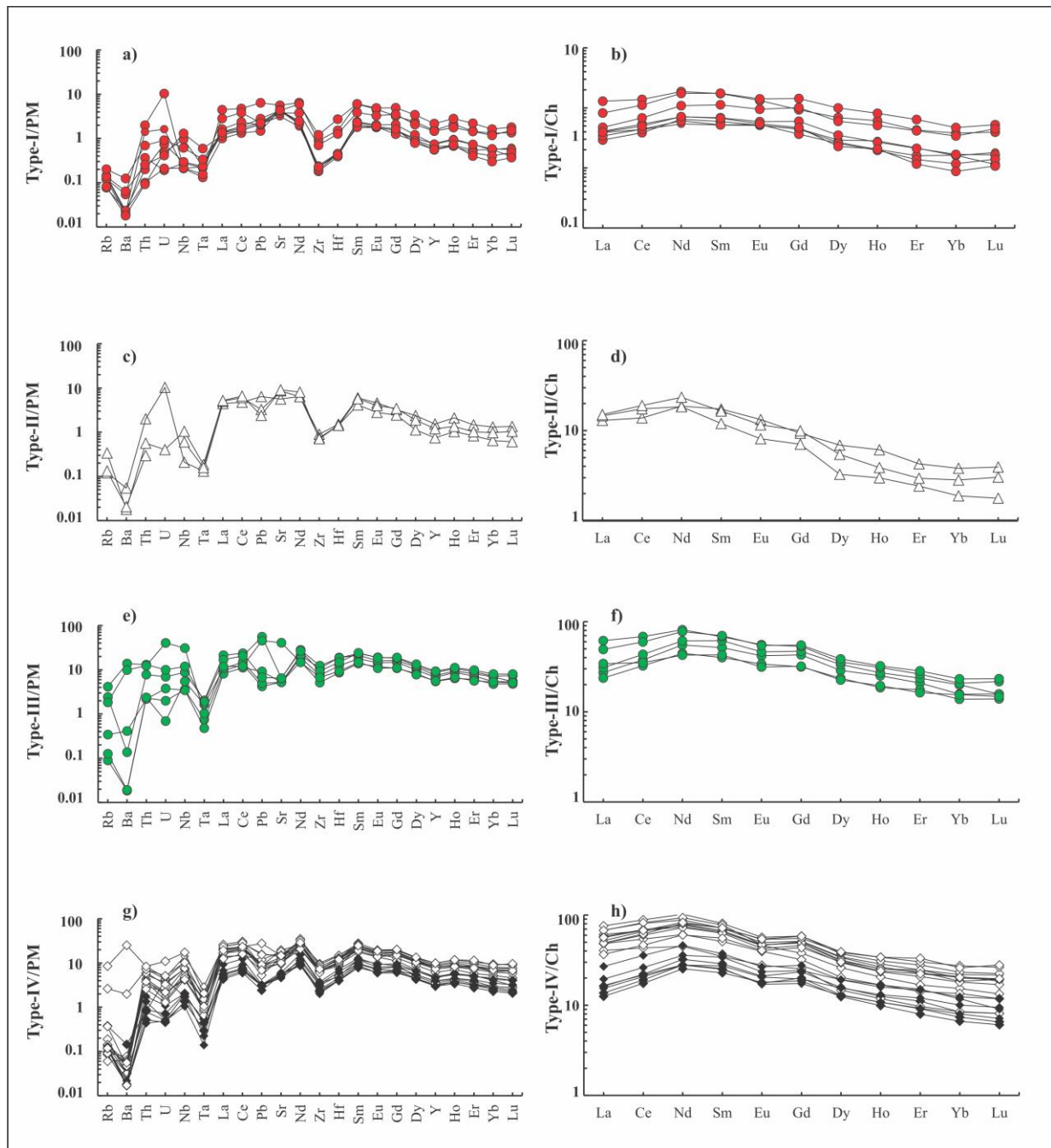


Figure 2.26 Chondrite-normalized (Ch) and primitive mantle-normalized (PM) trace element patterns and REE patterns of classified clinopyroxenes (Ch and PM values after Sun and McDonough, 1989). The four defined types of clinopyroxene are plotted in the different diagrams. In figures g-h filled diamond refer to the type-IV cpx from the host lavas (Hb) and cpx rim of Type-I from the minettes- While empty diamond refer to Typ- IV cpx from the pillow lavas and rim of type I and II from the tephrite and kersantite dykes.

2.4.4 Whole rock geochemistry

The IUGS classifications as well as the TAS diagrams (e.g. Le Bas *et al.*, 1986; Le Maitre, 2002) cannot account for the variability of high alkaline rocks displaying peculiar mineral assemblages (e.g. lamprophyres, kimberlites, carbonatites), and therefore the classification of those rocks only based on whole rock geochemistry is not possible. A well known example are the lamprophyres characterized by the occurrence of phlogopite or amphibole and the lack of early-crystallized feldspars (Rock, 1997). In order to classify the investigated samples from the Salavat Range we have combined their modal mineralogy and mineral chemistry to interpret their bulk rock major and trace element contents. Below, the main geochemical characteristic of those samples are described.

2.4.4.1 Major elements and rock classifications

Based on major geochemical features, abundance and chemical characteristics of mineral assemblages I classified the investigated lavas into High MgO-(HM) and Low MgO-(LM) lavas. Less voluminous plutonic rocks and sub-volcanic andesitic lavas are grouped together (Ps-rocks).

Based on bulk rock geochemistry, the most important character of all investigated samples is their high alkali content (K_2O+Na_2O ; 3.8-12.1 wt.%). Even in the most primitive samples with low evidence of accumulation of feldspar and phlogopite, this alkali content is relatively high, thus the role of mineral assemblages to control that alkali content seems to be insignificant. Although variety of samples expand from silica under-saturated to silica-oversaturated rocks, HM- and LM- lavas are mainly characterized by low silica content (SiO_2 ; 44-50 wt.% see table 9 appendix) with normative nepheline. Moreover, those samples follow the trend of classical alkaline rocks (Fig. 2.27a). Alkaline index from Le Maitre *et al.*

(1989) is used to describe the alkaline affinity of alkaline rocks. This index vary from $\text{Na}_2\text{O} > 2 > \text{K}_2\text{O}$ for sodic rocks (Na), to $1 < \text{K}_2\text{O}/\text{Na}_2\text{O} < 2$ for potassic rocks (K), to $\text{Na}_2\text{O} > 2 < \text{K}_2\text{O}$ and $\text{K}_2\text{O}/\text{Na}_2\text{O} < 1$ for transitional compositions (tk), and $\text{K}_2\text{O}/\text{Na}_2\text{O} > 2$ for highly potassic (HK) series. As showed in Fig. 2.27b three groups of classified rocks could be distinguished based on $\text{K} > \text{Na} > \text{HK} > \text{tk}$ in their alkali index evolution.

It is clear that the use of only major elements is not precise; especially when high Loss-on-ignition (LOI) values occur for some samples. However, the high value of LOI maybe because of altered groundmass and or mineral accumulations. Petrography observations indicated there is no link between some degree of alterations in samples and LOI ranges. In fact, variable LOI; 1.7-11.5 wt.% for HM-lavas, 4.3-9.3 wt.% for LM-lavas and 1.3-6.4 wt.% for Ps- rocks, can be due to the abundant presence of volatile-bearing phases such as phlogopite, amphibole, zeolites, and carbonates which is well consistent with petrography. Further, all the major elements data have been recalculated to 100% anhydrous basis. By the way, considering the less mobile elements (i.e. Th and Co), the alkaline affinity also have been checked based on classification of Hastie et al. (2007), all samples plot on the high-K and shoshonitic field (not shown). It implies not only using major elements on geochemical classification is reasonable but also alkalinity of the rocks may represent melt characteristics. In the following, I describe the main characteristics of each group.

2.4.4.1.1 High MgO (HM)-lavas

The group consists of host lavas (H-a) as well as lamprophyre and tephrite as dykes or lava flows and includes the most primary samples, characterized by the highest content of MgO (7.8-10.1 wt.%; 3.7-7.3 wt.%; 4.3-6.1 wt.%, respectively), Cr (380.1-503.4 ppm; 24.4-157.3 ppm; 27.3-76.3 ppm, respectively) and Ni (146.26-196 ppm; 15.4-55.5 ppm; 13.4-22.9 ppm,

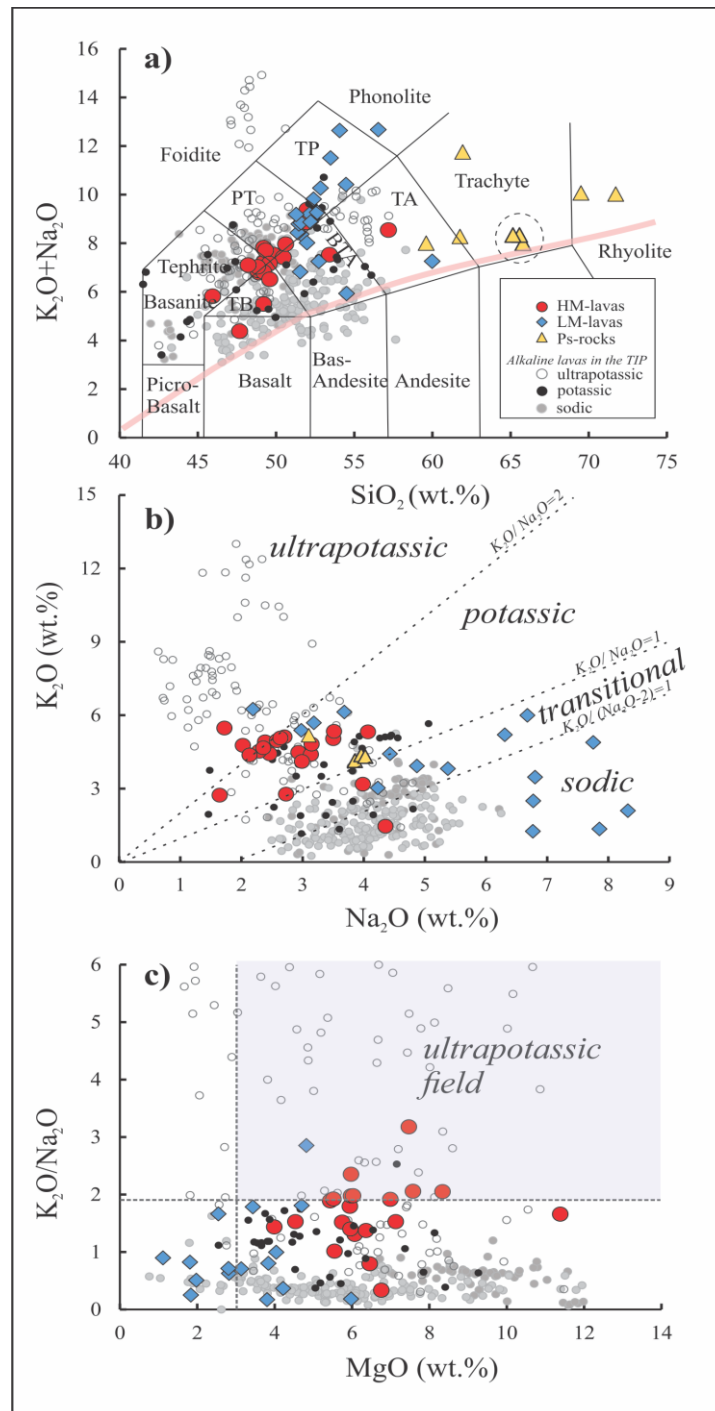


Figure 2.27 (a) Total alkali vs silica diagram (Le Maitre, 2002), (b) K₂O vs Na₂O diagram, (c) K₂O/Na₂O vs MgO diagram for classification of the investigated rocks from the Salavat Rang. All the major elements recalculated on a volatile-free basis. The pink line highlights the transition between alkaline and sub alkaline magma series (after Irvine and Baragar, 1971). Dashed circle in (a): hornblende andesite in Ps-rocks. The shaded field in (c) is after Foley et al., 1987. The data for alkaline lavas from the TIP come from literature (referred in the table 10 of appendix).

respectively). In addition all samples have high CaO (5.02-11.8 wt.%) and low TiO₂ (0.67-0.92 wt.%, and Al₂O₃ (10.3-16.2 wt.%) contents and are silica under-saturated (*ne*-normative; 2.06-8.6 %). They plot above the alkaline trend in the TAS (total alkali versus silica) diagram of Le Bas et al. (1986). Host basalts have the lowest content of SiO₂; 42.3-46.5 wt.% and Na₂O+K₂O; 3.8-6.1 wt.%, and plot in the field of tephrite basanite (Fig. 2.27a), whereas lamprophyres with more elevated and varied SiO₂ contents of 44.1-53.04 wt.%, and total alkalis (Na₂O+K₂O) contents of 5.42-9.04 wt.%, plot in a wide range from tephrite to phono tephrite and basaltic trachy-andesite fields (Fig. 2.27a). In comparison to the latter, tephrite dykes are characterized by a narrow range of composition (SiO₂ 45.9-48.4 wt.% and Na₂O+K₂O; 6.3-7.6 wt.%) and plot only in the tephrite basanite field. Their limited range of composition is also coherent with their limited variability in petrographic features and mineral components. Based on alkali diagram (Fig. 2.27b), all samples mainly plot in the potassic-ultrapotassic fields in agreement with K₂O/Na₂O and MgO diagram, in which only few samples plot in the ultrapotassic field (Fig. 2.27c). In fact, three samples of lamprophyres and two samples of tephrite dykes rank as high potassic (e.g. M-71, M-112, M-80), whereas few samples rank in sodic (e.g. M-113) or transitional potassic series while the remaining samples of HM- lavas plot in the potassic series. In Fig. 2.27, the investigated rock compositions are compared with the other alkaline lavas from the TIP (See references in table 10 in appendix). The studied lavas mainly share alkali content with ultrapotassic and potassic lavas from the TIP. Accordingly, lamprophyres characterized by low TiO₂ (0.52-0.96 wt.%), P₂O₅ (0.24-0.59 wt.%), total Fe₂O₃ (7.02-12.5 wt.%) and Al₂O₃ (13-17.1 wt.%) contents, and with K₂O ranging from 1.4 to 5.15 wt.% are similar to those reported from the TIP and classified as “calc-alkaline” type-lamprophyres (e.g. Rock, 1991, Fig. 2.28). However, the TiO₂ content of the lamprophyres from Salavat Range is lower than that of lamprophyre from NW Iran, and close to those of worldwide calc-alkaline lamprophyres and orogenic lamproites (Fig. 2.28b).

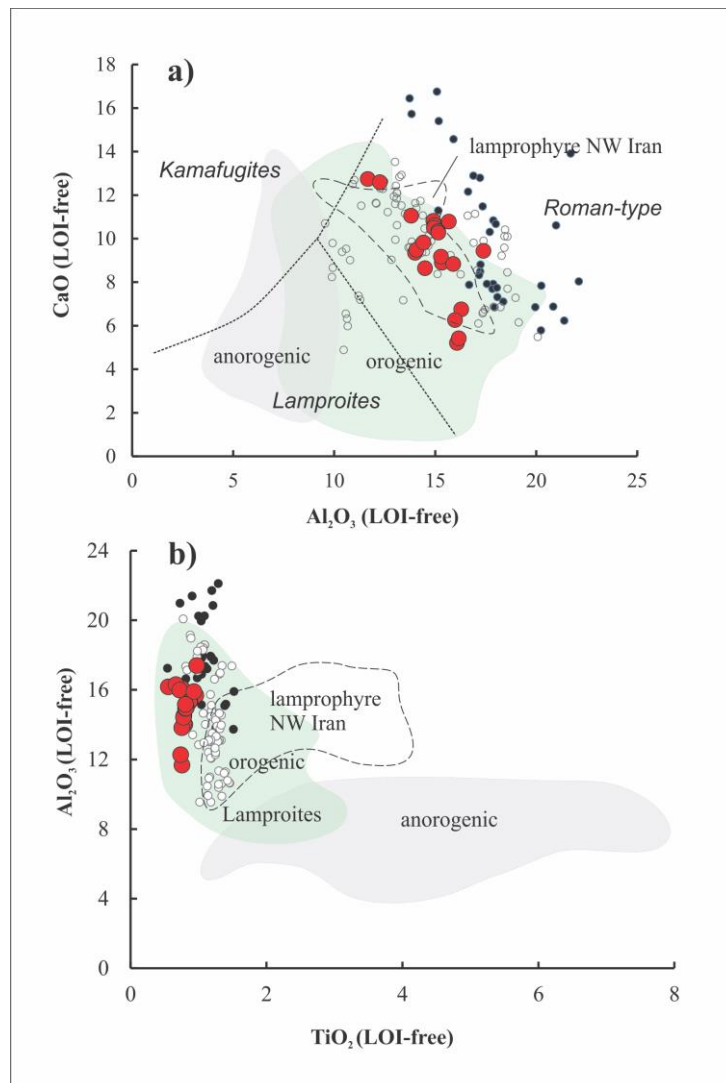


Figure 2.28 a) CaO vs Al₂O₃ diagram (Foley et al., 1987) b) Al₂O₃ vs TiO₂ classification diagram for LM-lavas from the Salavat Range. Fields for worldwide lamproites and lamprophyres from NW Iran are from Lustrino (2016) and Aghazadeh et al., 2015, respectively, symbols are same as Fig.2.27.

2.4.4.1.2 Low MgO (LM)-lavas

The group consist of lavas and pyroclastic rocks including host lavas (Hb), analcime-bearing lavas and analcimites. Similar to HM-lavas, these lavas are silica under-saturated (*ne*-normative; 0.75-19.9 %) and also follow the alkaline trend (K₂O+Na₂O; 7.6-12.1, Fig. 2.27a). They have relatively higher SiO₂ (48-54.5 wt.%), and lower CaO (2.8-7.9 wt.%) contents than

HM-lavas. The LM-lavas are alkaline with of i) sodic affinity ($\text{Na}_2\text{O} > 2 \text{K}_2\text{O}$) for analcime-bearing lavas, or ii) potassic affinity for the pillow lavas (Hb). They have higher Al_2O_3 (16.6-21.9 wt.%) and Na_2O (2.1 -7.7 wt.%) contents than those of HM-lavas and lower MgO content ($\sim < 6$ wt.%) with similar range of TiO_2 (0.5-0.9 wt.%). Additionally, they have relatively similar Na_2O (> 2.1 wt.%) than sodic lavas from the TIP (> 2.5 wt.%), but their average K_2O (> 3 wt.%) content is slightly higher than that of the sodic alkaline lavas from the TIP (< 3 wt.%) (Fig. 2.27b).

2.4.4.1.3 Plutonic and Sub volcanic (PS)-igneous rocks

This group included plutonic intrusions and sub-volcanic lavas. Their composition range from monzogabbros to alkali feldspar syenites in plutons with MgO: 3.5-0.5wt.%, Cr: 95.1-31.03 ppm, Ni: 17.8-26-2.8 ppm. The subvolcanic lavas are hornblende andesites with MgO; 1.4-2.7 wt.%; Cr; 22.4-60.02 ppm and Ni; 7.9-13.1 ppm. In addition, CaO and TiO_2 range from 5.06 to 1.1 wt.% and from 0.6 to 0.1 wt.% from mafic to felsic intrusions, respectively. The composition of subvolcanic hornblende andesite is different from those of mafic and felsic intrusion but mainly plot in the middle of the range defined by the two latter (e.g. CaO and TiO_2 ; 3.4-5.06 wt.% and 0.4 wt.%, respectively). Thus, we discuss their characteristics in the same group. Contrary to HM- and LM-lavas, the hornblende andesite (SiO_2 ; 61.7-65.7 wt.%) are silica oversaturated (Q_z -normative; 10.1-18.2 %), with a total alkali lower than evolved LM-lavas following the calc-alkaline-alkaline subdivision line ($\text{K}_2\text{O} + \text{Na}_2\text{O}$; 7.9-8.2 , Fig. 2.27b).

. The total alkali versus SiO_2 diagram of Middlemost (1994) was used to classify the plutonic sample. K_2O versus SiO_2 diagram (after Peccerillo & Taylor, 1976) allows to define the alkaline affinity of samples (Fig. 2.29a). Based on the chemical classification for plutonic rocks; intrusions plot in syeno-diorite to syenite fields (SiO_2 ; 59.6-71.7 wt.% and $\text{K}_2\text{O} + \text{Na}_2\text{O}$;

8-11.7). They plot in the potassic field (e.g. K_2O ; 4.6-6.7 wt.%) similarly to potassic plutonic rocks from the surrounding regions. Interestingly both intrusions and andesite lavas plot in the field of adakitic and/or potassic rocks with adakitic signature from the TIP (Fig. 2.29).

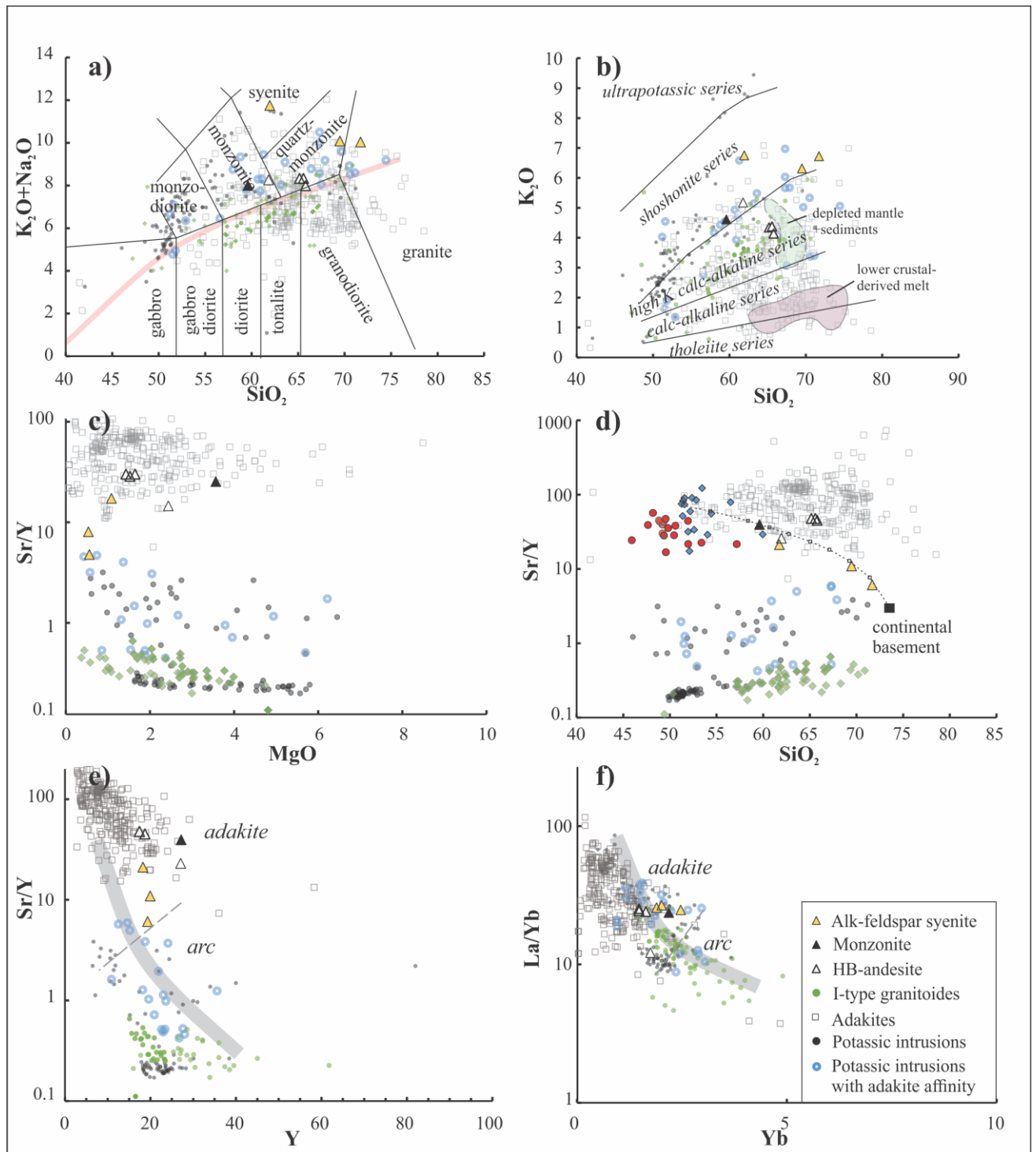


Figure 2.29 Diagrams of alkali oxides (K_2O+Na_2O , K_2O) vs SiO_2 (a and b), Sr/Y vs MgO (c), Sr/Y vs SiO_2 (d), Sr/Y vs Y (e) and La/Yb vs Yb (f) showing that the adakitic geochemical signature of Ps-rocks overlaps with field of adakites from the TIP. Grayed data for adakite and intrusions from the TIP taken from the literature. The line in (a) represents the boundary between alkaline and sub alkaline magma series (Irvine and Baraggar, 1971). Division lines for magmatic series in (b) are after Peccerillo and Taylor (1976) while data for adakites from arc like fields are from Drummond and Defant (1990) and Martin (1999). The fields for adakite melts derived from low degree of partial melting of lower crusts and for melting products of heterogeneous sources (depleted mantle plus sediment) are from experimental studies from Qian and Hermann, 2013 and Wang et al., 2017 respectively. Dashed line in (d) represents the mixing line between pillow lavas and continental basement material in the NW Iran (continental basement composition taken from Shahzedi et al., 2017).

2.4.4.2 Trace elements

Trace element analyses of representative samples from the three groups defined above are listed in table 9 appendix. Incompatible trace element characteristics are illustrated by primitive mantle (PM) - and chondrite- normalized (Sun & McDonough, 1989) trace elements and rare earth element (REE) patterns in Fig. 2.30. Although the three groups are characterized by various modal mineralogy, broad range of mineral compositions and relatively different major and trace element contents (see section 2.4.1-3). They all commonly display trace element patterns with similar features. As illustrated in figure 2.30, the patterns mark enrichment in large ion lithosphere elements (LILE: i.e., Rb, Th, U, Ba) relative to high field strength elements (HFSE: i.e., Nb, Ta and Ti). Moreover, they show a peak for Pb and a trough for Sr. Besides, the average value for the most primitive potassic rocks occurring in the plateau is also shown on figure 2.30, as we can see the general peak and trough of trace elements from the three groups of investigated rocks resemble to this average value. However, there is slight differences in term of trace element concentrations between the three groups whereas the most evolved samples of LM-lavas and Ps intrusions have patterns close to the one of the average potassic rocks from the plateau. However, within the three groups of classified rocks trace element contents slightly change from samples that are more primitive to evolved ones. As an example

in HM-lavas, the tephrite dykes display a slight enrichment of LILE (e.g. Sr, Th, U) and HFSE (Nb, Ta, and Zr) in comparison to host lavas and lamprophyres. Interestingly, sample with the highest MgO content in LM-lavas (host lava Hb) show similar values to those of the tephrite dykes, whereas in the more evolved lavas (analcimite and analcime-bearing lavas), Sr and HFSE depletion are gradually diluted (see Fig. 2.30b). In addition, a phosphorous anomaly, owing to apatite fractionation, may occur in some LM-lava. In PS-group, trace element spider-diagrams is broadly similar to those of HM- and LM-lavas in term of Rb, Th and U enrichment. They also display a Pb peak, but the HFSE depletion become insignificant as one progress from mafic intrusions to felsic samples (Fig. 2.30c). Moreover troughs for Sr, Ba, P, and Ti increase from mafic to felsic samples. Finally their extensive depletion of Ba, Sr, P, and Ti suggest the extreme fractionation of apatite and maybe amphibole. Hornblende andesites in term of Nb, Ta and Sr depletion and moderately flat slope for middle REE are similar to felsic intrusions, but sample M-68 containing cpx-bearing xenoliths (see section 2.4.1.1.5) and characterized by a pattern slightly depleted in LREE and HFSE. To sum up geochemical fingerprints of orogenic systems (e.g. LILE enrichment and HFSE depletion) is more prominent in HM- lavas, whereas two LM-lavas and the Ps-rocks display an anorogenic signature.

REE patterns of all samples are characterized by relatively high L_{an}/Y_{bn} . (6.3-24.1). The LREE/HREE ratios in some lithology are rather uniform (e.g. tephrite and host lavas (Hb): ~11 and ~9, respectively), whereas in lamprophyres and host lavas (Ha), ranged they are quite heterogeneous (6.3-13). However, the average highest to lowest values dramatically decrease from Ps rocks (with hornblende andesite > intrusions), down to LM-lavas (analcimite, analcime bearing lavas > host lavas), and finally reach the minimum in HM-lavas (lamprophyre < host lavas < tephrite). It must be highlighted that most of the samples are characterized by none or weak Eu anomalies (Eu/Eu^* : ~0.7- 0.9). This anomaly is only significant in the felsic intrusions (Eu/Eu^* = 0.45-0.72) (Fig. 2.30c').

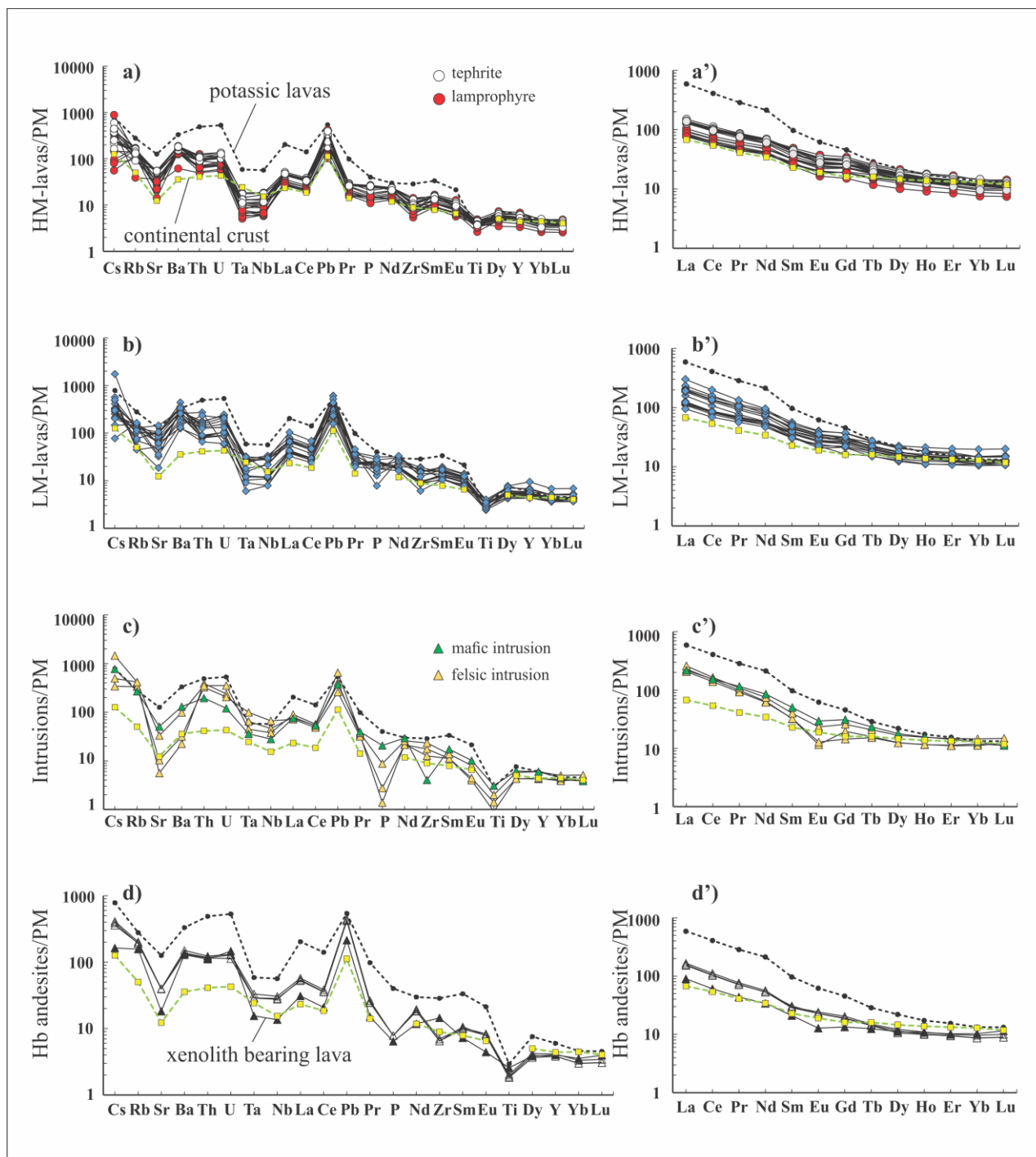


Figure 2.30 Whole rock trace element and REE patterns normalised to chondrite and primitive mantle (McDonough and Sun, 1989), for investigated HM-lavas (a-a'), LM-lavas (b-b') and Ps-rock (c to d'). The dashed line represents an average for representative potassic lavas from the TIP taken from the literature (see table 10 in appendix for references), and the average Continental Crust from Hofmann, 1988.

2.4.4.3 Isotope geochemistry

Sr and Nd isotopic compositions of selected samples from Salavat Range are given in table 9 appendix and plotted in figure 2.31. Due to the lack of geochronological measurement for most of the investigated samples, the data are not interpreted based on initial Nd and Sr isotopic ratios. However, due to previously published geochronological results (e.g. Alberti *et al.*, 1976), a ~47 Ma age correction was tested for HM-lavas. The result shows that none of the isotopic compositions are affected by radiogenic growth. All together $^{87}\text{Sr}/^{86}\text{Sr}$ and $^{143}\text{Nd}/^{144}\text{Nd}$ vary from 0.70473 to 0.70673 and from 0.51254 to 0.5128, respectively. They show relatively restricted range of Sr and Nd ratios correlated together and plotting within the mantle field with most of the samples plotting near the Bulk Silicate Earth (BSE). On $^{87}\text{Sr}/^{86}\text{Sr}$ vs $^{143}\text{Nd}/^{144}\text{Nd}$ diagram (Fig. 2.31.), compositions of reference mantle sources; OIB, DMM, EMI, EMII and of lamproites, cumulative xenoliths and alkaline lavas from the TIP are reported for comparison.

Although all studied samples plot in the mantle array indicating their dominant mantle sources, the Nd-Sr isotopic ratios from each subgroup define moderately wide ranges, evidencing the role of other parameters (e.g. heterogeneity in some sources or other sources than the mantle ones). For example, minette lamprophyre, host basalt of HM-lavas (M-112, M-118, respectively) display the highest $^{87}\text{Sr}/^{86}\text{Sr}$ ratios (0.706) with a tendency towards EM II located within the enriched quadrant of the diagram. They scatter towards Lamproites fields corresponding to ultrapotassic rocks from the TIP. By contrast, the samples with the lowest

$^{87}\text{Sr}/^{86}\text{Sr}$ and highest $^{143}\text{Nd}/^{144}\text{Nd}$ ratios, (i.e. M-113) show similar value to pillow lavas with the highest radiogenic $^{143}\text{Nd}/^{144}\text{Nd}$ (0.5127-0.5128) from the LM-lavas group. They show similarities with lavas with OIB mantle sources. As an example they plot close to the field of

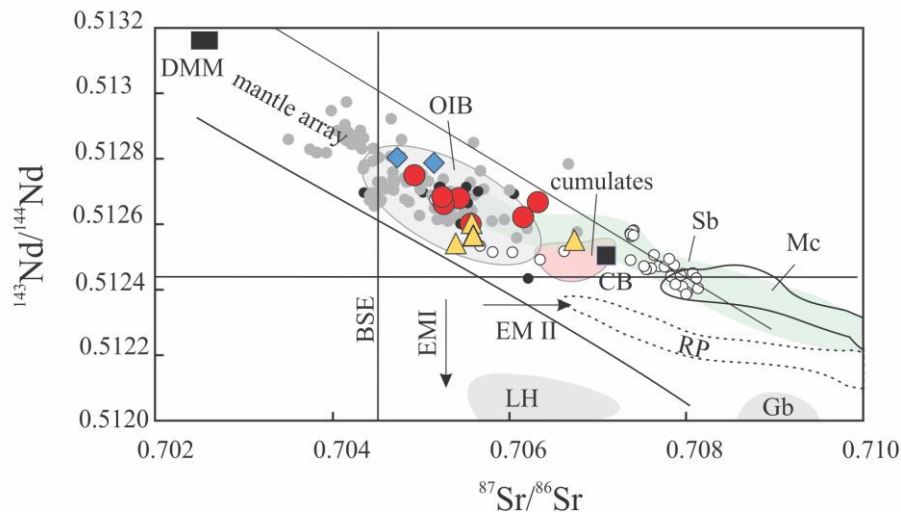


Figure 2.31 $^{143}\text{Nd}/^{144}\text{Nd}$ versus $^{87}\text{Sr}/^{86}\text{Sr}$ isotopic diagram for investigated rocks compared with the mantle components DMM and OIB and alkaline lavas from the TIP (references in table 10 of appendix). DMM== Depleted MORB Mantle, OIB= Oceanic Island Basalt; (after Zindler & Hart, 1986); LH Leucite Hills lamproites (Mirnejad and Bell, 2006), GB Gaussberg lamproites (Murphy et al., 2002) RP; Roman province, Sb, Serbian lamproites; Mc Macedonian lamproites (After Lustrino and Wilson, 2007 and references therein), CB, Continental basement (Shahzedi et al., 2017) cumulates field: data from cumulates hosted in the ultrapotassic lavas of NW Iran (Khezerlou et al., 2017), symbols are same as Fig.2.27.

the alkaline lavas from the plateau characterized by mainly sodic affinity. The remaining samples plot between the two ranges: that of minette lamprophyre and host basalt of HM-lavas and that kersantite lamprophyres and tephrite pillow lavas.

2.4.4.4 Geochemical variations in the Harker-type diagrams

2.4.4.4.1 Major and trace element variations

As mentioned above all the investigated rocks from the Salavat Range subdivided into three types are characterized by a wide range of volcanic and plutonic lithologies for a relatively large range of MgO (from 0.5 to 11.4 wt.%). In the Harker-type diagrams, selected major oxides

and trace elements show an overall relatively straight trend between the three types of rocks (Fig. 2.32-33) with the highest MgO, CaO, Fe₂O₃, Cr, V, Sc, Ni values shown by the HM-lavas whereas their Al₂O₃, Zr and Nb contents are relatively lower. Some elements do not define a general trend (e.g. K₂O and Na₂O), or that define individual trends only for LM-lavas and intrusions (e.g. Na₂O, SiO₂, Al₂O₃, Nb, Ba and Sr). A simple calculation of the fractional crystallization vectors for major rock forming minerals was used to assess if mineral fractionation could explain the elemental features of the investigated rocks. The most reasonable sample to take as hypothetical parental melt for classified rocks is a sample from the HM-lavas group (M-116) characterized by MgO content of 11.38 wt.%. In figure 2.32 I reported the trends reflecting the fractionation of the rock forming minerals; clinopyroxene, plagioclase, alk feldspar, amphibole, biotite, analcime and Fe-Ti Oxides. Below the elemental variations for each types of investigated rocks are detailed.

2.4.4.4.1.1 HM-lavas

The marked decrease of Ni and Cr with MgO in host lavas (Ha) require olivine and clinopyroxene fractionation, respectively. Olivine is totally absent in the primitive HM-lavas, but occurs occasionally in some tephrite dykes with lower MgO content. In the other hand, positive correlation of CaO and SiO₂ and negative correlation of TiO₂ and Al₂O₃ with MgO, imply that most of the other minerals (e.g. feldspar and biotite) do not play a critical role in the elemental variation but clinopyroxene. K₂O and Na₂O are from HM- and LM-lavas are scattered (Fig. 2.32 g-h), whereas the lamprophyre samples with the lowest K₂O are commonly the one with the highest Na₂O. In fact, at first instance, the comparison of Na₂O content of HM-lavas with their petrographic features is matter of confusing; for example, tephrite contain analcime and feldspar forming the groundmass but they have lower Na₂O content (2-3.9 wt. %) than those of lamprophyres displaying the same range of MgO but devoid of those minerals (e.g. M-

113; Na₂O 4.03 wt. %). Similarly, phlogopite is frequent in lamprophyres, but tephrites which do not contain phlogopite and is lower in modal feldspar display higher Ba and Sr contents.

2.4.4.4.1.2 LM-lavas

In this group CaO, Al₂O₃, TiO₂, Fe₂O₃ and V trends evidence fractional crystallization of clinopyroxene and Fe-Ti oxides (Figs. 2.32-33). Lack of Eu anomaly, and increasing Sr and Al₂O₃ with decreasing MgO denote that the fractionation of plagioclase is insignificant and that fractionation of other mineral affected the concentration of those elements (e.g. analcime, see below). We cannot avoid the fact that analcimization has a great impact on geochemistry of alkaline rocks, but it only affects a restricted number of chemical parameters (e.g. Prelević *et al.*, 2004). Origin of analcime in the LM-lavas from this region is still a matter of debate. Two main hypotheses are proposed; (i) ionic exchange and replacement of leucite (L-type) or Na-rich phases such as feldspar or ii) primary igneous analcime (P-type) (Didon & Gemain, 1976; Comin-Chiaramonti *et al.*, 1979). The compositions of the analcimes from the present study are closer to those of L-type (see section 2.2.4.2). Due to the high modal content of analcime of the LM-lavas especially for evolved samples, it is likely possible that analcimization impact the concentration of some elements (e.g. Al₂O₃, Ba). According to Prelević *et al.* (2004), analcimization could leads to depletion of K₂O (or increase in Na₂O), Cs and Rb but does not have a great impact on the concentration of other trace elements (e.g. Ba). As an example pillow lavas (Hb) (LM- lavas) which contain less analcime than tephrite dykes (HM-lavas) have higher Ba content. In addition, there is no link between the abundance of analcime in LM-lavas (and even in tephrite-HM-lavas) and the Cs content. High Ba and Sr are associated with high Na₂O. It could be possible that occurrence of alkali sodic feldspar in more evolved lavas lead to those high concentrations. However, high Na₂O, Sr and Ba contents are also observed in more primitive samples (tephrite dykes compared to lamprophyres in HM-lavas), evidencing that

such elemental concentration may represent melt characteristic rather than the accumulation of some mineral phase.

2.4.4.4.1.3 Ps- rocks

The positive correlation of MgO with TiO₂, Fe₂O₃ and CaO, and the negative one with SiO₂, are in agreement with a clinopyroxene and Fe-Ti oxides fractionation process leading to the differentiation of the felsic intrusions from the mafic ones. In felsic samples, there is a dramatic drop of Sr and Ba contents and also a decreasing of Al₂O₃ and Na₂O contents at decreasing MgO. Those features could be related to the fractionation of biotite or feldspars. The strong negative spikes of Sr and Eu observed in normalized patterns, such as those of the investigated felsic plutonic rocks, are commonly interpreted as indicating a prior plagioclase fractionation process. Moreover, accumulation of zircon probably affects the Zr content of evolved compositions, which finally lead to the enrichment observed in felsic intrusions.

As mentioned before, although hornblende andesites have a composition intermediate between those of mafic and felsic intrusions, they differ by their mineral assemblage (high modal content of amphibole and plagioclase phenocrysts), and deviate from the general trend defined by Ps-rocks by lower K₂O, Zr, and Y values (Figs. 2.32g-33g). However, hornblende andesite lavas exhibit xenoliths especially clinopyroxene-bearing xenoliths (M-68). Nevertheless, they have isotopic values, which overlap with that of the investigated intrusions, indicating that both share the same sources.

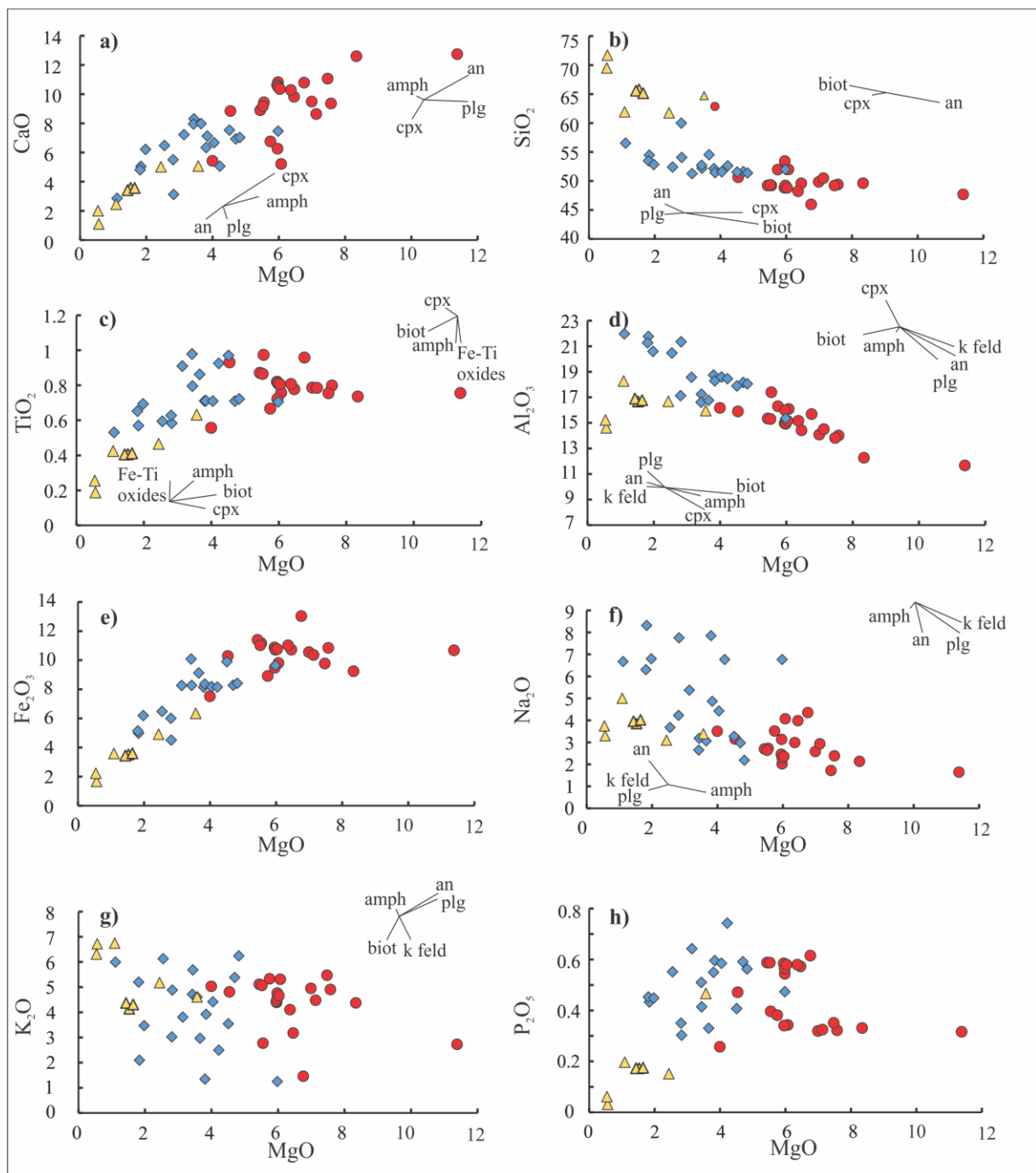


Figure 2.32 Variation diagrams for selected major oxides (wt.%) from investigated rocks. Plots of a) CaO, b) SiO₂, c) TiO₂, d) Al₂O₃, e) Fe₂O₃, f) Na₂O, g) K₂O, h) P₂O₅ vs MgO (wt.%). The arrows indicate the evolution of composition of the whole rock during single fractional crystallization of cpx (clinopyroxene), biot (biotite), an (analcime), amph (ampibole), plg (plagioclase), K-feld (potassium feldspar), Fe-Ti oxides (top right corner of diagram) or during accumulation process of those minerals (down left corner of diagram). Calculation for FC model is based on more primitive HM-lava M-116, and for accumulation is based on LM-lava M-128 (colorless clinopyroxene-free lavas), the average major elements contents for minerals is based on the results of mineral analysis performed during the present study, symbols are same as Fig.2.27.

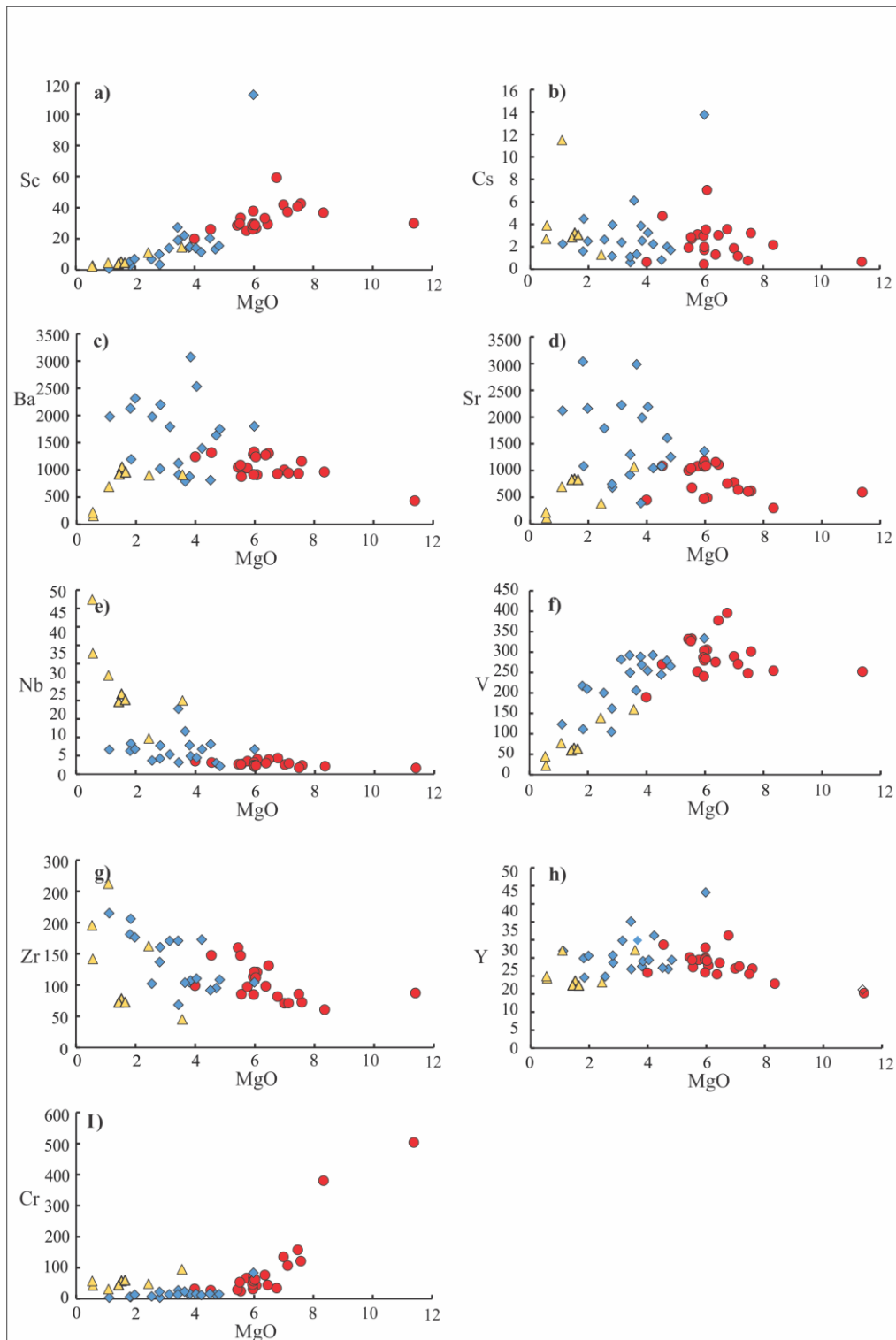


Figure 2.33 Variation diagrams for selected trace elements (ppm) vs MgO (wt.%) for investigated rocks, symbols are same as Fig.2.27.

2.4.4.4.2 Isotopes

By comparison to major elements, whose contents are related in a closed system to the magma path evolutions (e.g. fractional crystallization), REE and especially isotope values are more dependent on magma source characteristics. It is also well demonstrated that open system processes (e.g. magma mixing and/or crustal assimilation) highly influence the overall isotope or trace element contents of magmas during their evolution, even when fractional crystallization

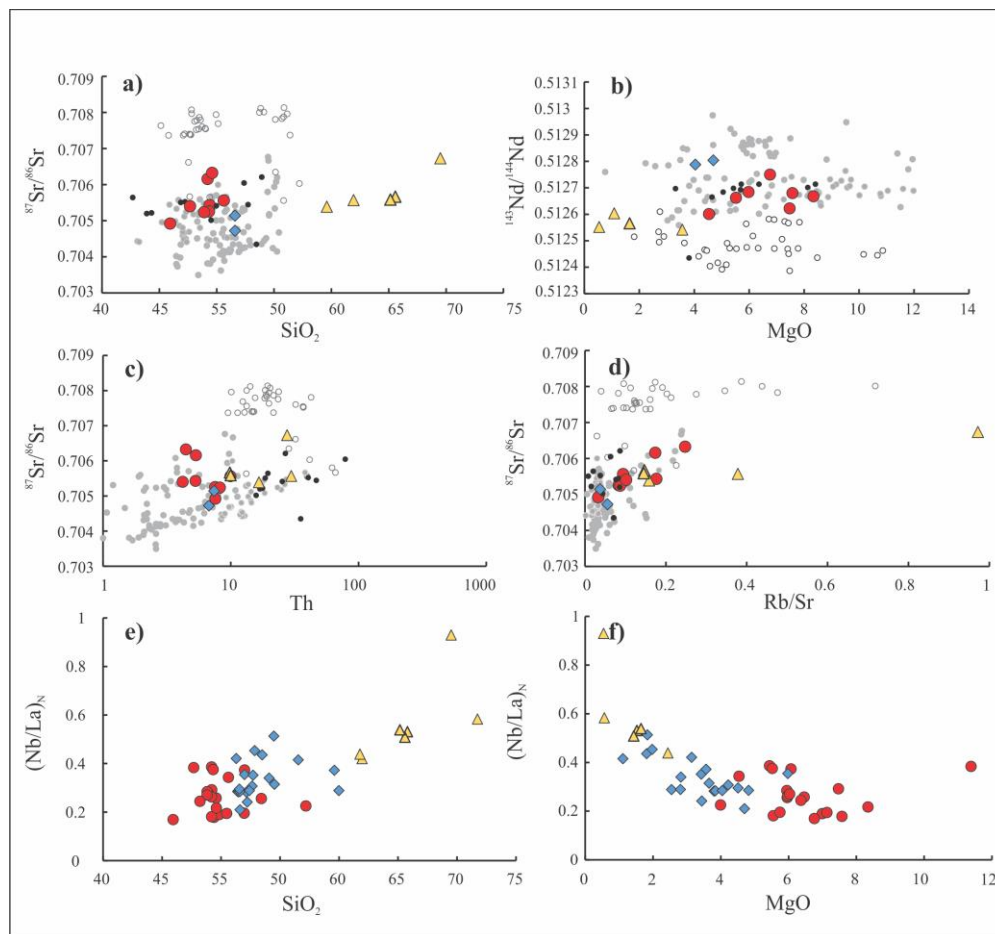


Figure 2.34 a) $^{87}\text{Sr}/^{86}\text{Sr}$ vs SiO_2 , b) $^{143}\text{Nd}/^{144}\text{Nd}$ vs MgO , c) $^{87}\text{Sr}/^{86}\text{Sr}$ vs Th, d) $^{87}\text{Sr}/^{86}\text{Sr}$ vs Rb/Sr , e) $(\text{Nb}/\text{La})_N$ vs SiO_2 and f) $(\text{Nb}/\text{La})_N$ vs MgO diagrams for investigated rocks including a comparison with alkaline lavas from the TIP, symbols are same as Fig.2.27.

process also operate (e.g. De Paolo, 1981, Powell, 1984). The composition of the three groups of investigated rocks are displayed on binary diagrams for Sr and Nd isotopes versus both major oxides (MgO and SiO_2) and trace elements (Th, Rb and Sr) (Fig. 2.34). Based on these

diagrams, it becomes likely that mineral fractionation could not explain the observed geochemical diversity of the rocks; whereas the role of different mantle sources with or without crustal components is self-evident by: i) the scatter of isotopic values for the same lithology (e.g. lamprophyres). ii) the higher Nd-isotope values in evolved LM-lavas (e.g. pillow lavas; Hb). iii) the positive correlation of Sr isotopes and SiO₂ in the alkali feldspar syenites.

2.5 DISCUSSION

The geochemical features such as the LILE and LREE\HREE enrichments as well as the Sr-Nd isotopic features similar to those of the alkaline magmatism from the Turkish Iranian Plateau (TIP) evidence not only a genetic link between the three types of rocks defined in the present study, but also a possible link between these rocks and the occurrence of alkaline rocks from the TIP. However, in the Salavat Range, based on bulk rocks and mineral chemical and isotopic compositions, it appears that fractional crystallization is not the main process explaining the major and trace element patterns of the investigated rocks. Below, several lines of evidence are discussed in order to evaluate how additional processes might control the final geochemistry of the studied samples and to confirm the possible link with the alkaline magmatism from the entire plateau.

2.5.1 Role of continental crust

Although experimental results and studies of mantle xenolith-bearing alkaline rocks have well demonstrated that alkaline melts mostly originate from mantle source(s) and exclude a crustal origin (e.g. Rock, 1991; Foley *et al.*, 1992; Pilet *et al.*, 2008; Niu *et al.*, 2011), several studies demonstrated that the composition of alkaline melts could be modified significantly by

mineral fractionation at shallow crustal depth with or without contamination and/or assimilation of the surrounding crust (e.g. Prelević *et al.*, 2004, 2015; Stepanov *et al.*, 2017).

In order to constrain the role of the continental crust, we first discuss if geochemistry of the investigated rocks classified into three types and considered as mantle-derived are modified by the overlying continental crust. In several locations of the Iranian plateau, granitoids and/or orthogneiss crustal rocks are largely exposed (see Hassanzadeh *et al.*, 2008). They represent crustal fragments from the northern margin of Gondwana, rifted away during the opening of the Paleotethys during the Paleozoic. Thereafter they were exposed at a large-scale by crustal extension and exhumation processes and are considered as the basement of the plateau (e.g. see Stampfli, 2000; Shahzeidi *et al.*, 2017; Hassanzadeh *et al.*, 2008). In the NW of Iran, Cadomian crustal basement is exposed along the Tabriz fault (Mishu granitoids 500 Ma Shahzeidi *et al.*, 2017). Generally, the granitoids basement, consisting of Si-rich rocks, would lead to considerable changes in the geochemistry of the contaminated melts and related rocks. As mentioned in the geochemical classification, for the Salavat Range, Ps-intrusions and hornblende andesite lavas have highest SiO₂ contents in comparison to other classified rocks. However, Ps-rocks similarly to the HM and LM-lavas have trace elements and LREE contents higher than those of the average continental crust (Fig. 2.30 c-d'). They also display isotopic ratios plotting within the mantle array. Thus, they clearly have a genetic link with mantle-derived melts (Fig. 2.31). However, there are evidences pointing out the possible involvement of the continental crust particularly in the genesis of the Ps-rocks. There is a strong increase of (Nb/La)_N ratio with increasing SiO₂ and decreasing MgO in PS- intrusions (Fig. 2.34e-f), characterized by the highest Th/La (0.3-0.6) and lowest Sm/La (≤ 0.14), ratios which all indicate a major role of the continental crust (e.g. Plank, 2005). Moreover, sample M-55A characterized by the highest value of (Nb/La)_N (0.92) and a positive correlation between SiO₂ and ⁸⁷Sr/⁸⁶Sr (Fig. 2.34a), clearly indicating contamination by continental crust. As mentioned in section

2.4.4.2 the highest Nb-Ta-Ti depletion is remarkable in the most primitive samples of HM- and LM-lavas. However by comparison the one of the Ps-rocks appears diluted. In the HM and LM-lavas the $(\text{Nb/La})_N$ ratio is therefore not only lower (0.16-0.38) than the one of Ps-rocks but also than that of the crustal basement (0.4) and the lower continental crust (0.6 Rudnick & Gao, 2003). In the other hand in figures 2.34e-f the HM-lavas differ from the Ps-rocks by a relatively limited and scattered range of $(\text{Nb/La})_N$. In addition, most of the analysed trace elements of HM-and LM-lavas do not vary much with SiO_2 content, whereas in Ps-rocks the elemental variations is more scattered. Moreover, investigated lavas are all silica undersaturated, thus assimilation of crustal components cannot be the main responsible for their geochemical signature, and they likely display characteristics of their parental mantle-derived melt(s).

Ps- group is characterized by some geochemical features similar to those of adakites (e.g. high Sr/Y, $\text{Al}_2\text{O}_3 > 15$ wt.%, Sr > 400 ppm, Yb < 18 and Yb < 1.8). In fact, magmatism with adakitic affinity has been frequently reported in the Turkish Iranian plateau (e.g. Jahangiri, 2007; Omrani *et al.*, 2008; Karsli *et al.*, 2010; 2011; Eyuboglu *et al.*, 2012; Pang *et al.*, 2016; Ahmadian *et al.*, 2016). Apart of this adakitic magmatism, the plateau is characterized by plutonic intrusions and sub-volcanic rocks displaying a wide range of compositions. In figure 2.29 plutonic intrusions and sub-volcanic rocks with calc-alkaline affinity (I-type intrusions, e.g. Nabatian *et al.*, 2014), potassic (A and I type intrusions, e.g. Karsli *et al.*, 2012, Aghazadeh *et al.*, 2010) and adakitic affinity (e.g. Jahangiri, 2007; Karsli *et al.*, 2010; 2011; Eyuboglu *et al.*, 2012; Azizi *et al.*, 2014; Pang *et al.*, 2016) are shown. Interestingly, a transitional component between potassic alkaline rocks (shoshonite) and adakites is also reported (e.g. Castro *et al.*, 2013; Ahmadian *et al.*, 2016). Intrusions from the Salavat Range resemble in term of major and trace elements to the adakitic rocks reported from the TIP. However, felsic intrusions with higher Yb are similar to arc-like rocks and are characterized by Eu anomalies. (Figs. 2.29f, 2.30c'). It should be noticed that the decreasing of Sr in felsic intrusions coherent

with negative Eu anomalies also indicate the role of mineral fractional (e.g. feldspar) in the history of those plutonic rocks. Thus trace element patterns also reflect the impact of fractionation of minerals. Moreover, such samples from felsic intrusions showing a dramatic drop of Sr/Y ratio plot out of the adakite field from the plateau and follow a trend transitional between those of adakites and shoshonites (Fig. 2.29d). In Ps-rocks, high Sr/Y ratio, lack of Eu anomalies, relatively low MgO (< 4.5 wt.%), and high SiO₂ (60-65.7 wt.%) contents of hornblende andesites better fit with the adakites (e.g. Fig. 2.29).

Although the first adakites reported from the Iranian plateau were interpreted as melting products of subducted oceanic crust (Omrani *et al.*, 2008; Jahangiri, 2007), several authors later demonstrated that the geochemical characteristics of those TIP adakites e.g. low MgO, Cr and Ni and high SiO₂ contents, enriched Sr-Nd isotope data as well as the trace element melting modeling are not in agreement with an oceanic slab melting. They demonstrated that fractional crystallization of mantle-derived melts or melts derived from melting of the lower continental crust are more consistent with observed geochemistry (e.g. Karsli *et al.*, 2010; Pang *et al.*, 2016). Fractionation of volatile-rich mantle products may indeed lead to adakitic fingerprints (e.g. Chiaradia, 2009). The coeval mafic magmas with adakitic magmatism, and the occurrence of magmatic products with chemical affinity intermediate between shoshonites and adakites (e.g. Ahmadian *et al.*, 2016; Omrani *et al.*, 2008; Castro *et al.*, 2013) lead to propose that the adakite affinity may result from the fractional crystallization (FC) of alkaline melts or the combination of that FC of alkaline melts with shallower depth processes (e.g. mixing and/or contamination) (e.g. Ahmadian *et al.*, 2016; Azizi *et al.*, 2014). In the Salavat Range the relatively high Sr/Y ratio similar to that of adakites could be seen even in the mafic HM-lavas (Fig. 2.29d), which may indicate that this high Sr/Y could directly reflect the parental melts. However, the tephrite dyke (samples M-84) has an isotope range (¹⁴³Nd/¹⁴⁴Nd) close to that of the mafic Ps-intrusions. It may indicate that these two types of rocks share the same parental

melts. The discrepancy observed between the trace element patterns of mafic and felsic intrusion cannot be explained by simple fractional crystallization (FC) or assimilation (AFC) of continental crust, (e.g. FC must lead to increase the trace element concentration in felsic intrusion). The observed REE dilutions is better explained by a mixing model of mafic intrusion with continental crust, which is also coherent with isotope values (Fig. 2.29d and Fig. 2.42).

In figure 2.29d, mixing lines of continental basement from NW Iran with the LM-lavas characterized by the lowest Sr and relatively high Sr/Y ratio (pillow lavas) are reported. Hornblende andesites do not perfectly fit with a mixing line. In the other hand the partial melting of lower continental crust, resulting from the thickening of the crust is one the most favorable scenario proposed to explain the origin of adakites occurring within the Alps-Himalaya orogenic belt (e.g. Karsli *et al.*, 2012, Pang *et al.*, 2016 and Guo *et al.*, 2007). Experimental results pointed out that partial melting of the lower continental crust mainly leads to the formation of adakitic melt (e.g. Qian & Hermann, 2013). Adakite melts derived from the melting of the lower crust have slightly higher SiO₂ content with low K₂O. Whereas the investigated samples have higher K₂O (see Fig. 2.29b), and plot in an intermediate position between melt with potassic affinity and melt derived from the lower continental crust. In figure 2.35 the average trace element pattern of adakitic rocks derived from the melting of the lower continental crust is shown (taken from Qian & Hermann, 2013). Hornblende andesites have a very similar trend to that of this melt, with slightly higher REE content. Elemental concentration of the hornblende andesites as well as their different mineral compositions and assemblages could not be derived from fractional crystallization of more primitive lavas. However, there are some evidences indicating a relevant petrogenetic link between those hornblende andesites and alkaline melts (e.g. HM-lavas) with also the influence of crustal derived melts. For example although, hornblende andesites have whole rocks and mineral compositions (e.g. amphibole) of classical calc-alkaline series, hornblende with similar compositions than those of lamprophyres

occasionally occurs in the cumulative xenoliths uplifted by these lavas. Moreover, the hornblende andesites hosting those xenoliths, have slightly different trace element patterns than those of the xenolith-free ones (e.g. close to the HM-lavas). Amphibole as early-crystallized mineral may record the compositional variation of the equilibrium melt. They have Mg# ranging from 0.6 to 0.87 and thus the Mg# of melts in equilibrium with those amphiboles is relatively high (0.83-0.75), whereas commonly in andesite melt this Mg# < 0.65 (e.g. Alonso-Perez *et al.*, 2009). It means that those amphiboles must be in equilibrium with moderately primitive melts. The values are close to the values of amphiboles in equilibrium with the primitive melts of kersantite lamprophyres (0.8-0.85). Thus, we may consider that melts similar to the parental ones of lamprophyre kersantites played a role in the genesis of the hornblende

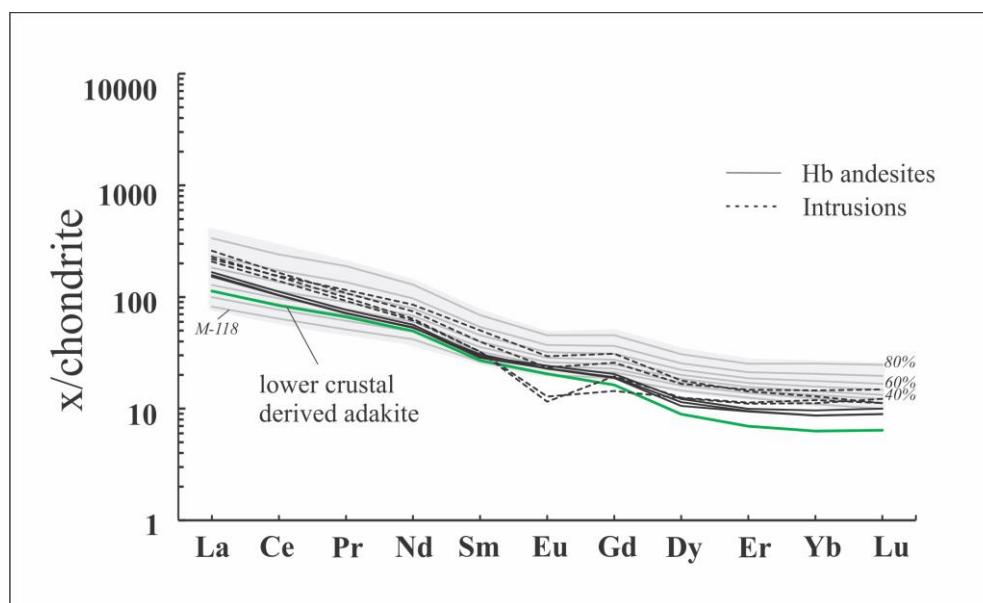


Figure 2.35 Diagram illustrating that chondrite-normalized (Sun and McDonough, 1989) REE patterns of Ps-rocks differ from fractional crystallization (FC) trends (gray lines) produced by 20 to 80 % fractionation of cpx (45)-amph (30)-plg (15)-bit (10) from the most primitive HM-lava taken as starting composition (M-118). The average composition of the 204 samples of adakites derived from the melting lower crust is shown as green line (see references in supplementary data table; Qian & Hermann, 2013). Hornblende andesites from the Salavat Range are more comparable to the lower crustal derived rocks than to FC products.

andesites. However, none of the fractional crystallization models applied to primitive samples fitted with trace elements concentrations of hornblende andesite. Whereas, in term of isotopic ratios the values plot in a field intermediate between the one defined by HM-lavas (tephrite and kersantite) from the plateau and the one of the lower continental crust (see Fig 2.42 section 2.5.3). It indicates that a combination of mantle derived melt(s) and continental crust is the most favorable composition to explain the final geochemical characteristic hornblende andesites.

2.5.2 Presence of several mantle-derived melts; evidence from macrocrystal compositions

Generally, mantle-derived melts such as alkaline melts before they reach to the surface are collected into reservoirs at shallow depth where they may crystallize macrocrysts. Depending on the variation of several physico-chemical factors (e.g. pressure, temperature, volatile contents and chemical composition of melt) some zoning features could appear and characterize those macrocrysts. Accordingly, the change in chemical composition due to the evolution of the original melt during mineral crystallization/accumulation (e.g. Larrea *et al.*, 2013; Ubide *et al.*, 2014; Jankovics *et al.*, 2016), or the mixing with another mantle-derived melt (e.g. Muravyeva *et al.*, 2014; Tappe *et al.*, 2016), and/or interaction with crustal components could also be recorded during the mineral growth history by zoning patterns (e.g. Zhu & Ogasawara, 2004; Jankovics *et al.*, 2016). Thus, early-crystallized mafic minerals such as clinopyroxene could be important record of the magmatic history.

The TIP is characterized by the wide occurrence of various alkaline magmatic rocks (potassic and sodic) whose nature of sources is mainly based on their bulk rock chemistry. In the investigated samples, some clinopyroxenes display complex zoning patterns characterized by strongly different colorless and green colored zones, characterized by significantly different chemical composition. Various zoning patterns frequently appear together in the same rocks,

particularly in lamprophyres and tephrites (HM-lavas). Below I discuss the origin of colorless and green colored clinopyroxenes, in order to consider the possible genetic link between their hosted rocks.

2.5.2.1 Origin of Colorless/green colored clinopyroxenes

Colorless and green colored clinopyroxenes are frequently reported as single crystals or accumulations in lavas (e.g. lamprophyre, basanite, tephrite, or nephelinite). They are frequently found in many magmatic provinces from the Mediterranean region. i.e. Catalonian Coastal Range (e.g. Ubide *et al.*, 2014), French Massif Central (e.g. Wass, 1979; Pilet *et al.*, 2002), Eifel (e.g. Duda & Schmincke, 1985; Shaw, 2002), Pannonian Basin (e.g. Dobosi, 1982; Dobosi & Fodor, 1992, Jankovics *et al.*, 2016), Italy (Barton *et al.*, 1982), West and Central Anatolia (Semiz *et al.*, 2012; Paltevoet *et al.*, 2014), and finally NW Iran (this study). However, if they are frequently described in alkaline rocks their origin is still matter of debate.

2.5.2.1.1 colorless clinopyroxene

The major element composition of colorless clinopyroxenes overlapp with compositions of clinopyroxene crystallized at relatively high-pressure conditions (e.g. xenoliths or Cr-diopside Fig. 2.19), accordingly they were interpreted as disaggregated upper mantle xenoliths, or as high-pressure crystallization products of their host-lavas (e.g. Wass, 1979, Shaw & Eyzaguirre, 2000; Semiz *et al.*, 2012; Prelević *et al.*, 2015). Additionally an origin by accumulation of crystals resulting from the reaction at the interface between a differentiated melt and carbonate host rock before the eruption at the surface has also been suggested (Di Rocco *et al.*, 2012). In the Salavat Range, the geochemical bulk-rock characteristics of the HM-lavas evidence that the effect of crustal contamination is insignificant (see above). Moreover the lack of carbonate sequences within the crustal basement from the region, as well as the lack of skarn preclude an origin of the investigated clinopyroxenes as disaggregated accumulation

resulting from reaction at melt-carbonate rock interface. Colorless clinopyroxenes are abundant in HM-lavas; as core, rim of macrocrysts, or as bright bands of phenocrysts, whereas they are totally absent in the LM-lavas. They have more primitive composition (highest MgO and lowest TiO₂ and Al₂O₃) than other phenocrysts and microcrysts as well. However, an evolutionary trend linking them to microphenocrysts and microliths points out that they are co-magmatic. Accordingly, this trend preclude their origin as xenocrysts. Moreover, although their composition is similar to those of high-pressure clinopyroxenes (e.g. from lithospheric mantle xenoliths) they display magmatic texture (oscillatory zoning), indicating that they are not derived from mantle xenoliths.

Generally, macrocrysts being cogenetic with host-lavas are classified as phenocrysts. To test this hypothesis for the colorless clinopyroxenes, I calculated the Mg# of melt in equilibrium with those clinopyroxenes (calculation is based on $Kd_{\text{Fe-Mg}}^{\text{mineral-melt}}$; 0.26 ± 0.05 taken from Akinin *et al.*, 2005). The results are reported in figure 2.36 in which the colorless clinopyroxenes with high Mg#, plot above the calculated curve, clearly indicating the lack of a long-term equilibrium with the host. Only the colorless clinopyroxenes from the sample characterized by the highest modal content of those clinopyroxene plot just above the curve. These evidences combined with petrographic observations, i.e. corroded cores and overgrowth rims, and mineral chemistry, i.e. spot analysis and 2D major elements mapping support the idea that we cannot consider the colorless clinopyroxene as phenocrysts. The best term to describe them is “antecrysts”: i.e. large crystals that do not share chemical composition with the surrounding magma, but crystallized in the same magmatic system from a more primitive melt (e.g. Davidson *et al.*, 2007, Larrea *et al.*, 2013).

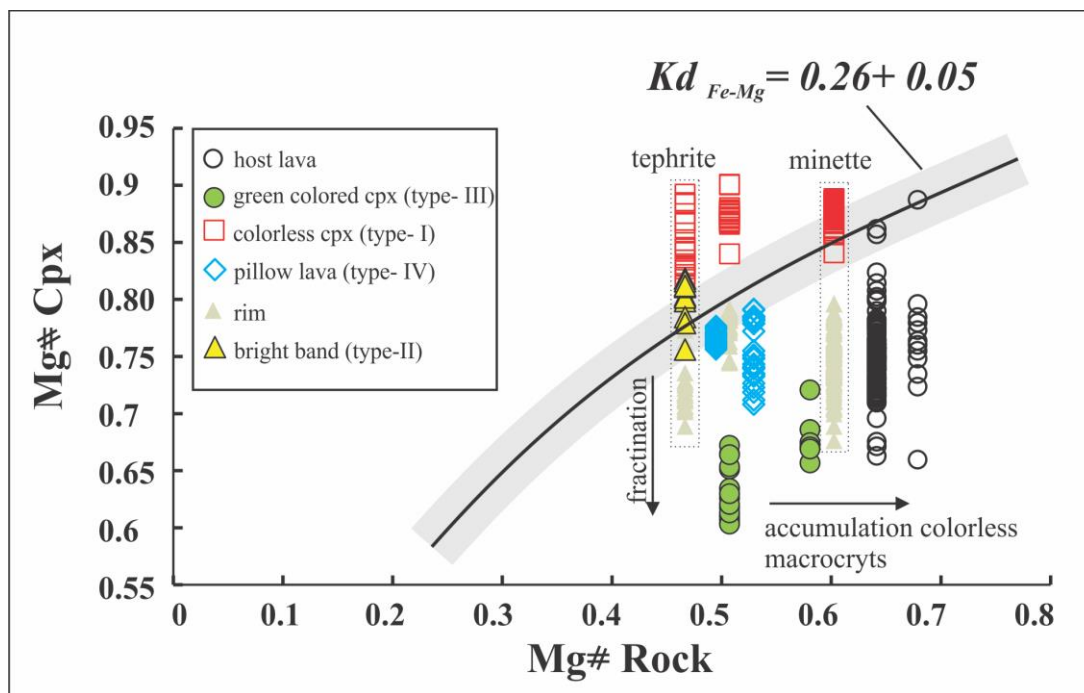


Figure 2.36 Mg# in clinopyroxene (cpx) vs Mg# in rock diagram. The black curve represents the mineral-melt equilibrium according to the Fe-Mg exchange (after Rhodes *et al.*, 1979) using distribution coefficient ($Kd_{Fe-Mg} = 0.26 \pm 0.05$) given by Akinin *et al.* (2005). Mineral in equilibrium with melt plot close to the curve, whereas when disequilibrium occur they plot far from the curve such as in the case of or late fractionation products.

2.5.2.1.2 Green colored clinopyroxene

I also focused on the Mg# and calculated the evolution of melts and of green colored clinopyroxenes in equilibrium with them (cpx types III and IV; Fig. 2.36). All green-colored clinopyroxenes have lower Mg# than colorless ones and plot within or below the curve. Thus, they are apparently in equilibrium with the surrounding groundmass representing the melt composition or influenced by fractional crystallization (e.g. rim). As mentioned in the zoning pattern description (section 2.4.3), green colored clinopyroxene categorized in to types III and IV. Interestingly green-colored clinopyroxene of type IV (e.g. pillow lavas) and rim of type I in tephrites plot just slightly below the curve thus may represent phenocrysts. In addition, they have similar composition than microphenocrysts and microliths from the groundmass. Thus, they are in equilibrium with the groundmass. Hence, they represent true phenocrysts.

The green-colored cores of clinopyroxene of type III plot below the equilibrium curve and also below those of Type IV. This observation as well as the occurrence of corroded edges indicate that they are in disequilibrium with their surrounding groundmass. Electron microprobe analysis points out that the chemical patterns of those clinopyroxenes correspond to reverse zoning in these patterns (see Fig. 2.24). Although reverse zoning may indicate the occurrence of xenocryst or redox condition changes due to crystallization of Fe-Ti oxides, mixing of melts is an additional possibility. Several origins have been proposed by previous studies to explain the frequent occurrence of green-colored clinopyroxenes in worldwide alkaline rocks. Numerous studies consider them as cognate phases resulting from i) high pressure melt crystallization (Wass, 1979) or ii) crystallization of evolved magma mixed with the mafic host magma (Dobosi & Fodor, 1992; Ubide *et al.*, 2014; Jankovics *et al.*, 2016). Numerous other studies consider that they represent disaggregated xenolith or xenocrysts from iii) wall rocks (Jankovics *et al.*, 2016; Zhu & Ogasawara, 2004) iv) metasomatic upper mantle (Pilet *et al.*, 2002; Barton & Bergen, 1981). Pilet *et al.* (2002) have even suggested that the wide occurrence of green clinopyroxene can reflect a general process linked to the origin and evolution of alkaline melts that directly relates to a specific type of metasomatism affecting the mantle beneath alkaline provinces. However, the association of zoning features related to magmatic texture (e.g. Fig. 2.22) with evolved compositions (Low Mg#) in the investigated green-colored clinopyroxenes from NW Iran rule out the mantle xenoliths disaggregation origin. Additionally, the similarity of their major and trace element compositions with those of phenocrysts from pillow lavas (type IV-a), seems to favor their origin as fractionation products from similar melts than those given the pillow lavas.

2.5.2.2 Bulk rock geochemistry; consequence of the macrocrystals accumulation

HM- and LM-lavas from the Salavat Range are relatively highly porphyritic lavas. As mentioned in the previous section, the green-colored clinopyroxenes from the LM-lavas (e.g. pillow lavas) are phenocrysts, whereas in the more primitive samples, HM-lavas display variable proportion of colorless antecrysts of clinopyroxene. Interestingly, in the HM-lavas, particularly host lavas (Ha) and minette lamprophyres, the samples with the highest modal proportion of antecryst have high MgO content (up to 11 wt.%). In HM-lavas the composition of the rim of antecrysts as well as those of clinopyroxene microphenocrysts and from the groundmass have the same composition than those occurring within the groundmass of LM-lavas. That indicates that differentiation is not the major process controlling the difference of composition observed between HM- and LM-lavas. It should be noticed that due to high accumulation of antecrysts in the more primitive samples (HM-lavas), the latter appear even more primitive, and thus, antecrysts from these samples plot within equilibrium curve. Such observation (Fig. 2.36) that colorless antecrysts of minette samples plot within or just slightly above the equilibrium curve disagrees with the optical and chemical features evidencing that those antecrysts are in disequilibrium with their surrounding groundmass. To test the influence of colorless antecrysts on the minette whole rock chemistry, the accumulation trend for clinopyroxene is reported in figure 2.32. cpx trend was calculated based on the average composition of colorless antecryst, in addition to the composition of the more primitive sample of LM-lavas lacking colorless antecryst (M-128) and considered as representative of the groundmass composition. As we may see in figure 2.32 the trend perfectly explains the major element concentration of HM-lava (particularly lamprophyres) in Harker-type diagrams. Regarding trace element patterns, it appears that the modal proportion of the antecrysts influences the LILE and HFSE's concentrations of HM-lavas. Indeed as mentioned in section

2.4.3.2, antecrysts (type I and II), are characterized by relatively depleted trace elements. Therefore the higher concentration of LILE and HFSE in lamprophyres (e.g. M-113) correspond to a decreasing of proportion of antecrysts (type I), whereas in minette samples or host lavas (Ha) with high proportion of antecrysts, LREE and HFSE are more depleted (Fig. 2.37).

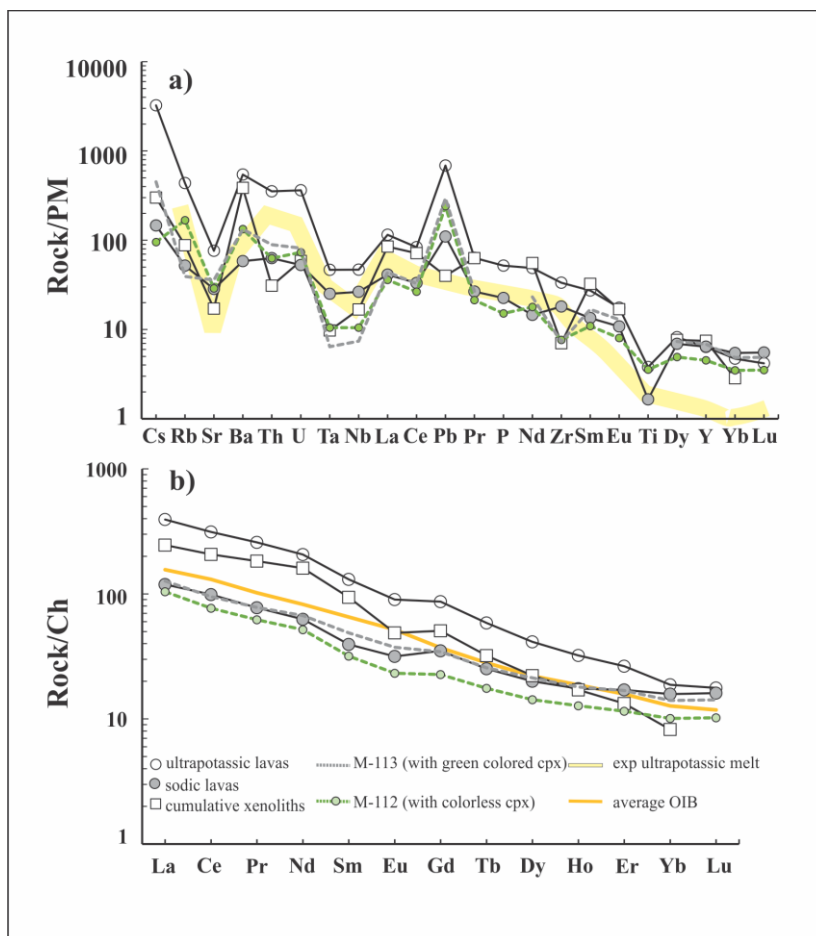


Figure 2.37 a) Primitive mantle trace element and b) chondrite-normalized REE patterns (Sun and McDonough, 1989) for alkaline lavas from the TIP (references in table 10 of appendix) and associated cumulative xenoliths (Kherzerlou *et al.*, 2017). Field for ultrapotassic rocks from experimental results is based on data from melting mixture starting composition (depleted mantle via sediments, Wang *et al.*, 2017). Data source for OIB; Sun and McDonough (1989).

The evidences of a compositional gap between antecrysts and phenocryst could indicate compositionally different melts, originated from similar or different sources (Tappe, 2004;

Orejana *et al.*, 2007 Grutzner *et al.*, 2013; Larrea *et al.*, 2013; Platevoet *et al.*, 2014). For example, in the case of similar sources several processes may lead to the observation of primitive and evolved components together; i.e. i) simple fractional crystallization at relatively high pressure of melt with mostly primitive component and later mixing of the formed evolved component with the primitive one (e.g. Orejana *et al.*, 2007; Wei *et al.*, 2015), ii) mixing of melts resulted from different degrees of melting of the same source (e.g. Tappe, 2004), iii) convective self-mixing (Couch *et al.*, 2001). However, in all the above mentioned cases mineral should have crystallized from melts with the same sources, thus their isotopic compositions must remain similar. Whereas in the investigated samples, there is considerable contrast in term of isotopes, between HM-lavas (with antecryst) and the LM-lavas (without antecryst). Accordingly this isotope contrast could be observed within the same lithology (e.g. lamprophyres) characterized by a variable modal content of colorless antecryst. As an example, sample with high modal content of antecryst have higher $^{87}\text{Sr}/^{86}\text{Sr}$ or lower $^{143}\text{Nd}/^{144}\text{Nd}$ ratios than those containing less antecrysts. Interestingly there are positive correlations between isotopic values and alkaline contents; one between K_2O and $^{87}\text{Sr}/^{86}\text{Sr}$ and Na_2O vs. $^{143}\text{Nd}/^{144}\text{Nd}$. Finally, it appears that lavas with high modal proportion of colorless antecrysts reflect potassic/ultrapotassic components characterized by low Nd isotopic ratios. In the other hand those with green-colored clinopyroxenes represent sodic components characterized by high Nd isotopic ratios (Fig. 2.38).

2.5.3 Nature of involved alkaline melts

Occurrences of alkaline magmatism are important because they are relatively rare and especially because they are representative of exotic uncommon mantle-derived melts (Wyllie, 1980; Foley *et al.*, 1987; 1992; Mitchell, 1995; Rock, 1991; Mitchell & Bergman, 1991). That added to their peculiar distribution in various geodynamic settings make them widely studied

(e.g. Lustrino & Wilson, 2007; Melchiorre *et al.*, 2017). Accordingly, considering the complexity of their origin and the importance of their study in orogenic systems, lead to the discovery of numerous alkaline outcrops distributed from the Central Anatolia to the East Iran (see chapter 3 and reference there in).

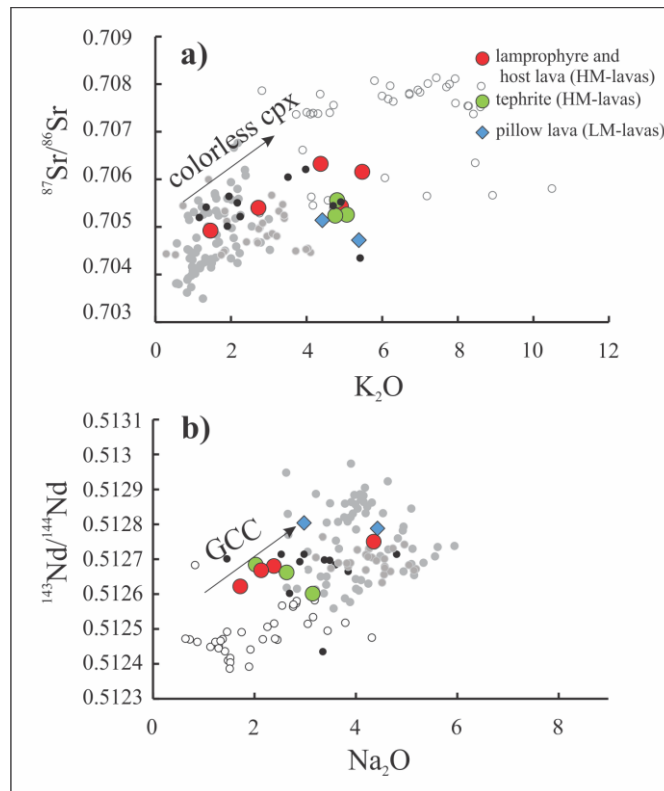


Figure 2.38 Bulk rock Sr-Nd isotope ratios vs alkali (K_2O and Na_2O) major elements (wt.%) for HM-lavas and pillow lavas of LM-lavas. The TIP alkaline lavas from the literature plotted to compare. (a) Arrow highlights the change of composition of lamprophyres towards those of ultrapotassic lavas in the TIP when the mode of colorless clinopyroxene increases, (b) whereas with increasing mode of green colored clinopyroxene (GCC) bulk rock composition changes towards OIB-like lavas in the TIP. Symbols are as in Fig. 2.27.

An overall overview of the geochemistry of the alkaline magmatism from the TIP, allows to subdivide it into potassic/ultrapotassic and sodic series, respectively (Fig. 2.27b). The alkaline sodic and potassic/ultrapotassic series, apart of their major elements, are also distinguished by their isotopic and trace element features (Fig. 2.31). In this chapter, we just briefly mention their main geochemical signatures, whereas in the next chapter their main characteristics are

describing in detail. In the TIP, alkaline sodic magmatic rocks display OIB-like signature such as HFSE and LILE enrichment in their trace element patterns, whereas ultrapotassic lavas are mainly distinguished by typical subduction-influenced patterns (e.g. HFSE depletion, LILE enrichment) (Fig. 2.37). Moreover, ultrapotassic lavas with low Pb/Ce, Nb/U, $^{143}\text{Nd}/^{144}\text{Nd}$ and high Th/Nb and $^{87}\text{Sr}/^{86}\text{Sr}$, reflect the contribution of continental material (or sediment-like components) whereas sodic lavas with high Pb/Ce, Nb/U, $^{143}\text{Nd}/^{144}\text{Nd}$, and low Th/Nb have characteristics of asthenosphere-derived melts (e.g. OIB) (Fig. 2.38). Ultrapotassic lavas with subduction influenced-patterns and sodic ones with OIB-like patterns should not coexist but their association has been described in numerous outcrops from the TIP (e.g. Prelević *et al.*, 2015; Aghazadeh *et al.*, 2015). Due to the long history of subduction beneath the TIP, magmatic rocks with orogenic (subduction influenced) and anorogenic (OIB-like) fingerprints, could be interpreted as reflecting the role of enriched mantle at varied lithosphere and asthenosphere depths. Subduction-related patterns could be indeed related to a mantle source located within the lithosphere whereas OIB like patterns could derive from an asthenospheric source upwelled during slab-window or slab-break off processes (e.g. Prelević *et al.*, 2015, Shafaii Moghadam *et al.*, 2014) or stuck between a flattened oceanic slab and the continental lithosphere (Verdel *et al.*, 2011). To sum up, according to those interpretations the source of sodic lavas could be located within the asthenosphere, whereas those for ultrapotassic lavas could be located within the lithosphere. Considering the fact that magmatism from the Salavat Range is classified as alkaline magmatism and plot within the two alkaline fields (Fig. 2.27b), and that their mineral and bulk rocks chemistry reflect the involvement of more than one melt in their genesis, thus we may conclude that those involved melts must have alkaline affinities (see previous section). Below the geochemical signature of those alkaline melts is evaluated in order to check if there is any link between them and the common alkaline magmatism from the TIP.

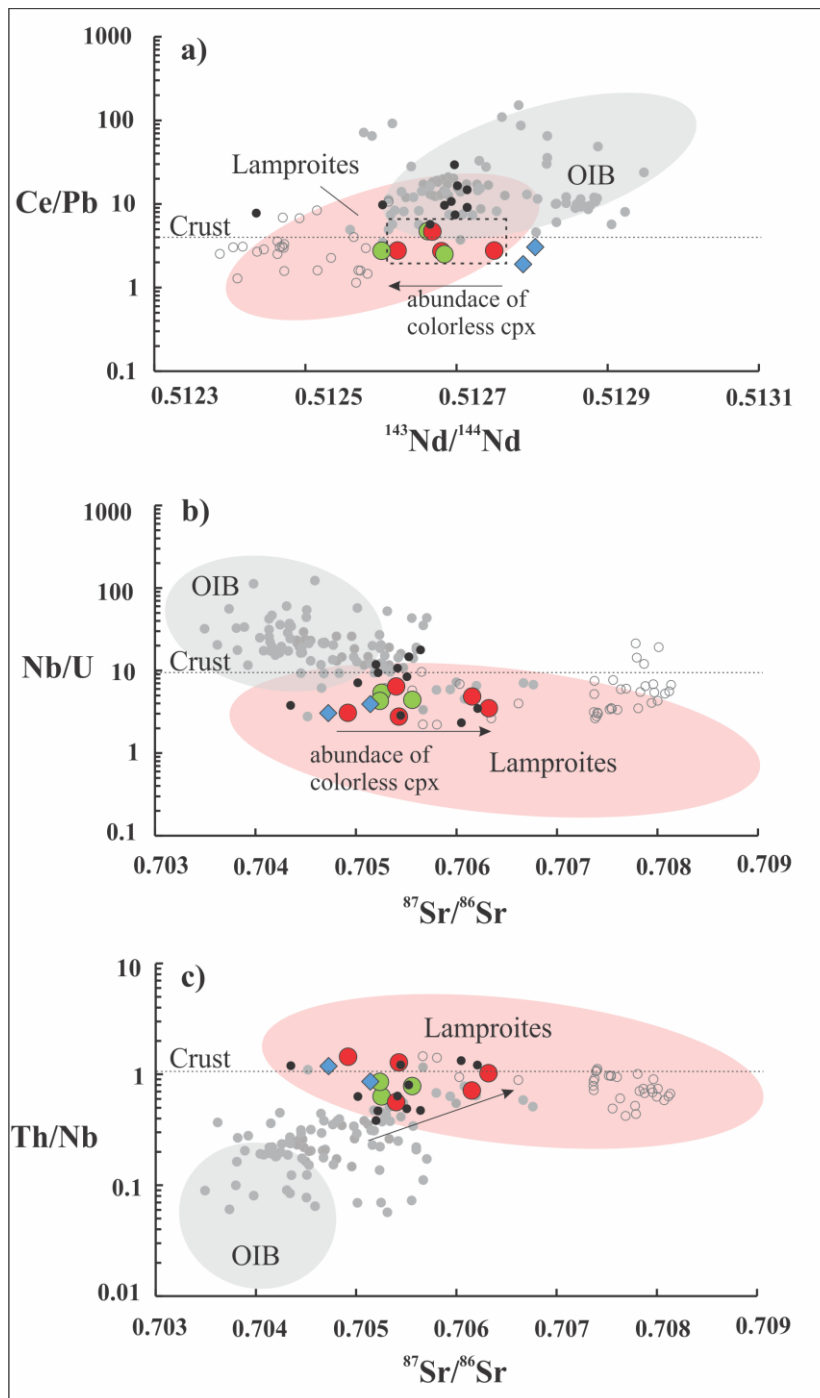


Figure 2.39. a) variation of Ce/Pb vs $^{143}\text{Nd}/^{144}\text{Nd}$ and b-c) Nb/U and Th/Nb vs $^{87}\text{Sr}/^{86}\text{Sr}$ to identify the change of bulk rock composition of HM-lavas and LM-lavas (pillow lavas) with increasing modal abundance of colorless clinopyroxene. As we see in these diagrams with increasing abundance of colorless clinopyroxene, the bulk composition changes towards the lamproitic composition from the TIP. Data source for OIB from GEOROC and lamproites from West Mediterranean after Prelevic et al. (2010). For the data source of alkaline lavas from the TIP refer to the table 10 of appendix. Symbols are same as in figure 2.38.

2.5.3.1 Major element

Low Al and Ti is one of the main characteristics to identify different potassic melts (e.g. Rock 1991, Mitchell & Bergmann, 1991; Cellai *et al.*, 1994 and Fig. 2.40). In addition, occurrence of exotic melt is characterized by the high MgO and CaO contents of clinopyroxene (Fig. 2. 41). The colorless clinopyroxene with high Mg#, represent the most primitive components. As we see in figure 2.41 colorless antecrysts (type I), with high CaO, have similar composition than clinopyroxene from the cumulative xenoliths occurring in lamproites from the TIP (Prelević *et al.*, 2015). In this diagram, antecrysts plot in the field of kamafugite melt, and follow the calculated curve for hypothetical kamafugite parental melt. In the other hand, bright band colorless clinopyroxenes (type II), with relatively low CaO, plot within the field of lamproites from the TIP, and follow the calculated curve for hypothetical lamproitic melt. Green-colored clinopyroxenes (e.g. type II), with lower MgO, don't plot within fields (or don't

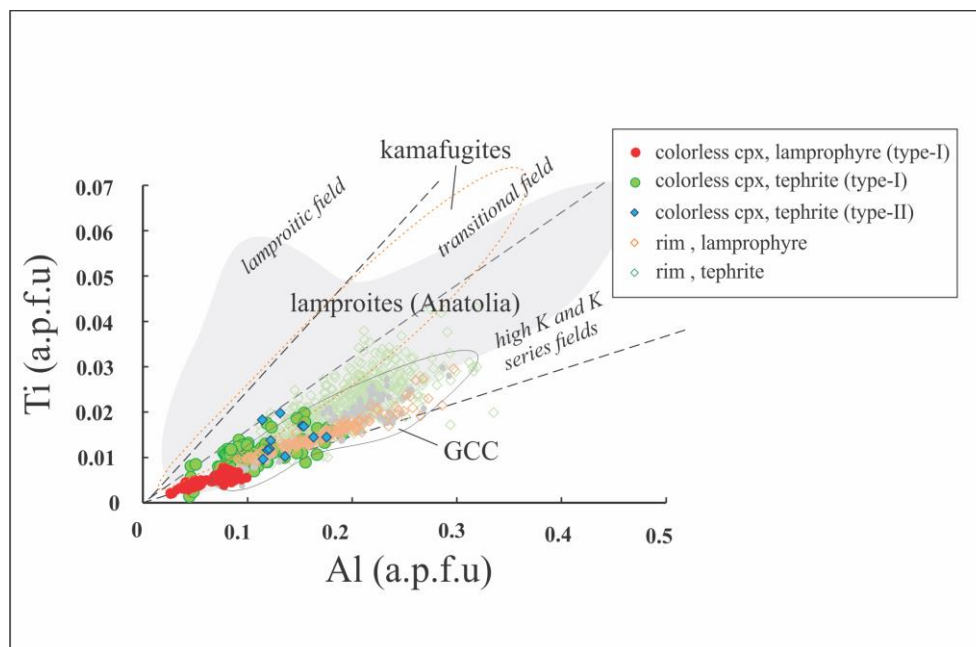


Figure 2.40. Ti (a.p.f.u) vs Al (a.p.f.u) of clinopyroxene for potassic and ultrapotassic lavas. Division lines and fields for kamafugites and lamproite from Anatolia are based on data of Semiz *et al.* (2012) and Prelevic *et al.* (2015) and reference therein.

follow hypothetical curves) of those two types of exotic melts. These observations associated to the positive correlation observed between the modal proportion of colorless antecrysts and the bulk rock K_2O content, point out the potassic/ultrapotassic affinity of HM-lavas (e.g. minette) which is linked to antecrysts and characteristics of exotic melt(s) (e.g. kamafugite or lamproite) in equilibrium with the latter.

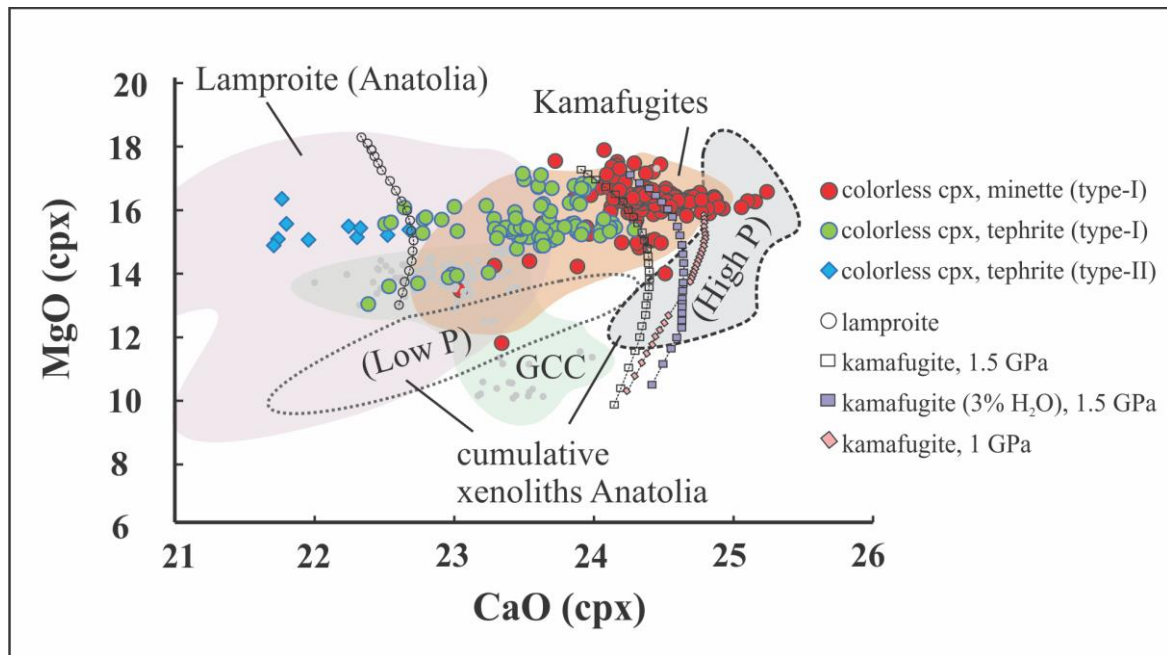


Figure 2.41. CaO (wt.%) vs MgO (wt.%) diagram for clinopyroxene (cpx) of HM-lavas from the Salavat Range. Shaded data represent green colored core (GCC) of clinopyroxene in HM-Lavas and those in pillow lavas (LM-lavas). Dashed lines represent CaO and MgO contents of clinopyroxene from cumulative xenoliths formed by exotic kamafugite and lamproite melts high and low pressures conditions (after Prelevic *et al.*, 2015). Trends represent composition of parental melt at different crystallization conditions after Prelevic *et al.* (2015). Field for kamafugites from the same reference.

2.5.3.2 Trace elements and isotopes

Trace elements could provide important and detailed information about the melt in equilibrium with minerals. To calculate the melt in equilibrium with colorless- and green-colored clinopyroxenes, I used the mineral/melt partition coefficients suggested for alkaline rocks (Ubide *et al.*, 2014). As we may see in the figure 2.42, calculated melts in equilibrium

with colorless- and green-colored clinopyroxenes are significantly different in term of REE enrichment and LREE/HREE fractionation as well. The liquids in equilibrium with green-colored clinopyroxenes have the highest REE concentration. They display nearly parallel patterns between them and with those of the most primitive LM-lavas (e.g. pillow lavas) suggesting their they are all cogenetic. Interestingly, these clinopyroxens (type III, IV) overlapped with fractionation product of sodic lavas in the TIP (Figs. 2.42c-d).

The colorless clinopyroxene antecrysts, type I and II, have significant high slop in REE and patterns relatively parallel to those of the enriched mantle components (e.g. Fig. 2.42b). However compared to enriched mantle or green-colored clinopyroxenes, they appear LREE depleted. In figure 2.37a lavas with the highest modal content of type I antecryst (e.g. minette) are compared to the cumulative xenoliths and ultrapotassic lavas from the TIP. They have similar trace element patterns than those of these cumulative xenoliths interpreted as cognate crystals of host ultrapotassic melt (e.g. lamproite or kamafugite) crystallized within the relatively high pressure conditions of the crust-mantle boundary (Khezerlou *et al.*, 2017; Prelević *et al.*, 2015; Semiz *et al.*, 2012). We therefore may consider that the investigated antecrysts and the exotic ultrapotassic lavas are cogenetic and that the former crystallized at relatively high pressures. Thus the type I clinopyroxene antecrysts from the Salavat Range are representative of the ultrapotassic melts from the TIP. However, the nature of the sources of ultrapotassic lavas from the plateau is still a confusing issue. In fact they do not display uniform compositions neither in term of trace element and isotopes (e.g. Prelević *et al.*, 2015; Aghazadeh *et al.*, 2015). They are characterized by isotope values (low Nd and variable Sr) which follow trends of the global Enriched mantle sources EM-I and EM-II. In the western Mediterranean, their chemical fingerprints have been related to depleted mantle (lithosphere) source with contribution of recycled pelagic sediments or continental upper crust (e.g. Prelević *et al.*, 2004; Prelević & Foley, 2007; Lustrino & Wilson, 2007; Avanzinelli *et al.*, 2009).

However, in the TIP, they are slightly more depleted in Sr isotopic ratios than their equivalents from the Western Mediterranean.

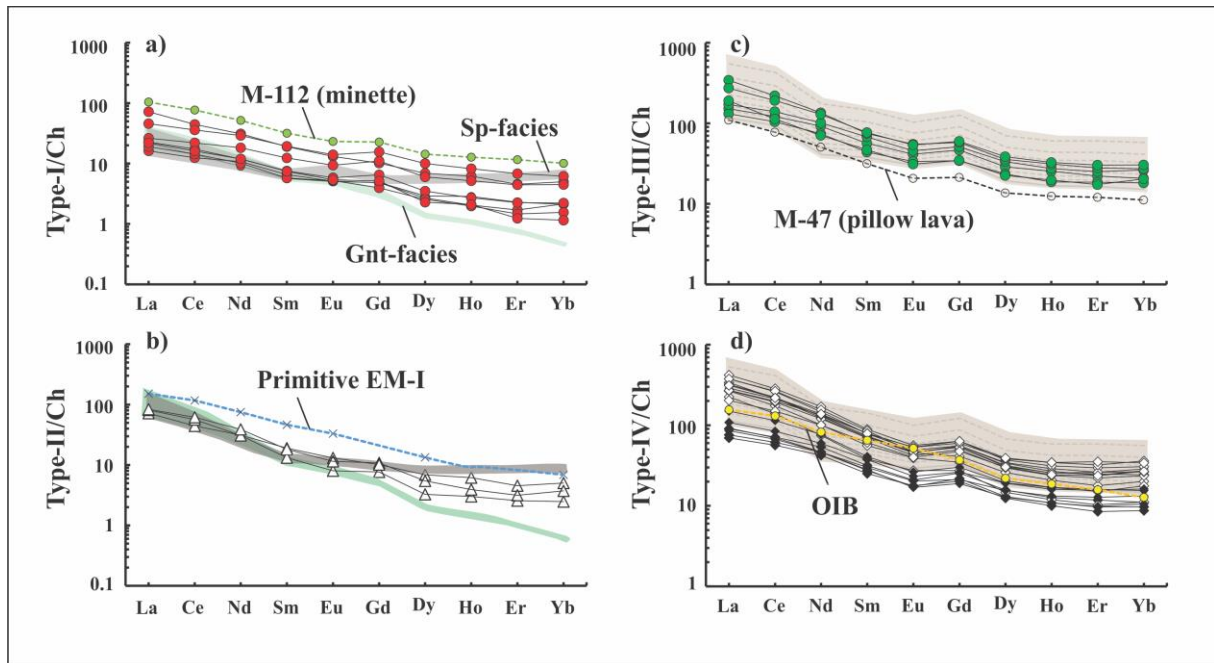


Figure 2.42. Chondrite normalized (Sun and McDonough, 1989) REE diagrams showing melt in equilibrium with colorless clinopyroxene from Type-I (a), Type-II (b), and green colored clinopyroxene from type-III (c) and -IV (d) zoned macrocrysts. Melt calculated based on $Kd_{\text{mineral-melt}}$ proposed by Ubide et al. (2014). In these diagrams results are compared to whole rocks of sample with the highest mode (M-112) and the lack of colorless clinopyroxene (M-47), respectively. Shaded fields: results of melting (a-b) and fractional crystallization models (c-d). Fractional crystallization trends represent 20 to 90% fractions of OIB type lava with Ol (35%) cpx (55%), plg (10%) (average OIB-like lavas from the TIP). Calculated partial melting model is based on non-modal batch melting model in the spinel (sp) and garnet (Gnt) mantle stability fields. Shaded fields represent 3-10% of melting. A heterogeneous composition (depleted mantle via varied 1% (a) to 7% (b) sediment) was used as starting composition. Mineral proportion and distribution coefficient are from McKenzie & O’Nions (1991).

There is no doubt that ultrapotassic melts are derived from a mantle with peculiar geochemical characteristics. Lamproite is one of the extreme composition of ultrapotassic exotic melts with high MgO and LREE/HREE, low CaO and Nd isotopic ratios and variable Sr isotopic ratios. Based on variability of their trace element patterns they are divided into orogenic and anorogenic lamproites displaying classical subduction-influenced and OIB-like patterns,

respectively (e.g. Mitchell & Bergman, 1991; Prelević *et al.*, 2008). Accordingly, their mantle sources are interpreted to be either asthenospheric or either lithospheric, but in both cases contribution of enriched components. In fact, the critical point of those interpretations is that the subduction-influenced patterns (arc-like melt) refer to residual minerals (e.g. spinel, amphibole, phlogopite) stable in the mantle lithosphere. Additionally, the anorogenic type of lamproite is traditionally distinguished from the orogenic type by lower Sr isotopic ratios related to the contribution of lower continental crust in their source whereas pelagic sediments (or upper continental crust) contribute to the source of orogenic type explaining their higher Sr isotopic ratios. However, regardless of this tectonic setting division, lamproitic melts known to be derived from multi components mantle sources are observed in continental settings and spread towards EM-I and EM-II. The occurrence of such types of melts with both orogenic and anorogenic chemical fingerprints in some orogenic belts leads the authors to largely discuss in the literature the traditional subdivision (e.g. Prelević *et al.*, 2008). Moreover, there are several studies based on natural samples or experiments showing that such exotic melts not only may come from the base of the upper mantle (MTZ) but also that those MTZ-derived melts could display subduction-influenced patterns similarly to those of melts extracted from the shallow lithospheric upper mantle (Grassi *et al.*, 2012; Rapp *et al.*, 2008; Kuritani *et al.*, 2013, Wang *et al.*, 2016).

It is obvious that high alkaline contents of relatively primitive melts (MgO) cannot be derived from normal mantle source but require a highly enriched source (e.g. Sokol *et al.*, 2017; Wang *et al.*, 2017). In one hand, there is strong evidences for the role of depleted or ultra-depleted mantle in the generation of ultrapotassic melts (e.g. Weis & Demaiffe, 1985; Prelević & Foley 2007; Förster *et al.*, 2016). In the other hand, in order to explain the high K content of ultrapotassic/potassic melts, melting of K-enriched phase (e.g. phlogopite) to buffered K₂O in the melt is suggested (Foley; 1992; Ulmer & Sweeney, 2002; Conticelli *et al.*, 2013; Condamine

& Médard, 2014; Förster *et al.*, 2016). However, due to the abundance of depleted components in the shallow part of the upper mantle and the peculiar condition of stability of the phlogopite, these observations have been used in many studies to consider that in orogenic systems the sources of those melts are located within the shallow upper mantle (Peccerillo & Martinotti, 2006; Prelevic *et al.*, 2008, 2015). They simply suggest low degree of partial melting of phlogopite- or amphibole-bearing mantle in the spinel and/or garnet stability fields to produce those melts. The current studies frequently use calculated curves based on partial melting models in garnet or spinel stability field to explain the evolution of the observed chemical compositions of ultrapotassic rocks. In those diagrams not only ultrapotassic rocks, but also the majority of the alkaline lavas define fields located between those calculated curves. Their trace element contents define a field located a transient mantle field between those of the spinel to garnet stability fields and none of the samples follow the calculated melting curves (see as examples Fig. 18 from Prelević *et al.*, 2015, Fig.12 from Özdemir & Güleç, 2014). However, based on those kind of interpretation of this type of diagrams, the origin of the ultrapotassic rocks is interpreted following the classical model of sources located within the shallow lithosphere. At variance to those traditional phlogopite-bearing sources (e.g. Foley; 1992; Foley & Peccerillo, 1992), recent experimental results evidence that ultrapotassic melts can form at greater depth than those of the lithosphere (down to 5 GPa) from a free-phlogopite mantle source (Wang *et al.*, 2017). Interestingly the results show that those melts also display subduction-influenced chemical element patterns. Thus, this evidence combined with those of MTZ derived melts shows that it is not necessarily worth restricting the source of ultrapotassic lavas characterized by subduction like patterns to a shallow lithospheric mantle containing phlogopite.

In the present study to highlight the mantle source characteristics of the melts, and to assess the role of depleted source and contribution of sediment-like components, non-modal

batch melting model in the spinel and garnet mantle stability field were performed. The starting composition is heterogeneous (e.g. depleted mantle plus GLOSS: Global Subducted Sediments). Partial melting of mantle source either in the garnet- or either in the spinel- stability field led to various LREE/HREE ratios. Moreover variable proportion of garnet in the source either in the garnet stability field or either in the garnet to spinel stability field also lead to various LREE/HREE ratios (e.g. La/Yb). As we can see in figures 2.42a-b, the trace element patterns of the colorless clinopyroxenes (type I and II) are close to partial melting curves in the transient garnet-spinel stability field. Thus, slightly flat HREE slope for the type I, may represent less proportion of garnet in the source or re-equilibration of the melt at shallower depth. Moreover, in this figure, LREE concentration of the different theoretical patterns change based on the composition of the starting composition, i.e. starting composition with higher proportion of pelagic sediment lead to production of patterns with higher REE contents. Thus melt produced from an heterogeneous composition (depleted mantle mixed with 7% of pelagic sediments) have composition close to those of type II antecryst, whereas production of melt from a heterogeneous composition consisting mostly of depleted mantle as starting components (mixed with ~1 % of sediments), better fit with REE concentrations of the type I antecryst. We therefore conclude that clinopyroxene antecrysts derive from a mantle source mostly consisting of depleted mantle with minor sediment-like components. In a previous section of the discussion we showed that signal of sodic alkaline- (OIB-like melt) and ultrapotassic melts (lamproite-like melt) are recorded by melt in equilibrium with different types of clinopyroxene. To compare alkaline lavas from the TIP in term of alkalinity and isotope contents, melts with

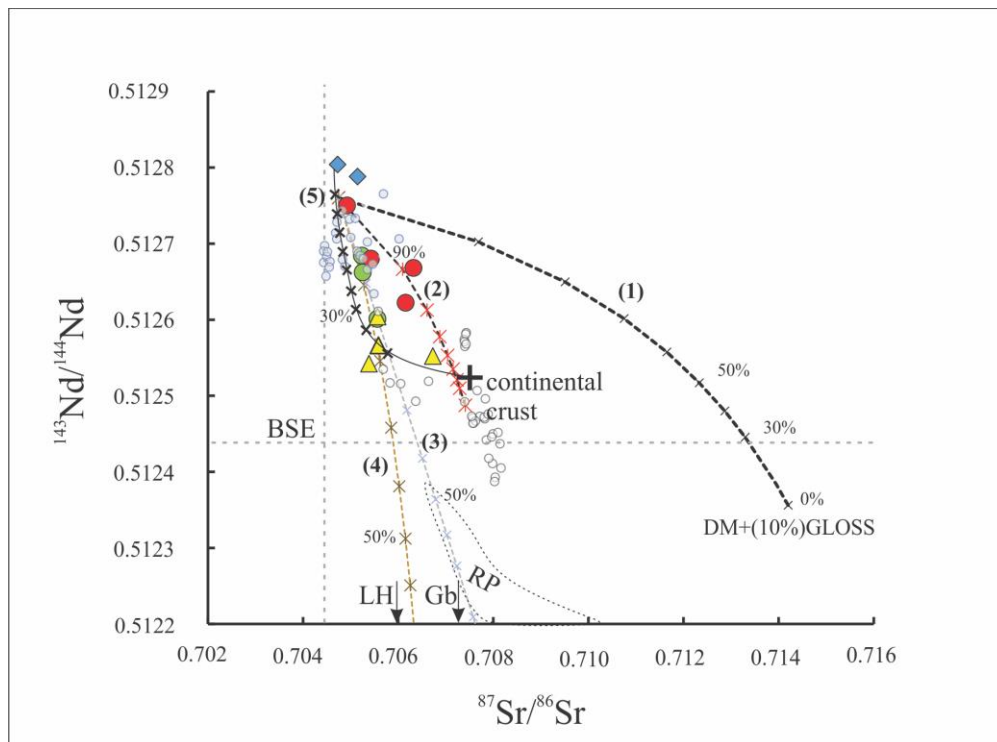


Figure 2.43 $^{143}\text{Nd}/^{144}\text{Nd}$ vs $^{87}\text{Sr}/^{86}\text{Sr}$ diagram illustrating the mixing of different compositions to explain the observed isotopic ratios of the investigated rocks. Numbers represent mixing line between two melt composition 1) melt resulting from low degree of melting of an heterogeneous depleted mantle including 10% recycled sediment mixed with the average OIB-like lava from the TIP; 2) mixing line between lamproitic and OIB-like lavas from the TIP; 3) mixing line between similar compositional poles to (1) but with those of GLOSS with lower $^{86}\text{Sr}/^{87}\text{Sr}$ ratio than the one reported as an average; 4) mixing line between EM-I derived melt (primitive mica lamprophyre, Buhlman *et al.*, 2000) and OIB-like lavas from the TIP; 5) Mixing line between pillow lavas (this study) and continental crust from the NW Iran. Data source and symbols are same as in figures 2.31 and 2.38.

high Sr isotopic ratios and high K content are ultrapotassic, whereas those with lower Sr isotopic ratios and slightly higher Na content are sodic lavas. Interestingly, this observation is in agreement with the two types of clinopyroxene observed in lavas from the Salavat Range whether samples with colorless-clinopyroxene antecryst following the ultrapotassic trend or samples with green-colored clinopyroxene, plotting in the field of sodic lavas. The best evidence for the role of lamproite-like and OIB-like melts in the formation and evolution of the magmatic rocks from the Salavat range is illustrated in the figure 2.43 by the calculated isotopic mixing curves. In this diagram mixing lines between melts produced by low degree partial melting of a heterogeneous source (depleted mantle plus GLOSS) and sodic melts are drawn.

As we see the representative sediment-like component contributing to the source of those rocks have a lower Sr-isotopic composition compared to the average value proposed for GLOSS i.e. $^{87}\text{Sr}/^{86}\text{Sr}$ 0.71730 (Palnk & Langmuir, 1998). In this figure the lamprophyres and the host lavas, with the highest modal content of type I clinopyroxene antecrysts, perfectly plot along the mixing line between lamproite and sodic alkaline lavas from the plateau, whereas the tephrites and the monzogabbros follow the mixing line between sodic lavas and an exotic melt characterized by a source with a relatively low Sr isotopic ratio (e.g. primitive anorogenic mica lamprophyre Buhlman *et al.*, 2000). As mentioned before those lavas are characterized by type II clinopyroxenes, which according to the interpretation of the melt in equilibrium with them must have the same type of source (see Fig. 2.42b). Finally, mixing line between OIB-like melt (i.e. pillow lavas) and upper crustal components well fit for alkali feldspar syenites, which is in agreement with our primary interpretations based on mineral and whole rock chemistry.

2.6 CONCLUSIONS

Integrated field study, mineralogical and petrographical features as well as geochemical and isotopic data of magmatic rocks from the Salavat Range allow to subdivided them into three groups; HM and LM- lavas, Ps –rocks (plutonic intrusions, and hornblende andesites). HM and LM lavas are typically highly porphyritic volcanic rocks displaying abundant macrocrysts of clinopyroxene (phenocrysts or antecrysts) with complex zoning patterns. I subdivided those macrocrysts based on optical properties and chemical characteristics into colorless- and green colored-crystals with high Mg# and REE depleted patterns and low Mg# and REE enriched patterns, respectively. Then, I classified the complex zoning patterns of those two types of clinopyroxene macrocryst into Type I, II, III, and IV. Colorless antecrysts (Type I and II) and green colored-clinopyroxenes (type III and IV) are respectively in disequilibrium and mostly in

equilibrium with their respective surrounding groundmass. I demonstrate that all those clinopyroxenes have a magmatic origin, and that physical observations and geochemical data are coherent. Chemical compositions of colorless and green colored clinopyroxenes confirm that the two types are not cogenetic. The colorless type-I and II clinopyroxenes crystallized from exotic melts similar to kamafugite or lamproitic melts (mainly ultrapotassic) from the TIP, which represent products of the melting of depleted mantle sources enriched by sediment-like components. In the other hand green-colored clinopyroxenes crystallized from two types of melts genetically linked. i) They are product of the fractional crystallization sequence from a melt with composition close to those of the sodic alkaline melt from the TIP (asthenospheric enriched mantle-derived melts) and ii) They crystallized from heterogeneous melts resulting from the mixing of the evolved sodic melts mentioned above with melts in equilibrium with the colorless clinopyroxenes. That mixing process generates melts with transitional compositions between those of sodic and ultrapotassic melts but the overall affinity remains potassic.

Moreover, those evidences are in agreement with the major role of at least two main different alkaline mantle-derived melts, to explain the diversity of observed whole rock major, trace elements and isotope compositions. Obviously described geochemical diversity cannot simply be explained by magmatic processes alone (fractional crystallizations or simple partial melting). The occurrence of various types of melts play a critical role, particularly in order to explain the geochemical diversity of the HM-lavas. In the HM-lavas the large occurrence of colorless clinopyroxenes (antecryst or bright bands), lead to modify the composition of the host-rocks becoming more mafic and depleted in term of trace elements and Nd-isotopic rations. On the contrary the LM-lavas are rich in green-colored clinopyroxenes representing REE enriched melts with higher Nd isotopic rations. Moreover, I evidenced that the geochemical diversity of the investigated and classified rocks is not only linked to the role of various mantle-derived alkaline melts, but also reflect a slight impact of some crustal components. Particularly in Ps-

rocks, in which processes including (i) involvement of the melt derived from lower crust and (ii) combination of fractional crystallization of the mantle derived melts and contamination by continental crust lead to the adakite signatures observed in hornblende andesites and alkali feldspar syenites. All the above evidences implies to consider a scenario involving various alkaline melts as the major parameters controlling the lateral geochemistry of potassic rocks from the Salavat Range. This scenario is not consistent with the classical one for NW Iran proposed for years and considering that those rocks represent potassic melts simply derived from a phlogopite-bearing mantle source.

Chapter III: Transport of Volatile-rich Melt from the MTZ by Compaction pockets: Implication for Mantle Metasomatism and the Origin of Alkaline Lavas in the Turkish-Iranian Plateau

3.1 INTRODUCTION

In the previous chapter, we show that the alkaline rocks in the Salavat Range involve two mantle derived alkaline melts. These melts have ultrapotassic and sodic affinities. In fact, alkaline magmatism in the TIP is the main characteristics of the plateau. Petrologically, they have a large diversity of compositions ranging from ultrapotassic/potassic to sodic. The alkaline rocks are interpreted in the frame of collisional and post-collisional processes, especially for those are younger than 30Ma. However, in the Salavat Range those rocks are dated ~47 Ma and thus is interpreted as a magmatism due to oceanic slab subduction in interaction with mantle wedge. In addition, Salavat range has a similar composition than the alkaline melts produced after the collision. Accordingly, the alkaline volcanism is not specific of the collision. In the present section, we want to show that, in the TIP, the alkaline volcanism may be link to the BMW: i.e. to the subduction-related material stoked in the MTZ, then differentiated and finally intruded in the asthenosphere below the continental plate.

3.2 GENERAL GEOLOGY OF TURKISH-IRANIAN PLATEAU (TIP)

The TIP is one of the main plateaus in the Alpine-Himalayan orogenic belt. It extends from Anatolia to East Iran. Its rise initiated at the Oligo-Miocene (e.g. Copley & Jackson, 2006; Bottrill *et al.*, 2012; François, *et al.*, 2014). Its altitude ranges from 500 m in the east of Iran to 1.5-2 km in Anatolia. To the North, it is separated from the Scythian platform by the Great Caucasus Suture. To the South, it is separated from Arabia by the Bitlis-Zagros Suture. The plateau consists of several pre-Mesozoic terranes (interpreted as “micro continents”) which

accreted at different times. The eastern part of the TIP results from the 210-220 Ma collision along Eurasia of two major blocks: Alborz and Central Iran (Stampfli, *et al.*, 2002, 2013; Berra & Angiolini; 2014). To the West, the Sakarya and the Transcaucasia micro-continents collided Eurasia 300 Ma ago (Belov *et al.*, 1978). The Anatolid-Tauride and probably also the South Armenia microcontinents collided with Sakarya and Transcaucasia, respectively, during the Late Cretaceous or the Paleocene-Eocene (~90-30 Ma) (Şengör & Yilmaz, 1981; Sosson *et al.*, 2010; Rolland *et al.*, 2012; Meijers *et al.*, 2015).

The opening and closing of several branches of the Tethys led to the agglomeration of various microcontinents and eventually to the formation of the TIP. These collisions are mainly direct consequences of subductions. Subduction of the Paleo-Tethys was mainly active along the Great Caucasus from 360 to 210 Ma (Stampfli *et al.*, 2002). From ~ 200 to 80 Ma, subduction of the Neo-Tethys developed along the Sakarya terrane, the Transcaucasia –arc system and the Sanandaj-Sirjan continental arc parallel to the Izmir-Ankara-Erzincan (IAE), the Lesser Caucasus and the Zagros Sutures, respectively (Adamia *et al.*, 1977, 2011; Şengör & Yilmaz, 1981; Yilmaz *et al.*, 2000; Hassanzadeh & Wernicke, 2016). Some authors argue that the Neo-Tethys subductions were active even later, from Late Cretaceous to Cenozoic, beneath the Sakarya terrane (Pontides), the Armenia block and the Iranian plateau, along the IAE, the Lesser Caucasus and the Zagros Sutures (Berberian & King, 1981; Alavi, 1994; Agard *et al.*, 2005, 2011; Ghasemi & Talbot, 2006). However, there is no direct link between the volume and composition of melt production along these sutures and subduction rates (e.g. Mc Quarrie *et al.*, 2003). To explain this mismatch, Verdel *et al.* (2011) proposed that the subducted slab was locally flat, and consequently the thermal regime was too cold to produce large degrees of melting. Alternatively, it was suggested that subduction decreased and thereafter post collision processes took place: a slab break-off, a slab hanging (Agard *et al.*, 2011), or back-arc basin opening (Vincent *et al.*, 2005). A consensus progressively appeared

to propose that the collision between Arabia and the Iranian plateau occurred from ~30 Ma to ~10 Ma (McQuarrie *et al.*, 2003; Francois *et al.*, 2014), leading to a decrease in convergence rate by 30% from 13 Ma to 5 Ma (Austerman & Iaffaldano, 2013). However, along the central and southeastern part of the Zagros Suture, delamination, slab break-off or subduction (i.e. Makran) are still active (Agard *et al.*, 2011; Mohammadi *et al.*, 2013; François *et al.*, 2014). In the Bitlis region, the suture is still active but mostly due to the delamination of the Arabian plate (e.g. Gogus *et al.*, 2011). Parallel to the Lesser Caucasus, a linear zone of recent magmatism is interpreted in terms of delamination of the underlying continental lithosphere (e.g. Neill *et al.*, 2015).

3.3 SURFACE MAGMATISM IN CORRELATION WITH TOMOGRAPHY AND GPS DATA IN THE TIP

All over the TIP, the Late Cretaceous-Early Cenozoic up to present magmatism is extremely voluminous. From West to East, the main magmatic zones are: Central Anatolia, East Pontides-East Anatolia, Lesser Caucasus- NW Iran, Alborz, Central-East Iranian microcontinent and finally the linear magmatic belt of Urumieh- Dokhtar parallel to the Zagros Suture (Fig. 3.1). We summarize below the distribution of continental magmatism during the four periods mentioned in the introduction and advance correlation with deeper structures obtained from published seismic tomography information.

Many high precision seismic tomography images have been published in the last decade. We adapted tomography maps (Figs. 3.2 and 3.3) based on the 150 km depth S or P waves anomaly models over Central Anatolia (Fichtner *et al.*, 2013), extending from the East Anatolia to the Lut Block (Alinaghi *et al.*, 2007). These maps reveal several low velocity elliptical bodies (~ 100-150 km along the shortest axis and 200 km along the longest axis) which present a drastic velocity contrast of up to 10 % with their surroundings. We call these low velocity

anomalies “Compaction pockets”, by reference to their shape. Finally, the stress field deduced from the GPS velocity field (adapted from Aktug *et al.*, 2013 and Masson *et al.*, 2014) is illustrated in figures 3.2c and 3.3b. In the following we will note that all the young volcanoes and associated lavas are located in zones where the direction of maximum tension ($\vec{\sigma}_3$, or less compressive principal stress) is horizontal, thus we will also stress the link between the distribution of those young volcanoes and, the location of the “Compaction pockets” at depth.

3.3.1 Central Anatolia

Central Anatolia is enclosed in the Anatolid-Tauride block. It is limited by the Pontides to the North and by the Hellenic trench and the Bitlis-Zagros Suture to the South (Fig. 3.1). The late Cretaceous–Oligocene alkaline-calc-alkaline A and I-types granitoids occur in several sites, interpreted as resulting from Late Cretaceous, early to middle Paleocene (57-60 Ma) and Oligocene (28-30 Ma) rapid exhumation processes (*period 2 and 3*) (i.e. Bozturge *et al.*, 2007, Boztug & Jonckheere, 2007). According to these studies, exhumation results from a regional compressional regime due to Arabia-Eurasia collision affecting the area located between the Greater Caucasus and the Bitlis-Zagros Sutures. Magmatism younger than Oligo-Miocene (*period 4*) occurs in three main zones: the Galatia volcanic Province (GVP), the Kırka-Afyon-Isparta (KAI) magmatism line and the Central Anatolia Province (CAP) (Fig. 3.2c). The magmatism in the GVP is located along the North Anatolia fault and mainly consists of alkaline lavas (Wilson *et al.*, 1997). The CAP covers an area of 300×20 -25 km with a $\vec{\sigma}_3$ oriented NE-SW. Magmatism is characterized by mostly mafic to intermediate calc-alkaline to alkaline lavas (i.e. Hasndagh and Erciyes volcanoes) (Temel *et al.*, 1998, Aydin *et al.*, 2014, Köprübasi, *et al.*, 2014) with only few tholeiitic lavas outcrops around the Hasandagh volcano (Köprübasi *et al.*, 2014). All lavas are interpreted as originating in a post –collisional setting, however there is no link between magmatic composition and time.

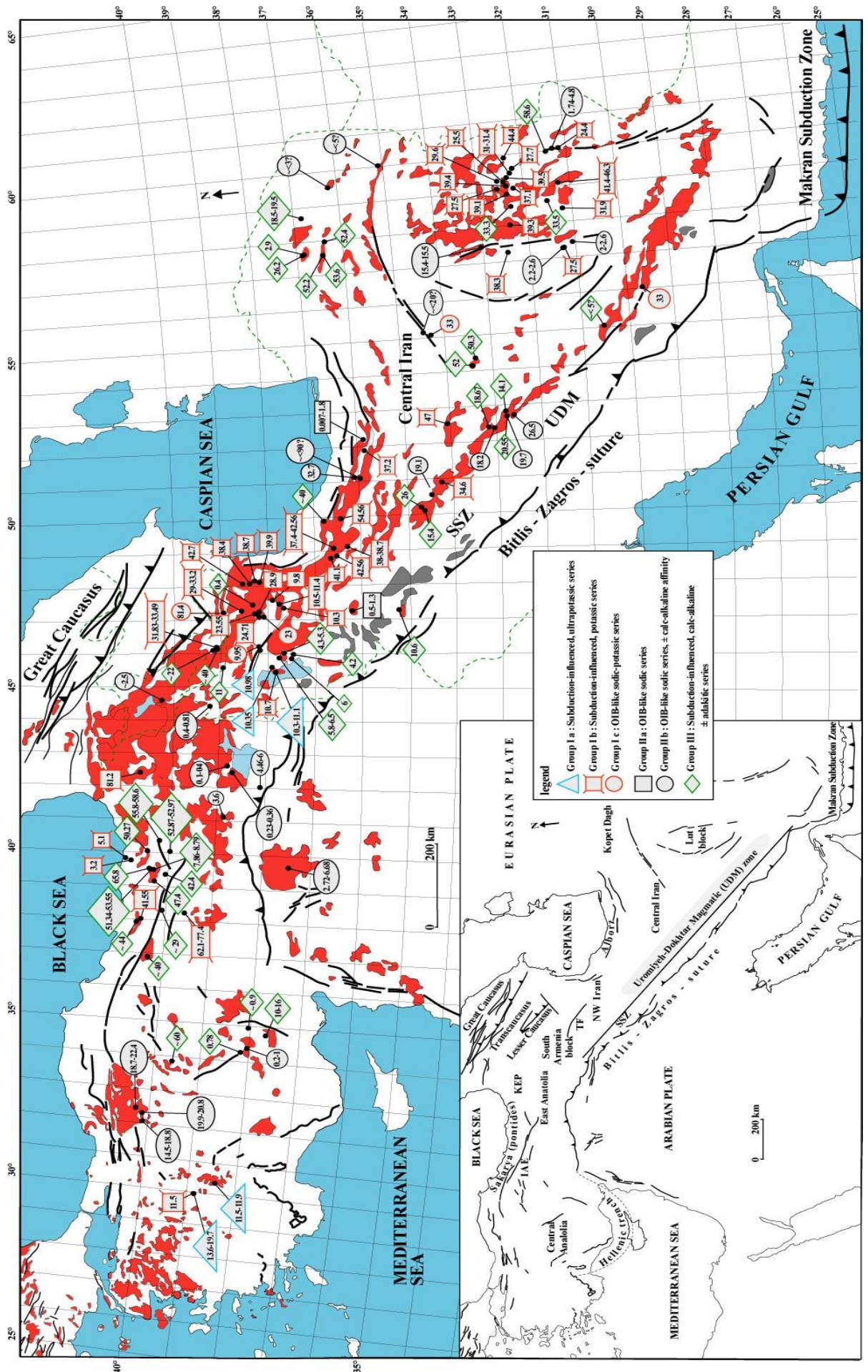


Figure 3.1.(a) Regional tectonic setting of TIP with main tectonic divisions in relation to the Arabian and Eurasian plates. (b) Schematic map showing the distribution of the continental magmatism (adapted from the Middle East geological map (Aghanabati, 1986). Grey shaded areas are older than ~100 Ma and those in red are younger than 80 Ma. Colored symbols correspond to the different groups of rocks defined in the geochemistry section. Key features: KEP, Kars- Erzurom plateau; IAE, Izmir-Ankara-Erzincan; TF, Tabriz fault; SSZ, Sanandaj-Sirjan zone; UDM, Urmieh-Dokhtar magmatic zone. The numbers in the symbols correspond to the ages (in Ma) of the lavas in the each locality (references included in supplementary material). Only ages younger than 80 Ma are shown.

As an example, magmatic affinities of Hasandagh lavas shifted from older alkaline to younger calc-alkaline, whereas a reverse trend is observed for the alkaline to calc-alkaline lavas from the Erciyes volcano (e.g. Köprübasi *et al.*, 2014). However all these observations are linked to mixed asthenospheric and continental crust sources (Aydin *et al.*, 2014, Köprübasi *et al.*, 2014). Along the KAI and GAP lavas have strong alkaline affinity (i.e. ultrapotassic and sodic), whereas their sources are interpreted as an enriched-asthenospheric source that interacted with the overlying lithosphere (e.g. Wilson *et al.*, 1997, Prelević *et al.*, 2015).

Two North-South vertical tomography sections across central Anatolia along longitudes 35 E and 37 E are displayed figures 3.2d and 3.2e, respectively. These figures show that the bottom of the compaction pockets lies at around 300 km depth and their centers at 150 km depth. Figure 2c compares the compaction pocket at 150 km depth with the location of major faults at the surface. All these faults stand within the red areas defined by the compaction pockets. (Figs. 3.2a and b) In figure 2a, the “blue” zones correlate with local sedimentary basins. Miocene to present volcanic provinces (e.g. GV, CAP, KAI) are also systematically located close to the fault zones located over the compaction pockets (Fig. 3.2c). These volcanic provinces were shown to be under an extensional regime with horizontal $\vec{\sigma}_3$ (e.g. Toprak *et al.*, 1996; Dhnot *et al.*, 1998; Adiyaman *et al.*, 2001), a feature perfectly supported by the available surface kinematic data (Fig. 3.2c). For instance, the magmatic rocks belonging to the CAP and to a lesser extent to the GAP develop orthogonally to the direction of $\vec{\sigma}_3$. Such observations indicate that the melt provided in the vicinity of the compaction pockets number 1 may flow

through a locally very thin lithosphere (~ less than 60 km thick) within an intricate set of vertical fractures (Fig. 3.2e).

3.3.2 The East Pontides- the East Anatolia

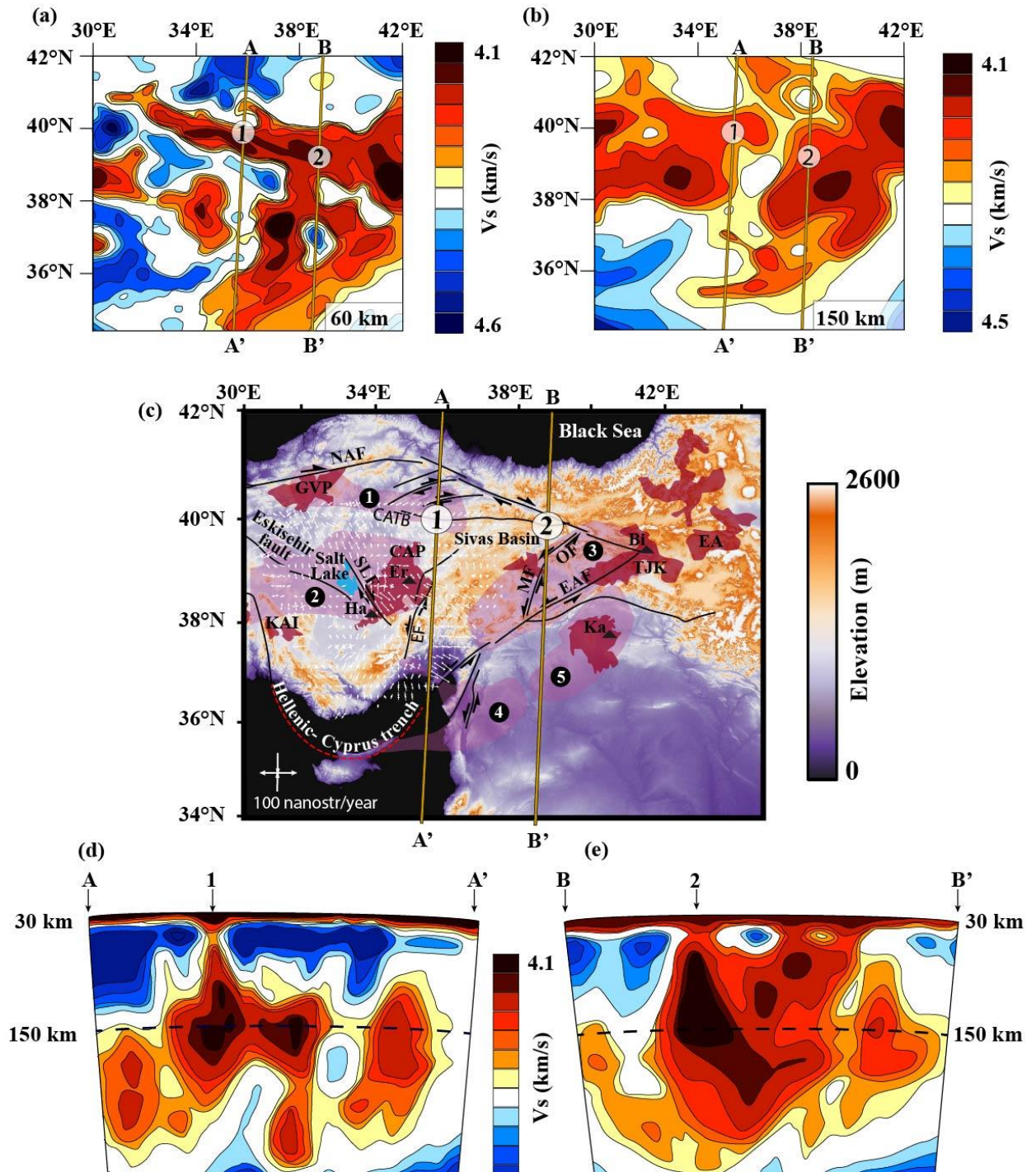
3.3.2.1 The east Pontides

The Pontides (Sakarya terrane) extends in the southern part of the Black Sea and parallel to the IAE Suture to the South (Fig. 3.1). The pre-Early Jurassic and Late Cretaceous metamorphic basements in the central and East Pontides, respectively (Boztug *et al.*, 2004; Topuz *et al.*, 2004), are unconformably overlain by late Jurassic to Upper Cretaceous sedimentary and volcanosedimentary sequences (Boztug, 2008). The intensity of magmatism decreases towards the South. Magmatic units younger than Late Cretaceous-Early Cenozoic are widespread in the Eastern Pontides. Magmatic units mainly consist of Late Cretaceous lavas and pyroclastic deposits (*period 1*: arc type) and Paleocene to Miocene volcanic and

Figure 3.2. Map views through S- wave tomographic model velocity at 60 km (a) and 150 km (b) depth adapted after Fichtner *et al.* 2013. (c) Topography map of the Central Anatolia; white arrows represent the projections of the horizontally oriented directions of maximum strain derived from GPS data (Aktug *et al.*, 2013), black triangles represents the centre of active volcanoes, black lines represent major faults. Recent volcanic fields are shaded in red, the 150 km deep sections of the compaction pockets, extracted from figure 3.2b, are shaded in pink. The figure 3.2b indicates that compaction pockets stand beneath 1 to 2 km high mountainous regions. In addition, the North Anatolia Fault (NAF) and the Central Anatolia Thrust Belt (CATB), including many shear faults, border the compaction pocket number 1. compaction pocket number 2 is bordered to the South by the Eskisehir fault, along the Eastern border by the Ecemis North-South fault system and by the CATB to the North. compaction pocket number 3 is bordered by the Ovacik Fault (OF) to the North, by the East Anatolian Fault (EAF) to the Southeast, against the Triple Junction Kartava (TJK), and finally by the NAF originated at TJK to the Northeast. The major section of Salt Lake fault (SLF) runs through the area covered by compaction pocket 2, while the major section of Malatya fault (MF) runs through the area covered by compaction pocket 3. All the volcanic regions are located at the border of compaction pockets, except Karacadag volcano, which is located above the central part of compaction pocket 5. (d) & (e) Vertical sections through the S- wave velocity tomographic model. The compaction pockets correspond to the zones of low velocity, in red. They are centred at 150 km depth and extend to of 300 km depth. Key to marked features: GVP: Galatia Volcanic Province; CAP: Central Anatolia Province; KAI; Kırka-Afyon-

Chapter III : Transport of volatile-rich melt...

Isparta; EA: East Anatolia. Name of Quaternary volcano (triangles); Ha: Hasandagh, Er: Erciyes, Bi: Bingol, Ka: Karacadag. High-resolution topography image obtained from <http://srtm.csi.cgiar.org/>.



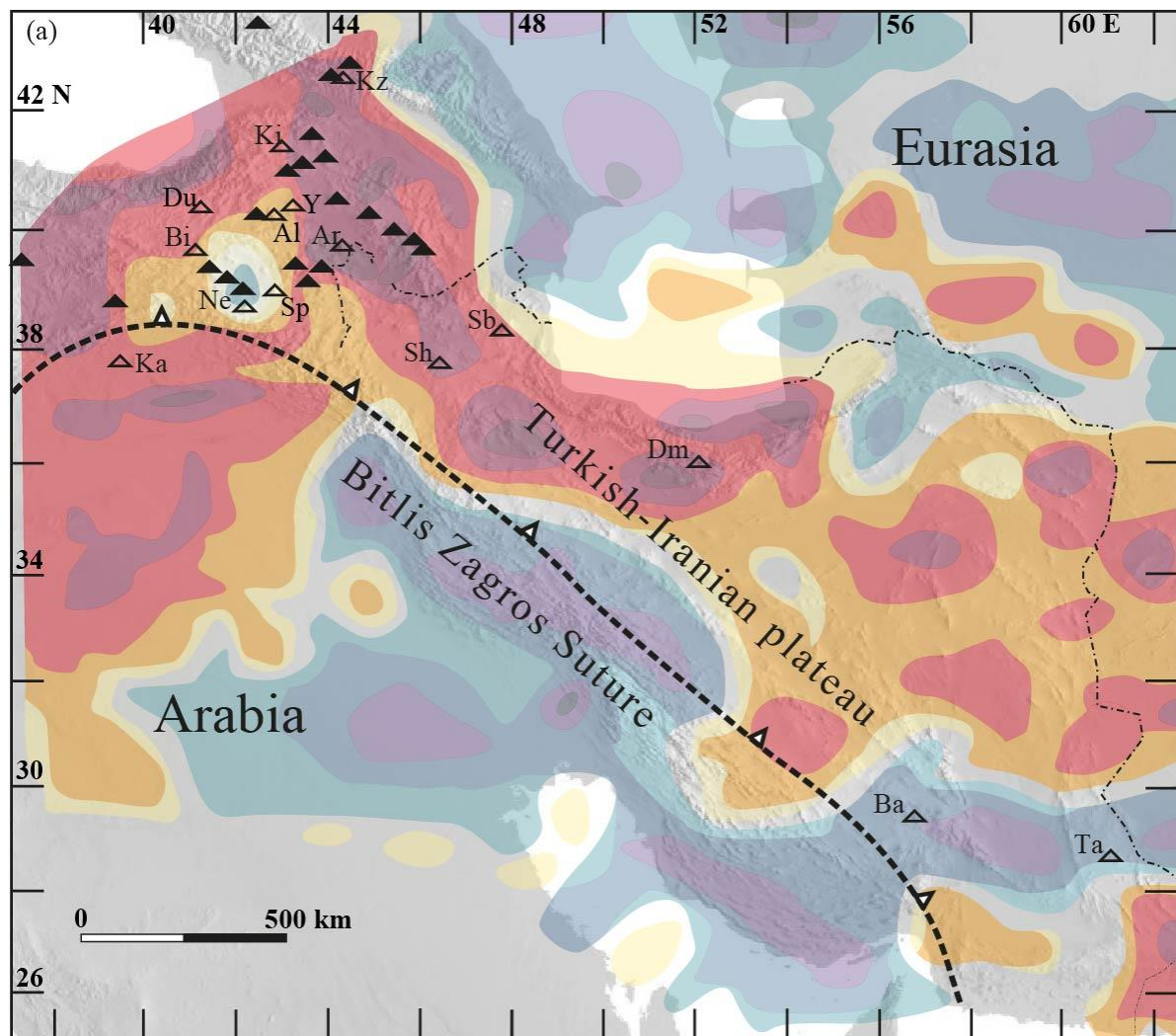
plutonic rocks. The Cenozoic magmatism, mainly attributed to a post-collisional setting, has adakitic to alkaline affinities and occurred during the Eocene (*periods 2 and 3*) and the Middle Miocene-Pliocene (*period 4*) (e.g. Aydin *et al.*, 2008; Karsli, 2010, 2011; Eyuboghlu *et al.*, 2012). Based on tomography images this magmatic activity develops above two-overlapping compaction pockets (numbers 7 and 8) in the zones where $\vec{\sigma}_3$ is horizontal (Fig. 3.3b).

3.3.2.2 The East Anatolia (EA)

The EA magmatism is widespread: it occurs from the Kars-Erzurum plateau (KEP) to the North to the Bitlis Suture to the South (Fig. 3.1). It consists of 300-350 meters thick Plio-Quaternary sub-aerial lava flows and pyroclastic deposits (*period 4*) covering a huge zone of about 15,000 km² (i.e. Suphan, Nemrut and Bingol volcanoes). The chemical compositions range from mildly alkaline to calc-alkaline (e.g. Pearce *et al.*, 1990), with few reports of tholeiitic compositions (e.g. Özdemir, 2016). In the Southern side of the Bitlis Suture, Plio-Quaternary mafic lavas marked as the Karacadag volcano, have alkaline compositions (Pearce *et al.*, 1990; Lustrino *et al.*, 2010). In the North of the KEP, the volcanic region (i.e. Kisirdagh) lies in a zone of horizontal $\vec{\sigma}_3$. In addition this area overlies three compaction pockets (numbers 8 to 10), below which the direction of $\vec{\sigma}_3$ is essentially vertical, which provides an explanation as to why no young lavas erupted at the top of these compaction pockets (Fig. 3.3b). On the contrary, the mafic lavas of the Karacadag and Bingol volcanoes sit either above or at the border above compaction pockets numbers 5 and 3, respectively (Fig. 3.3b). It is important to note that these volcanic regions occur in zones where the direction of $\vec{\sigma}_3$ is horizontal (see Masson *et al.*, 2014, and Fig. 3.3b), allowing deep melts to rise to the surface.

There is an important exception to this correlation between the location of volcanism, compaction pockets, and the estimated stress field at the surface: a region of intense and recent volcanic activity in the North of Bitlis Suture which is located above a high velocity body at

120–210 km depth (Fig. 3a and Alinaghi *et al.*, 2007; Skobeltsyn *et al.*, 2014). However, this high velocity domain is overlain by a very low velocity horizon reaching the base of the crust (Özacar *et al.*, 2010; Skobeltsyn *et al.*, 2014). These observations have been interpreted as a gradual rollback of the Bitlis slab and its consecutive break-off, thereafter responsible for the widespread volcanism and uplift of the region (Şengör *et al.*, 2003; Keskin *et al.*, 2008; Skobeltsyn *et al.*, 2014). Such a process represents the standard model proposed to explain the hydrated and hybrid asthenospheric and lithospheric mantle sources (< 150 km) proposed for the alkaline lavas.



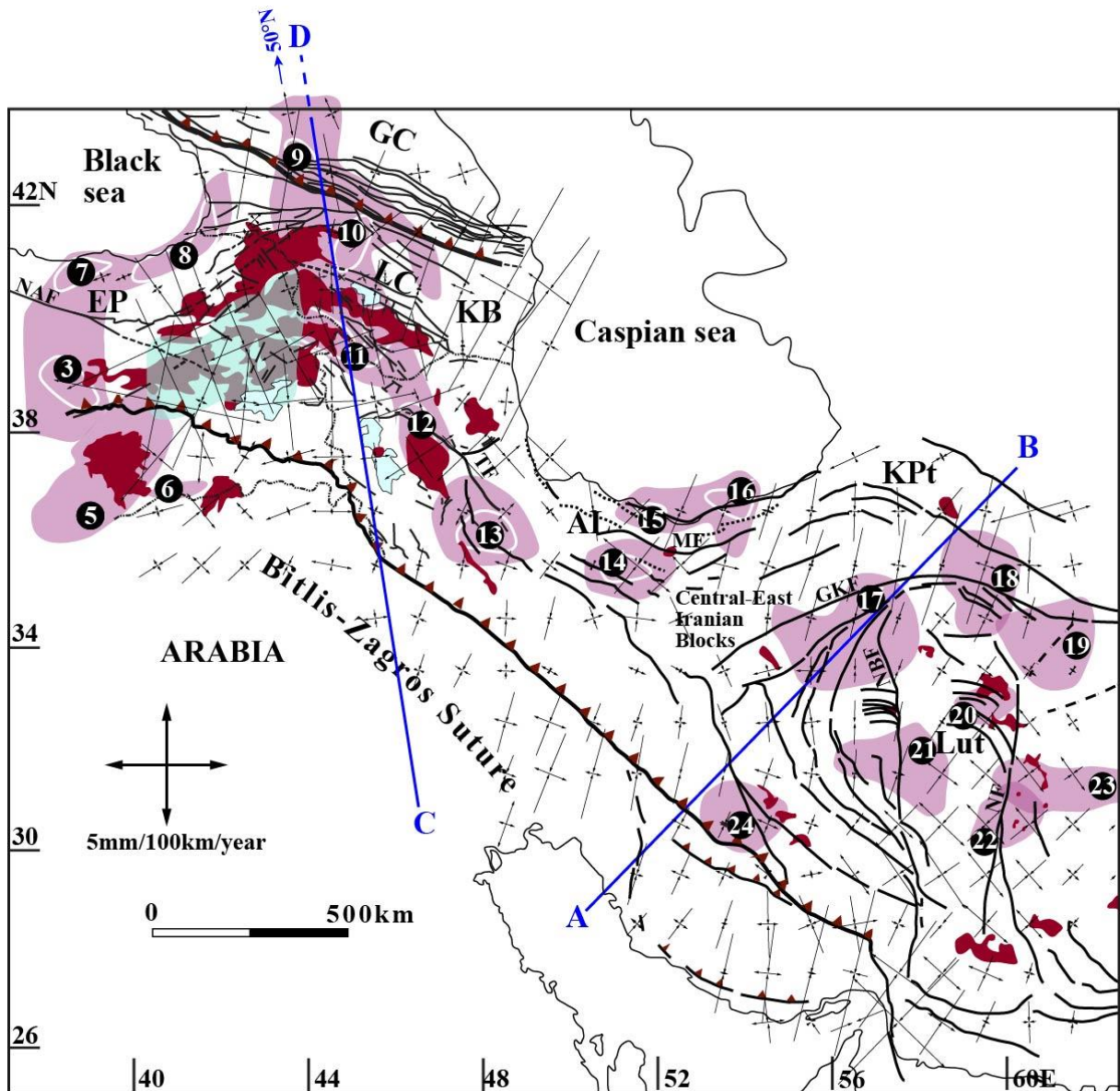


Figure 3.3. (a) The map represents a 150 km deep horizontal section of the P-wave anomalies field of the TIP along with the neighbouring Eurasia and Arabia lands. The blue and red colours represent Alinaghi et al. (2007)' high and low- velocity anomalies regions, respectively. Triangles represent Middle Miocene to Holocene volcanic centres obtained from Neill et al. (2015). (b) Structural map showing the main tectonic units of the TIP, including major faults (black bold line), non-recognized hidden faults (black dashed line) and locations of compaction pockets (pink area; low velocity anomalies obtained from figure 3.3a except for number 5 compaction pocket which is taken from Fichtner et al. 2013), centre of compaction pocket contoured by a white line. All red areas correspond to the locations of recent magmatic fields. We coloured in light blue the high velocity area below Suphan volcano deciphered in figure a. In the text we refer to compaction pocket 12 as the ‘‘Sahand compaction pocket’’, because it is located beneath the recent Sahand volcano and along the southern side of the Tabriz fault (TF). compaction pocket on 13 is the Kurdistan compaction pocket because it is located along the TF and is crossed by the recent Ghorveh-Kurdistan lavas flows. compaction pocket on 14 is the ‘‘Damavand compaction pocket’’,

because it is bordered to the North by the Mosha fault (MF) over which lies the famous recent Fig. 3.3 (continued) Damavand volcano. In the Central Alborz, two overlapping compaction pockets (numbers 15 and 16) are not associated with recent magmatism. They are referred as the “Central Alborz compaction pockets”. The black arrows represent the projections of the horizontally oriented directions of maximum strain derived from Masson et al. (2014)’ GPS data. Blue lines A-B and C-D correspond to the paths along which figures 4 and 5 vertical tomography maps has been extracted, respectively. Key to marked volcanoes on figure a: Kz: Kazbek, Ki: Kisirdagh, Du: Dumlu Y: Yaglicadag, Al: Aladag, Ar: Ararat, Bi: Bingol, Ne: Nemrut, Sp: Suphan, Ka: Karacadag, Sh: Sahand, Sb: Sabalan, Dm: Damavand, Ba: Bazman, Ta: Taftan. Key to marked features on figure b: GC: Great Caucasus, LC: Lesser Caucasus, KB: Kura Basin, EP: East Pontides, AL: Alborz KPt: Kopet Dagh, NAF: North Anatolia fault, TF: Tabriz fault, MF: Mosha fault, GKF: Great Kavir fault, NBF: Nayband fault, NF: Nehbandan fault.

3.3.3 The Lesser Caucasus- NW Iran

Over the Armenia, Sabalan and Sahand blocks, a voluminous magmatism dated from 80 Ma to present spreads North-South from the Lesser Caucasus to the Arabian foreland (Fig. 1). Late Cretaceous to Eocene transitional high K calc-alkaline to potassic lavas and pyroclastic deposits (*period 3*) interlayered with sedimentary sequences follow the Lesser Caucasus, the Armenia block and then the Talysh Mountain in the North East border of the Sabalan Block (Vincent *et al.*, 2005). Eocene to Oligo-Miocene lavas and associated plutonic rocks (*period 4*) with high K calc-alkaline to potassic affinities only occur in the Armenia and Sabalan blocks (Aghazadeh *et al.*, 2010; Castro *et al.*, 2013; Moritz *et al.*, 2016). Plio-Quaternary eruptions (younger than 3 Ma) are mainly exposed in the South of the Armenia block parallel to the Lesser Caucasus Suture and consist of medium to high K calc-alkaline mafic to intermediate lavas and pyroclastic deposits (e.g. Neille *et al.*, 2015). They form a linear volcanic chain occurring within a zone characterized by a high magnitude of the horizontal $\bar{\sigma}_3$ (Fig. 3.3b). In the Sabalan and Sahand blocks, the famous Plio-Quaternary volcanoes (Sabalan and Sahand) display intermediate to felsic lavas. Their pyroclastic eruptions produced cinders of calc-alkaline composition with adakitic affinity (Ghulamghash *et al.*, 2016; Pang *et al.*, 2016). To the North

of the Sabalan block, magmatic events with ages ranging from 80 to 11 Ma, are dominated by alkaline ultrapotassic and potassic compositions (Aghazadeh *et al.*, 2010; Aghazadeh *et al.*, 2015). To the South of the Tabriz fault, in the Sahand block, evidence of volcanic eruptions are limited and characterized by ages ranging from 11 Ma to present (*Period 4*). The 11 Ma lavas have an alkaline potassic to ultrapotassic composition (Pang *et al.*, 2013; Shafaii Moghadam *et al.*, 2013; Aghazadeh *et al.*, 2015). In both blocks, the intensity of the tensile stress is significantly high compared to other regions of the plateau (i.e. East Anatolia, Fig. 3.2), similarly the direction of $\vec{\sigma}_3$ is horizontal.

Between latitudes ranging from $\sim 38^\circ$ E to 54° E (Fig. 3.3a), the compaction pockets occur within a negative S-wave velocity anomaly band (~ 950 km wide in the North-South direction and ~ 1300 km long in the East-West direction). This low velocity anomaly initiates around the East Anatolian fault and East Pontides, then it follows the Lesser and Great Caucasus Mountains, the Northwest of Iran, and ends below the Alborz range. The most intense recent volcanoes and a dense set of fractures are observed from latitudes ranging from 38° E to 48° E. Figure 3.3b illustrates that the numerous compaction pockets (numbers 9, 10, 11) below this area may actually provide the melt that flows within the faults and eventually supplies the volcanoes. This reminds observations made over Central Anatolia (e.g. Dirik & Goncuoglu, 1996; Karaoglu *et al.*, 2016 and Fig. 3.2). We explain these features by a horizontal tensile stress field ($\vec{\sigma}_3$), similarly to the proposition of Gogus & Pyskywec (2008). This setting agrees with Koulakov *et al.* (2012), who proposed for the Caucasus region (compaction pockets number 9-11 Fig. 3.3b) that crustal thickening and the transformation of lower crust material into eclogite trigger the delamination of the c.a. 100 km thick lithosphere by sinking drops about ~ 250 km thick, that drive upward the surrounding hot and partially molten asthenosphere. For Koulakov *et al.* (2012) this process explains the formation of the compaction pockets, which would thus consist of hot asthenosphere material rising up to Moho depth. This is a plausible

interpretation for the narrow slow S-velocity channels seen to connect with faults above some specific regions (e.g. LC and GC in Fig. 3.3b). But the clear presence of a c.a. 100 km thick lithosphere-capping most of the compaction pockets (Fig. 3.4) indicates that they do not constitute hot asthenospheric diapirs intruding a dripping lithosphere.

The tomography section from the surface down to 1000 km depth along profile CD (drawn in Fig. 3.3b) joining the Bitlis-Zagros Suture to the Great Caucasus is presented in figure 4. From Arabia up to the clustered compaction pockets area between 38° E to 48° E described above, a high velocity zone extends down to 200~300 km depth. Three overlapping compaction pockets (numbers 9, 10 and 11) extend between the Lesser Caucasus to the Great Caucasus (Fig. 3.3b). Once again, their centers lie at 150 km depth, but their base can reach ~350 km depth. Another high velocity horizon lies between 200-350 depths down to 700 km depth, extending continuously from Arabia to the Great Caucasus. This zone presents a North-South shape of high velocity lithospheric wedge, with a tip at the Northern limit with the Great Caucasus and a rear reaching 400 km in thickness below the axis of the Scythian craton. We infer that the underlying low velocity material originated at the base of the transition zone and flowed along the base of this wedge up to the surface below the Kazbegi volcano in the Great Caucasus Suture (Fig. 3.3a). The characteristics of the tomography model inside the crust and lithosphere along the Lesser Caucasus to the Great Caucasus (Fig. 3.4b) indicate that fluids suspected to concentrate within the compaction pockets migrate up to the surface. As for the Central Iran cross-section (see below and Fig. 3.5), the compaction pockets themselves do not penetrate within the ~100 km thick lithosphere. However, we observed narrow low velocity channels confined around faults, which connect the compaction pockets to the volcanoes. This in turn is a similar observation to that made for Central Anatolia (Fig. 3.2).

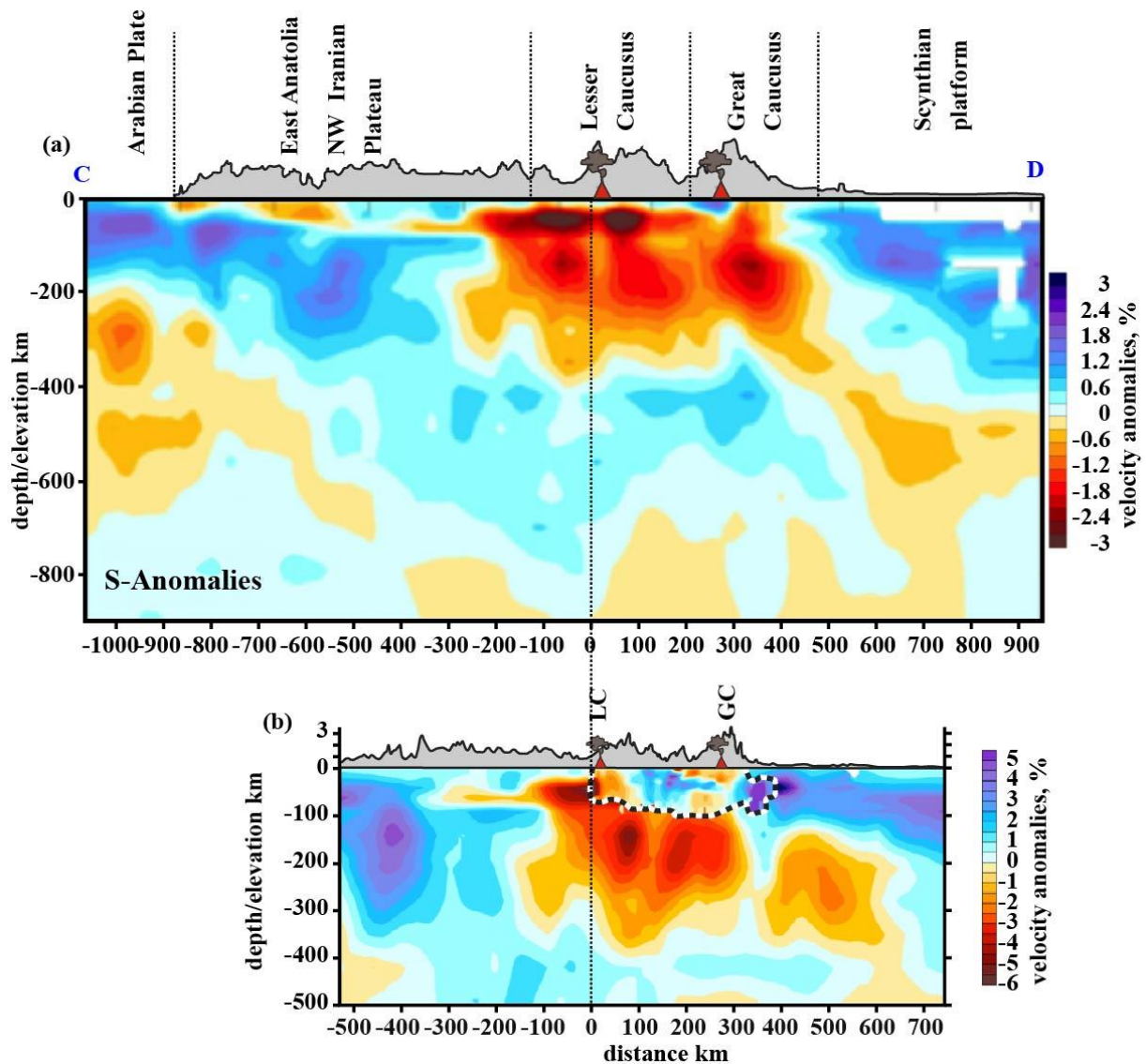


Figure 3.4. A and B vertical S-waves velocity anomaly cross-sections joining the Zagros to the Great Caucasus, following the C-D line from figure 3b, indicate present of low velocity anomalies beneath TIP. The topography along the profile is indicated in figures a and b. The dashed line in figure b represents the lithosphere-asthenosphere boundary (LAB), figure a and b obtained from Koulakov et al. 2012 and Zabelina et al. 2016, respectively.

3.3.4 Alborz

The Alborz magmatic belt crops out parallel to the southern margin of the Caspian Sea. It is approximately 600 km long and 100 km wide; it extends from Caucasus-NW Iran to the Northeast of Iran in Kopet Dagh. Cretaceous to Eocene alkaline volcanic activity occurred in the Central part of Alborz and in its western part, named Talysh (Vincent *et al.*, 2005; Asiabanha & Foden, 2012). In the Central part of Alborz an exceptionally thick Eocene high-K calc-alkaline to potassic pyroclastic and lava (*period 3*) sequence (~5km), is known as the Karaj formation. Quaternary magmatism (*period 4*) forms several very high summits (> 4000m) such as the famous Quaternary strato-volcano “Damavand” (5671m), located in the central part of Alborz. The latter mostly consists of thick alkaline lava flows and subordinate pyroclastic breccia and lahar materials (Davidson *et al.*, 2004; Liotard *et al.*, 2008; Mirnejad *et al.*, 2010). Generally, Alborz is under compression and thus extension is oriented vertically ($\vec{\sigma}_3$), except along the Mosha fault, around Damavand volcano, where $\vec{\sigma}_3$ is horizontal. This information may be linked with the restriction of the present volcanic activity to the Mosha fault (MF, Fig. 3.3b). When studying the associated tomography data (Fig. 3.3), a 250 km wide elliptic low velocity domain appears centered on the “Sahand compaction pocket” at 150 km depth. In addition, a seismic profile from Sahand to Sabalan volcanoes (Bavali *et al.*, 2016) highlights the structure of the lithosphere; a network of low P-waves velocity anomalies is evidenced, deeply-rooted to the Sahand compaction pocket connected to both volcanoes. Similarly, we use this observation to infer that the magmatic source feeding the Damavand volcano is linked to the surrounding compaction pockets.

3.3.5 Central-East Iranian microcontinent (CEIM)

The CEIM consists of Central Iran (Yazd and Tabas blocks) and East Iran (Lut block) (e.g. Alavi, 1991). Central Iran is mainly limited by NNE-SSW oriented faults (e.g. Great Kavir and Naiband faults). In Central Iran, there are only a few reports of Eocene magmatic activity (e.g. Amidi *et al.*, 1984; Torabi *et al.*, 2014; Ahmadian *et al.*, 2016). Due to the recognition of Eocene metamorphic core complexes (e.g. Verdel *et al.*, 2007, Kargaranbafghi *et al.*, 2015) and stratigraphic evidence of subsidence during the Eocene, Vardel *et al.* (2011) suggested that the discrete nature of Eocene magmatism (“flare up” period in Iran) may be linked to slab flattening beneath the Central Iranian blocks. However, few younger alkali basaltic bodies crop out along the Great Kavir and Naiband faults (e.g. Saadat *et al.*, 2010; Rajabi *et al.*, 2014; Kheirkhah *et al.*, 2015).

To the East, the main magmatic unit is located around the Lut block (Fig. 3.1). It has an elongated shape extending over 100 km from North to South. The block is bounded by major faults and ophiolite Sutures (*period 2*). The different volcanic, sub-volcanic and, plutonic units have an age ranging from Jurassic to Quaternary. Jurassic plutonic outcrops (*period 1*) are restricted to few localities (165-162 Ma; Esmaily *et al.*, 2005). The major magmatic events occurred during the Cenozoic (*period 3*) and led to the emplacement of various high-K calc-alkaline to potassic rocks (Arjmanzadeh *et al.*, 2011; Pang *et al.*, 2013; Beydokhti *et al.*, 2015). Recent Quaternary volcanic rocks (*period 4*), mostly alkaline basalts, were emplaced along some faults (Walker *et al.*, 2009; Saadat *et al.*, 2010; Saadat & Stern, 2012).

From ~ 54° E to 62° E in the East of the TIP we identified seven individual compaction pockets (Fig. 3.3b, compaction pockets numbers 17-23) extending within a huge low velocity zone (~900 km long along the North South axis and ~800 km wide along the East-West axis). They clearly remain distant from each other (Fig. 3.3, tomography at 150 km depth). The active strike-slip faults (maximum length ~650km) are interpreted to result from the collision between

the Arabian plate and the Iranian plateau (Hesami & Jamali, 2006; Walker *et al.*, 2009). This is consistent with the location of the compaction pockets below the region where $\vec{\sigma}_3$ is essentially vertical. Actually, recent magmatic activity occurs close to these faults, resulting from local extension associated to their slip motion (Walker *et al.*, 2009), in agreement with the regional horizontal orientation of $\vec{\sigma}_3$. We note that this magmatic activity occurs at the border of the compaction pockets.

The upper mantle tomography by Motaghi *et al.* (2015) between the Zagros Suture and the Kopet Dagh in Central Iran is shown in figure 3.5. The profile crosses the pair of overlapping compaction pockets located below Central Iran (compaction pocket number 17, Fig. 3.3b). The large-scale shape of the Bouguer anomaly from Motavali *et al.* (2011) highlights velocities minima over the Zagros and the Kopet Dagh areas, and a relative bulge in between, across the Central Iranian blocks. Detailed observation of the Bouguer profile from Motaghi *et al.* (2015) shows that this bulge is centered in between the pair of overlapping compaction pockets defined in Fig. 3.5, at distances of $x=0$ and $x=300$ km, respectively along the AB profile (drawn Fig. 3.3b). This profile shows that both compaction pockets present a minimum density of 3 g/cm^3 at a depth where the density reaches up to $\sim 3.4 \text{ g/cm}^3$ (Fig. 3.5c). Below the center of this gravity bulge, the crust-mantle interface appears to rise slightly, with a relatively low density ranging between $\sim 2.8 \text{ g/cm}^3$ and $\sim 3 \text{ g/cm}^3$. The center of these compaction pockets (number 17) lies at ~ 150 km depth, but their base lies at a depth of ~ 240 km, shallower than in Central Anatolia (~ 300 km depth, Fig. 3.2). This indicates either a dense mafic lower crust or buoyant mantle material. This is consistent with a proposition that both compaction pockets exert a buoyancy force upwards to the overlying Central Iranian lithosphere. 1D reflection profiles (Motaghi *et al.*, 2015) superimposed on the 2D tomography in figure 3.5b, indicate that the base of the Central Iranian lithosphere is located at about 120 km depth. Curiously, the compaction pocket cross-cuts the base of the lithosphere, suggesting that the low velocity material located

below 120 km depth might presently be free of melt. This observation is consistent with the absence of recent volcanic activity at the surface.

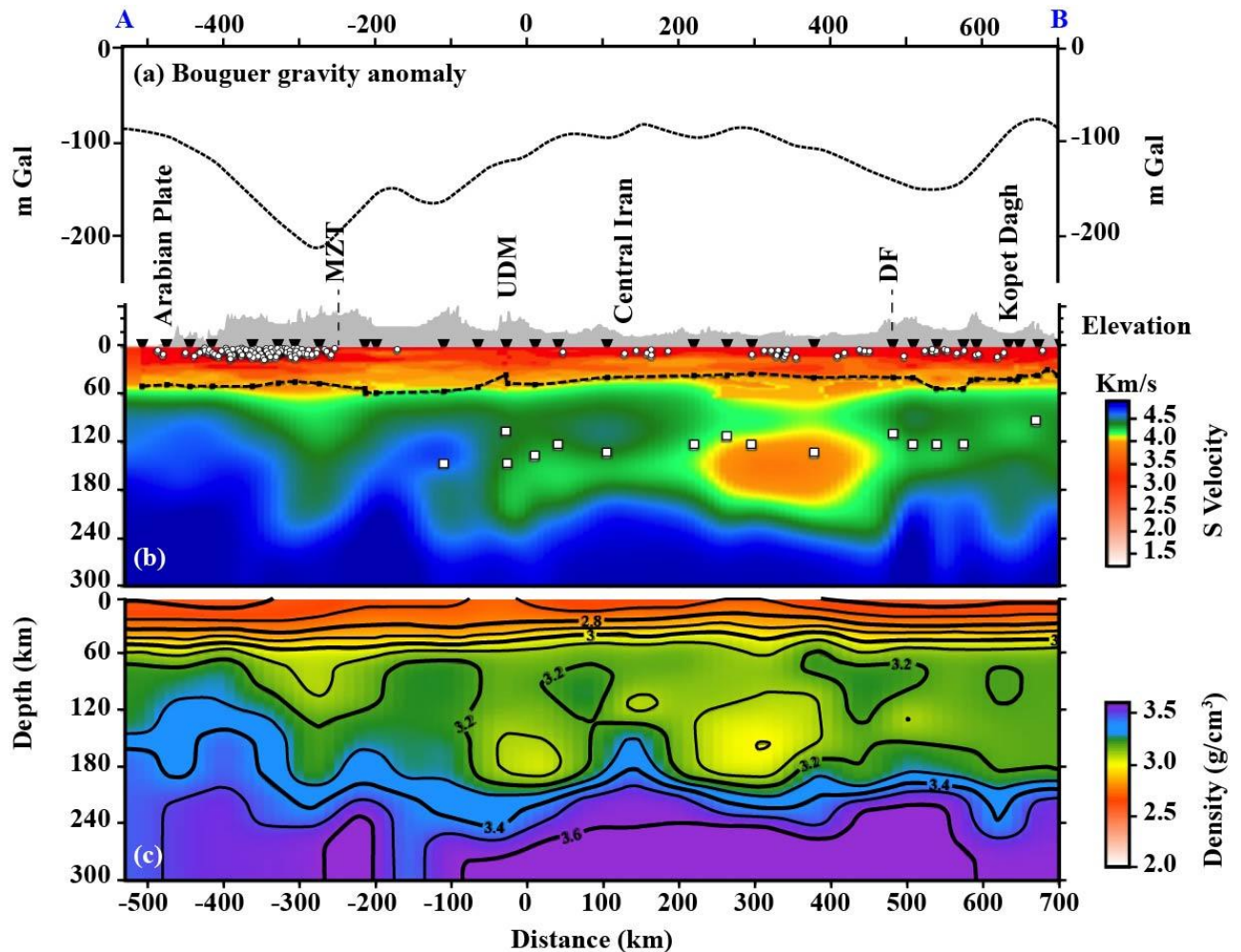


Figure 3.5. a) Bouguer anomaly, b) S-waves velocity anomaly c) density distribution that optimizes the relationship between S-waves anomaly and Bouguer anomaly across Central-East Iranian blocks joining Zagros to Kopet Dagh. The location of the profile is shown in figure 3.3b (after Motaghi *et al.*, 2015). White squares in figure b represent the LAB. The velocity and the density range through the surrounding to the centre of the main compaction pocket (at ~150 km depth) is 4.2 to 3.8 kms⁻¹ and 3.3 to 3.6 g/cm³, respectively. Such huge contrasts are possible only if the centre of the compaction pocket is essentially composed of partially molten mantle. This is compatible with the compaction model.

3.3.6 The Urmieh- Dokhtar Magmatic (UDM) zone

The main magmatic activity in Iran occurs over 1700 km along the Zagros Suture with a NW-SE orientation: It is named the “Urmieh-Dokhtar magmatic (UDM) zone”. This magmatism consists of calc-alkaline and alkaline series emplaced from the Late Jurassic to the Quaternary (Berberian & King, 1981; Amidi et al., 1984; Aftabi & Atapour 2000; Omrani et al., 2008, 2009, Torabi, 2009; Ghorbani & Bezenjani, 2011, Ghorbani *et.al*, 2014). The oldest magmatic events are represented by calc-alkaline plutons that cut across late Cretaceous magmatic and sedimentary terranes (Amidi *et al.*, 1984). During the Eocene to the Oligo-Miocene, this magmatism was mostly eruptive, with only rare alkaline plutonic intrusions recorded (i.e. Dargahi *et al.*, 2010). Some Eocene volcanic and pyroclastic deposit successions (*period 3*) have a thickness reaching 4 km (Stocklin, 1968; Berberian & Berberian, 1981). The Arabia-Central Iran collision likely triggered delamination of the overriding lithosphere (Francois *et al.*, 2014). These authors showed that such delamination below Central Iran is not correlated to voluminous magmatism after ~30 Ma, at least along the UMD. Due to the assumption of multi- stage subductions of the Neo-Tethys beneath the TIP (Berberian & King, 1981; Alavi 1994; Agard *et al.*, 2005, 2011; Ghasemi & Talbot, 2006) occurrences of calc-alkaline magmatism are interpreted in the context of a continental arc, whereas Amidi et al. 1984 proposed an intracontinental (possibly rift) magmatism for the UDM, due to the occurrence of alkaline magmatism.

Plio-Quaternary magmatism (*period 4*) rarely occurs in the UDM, however, calc-alkaline lavas and pyroclastic eruptions with adakitic signatures are reported in the central part, parallel to the Zagros Suture (Omrani *et al.*, 2008; Pang *et al.*, 2016). To the Northwest (e.g. Kurdistan provinces, Sahand and Sabalan volcanoes and East Pontides), young magmatism with both adakite and alkaline signatures is observed (Jahangiri, 2007; Ahmadzadeh *et al.*, 2010; Allen *et al.*, 2013; Azizi *et al.*, 2014). However, various sources for adakites including continental crust,

oceanic crust and the upper mantle have been proposed. The different hypotheses can be summarized as follow: i) melting of a subducted oceanic slab (Jahangiri, 2007; Omrani *et al.*, 2008), ii) partial melting of lower continental crust by (a) a slab break-off and the associated heat production due to the underlying mantle flow (Agard *et al.*, 2011; Eyuboglu *et al.*, 2011) or (b) the thickening of the continental crust due to continental collision (Karsli *et al.*, 2010; Pang *et al.*, 2016), iii) an alternative scenario regardless of any geodynamic models, considering the partial melting of a metasomatized mantle with a possible role of crystallization of amphibole at high pressure (Azizi *et al.*, 2014). However, recent magmatic activities parallel to the Zagros Suture, i.e. the Kurdistan province and the Central UDM, occurred in the vicinity of compaction pockets (number 13 and 24, respectively), correlating with a zone of horizontal $\vec{\sigma}_3$ (Fig. 3.3b).

3.4 GEOCHEMISTRY

3.4.1 Chemical classification of lavas

In this section, we present a synthesis of the petrological and chemical characteristics of the continental magmatic activity of the TIP extending from 80 Ma to present and from Central Anatolia to Eastern Iran. It is based on the synthesis of seventy publications (references in the appendix) which are the primary information that we used to construct a database covering the magmatic *periods 2, 3 and 4* (continental magmatism since the emplacement of ophiolites, i.e. younger than 80Ma). The geochemical signal provided by the rocks are too heterogeneous to be related to melting of a single source with or without associated crustal contamination and/or fractional crystallization (Özdemir *et al.*, 2006, Lustrino *et al.*, 2010; Asiabanha & Foden, 2012; Aydin *et al.*, 2008, 2014). In order to minimize the possible effects of shallow processes (crustal melting and fractional crystallization) overprinting the early, deep-seated history of the

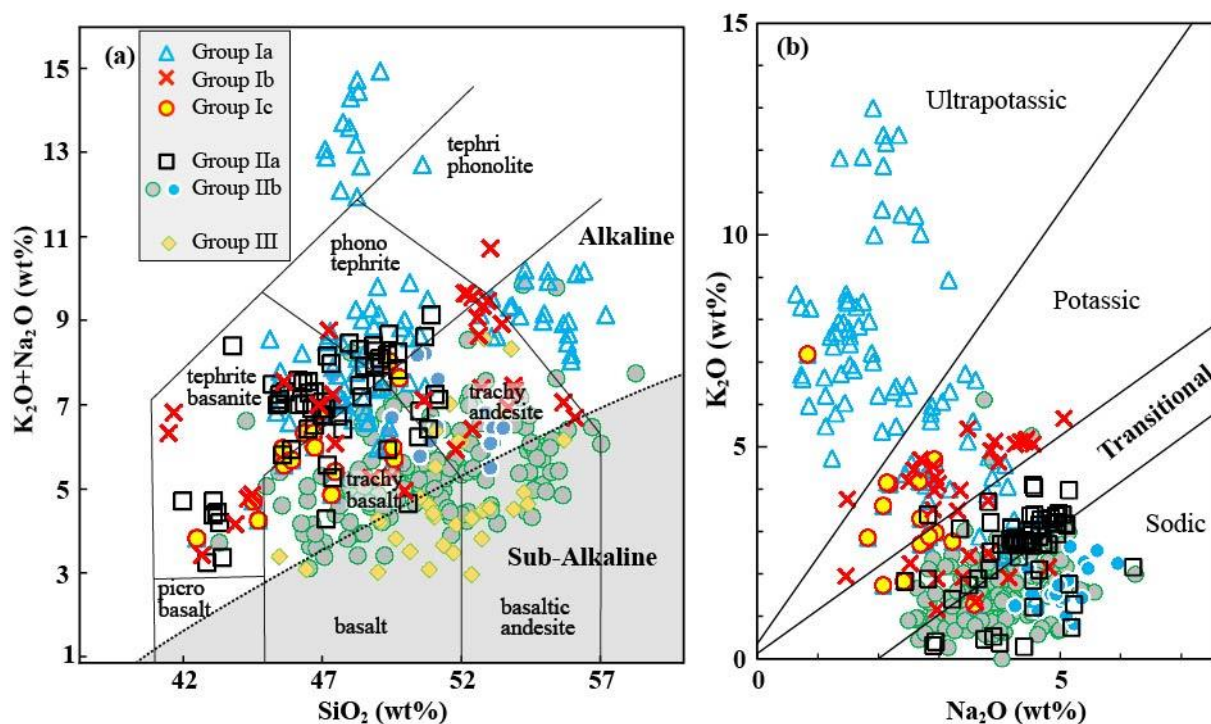
magmatic rocks, we focus our analysis of the database on mafic to intermediate ($\text{SiO}_2 < 55$ wt.%) lavas and pyroclastic volcanic rocks. Thus, the chemical characteristics of magmatic rocks considered in the following are expected to be as close as possible to those of their parental melt more or less directly issued from their mantle sources.

The representative major and trace element data as well as the isotopic ratios for these samples are presented in Table 10 appendix. Based on this database we propose a classification based on objective criteria (the analyses provided in the tables) rather than on published classifications that are far from being homogeneous from one author to the other and do not always follow the IUGS recommendations. From our analyses, we found that the volcanic and pyroclastic volcanic rocks could be subdivided into three main groups. Among them, I and II are the largest in terms of volume of data and are themselves subdivided into several subgroups, whereas group III is represented by a more restricted amount of samples. Below, we describe the geochemical and isotopic characteristics of these three groups and their subdivisions.

3.4.1.1 Group I

Based on the IUGS classification and systematic classification for exotic lavas (e.g. Mitchell & Bergman, 1991; Woolley *et al.*, 1996), most samples from this group are classified as lamproite, lamprophyre, leucitite, analcite or nepheline bearing- tephrite and phonolite, whereas few samples are classified as trachyandesite and trachyte (see references listed in *table 10.appendix*). On the total alkali versus silica diagram, all samples plot above the alkaline division line. SiO_2 content varies between 40-55.5 wt. %, whereas the $\text{Na}_2\text{O}/\text{K}_2\text{O}$ ratio is commonly < 1 . The high K_2O contents of these rocks reflect their potassic to ultrapotassic tendency ($\text{K}_2\text{O}/\text{Na}_2\text{O}; > 0.1-12.02$, Fig. 3.6b). This figure allows us to distinguish three subgroups: Ia, Ib, Ic. Group Ia samples have high variable K_2O content up to 12.02 wt.%, low TiO_2 content (0.8-1.67 wt.%), and variable MgO (1.7-10.8 wt.%), and Na_2O (0.83-4.4 wt.%)

contents. Group Ib is similar to group Ia in term of major elements concentrations i.e. low in



TiO₂ (0.9-1.4 wt.%), moderately high in K₂O (1.1-5.3 wt.%) and variable in MgO (2.3-7.9 wt.%) and Na₂O (1.3-4.5 wt.%) but have different isotopic signatures (see below). Whereas group Ic samples have similar K₂O (1.6-4.5 wt.%) and Na₂O (1.7-2.8 wt.%) than those from group Ib, they differ from group Ia and Ib by their higher TiO₂ content (~ 1.8- 3.6 wt.%), and by the absence of samples very poor in MgO (which ranges from 4.8 to 9.6 wt.%).

Figure 3.6. Geochemical variation diagrams for the purpose of lavas classification. The samples are restricted to the most primitive ones (SiO₂ < 55 wt. %). The major elements data are recalculated to a 100 % anhydrous basis. a) Total Alkali versus Silica diagram (TAS; Le Bas *et al.*, 1986); solid line is Irvine & Baragar (1971) 's boundary between alkaline and sub-alkaline rocks, b) K₂O versus Na₂O diagram showing classification of studied lavas into sodic, transitional from sodic to potassic, potassic and ultrapotassic series.

Trace element patterns of group I, evidence their LILE-enriched (Cs, Rb, Ba, Th, U) and Sr-depleted character. The HFSE (Nb, Ta, Ti) abundances are variable. Groups Ia and Ib

are characterised by strong HFSE depletions and Pb enrichment while group Ic rocks display smoother patterns with slight Nb, Ta enrichment and no Pb peak. On the other hand, all three groups display negative Sr and Ti anomalies. Elemental ratios involving fluid mobile elements (Ce/Pb and Rb/Ba), are highly variable in group Ia and Ib, whereas those involving more immobile elements display more restricted ranges (e.g. Th/Nb). Group I samples have broadly similar sub-parallel chondrite normalized REE patterns. They present a considerable enrichment in light rare earth elements (LREE) relative to heavy rare earth elements (HREE, $(La/Yb)_N$ up to ~ 60), whereas in detail, $(La/Yb)_N$ and $(Sm/Yb)_N$ are not significantly different for group Ia and group Ib. In turn for group Ic these two ratios are lower and more homogeneous.

The $^{87}Sr/^{86}Sr$ and the $^{143}Nd/^{144}Nd$ ratios of group I, as well as the global field of transitional kimberlite are illustrated in figure 3. 7. Although quite scattered, all the considered isotopic ratios plot within the mantle array. Group Ia, characterized by high and variable $^{87}Sr/^{86}Sr$ (0.7055-0.7080) and lower $^{143}Nd/^{144}Nd$ (0.51238-0.51261) ratios, plots close to the transitional kimberlites field. The range of $^{87}Sr/^{86}Sr$ (0.7043-0.7062) and $^{143}Nd/^{144}Nd$ (0.51243-0.51271) for group Ib, and Ic are respectively lower and higher than those from group Ia. Thus, they plot close to the field of Oceanic Island Basalt (OIB, Fig. 3.7).

3.4.1.2 Group II

This group mainly consists of lavas classified as olivine basalt, basanite, hawaiiite, mugearite, and trachyandesite (references in *Table 1.appendix*). All these volcanic rocks with Na_2O and K_2O ranging from 2.4-6.1 wt.%, and 0.68-6.08 wt.%, respectively plot within the sodic series field (Na_2O/K_2O ; > 1,7) (Fig. 3.6b). The rocks display variable SiO_2 (40.6- 55.2 wt.%), and total alkali (Na_2O+K_2O : 3.2-9.1 wt.%) contents. Based on major elements, the samples are divided into two subgroups IIa and IIb with alkaline and sub alkaline tendency,

respectively (Fig. 3.6a). The group IIa shows a higher and ore restricted range of MgO (6.6-11.7 wt.%), TiO₂ (1.3-2.2 wt.%), lower Al₂O₃ (12.5-16.01 wt.%), and SiO₂ (40.6-50.8 wt.%) than group IIb, which is characterized by MgO: 1.7-11.8 wt.%, TiO₂: 0.7-3.5 wt.%, Al₂O₃:12.2-19.08 wt.%, and SiO₂ 43.3- 55.2 wt.%.

In the primitive mantle and chondrite normalized trace element and rare earth element diagrams (Sun & McDonough, 1989), the higher concentrations of large ion lithophile elements (LILE) and LREE compared to those of HREE are highlighted. These diagrams evidence that the level of fractionation of LILE and LREE over HREE decreases from group IIa to group IIb (for example (La/Yb)_N decreases from 82.3 to 1.7). Group IIa and group IIb are characterized by HFSE (e.g. Nb, Ta, and Ti) depletion and enrichment, respectively (Fig. 3.8). The group IIa is characterized by high Ba (521-~ 2000 ppm), Th (9.7-38.2 ppm), Sr (~500-2800 ppm), Pb, (8.3-25.2 ppm) contents and relatively homogeneous range of high Ce/Pb (9.3-20.9) and Nb/U (3.3- 25.8) ratios, whereas, the group IIb is characterized by Ba:103- ~1600 ppm, Th:1.06- 17.3 ppm, Sr: < 1700 ppm, Pb: < 10, and highly variable Nb/U (2.7- 113) and Ce/Pb (0.38-71) ratios. In addition, the high (La/Yb)_N (15.1-82.3) and (Sm/Yb)_N (3.3-12.9) ratios for group IIa reflect the occurrence of mineral in the source with high partition coefficients (D) for HREE (e.g. garnet). The group IIb with flatter MREE-HREE slopes (Sm/Yb_N 1.5-4.4) evidences that the possible role of such minerals in their source is less significant than for group IIa. The Nd-Sr isotopic data for group Ia plot within the mantle array (Fig. 3.7). These values form a narrow range (⁸⁷Sr/⁸⁶Sr: 0.70441-0.70599 and ¹⁴³Nd/ ¹⁴⁴Nd: 0.51263-0.512706), located in the OIB field whereas, group IIb with highly variable ⁸⁷Sr/⁸⁶Sr: 0.7037-0.7067 and ¹⁴³Nd/ ¹⁴⁴Nd 0.51261-0.51297 values defines a wide range plotting between depleted and enriched mantle sources (Fig. 3.7).

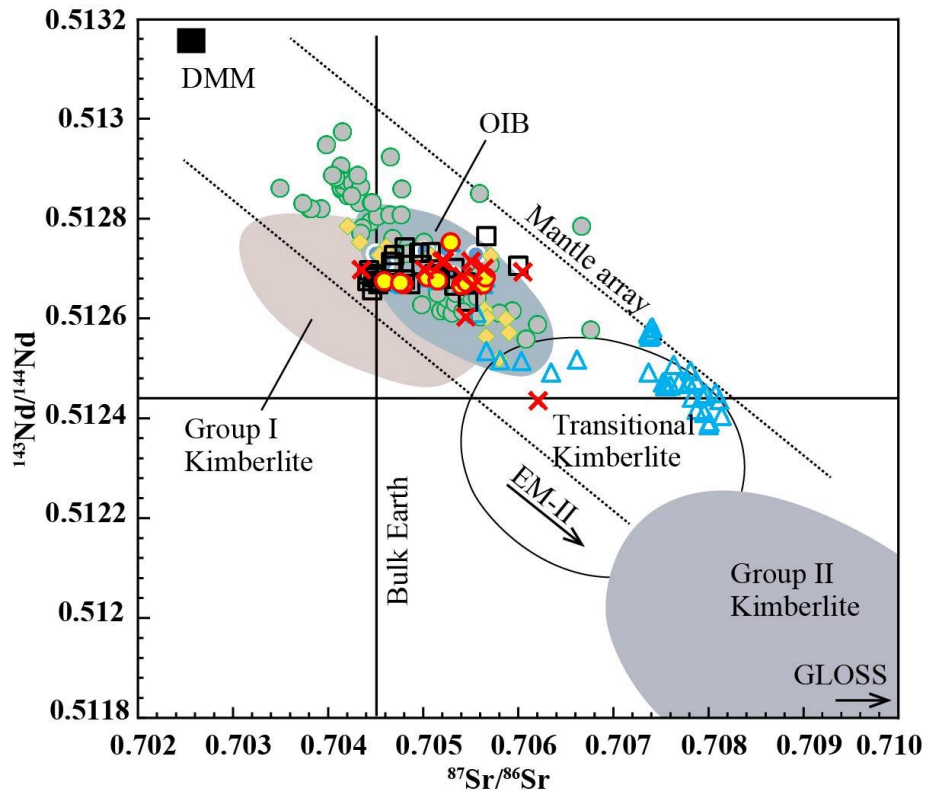


Figure 3.7. $^{143}\text{Nd}/^{144}\text{Nd}$ versus $^{87}\text{Sr}/^{86}\text{Sr}$ diagram for each group of lavas compared with the mantle components DMM and OIB. Abbreviations: DMM = Depleted MORB Mantle, OIB = Oceanic Island Basalt; (after Zindler & Hart, 1986); data sources; Group I, II and transitional Kimberlites (Becker & Le Roex, 2006).

3.4.1.3 Group III

These rocks mainly occur as pyroclastics rather than lava flows (e.g. “Karaj formation” in the geological section) and are classified as basalt and basaltic andesite. Whole rock silica content ranges from 47.1 to 54.4 wt.% (Table 10.appendix). Most samples are characterized by moderate Na_2O (1.6-4.7 wt.%), and variable K_2O (0.2-3.5 wt.%) contents, which on the total alkali-silica plot (Fig. 3.6.a), display a trend typical of calc-alkaline series. They are also characterized by low TiO_2 (0.8-1.7 wt.%) and variable MgO (2.1-10.1 wt.%) contents. In terms of major elements, this group is close to group IIb. Trace element abundances normalized to mantle and chondrite values evidence a LILE (Cs, Rb, Ba, Th, U, Pb) and LREE (La: $34\text{-}174 \times$

Chondrite) enrichment over HFSE (Nb, Ta, Ti) and HREE. This group has a distinctive HFSE depletion pattern characterized by homogeneous values, which differs from the variable HFSE depletion characteristic of group IIb. All samples have similar parallel REE patterns with $(La/Yb)_N$ ranging from 3.1 to 13.5. They show flat MREE-HREE patterns ($(Sm/Yb)_N$: 0.1-3.6) devoid of any Eu anomalies and are therefore similar to the REE patterns of the group IIb. Their mobile incompatible elements ratio such as Ce/Pb (1.3-13.9) and Nb/U (0.9-11.11), plot close to those of group IIb, but evidence a higher-level of crustal contamination (e.g. Fig. 3.15a). The variable range in $^{87}Sr/^{86}Sr$ (0.70420-0.7059) and $^{143}Nd/^{144}Nd$ (0.51252-0.51278) isotopic ratios of group III samples probably reflect the high heterogeneity of their mantle source.

3.4.2 Salient conclusions of the geochemical synthesis

An overview of geochemical characteristics of the most primitive lavas in the TIP showed their enrichment in terms of major alkali elements (Na and K), LILE, and REE fractionation related to various degrees of partial melting or to contrasts in mantle source composition rather than to fractional crystallization or crustal contamination. In a Sr vs. Nd isotopes diagram, most lavas plot close to the field of melts derived from enriched mantle sources (e.g. OIB, transitional Kimberlites). Group IIb is also centred on the OIB field but presents a much higher scatter along a line linking depleted (DMM) and enriched mantle (EM-II) sources. Moreover, based on the occurrence or lack of negative HFSE anomalies, their elemental features divide into “subduction-influenced” patterns and “OIB-like” patterns (Fig.3.8). Groups with higher K_2O (e.g. group Ia) and Na_2O (e.g. group II) content, have trace elements patterns similar to those of kimberlites and OIB, with, here again, subduction-influenced and OIB-like patterns, respectively (Fig. 3.8).

Previous studies showed that their mantle sources are enriched by metasomatism processes, which underwent low degree of melting (Allen *et al.*, 2013; Pang *et al.*, 2013; Shafai Moghadam, *et al.*, 2013; Saadat *et al.*, 2014; Prelević *et al.*, 2015). Several processes have been

proposed to account for the metasomatism of their mantle source: (i) an old subduction leads to a metasomatic mantle wedge or a continental lithosphere with heterogeneous source (e.g. Hassanzadeh & Wernicke, 2016), (ii) direct stacking of slabs leading to their interaction with the overlying asthenospheric mantle (e.g. Verdele *et al.*, 2011), and (iii) the ascent of volatiles-enriched convecting mantle material (e.g. Platevoet *et al.*, 2014; Saadat *et al.*, 2014; Prelević *et al.*, 2015) related to slab tearing or slab breakoff processes. However, in all cases frequently observed “subduction-influenced” patterns are interpreted as a shallow mantle reservoir characterised by HFSE depletions (e.g. subcontinental lithospheric mantle: SCLM). Interestingly, in some lavas (e.g. group Ia), the shallow mantle reservoir is combined with other components such as recycled sediments and residual hydrated minerals in order to account for the diversity of the observed “subduction-influenced” patterns and other features (high LREE/REE fractionation and Sr isotope) (e.g. Pang *et al.*, 2013; Shafai Moghadam *et al.*, 2013; Prelević *et al.*, 2015). It should be mentioned that several processes may control the geochemical characteristics of the sources of subduction-influenced lavas (HFSE- depleted), such as: (i) the presence of minerals with

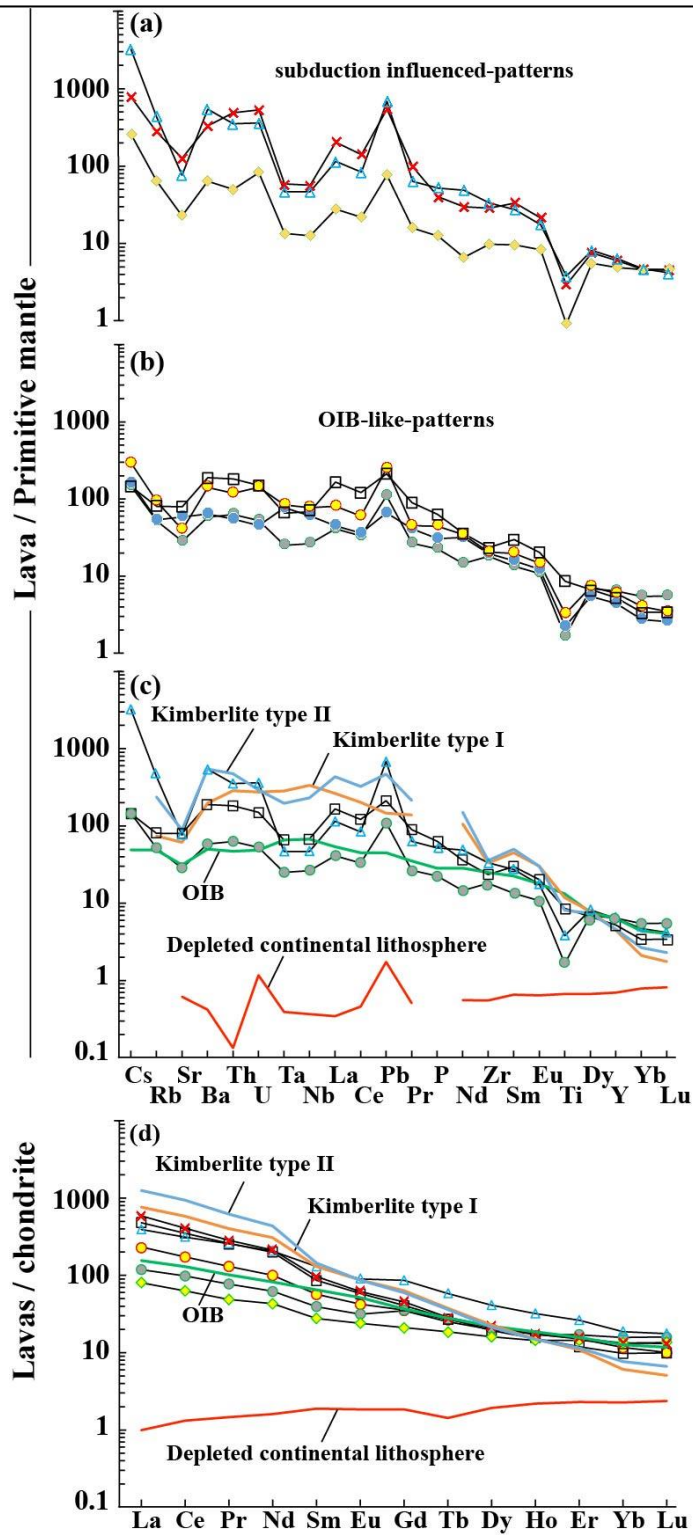


Figure 3.8. Primitive mantle- and chondrite -normalized (Sun & McDonough, 1989) multi-element distribution patterns of lavas. Various patterns showing two different subduction influenced- and OIB-like patterns for classified lavas.

high partition coefficients for HFSEs i.e. rutile, ilmenite, amphibole (Green & Pearson, 1987; Ionov & Hoffman, 1995; Tiepolo *et al.*, 2001), (ii) the presence of recycled sediments (Hawkesworth *et al.*, 1993) (iii) a HFSE-depleted mantle reservoir (i.e. subducted slab or extremely depleted mantle, Saunders *et al.*, 1988, McDonough, 1990, Prelević *et al.*, 2008), and finally (iv), other processes not directly linked to the source, i.e. crustal contaminations during magma ascent (e.g. Barth *et al.*, 2000). Thus, the link between such geochemical patterns and deep-seated mantle sources was also proposed to generate potassic exotic melts or even arc-like calc alkaline melts (Grassi *et al.*, 2012, Murphy *et al.*, 2002; Kuritani *et al.*, 2013, Wang *et al.*, 2016). Therefore, although most interpretations of the petrological and chemical characteristics of the “subduction-influenced” patterns in the TIP call for a major influence of the source, they do not necessarily imply that those sources are restricted to shallow mantle depths.

On the other hand, the occurrence of lavas with OIB-like patterns are frequently explained by the upwelling of enriched asthenosphere and/or a hybrid source resulting from the interaction between the asthenosphere and the overlying lithosphere (Wilson *et al.*, 1997; Özdemir & Güleç, 2014; Neill *et al.*, 2015;). However, in these interpretations there is no clear line to distinguish lavas with different “OIB-like” patterns like those identified here by group Ia, II a and b. To give an example, there is no clear explanation for the specific lavas classified as group IIa with respect to other OIB-like lavas.

Moreover, one of the major conclusions of our synthesis is that lavas that were interpreted by previous authors (e.g. Allen *et al.*, 2013; Mirnejad *et al.*, 2010) in contrasting ways due to contrasting tectonic and geographic settings (e.g. Damavand volcano and Kurdistan lavas), belong actually to the same OIB-like group according to our objective geochemical criteria. More precisely, in the case of Damavand volcano asthenospheric upwelling was invoked, while in the case of Kurdistan lavas, a richterite-bearing lithospheric mantle source hydrated during continental collision was proposed. However, the relationships between such

mantle sources other lavas with OIB-like patterns (e.g. group Ic and I Ib) have not been considered yet.

In the present study, we present an alternative model of “compaction pockets” rooted down to the MTZ. Our model should not be considered in contradiction but rather complementary to other interpretations of mantle sources relating depleted subducted slabs, crustal components (e.g. recycled sediment), residual hydrated/carbonated phases, and the overlying lithosphere. While all these already invoked processes allow to interpret the geochemical characteristics observed in the parental melt, we built our new “compaction pockets” model as we find it more consistent with the overall geochemical and geophysical data.

3.5 UPPER MANTLE TOMOGRAPHY BENEATH THE TIP, AND IDENTIFICATION OF COMPACTION POCKETS

Figure 3.9 displays horizontal cross-sections at 500 km and 700 km depth the P-tomography model by Nafi Toksöz et al. (2008), and which spans from 20° E to 60 °E and from 0° N to 50° N across the Africa-Arabia and Eurasian plates. The compaction pockets that are then identified below from this tomography and other studies, are primarily characterised by two main properties: (i) they occur far from any active subduction or slab detachment, and (ii) they are centred at a depth of ~150 km, clearly deeper than the lithosphere-asthenosphere boundary beneath the TIP (~100 km, Mohammadi *et al.*, 2013, Kind *et al.*, 2015) and deeper than global mantle wedge-related hydration processes (e.g. < 150 km).

We observe a whole set of compaction pockets sitting above a high velocity zone located a few hundred km North of the Hellenic trench, the Zagros Suture and up to the northern limit of the slab bending trace of the Makran subduction (Fig. 3.9). In addition, we observe one “slow” North-South oriented band that originates at the Afar triple junction (ATJ) and extends

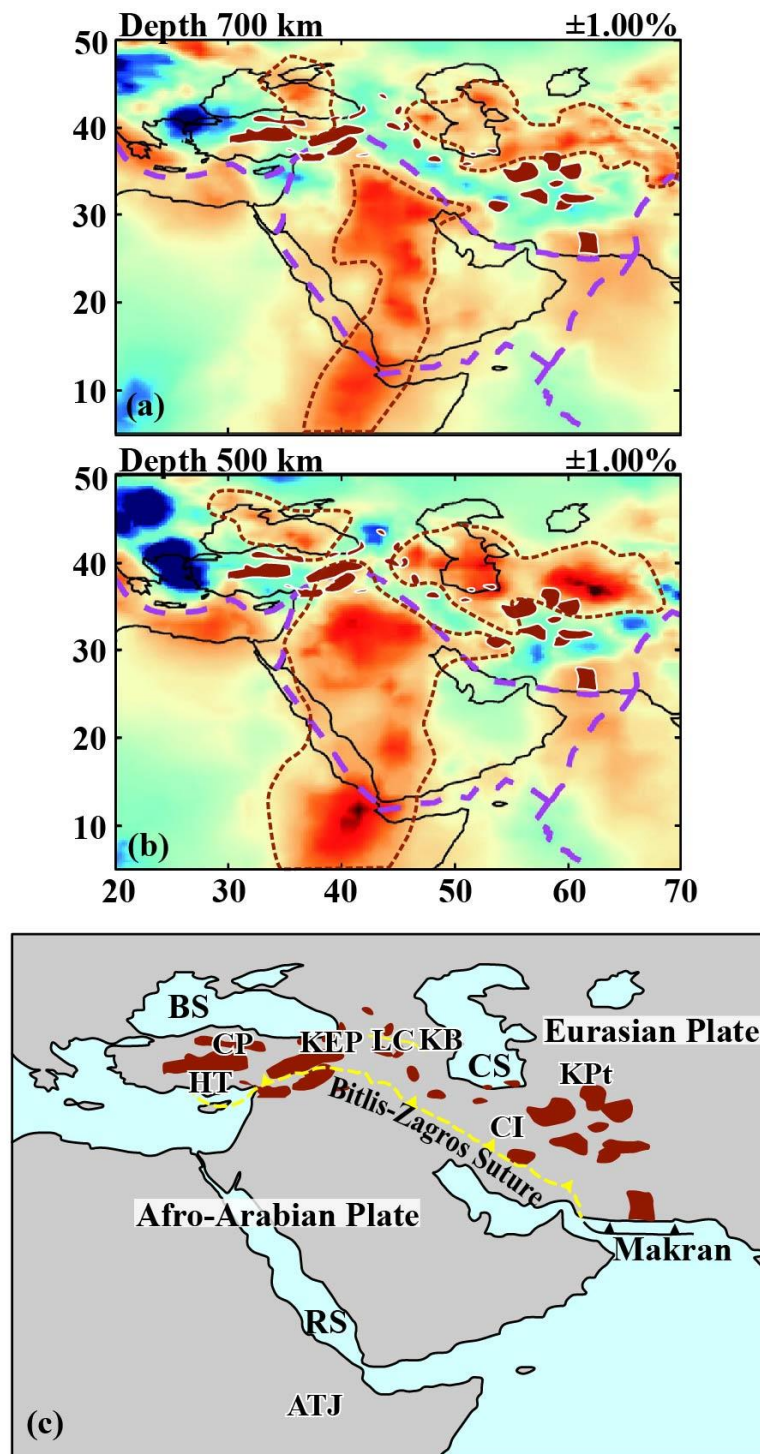


Figure 3.9. Middle East large-scale tomography model (P-wave anomalies) by Nafi Toksöz et al. (2008) (a) at 700 km and (b) at 500 km, respectively. Dashed purple lines are plate boundaries, black lines are coastlines, dashed red lines are border of low velocity anomalies and brownish-red area are identified compaction pockets considered in this study. It is sticking to note that the various compaction pockets set inside or at the border of a high velocity band, which likely represents the zone of stagnation and differentiation in the MTZ of the subducted slabs in the Bitlis- Zagros collision zone. Key features in the schematic maps (Fig. c) are RS: Red Sea, BS: Black Sea, CS: Caspian Sea, CP: Central Pontides, CI: Central Iran. Other abbreviations same on figure 3.3.

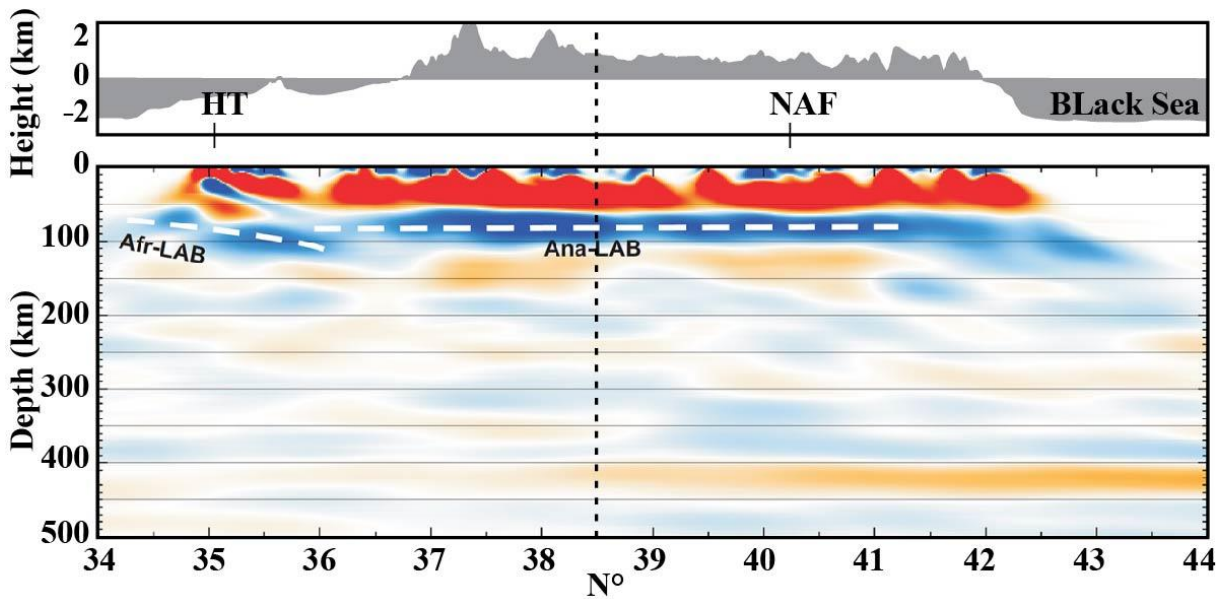


Figure 3.10. Display of S- receiver function along a North-South profile between 30 and 39 °E of Central Anatolia (Fig. 3.2c), from Kind et al. (2015), with modifications. Relief above it from the Hellenic trench (HT) to the Black Sea is shown. White dashed line corresponds to the LAB beneath Afro-Arabian plate (Afr) and Anatolia (Ana). Grey dashed line (38° 30' N) indicates appearance of a 40 km thick low velocity zone below 410 km depth, which is designed in this study as the low velocity layer. As seen in this figure toward the North, far away from the HT, the low velocity layer appears as stronger in colour. This domain approximately recovers a zone where the Central Anatolia compaction pockets crowds (i.e. Fig. 3.2c 38° N to 41° N).

through the Arabian plate up to the Bitlis Suture zone, whereas another one is East-West oriented, follows the Kopet Dagh, ends below the Kura basin, disappears below the Caucasus and finally re-appears below the Black sea. Actually, the fast and slow velocity contrast represents ~2%, usually interpreted as temperature and composition variations in the mantle beneath the TIP (Piromammo & Morelli, 2003; Faccena *et al.*, 2006; Özacar *et al.*, 2008; Tunini *et al.*, 2015). This is consistent with the fact that the MTZ- high velocity domain represents Tethys stagnant slabs and/or delaminated fragments of continental lithosphere (e.g. Özacar *et al.*, 2008; Skobeltsyn, *et al.*, 2014), and which can record few hundred °C temperature drop (Rabinowicz *et al.*, 1980).

Fig. 3.10 displays Kind *et al.* (2015) S-receiver functions along a North-South profile running from 30° E to 39° E. From 38.5° N to 44° N, the 410 km-interface presents a strong slow reflector penetrating down to ~450 km depth. It regresses moving south and becomes evanescent around the Hellenic trench. Globally, the low velocity layer results from (i) progressive thickening of the wadsleyite to olivine phase transition in presence of water (van der Meijde *et al.*, 2003), (ii) partial melting due to release of water during the phase transition (e.g. Karato, 2011). In addition, the physical and chemical evolution of stagnant slabs and delaminated continental lithosphere leads to a compositional gradient from denser eclogite to less dense harzburgite from the base up to the top of the MTZ (e.g. harzburgite has a density 1 % to 2% lower than eclogite and lherzolite, Shorttle *et al.*, 2014). Accordingly, the low velocity layer may essentially consist of carbonated and or hydrated harzburgite. It implies that the low velocity layer is gravitationally unstable (Rayleigh Taylor) and can diapirically intrude the olivine stability field (Motoki & Ballmer, 2015).

The H₂O-solubility in wadsleyite and ringwoodite mineral phases, known to form the MTZ, is extremely high: ~0.9 wt.% and 2.3 wt.%, respectively (Demouchy *et al.*, 2005; Pearson *et al.*, 2014). Moreover, at the top of the MTZ when wadsleyite transforms into olivine, the H₂O solubility drops from 0.9 wt.% to ~448 ppm (Demouchy *et al.*, 2005; Litasov *et al.*, 2009). Thus, the water released during this phase transformation leads to hydrous melting (e.g. Hirschmann 2006). Additionally, the solidus of carbonated peridotite is similar or even lower than that of hydrated peridotites (Fig. 11a). Together with the volatile-rich melt (e.g. kimberlite) solidus, this implies that the melt produced inside the olivine stability field likely has a kimberlitic- like composition. Because of the small wetting angle of inter-granular melts, melt phases in the mantle likely form a connected network making it permeable even for an extremely low local melt concentration: i.e. about 10⁻⁵ % according to Minarik & Watson (1995). However, a small melt concentration of several 0.01% is usually considered motionless

relative to the host solid mantle due to its low permeability. In contrast, at higher concentrations ($> 0.1\%$) melts can segregate from the mantle and move upwards (Hirschmann, 2010; Keller *et al.*, 2017). To conclude, we see that two hydrodynamic instabilities propel the kimberlite like melts upward: (i) the gravitational instability of the low velocity layer and (ii) the melt percolation process. For constant viscosity Rayleigh Taylor instabilities, the wavelength of the diapirs is $\sim 3h$ (Houseman & Molnar, 1997), where h is the thickness of the gravitationally unstable low velocity layer, i.e. $\sim 3 \times 40$ km. Then, once these diapirs are well developed, their velocity can be approximated by their Stokes velocity; i.e. considering their size (~ 120 km), their density contrast with the surrounding mantle ($\sim 1\%$) and the viscosity of asthenosphere ($\sim 10^{20}$ Pas, Karato & Wu, 1993), we obtain a velocity of the order of mantle convection velocities, i.e. < 1 m/yr. In the next section, we show how compaction of the mantle mush in the diapirs leads to the formation of Compaction pockets.

3.6 HOW COMPACTION POCKETS DEVELOP FROM VOLATILE-RICH MELTS CARRIED BY “ COLD WET DIAPIRS”

The free percolation of a non-reactive melt in a viscous-mantle is the aim of many studies which have been motivated by McKenzie (1984)'s pioneer work. Various studies have demonstrated that a major condition for the occurrence of magmons (i.e. mantle spherical-like propagating structures with a high melt concentration) is a strong vertical permeability drop at the top of the compaction domain (Scott & Stevenson, 1984; Wiggins & Spiegelman 1995, Rabinowicz *et al.*, 2002). Generally, this permeability drop is associated with the $\sim 1300^\circ\text{C}$ to 1170°C temperature drop through the convective boundary layer. We recall that this layer lies between the top of the horizon where the temperature adiabatically increases, and the base of the elastic lithosphere (Ceuleneer & Rabinowicz, 1992). This thermal range also corresponds to the domain where dry mafic melts start to crystallize, explaining why the interstitial volume

of melts drops in this zone and thus permeability of the mantle decreases. Such conditions are believed to trigger the formation of troctolitic sills within the mantle below ridge crests (Rabinowicz & Ceuleneer, 2005). In the case of the TIP, we see that the compaction pockets like for instance the ones displayed in figure 3.5b, are entirely enclosed well below the ~100 km thick TIP- lithosphere or eventually appear to be channelled inside narrow vertical conduits associated to lithospheric-scale faults (number 9-11 Figs. 3.3b and 3.4). This leads us to search for an alternative explanation for the permeability drop, which may lead to the development of the compaction pockets. In the following, we link them to the multi stages (e.g. 8GPa and 4GPa) precipitation of new mineral phases as a result of reactions between volatile- rich melt and the surrounding mantle.

The state and reaction of volatile-rich melts in the olivine-mantle stability field is the aim of many experimental and natural samples studies. They depend on the effects of alkalis, water and carbonate carrying phases on the surrounding mantle rocks (Ionov *et al.*, 1993; Konzett & Ulmer, 1999; Tronnes, 2002; Brey *et al.*, 2008, 2011; Gant *et al.*, 2014, 2017; Giris *et al.*, 2011; Ghosh *et al.*, 2014; Frezzotti & Touret, 2014; Malik & Dasgupta 2014; Novella & Frost 2014). Experimental results show that as result of such reactions hydrated and carbonated phases are stable in a varied range of pressures and temperatures. For example potassium richterite ($\text{KNaCaMg}_5\text{Si}_8\text{O}_{22}(\text{OH})_2$) is a well-known hydrous mineral phase stable in the upper mantle between 6.5 to 8 GPa, at temperature ≤ 1300 °C (Konzett & Ulmer, 1999), whereas the stability field of phlogopite ($\text{KMg}_3\text{AlSi}_3\text{O}_{10}(\text{F}, \text{OH})_2$) is limited to a pressure ≤ 6 GPa for temperatures up to 1300 °C (Tronnes, 2002; Enggist *et al.*, 2012, Fig. 3.11b). Moreover, at a pressure ≤ 8 GPa and a temperature of ~ 1300 °C, carbonated phases (i.e. magnesite and alkali magnesite) are stable (Brey *et al.*, 2011). Between 5 GPa and 4, a carbonate phase (i.e. magnesite) is also stable, but in order to coexist with phlogopite, a temperature lower than 1200°C and 1250°C at 5 GPa and 4 GPa, respectively is required (Enggist *et al.*, 2012).When

combining these various phase stability fields and associated changes, we see that around a temperature of 1300°C and a pressure of 8 GPa to 6.5 GPa (i.e. ~240 km to 195 km depth), the reaction of volatile-rich melt with surrounding mantle leads to the precipitation of richterite and carbonate phases. In addition, between 4 and 5 GPa and a temperature ~1200 °C to 1250 °C, phlogopite and carbonate phases precipitate (Fig. 3.11b).

In figure 3.11 is drawn the minimum and maximum temperature estimation of the mantle adiabat derived by Katsura et al. (2010). Both profiles differ by 100°C (yellow area in Fig. 3.11). As we can see, except at the wadsleyite-rigidite and olivine-wadsleyite phase transitions, the profiles increase approximately linearly with depth, consistent with a mantle adiabatic gradient of ~0.5 °C/km. Moreover, the temperature versus depth profile in the mantle needed to precipitate hydrated and carbonated phases must be at least 100°C lower than that given by the minimum adiabat. The geochemical fingerprints of alkaline lavas in the TIP show that lavas originated from upper mantle sources metasomatized by hydrated and/or carbonated phases. Thus such metasomatism requires a temperature at least 100°C lower than the adiabat. This is consistent with the fact that long-lived subduction along the Bitlis-Zagros Suture leads to a few hundred °C drop of temperature of the upper mantle below the TIP (e.g. Rabinowicz *et al.*, 1980).

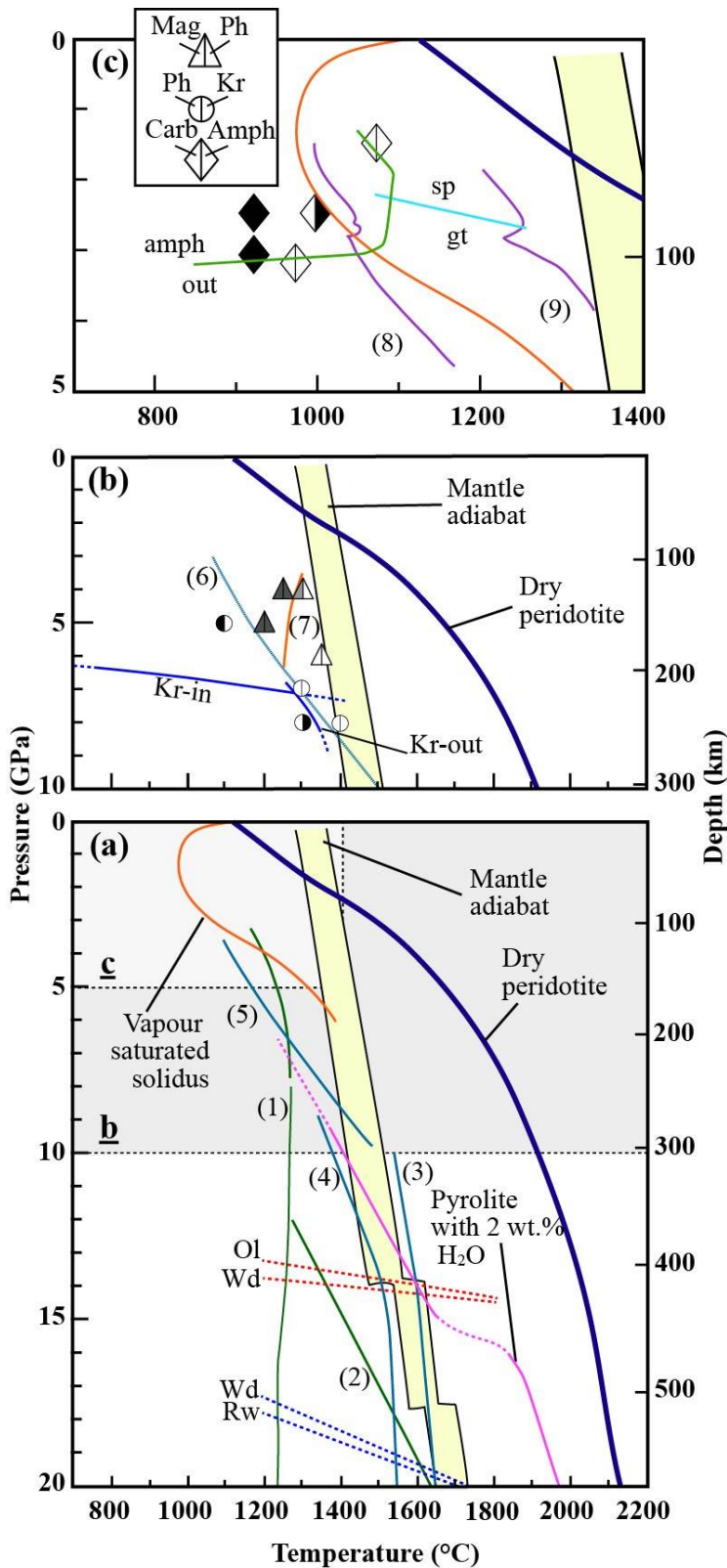


Figure 3.11. Pressure-temperature diagram to illustrate a) the solidus of different mantle components resulting from melting experiments, including mantle adiabatic temperature (after Katsura *et al.*, 2010), (b) and (c) phase relation of hydrated and or carbonated phases in the upper mantle. Key features for solid and dashed lines: dark blue, solidus of dry peridotite from Herzberg *et al.* (2000), pink line solidus of pyrolite (2 wt.% H₂O after Litasov & Ohtani, 2002) and orange one solidus of vapour saturated peridotite (Green, 2015). Dashed red and blue lines

Fig. 3.11 (continued), (Fig. a) show the Wadsleyite (Wd) and Ringwoodite (Rw)- out boundaries, respectively. Solid blue and green lines (Figs. b and c) show K richterite (Kr) and Ca-amphibole (amph)- out boundaries obtained from Konzett et al. (1997) and Green, 2015. Numbers correspond to (1) solidus of carbonated eclogite (with 4.4 wt.% CO₂) (Ghosh *et al.*, 2014), (2) solidus of carbonated eclogite (Keshav & Gudfinnson, 2010), (3) solidus of fertile peridotite (with 5wt.% CO₂) (Rohrbach & Schmidt, 2011), (4) Solidus of alkali rich peridotite (with 5 wt.% CO₂, 5) (Ghosh *et al.*, 2009), (6) solidus of carbonate-bearing fertile peridotite (Dasgupta & Hirschmann, 2006), (7) solidus of phlogopite-bearing carbonated peridotite (Enggist *et al.*, 2012), (8) solidus of kimberlite and (9) MARID xenoliths (Eggler, 1989). Phase relation of K-richterite with phlogopite obtained from Konzett et al. (1997), phlogopite with magnesite from Enggist et al. (2012), Ca-amphibole and carbonated from Green, 2015. Dark quadrant means that the corresponding phase is present. Abbreviations are: Kr, potassium richterite; Ph, phlogopite; Amph; Ca-amphibole; Mag; magnesite and Carb; Carbonate.

3.6.1 A model of compaction waves for rising mantle melts

In figure 3.12, we modified a dimensionless model by Grégoire et al. (2006) adapted to the description of the development of compaction waves when a partially molten mantle layer with a constant melt volume ϕ_{sc} meets a horizon with nearly zero melt concentration. In this experiment, the compaction length L defines the height scale of propagating fluids connected through the pores of the solid matrix and verifies:

$$L = \sqrt{\frac{\eta k(\phi_{sc})}{\mu \phi_{sc}}}, \quad (1)$$

Where, η and μ represent the effective bulk viscosities of the mantle and of the kimberlitic melt, respectively. $k(\phi_{sc})$ is the permeability of the partially molten layer with a fluid concentration ϕ_{sc} . The excess pressure p_{eff} , i.e. the difference between the melt and solid pressures is integrated along the compaction length L over which the porous network is connected, and defined with:

$$p_{sc} = \delta\rho Lg, \quad (2)$$

Where, g is the gravity constant, and $\delta\rho$ is the contrast in density between mantle and melt.

The time scale t_{sc} , representing the time taken for the melt to move upward over a distance of one compaction length L , is given by

$$t_{sc} = \eta/p_{sc}. \quad (3)$$

Finally the Darcy's velocity V_{sc} is scale is:

$$V_{sc} = L/t_{sc} = \frac{\delta\rho g L^2}{\eta}. \quad (4)$$

Melt concentration ϕ_{sc} is equal to the degree of melting, here assumed to be 0.75 vol%, i.e. 0.6 wt.%, chosen within the range proposed by Canil & Scarfe (1990) and Dalton & Presnall (1998). Maaløe & Scheie (1982) estimated a permeability $k(\phi_{sc}) = 10^{-15} \text{ m}^2$ for rocks with millimetre-size grains, $a=1\text{mm}$, and melt fraction $\phi_{sc} = 1\%$, whereas Faul (1997) suggested a permeability an order of magnitude lower. Based on recent experimental data the following simple rule is derived (Wark and Watson, 1998):

$$k = a^2 \times \phi_{sc}^3 / 200 \quad (5)$$

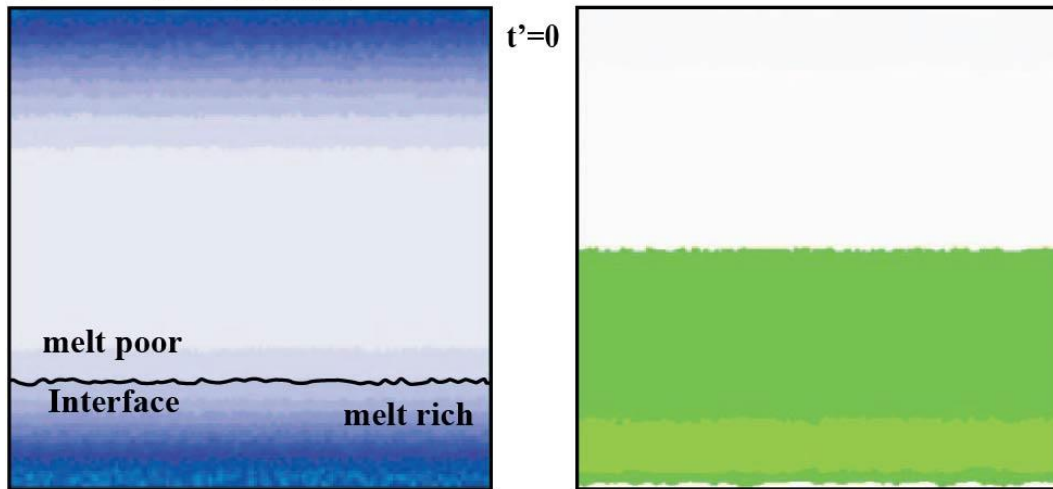
Which corresponds to $5 \times 10^{-15} \text{ m}^2$ when $a=1\text{mm}$ and $\phi_{sc} = 1\%$.

Typical grain sizes of rocks that deform by dislocation creep in the upper part of the upper mantle having a size $a \sim 3\text{--}4 \text{ mm}$ (Karato & Wu, 1993), we evaluate $k(0.75\%) = 3 \times 10^{-14} \text{ m}^2$. The viscosities of kimberlite melt (μ) are known to be low because of their low Si content and high concentrations of CO_2 and H_2O . However, they are estimated to vary from 0.01 to 1 Pa.s, with a most probable value around 0.1 Pa.s (McBirney & Murase, 1984; McKenzie, 1985, 1989). While recent experimental estimation rises it from 0.1 to 1.4 at 5.5 GPa and a temperature of 1300 °C (Persikov *et al.*, 2017). Following the study by Karato & Wu (1993), who estimated that the viscosity of wet asthenosphere is of the order of 10^{19} Pa.s between 300 km to 100 km depth, we choose a slightly greater value $\eta \sim 10^{20} \text{ Pa.s}$, assuming that the mantle is a few 100°C cooler than the adiabat. Finally, between 300 km and 200 km depth, the maximum density of a kimberlitic melt ranges between 2700 kg/m^3 and 3100 kg/m^3 , with a mean of 2900 kg/m^3 (Spera, 1984). Considering that the surrounding mantle density at these depths is $\sim 3600 \text{ kg/m}^3$, a conservative value for $\delta\rho$ is $\sim 700 \text{ kg/m}^3$.

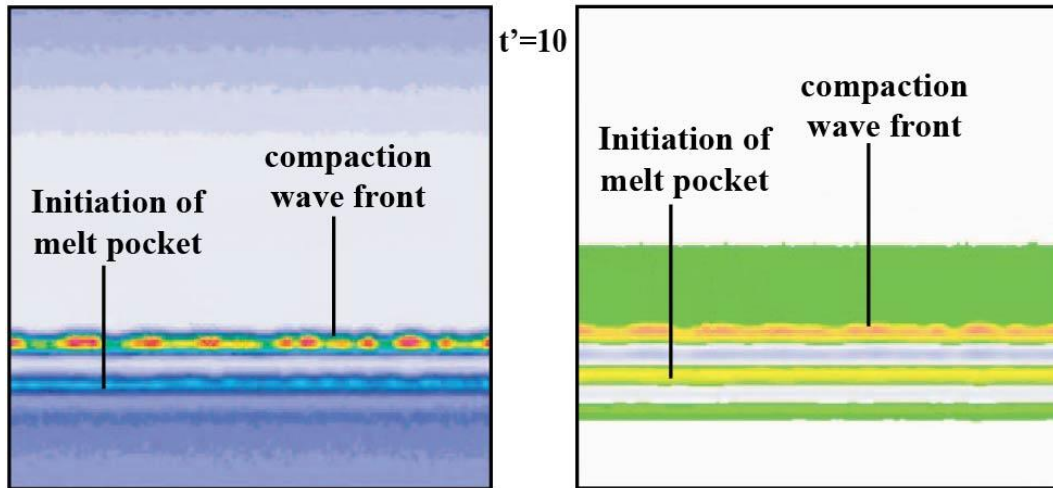
MELT CONCENTRATION

EXCESS PRESSURE

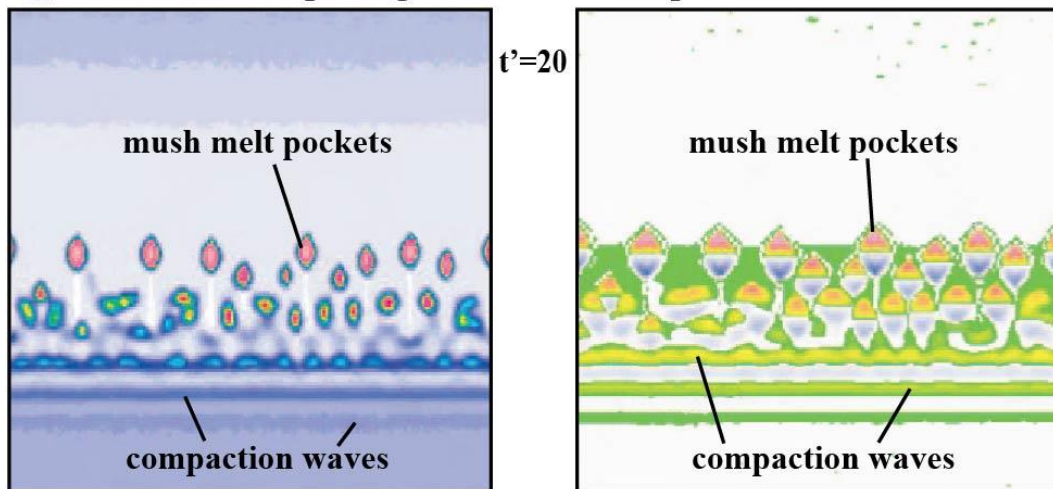
(a) 75L=1500km Initiation of the model



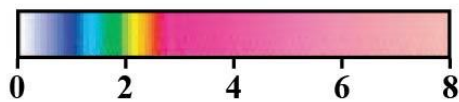
(b) Development of the horizontal waves



(c) Splitting of the waves into pockets



dimensionless melt concentration



dimensionless excess pressure

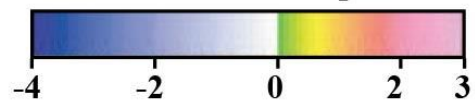


Figure 3.12. Gregoire et al., (2006)' compaction experiment. From top to bottom (snapshots a, b and c, respectively) are drawn the $t'=0$, $t'=10$ ($3.4 \cdot 10^5$ yr), and time $t'=20$ ($6.8 \cdot 10^5$ yr) snapshots of the dimensionless melt concentration by volume and excess pressure fields in an experiment with a computing box size of $75 L$ (1500 km). At time 10 ($3.4 \cdot 10^5$ yr), the wave front is planar, but inside the top wave several pockets are initiated. Thereafter, the planar wave splits and each pocket is individualized. At the end of the experiment, occurring at time 20 ($6.8 \cdot 10^5$ yr), the first swarm of melt pockets has moved up by about $25 L$ (500 km), i.e. with a mean upward velocity of about 0.4 m/year. They have a width of about $6L$ (120 km), and the maximum melt concentration inside the pockets is about $12 \times \phi_{sc} = 0.75\%$ (see text) i.e. 9 volume %. It should be noted that there is a strong interaction between melt pockets generated inside successive planar waves. At the top of each pocket, excess pressure reaches a maximum of about $3.2 p_{sc}$ (0.45 GPa, a value high enough to trigger the fracture of the overlying rock ($>40-50$ MPa)).

Using the above parameters values, we deduce that L is 20 km, then we propose the following scenario:

a) Just below the interface between the melt poor and melt rich horizon (that we assume to be located just above the depth of richterisation, (i.e. at a lithostatic depth corresponding to 8 GPa and at a temperature of 1300°C) a first wave develops which is essentially planar with a vertical thickness $\sim 4L$ (80 km). Horizontal melt fluctuations with a wavelength $\sim 6L$ are superimposed to the planar wave. The resulting melt impregnation consists in oblate shape pockets (with a horizontal elongated axis) included inside the planar wave (Fig. 3.12a). In geological terms, such a Compaction pocket forms a huge sill.

b) Thereafter, this wave percolates upward; at time $t'=5$ (~ 0.2 Ma), the wave has shifted upward by a distance $\sim 5L$ (100 km) inside the melt-poor horizon, while a new wave emplaces again just below the initial position of the poor and rich melt interface.

c) The second wave usually has a lower melt concentration than the upper one (Rabinowicz & Ceuleneer, 2005). Particularly, in the upper wave horizontally-wider melt pockets individualise and the maximal dimensionless melt concentration reaches $\sim 2\phi_{sc}$, height reaches $\sim 4.3L$ (~ 90 km) and length $\sim 8L$ (~ 160 km). Finally the maximum excess pressure at the top of these melt pockets is $\sim 2p_{sc}$.

d) As time goes on, melt pockets detach from the successive horizontal waves. This leads to the regression of the horizontal basal waves, where melt content eventually transfers to the few detached pockets.

e) Finally, the individual pockets interact. The melt contained within a pocket is observed to pour inside another one located just above it. At dimensionless time $t'=20$ (0.4 Ma), the melt concentration in pockets reaches $8\phi_{sc}$ ($\sim 6\%$).

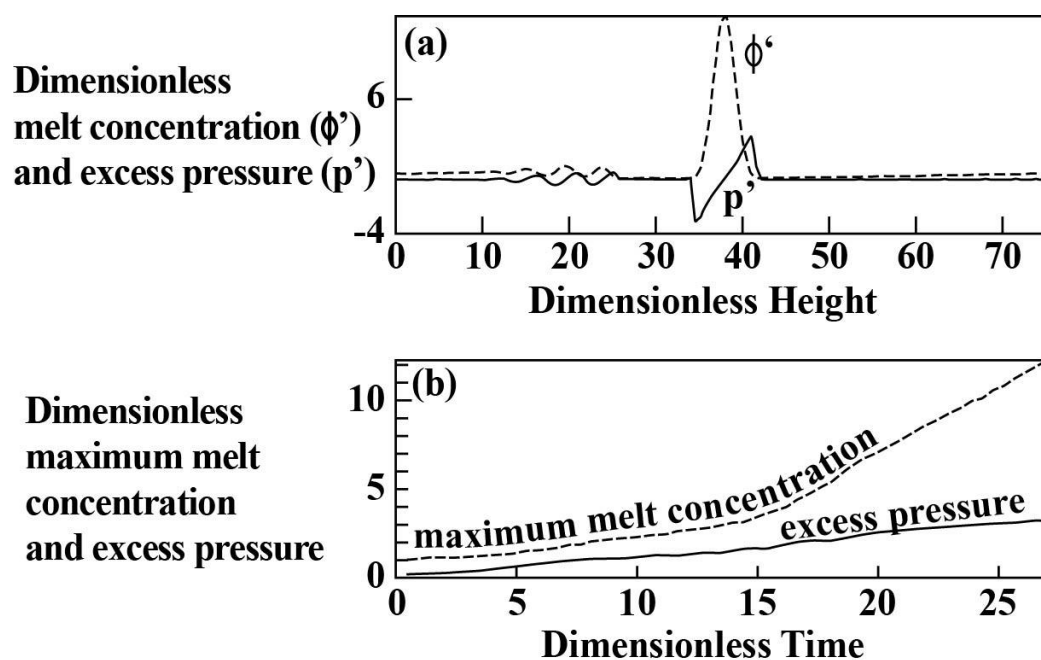


Figure 3.13. Obtained from Gregoire et al. 2006: (a) the dimensionless melt concentration (ϕ') by volume (dashed line), and the excess pressure p' vertical profile (continuous line) taken at time 27 along the left lateral face of the model of figure 3.12. (b) The time evolution of the maximum melt concentration (dashed line) and the excess pressure (continuous line) during the numerical experiment. It should be noted that the maximum pressure and melt concentration increase linearly and quadratically with time, respectively.

3.6.2 Application of propagating compaction waves and melt distribution inside cold diapirs below the TIP

Melt pockets in the upper wave after 0.2 Ma have the observed dimensions of the compaction pockets, i.e. ~90 km high and ~160 km long, and the correct distribution, i.e. some large pockets overlap with small ones (Fig. 3.12b). Nevertheless, the melt concentration inside these pockets remains low with a dimension value of $2\phi_{sc}$, i.e. 1.5 vol%. (we recall that production of volatile-rich melt above the MTZ represent 0.75 vol%). Because the size of the compaction pocket is ~ 100 km, it means that the interstitial melt contained in a 2D-domain of ~ 140 km size inside the root of the diapir eventually concentrates inside the compaction pocket. compaction pockets equally develop in two orthogonal horizontal directions. It means that up to $\sim 4\phi_{sc} = 3\text{vol}\%$, may concentrate inside the ellipsoid compaction pocket, originating from a 140 km-size volume included inside the root of the diapir. That melt concentration may be locally greater (actually, the maximal melt concentration predicted in pockets at time 20 is $8\phi_{sc}$, i.e. 6 %, Fig. 3.12c), but the mean value of 3 vol % likely is a maximum considering the limited melt volume contained inside the diapir.

The individual set of melt pockets of figure 3.12c displays a typical spatial distribution obtained from compaction experiments and from steady-state solitary wave solutions under freely percolating melt conditions (Rabinowicz *et al.*, 2001; Cai & Bercovici, 2016). Actually, the top wave displayed Fig. 3.12b can be assimilated to the first sill-like wave that initially formed at time $t'=0$ and at 8 GPa (~240 km, Fig. 3.12 a) and which thereafter rises during 2.5×10^5 yrs (time 10) by a height of ~100 km ($\sim 5L$, see above) to reach depth ~140 km. We can deduce that within 2.5×10^5 yrs, the mean vertical Darcy velocity of the melt is $100 \text{ km} / 2.5 \times 10^5 \text{ yrs} = 40 \text{ cm/yr}$, i.e. a velocity again similar to that of mantle convection. In contrast to the end of the numerical experiment (Fig. 3.12c) where the top wave individualizes, the different compaction pockets below the TIP cannot really individualize because they would require to

propagate vertically over several hundreds of km, which greatly exceed the ~40 km thickness of the overlying asthenosphere below the TIP lithosphere. This indicates that the “compaction pockets”, particularly those located beneath Central Iran, Lesser Caucasus and Central Alborz represent immature compaction pockets, e.g. far from their steady state.

This model may explain how the melt disseminated into a wet-cold diapir may concentrate from 410 km up to 120 km depth to form the low velocity elliptic structures observed in tomography sections. It represents an alternative to the model developed by Litasov et al. (2013) and then by Morra et al. (2015) where 1 km-size magmons form at the top of the low velocity layer, and thereafter aggregate to form 100 km-size structures. Actually, the difference between these two models and ours stands in the 4 orders of magnitude difference in the assumed effective viscosity of the partially molten mantle: in our study it equals $\sim 10^{20}$ Pa.s, while in Litasov et al. (2013) and Morra et al. (2015) it approaches $\sim 10^{16}$ Pa.s. A 10^{20} Pa.s viscosity for a wet cold mantle (a few 100 °C below the mantle adiabat) is realistic; an exponential melt-weakening factor proportional to $\exp(-\alpha\phi)$, with $20 < \alpha < 30$, has been experimentally constrained (Mei *et al.*, 2002). Since ϕ , the volume of kimberlite-like melt produced during hydrous melting, is $< 1\%$ (see below), partial melting likely decreases the mantle's viscosity by at most 30%. This means that a mantle with 1% of interstitial melt is unlikely to have a viscosity as low as 10^{16} Pa.s.

The model in figure 3.12 shows that the excess pressure at the top of the compaction pocket (just below the zone of obstruction due to precipitation of new mineral phases, i.e. richterite), ranges from 0.14 to 0.52 GPa ($1 \times p_{sc}$ to $3 \times p_{sc}$ in Fig. 3.13). Such an overpressure range likely leads to tensile or shear fracturing of the host mantle along with channelization of the melt through pipes. In the mantle metasomatism literature, such pipes are designated as dyke swarms by analogy with cratonic kimberlite dykes (Spera, 1987; Rubin, 1993; Grégoire *et al.*, 2006). Grégoire et al. (2006) modelled the generation of several km high, ~1 m thick self-

propagating melt-carrying cracks at the top of large compaction pockets, and which they associated to dyke swarms. More recent modelling taking into consideration the dynamic interaction between mantle convection, diapiric flow and melt percolation has been developed (Keller & Katz, 2016; Keller *et al.*, 2017). In particular, Keller *et al.* (2013) showed how diapirism combined with compaction may produce a stress field that reaches the elasto-plastic yield, thus producing either dyking or shear failure by which buoyant melt can be extracted upwards. We think that a similar mechanism drives melt extraction at the top of our melt-rich “Compaction pockets”. For sake of simplicity below we shall simply refer to this mechanism as “dyke swarms”.

3.6.3 How melts are extracted from ascending Compaction pockets from 8 GPa up to 4 GPa (~240 km up 120 km depths)

In the following, we consider the evolution of a compaction pocket that developed above the MTZ. We assume that: (i) the temperature at 410 km depth is 1370 °C, (ii) the temperature from 410 km up to 120 km depth linearly decreases by ~ 0.5 °C/km, (iii) $\phi_{sc} = 0.75\text{vol}\%$, (iv) $\delta\rho$ is ~ 700 kg/m³, (v) the crystallization of minerals occurs at a linear rate of 1 wt.% per 5 °C below the liquidus temperature (e.g. Kavanagh & Sparks, 2009) and (vi) the vapour saturated solidus between 5 GPa and 4 GPa linearly decreases from ~ 1300 to ~ 1200 °C (Fig. 3.11). Multi-stages melt extractions during the ascent of a compaction pocket are illustrated in schematic cartoons of figure 16. We start with a compaction pocket lying at a depth between 320 to 240 km (*stage 1*). Melt distribution and effective pressure is assumed to be similar to that found in the compaction pockets of figure 3.12b. Consequently, due to high effective pressure at the top of the compaction pocket, melt flows through pipes oriented in the direction of maximum compression ($\vec{\sigma}_1$). Thus, melt can pond in the lithosphere up to the sub-surface if the direction of maximum tension ($\vec{\sigma}_3$) through the lithosphere is horizontal.

According to the discussion in the previous section, the mean melt concentration inside a compaction pocket represents at most 3 vol% (2.4 wt.%). Considering that crystallization of 1 wt % melt produces an excess temperature of ~ 5 °C, 2.4 wt.% of melt produces 12.5 °C. Assuming that the compaction pocket moves up, the temperature decreases due to adiabatic decompression (0.5 °C/km) is compensated by the increase induced by crystallization (5 °C per 1 wt.% of melt), implying that the temperature of the compaction pocket remains near ~ 1300 °C, a value close to the stability field of potassium richterite and/or the solidus of carbonated peridotite between 8 and 6.5 GPa (Fig. 3.11b). Accordingly, if we assume that the local melt concentration is 3 vol% or 6 vol% (corresponding to the mean and the maximum melt concentrations in the compaction pocket, respectively), melt solidification is completed when the top of the compaction pocket moves up from ~ 240 km depth to $\sim 240-25 = \sim 215$ km or to $\sim 240-50 = \sim 190$ km, respectively.

At a depth shallower than 6.5 GPa (~ 195 km) the fertile hydrated and/or carbonated peridotite partially melts (due to the reaction of volatile- rich melt with the surrounding mantle). As soon as partial melting occurs in the compaction pocket, temperature drops below 1300 °C. Finally, partial melting stops when the temperature crosses the adiabat and melt concentration reaches the same value as the one in the compaction pocket at *stage 1*. When the top of the compaction pocket reaches a depth < 6.5 GPa, the effective pressure at its top likely is lower than at *stage 1*. This is due to the fact that at the ~ 6.5 GPa corresponding depth, there is no melt left in the compaction pocket, cutting any hydrodynamical connection between the overlying and underlying melts. Thus the melt concentration in the overlying part of the compaction pocket is significant. The effective pressure (p_{eff}) at the top of the compaction pocket roughly equals the weight of the overlying melt column:

$$p_{eff} = \sim \delta \rho g h, \quad (6)$$

where h represents the difference in depth between the top of the compaction pocket and the 6.5 GPa phase change. When $h = 30$ km (i.e. the top of the compaction pocket reaches 165 km), $p_{eff} = 210$ MPa, the lithostatic pressure is just greater than 5 GPa and the adiabatic temperature is 1260 °C. This elevated p_{eff} likely exceeds the medium's strength at the top of the compaction pocket, and leads to melt extraction by dyking or shear fracturing (*stage 2* Fig. 3.16).

Because of the adiabatic gradient, the temperature between 5 and 4 GPa drops from 1250 °C down to 1235 °C, which is respectively lower and higher (~ 35 °C) than the vapour saturated solidus at these two corresponding depths (Fig. 3.11). Such a temperature excess together with the absence of stable hydrous phases (Figs. 3.11b and c) leads to a maximum melting amount of 7 wt.% at 4 GPa (see above, assumption v). But then when the melt fraction inside the “compaction pockets” exceeds 5%, the effective viscosity of the mantle dramatically drops (Kelemen *et al.*, 1997). This leads to a major change in the mode of melt migration (Rabinowicz & Toplis, 2009). In particular, the compaction length decreases by 2 orders of magnitude and leads to the formation of pockets of deconsolidated mantle of sizes of a few km such as those predicted by Litasov *et. al* (2013).

At depths shallower than 4 GPa, a temperature of 1200°C corresponds to the stability field of phlogopite and magnesite (Fig. 3.11b). Henceforth, such metasomatized mantle tends to become melt-free and consequently strengthens, behaving then more elastic-brittle than viscous. Currently, the base of the lithosphere below Central Iran is located at 120 km depth, and accordingly it may reflect the limit between the melt-free and the partially molten metasomatized mantle (white square in Fig. 3.5). This means that the compaction pocket is also melt-free when it penetrates to a depth just shallower than 4 GPa. This property explains why the seismic velocity remains very slow compared to the normal lithosphere, and implies that lithosphere below Central Iran is metasomatized.

The few km-size pockets described above form between 5 and 4 GPa corresponding depths, leading to a dramatic concentration of melt there. The pressure p_{eff} at the top of the compaction pockets increases, reaches the medium's strength which then fails, thus leading to the last stage of melt extraction (*stage 3*, Fig. 3.16).

3.7 LINK BETWEEN VOLATILE-RICH MELT PERCOLATION INSIDE “ COMPACTION POCKETS” AND CONTINENTAL ALKALINE MAGMATISM IN THE TIP

3.7.1 Extraction of volatile-rich melt at 8 GPa and origin of group Ia lavas

Experimental results indicate that melts originated from ~10 to 6 GPa (i.e. ~300-180-km depth) may have geochemical characteristics close to those of lamproites or type II kimberlites (Ulmer & Sweeney, 2002; Mitchell, 2004; Novella & Frost, 2014). The mantle source of such deep-originated melts is supposed to be hydrated and/or carbonated (Brey *et al.*, 2008; Grassi *et al.*, 2012; Girnir *et al.*, 2011; Novella & Frost 2014; Ghosh *et al.*, 2014). For example Girnir *et al.* (2011)'s experimental results show that a primary kimberlite melt can be in equilibrium with garnet harzburgite assemblages at 8-6 GPa and variable volatile contents (i.e. ~15 wt.% CO₂ under anhydrous condition to 20 wt.% H₂O and low CO₂). Those conditions are similar to those of the first stage of our model, when the “harzburgite-like peridotite” inside compaction pockets is located at a depth greater than 8 GPa. However, in our case study, it appears that the trace element and isotopic features (high Sr isotopic ratios, high enrichment in Th, U, LILE and HFSE depletion) of group Ia lavas (Fig.3.10a) are related to the contamination of a mantle source by a crustal-like component or to a hydrated/carbonated metasomatised mantle source (Shafai Moghadam *et al.*, 2013; Prelević *et al.*, 2015). Moreover, the presence of

recycled slab-derived sediments within the MTZ has been indicated by many other studies (Grassi *et al.*, 2012; Rapp *et al.*, 2008; Kuritani *et al.*, 2013, Wang *et al.*, 2016). In figure 3.14a, MORB-normalized trace element plots of group Ia lavas are compared with the MTZ-derived, lamproitic melts (Gaussberg lamproites, Murphy *et al.*, 2002) and average continental crust (Hofmann, 1988). As we can see in this figure, REE concentrations of group Ia lavas nearly extend to the MTZ-derived lamproites, whereas LREE enrichment and HREE depletion of Gaussberg and group Ia lamproites relative to continental crust are higher and lower, respectively. Murphy *et al.* (2002) interpreted that it is unlikely such features represent crustal contaminations (in case of contamination, LREE's enrichment decrease). In addition, the positive Pb and negative Sr, Nb and Ta anomalies present in a MORB-normalized trace element diagram appear as nearly flat when normalized to GLOSS (Fig. 3.14b). In fact, the normalization to GLOSS values (Plank & Langmuir, 1998) removes the effect of inheritance concentrations of elements from continental crust (i.e. Pb) and processes linked to dehydration during subduction (i.e. Nb and Ta) (see Murphy *et al.*, 2002). In addition to the role of recycled sediments, the HFSE depletion of exotic lamproitic melts may indicate a link to a mantle source located at much greater depth, derived from an extremely depleted deep mantle (Murphy *et al.*, 2002; Prelević *et al.*, 2008). In fact, the HFSE contained in most melts worldwide may be linked to the presence of heterogeneous enriched and depleted lithologies sinking into the mantle, i.e. eclogite (i.e. a garnet-rich component) and harzburgite with enrichment and depletion in HFSE, respectively (e.g. McDonough, 1991; Niu & Hekinian, 1997). Thus, harzburgite as a reservoir plays a role to HFSE depletion in the source. Thus, those features may reflect directly the generation of the group Ia parental melts of a depleted mantle during the initiation of Compaction pockets at 240 km depth (Fig. 3.16c).

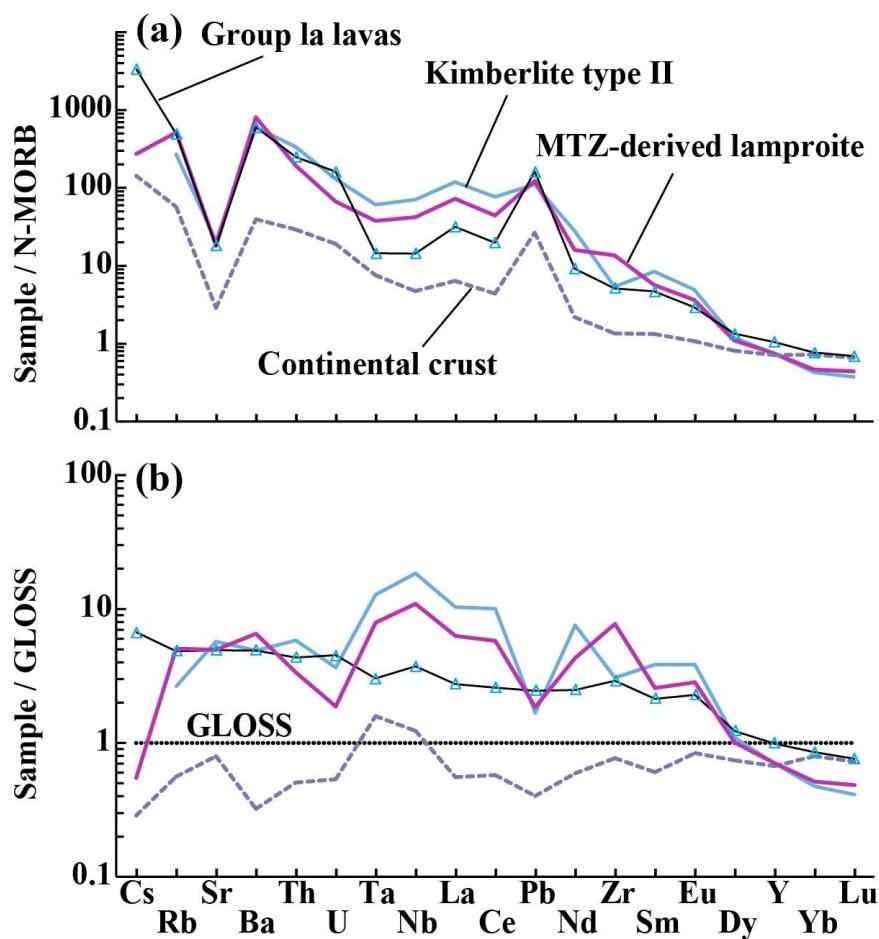


Figure 3.14. (a) N-MORB normalized (Sun & McDonough, 1989) and (b) GLOSS normalized (Plank & Langmuir, 1998) trace element concentration of average group Ia lavas. Compared with average kimberlite type II (Becker & Le Roex, 2006), the MTZ-derived lamproite (Murphy *et al.*, 2002) and continental crust (Hofmann, 1988).

Some studies (e.g. Waters, 1987; Grégoire *et al.*, 2003) showed that volatile-rich melts originated from deep-seated mantle sources could not only lead to the diversity of exotic lavas at the surface (e.g. kimberlite and lamproite), but also crystallize the MARID xenoliths (rocks consisting of mica-amphibole(K-richterite)-rutile-riopside) directly within the cratonic upper mantle. Thus, it is possible that dyke swarms triggered at pressures greater than 8 GPa may cross-cut the upper mantle and crystallize as cumulates within the cold lithosphere ($\sim 900^{\circ}\text{C}$) at pressures ranging between ~ 2 and 0.5 GPa. Regarding the TIP, particularly in Anatolia, NW Iran and the south of Lut block, cumulative xenoliths originated from different levels

(lithospheric mantle, lower and middle crusts) have been transported to the Earth's surface by multiple magmatic pulses (i.e. Eocene, Miocene and Quaternary; Semiz *et al.*, 2012; Saadat *et al.*, 2014; Prelević *et al.*, 2015; Khezerlou *et al.*, 2017). The isotopic compositions of those cumulates (i.e. $^{87}\text{Sr}/^{86}\text{Sr}$; 0.7068- 0.7095 and $^{143}\text{Nd}/^{144}\text{Nd}$; 0.5124- 0.5126, Khezerlou *et al.*, 2017) are similar to those of group Ia lavas. Moreover, these cumulate xenoliths mainly consist of phlogopite, amphibole, clinopyroxene, carbonate, and Fe-Ti oxides similar in composition to phenocrysts in the host lavas, supporting the idea that they share similar parental melts. Similarly to host lavas, it is suggested that the cumulative xenoliths issued from exotic volatile-rich melts originated from a deep mantle source (i.e. kamafugite or lamproite, Prelević *et al.*, 2015), which at shallower depths could indeed crystallize as cumulates (Fig. 3.16c).

3.7.2 The generation of OIB-like melt from 6.5 to 5 GPa and the origin of group IIa lavas

The precipitation of hydrated and carbonated phases metasomatizes the mantle, and low degrees of melting of fertile peridotite produces super chondritic Nb/Ta melts (e.g. Green, 1995, Ionov *et al.*, 1993). In terms of trace element contents and isotopic compositions, the group IIa lavas have a transient composition between OIB's and Type I kimberlites (Fig. 3.15a). Although, those lavas have the characteristics of OIB-like alkali basalts (super chondritic Nb/Ta), highly enriched in Sr, Ba, Th, U, and LREE, they differ from classical OIB by some elemental characteristics (e.g. higher Nb/Ta: 15.8-20.9: Zr/Hf :~40-50 than OIB's: 15.9 and 37.5-45, respectively, e.g. Pfäner *et al.*, 2007). Allen *et al.* (2013) and Mirnejad *et al.* (2010) proposed that the mantle source of these lavas is located at a depth greater than 120 km, and that it must contain a hydrated phase (e.g. richterite) or deep-seated metasomatized mantle by slab derived fluid/melt, respectively. It should be noted that although Allen *et al.* (2013) linked the origin of richterite in the source of the Kurdistan lavas to the occurrence of a previously

hydrated and relatively thick lithospheric mantle beneath the Zagros Suture, this scenario cannot apply to similar group IIa lavas occurring far away from the Zagros Suture (i.e. those from the Damavand volcano). Accordingly, the occurrence of some group IIa lavas near the borders of the Central Alborz and the Kurdistan compaction pockets (Fig. 3.3b) suggests that the origin of group IIa lavas would be better explained by the presence of compaction pockets than by the presence of a thick lithosphere beneath the suture zone.

It is well documented that mantle sources of a majority of alkali OIBs as well as those of Type I kimberlite are located at great depth and that such melts cannot be produced by the melting of volatile-free peridotites (e.g. Davis *et al.*, 2011; Sokol & Kruk, 2015). Therefore, their sources must additionally contain hydrated and/or carbonated phases or recycled oceanic and/or continental crust components (e.g. Willbold & Strack, 2006, Pilet *et al.*, 2008, Davis *et al.*, 2011, Sokol & Kruk, 2015). As mentioned before, due to the stability of K-richterite and alkali carbonates at great depth, the melts in equilibrium with such K-rich hydrated-carbonated peridotite should display a geochemical fingerprint reflecting the occurrence of such residual phases. Thus lavas with relatively high K₂O content (e.g. ~2- 5.8 wt.%), large negative Nb and Ta anomalies and high Rb/Ba ratio of the K-richterite (Wagner & Velde, 1986; Gregoire *et al.*, 2003) lead to the buffering of the melt composition around high Rb/Ba ratio and high K₂O and TiO₂ concentrations. Similarly, Allen *et al.* (2013), related such geochemical characteristics of the OIB like group IIa lavas to the presence richterite in the mantle source. In addition, Malik & Dasgupta (2014) demonstrated that high CO₂ contents in the bulk melt-rock (hybrid mantle) systems lead to silica undersaturation and to the formation of strongly alkaline OIB-like melts. They also point out a positive correlation between the CO₂ content of the reactive system and the increasing degree of silica undersaturation or/and alkalinity of the melt. The group IIa lavas not only have a higher alkalinity index than other

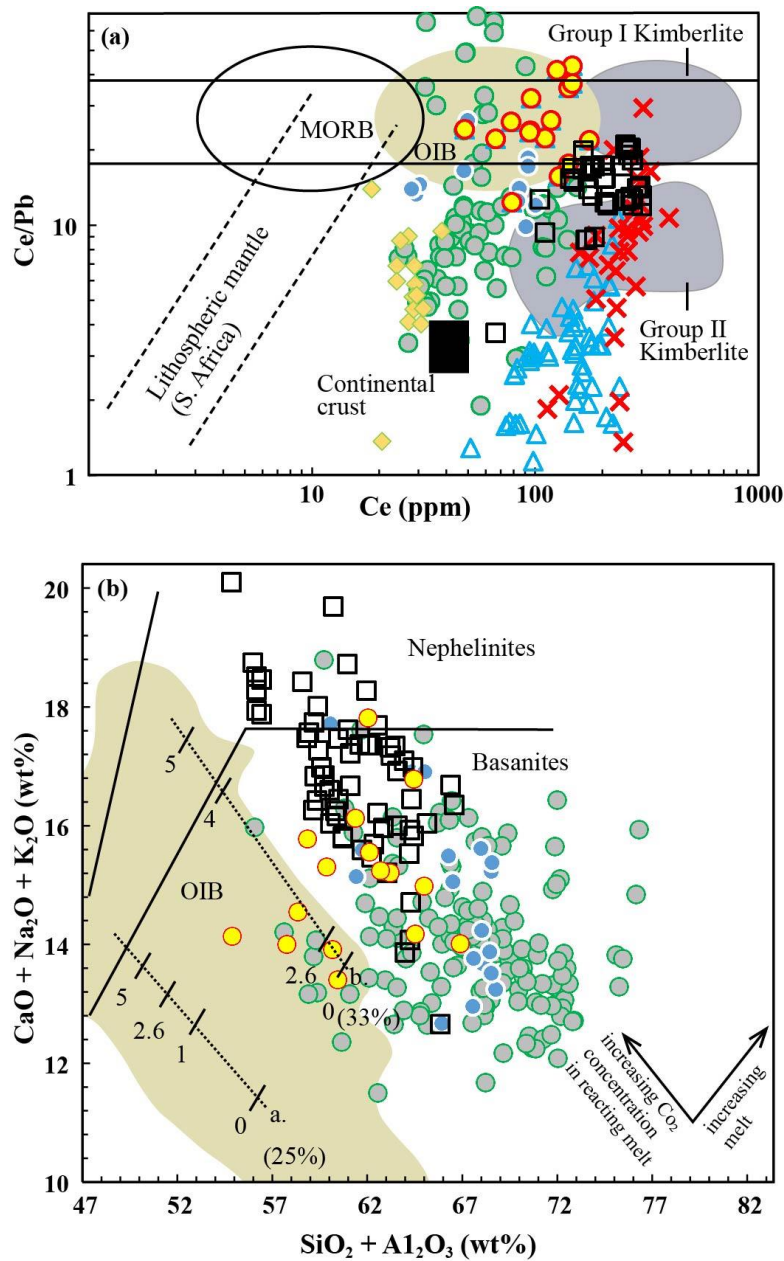


Figure 3.15. a) Ce/Pb versus Ce for classified lavas considered in this study. Symbols are same as in figure 3.8.b) Effect of Variable CO₂ on hybrid peridotite derived melt at 3 GPa and alkali or silica content of primary melts. The silica under-saturation and/or the alkalinity of melts increase with mantle hybridization by presence of higher CO₂ in the reacting melt. OIB field, trajectory of arrows and number next to them obtained from Malik & Dasgupta, 2014. In figure a, the data source for group I and II kimberlites are from Becker & Le Roex, 2006 and those for OIB, MORB after Zindler & Hart, 1986, and cratonic lithosphere and continental crust are from values given in the EarthRef data base and Rudnick & Gao, 2003, respectively.

OIB-like lavas (i.e. group IIb) (Fig. 3.15b) but also display a higher Zr/Hf ratio which may be evidence of a possible role of a carbonated metasomatism in their source (e.g. Dupuy

et al., 1992; Ionov *et al.*, 2002). Finally, we suggest that the group IIa parental melts originated at a depth corresponding to the destabilization of richterite (from 6.5 up to 5 GPa), and were extracted by a mechanism similar to the one mentioned in the modelling section.

3.7.3 The generation of OIB-like melt from 5 to 4 GPa and the origin of group IIb lavas

At the corresponding 4-5 GPa depth, partial melting of a hybrid mantle source containing recycled material is expected to be appropriate for the parental liquid of OIB (see Hirschmann *et al.*, 2003). The origin of the group IIb OIB-like alkali lavas, especially those erupted over Eastern of Iran, has been explained by the low degree of partial melting of a depleted and enriched heterogeneous mantle source (e.g. Kheirkhah *et al.*, 2015). These lavas show similar OIB like patterns (Nb-Ta enrichment, Sr-Nb isotopes) but lower K₂O and Rb/Sr contents than those of the group IIa lavas with presence of peculiar mineral phases in their source (i.e. richterite). However, none of the previously-mentioned hydrated and carbonated phases are stable at 4-5 GPa within the temperature range of *stage 3* (i.e. Fig 3.16 and modelling section). We therefore propose that parental melt of group IIb lavas originated from the partial melting of at the top of the compaction pocket at *stage 3*.

Accordingly, the few km thick deconsolidated mantle layer that settles along the 120 km depth (4 GPa) lithosphere-asthenosphere interface contains a hybrid volatile-rich melt. It is well documented that such melt is highly reactive when it percolates through a lithosphere, whether it has been previously metasomatized or not (Coltorti & Gregoire, 2008; Ackerman *et al.*, 2013; Grant *et al.*, 2014). Su *et al.* (2014) reported the occurrence of pyroxenite xenoliths in a group IIb lava from the North of the Lut block. These xenoliths provide valuable direct information on the composition of the lithospheric mantle (~40-70 km) beneath this region. The authors conclude that the lithosphere is non-cratonic and highly metasomatized. Moreover, they

observed spongy textures in some clinopyroxenes formed as a result of decompression melting due to an extensional tectonic regime. However, such textures can also result from the interaction and/or infiltration of alkali-rich silicated melt, kimberlitic-like melts, or low-density fluids through the continental lithosphere (e.g. Carpenter *et al.*, 2002; Bonadiman *et al.*, 2005; Shaw *et al.*, 2006).

3.7.4 Application of the model to explain the generation of the classified lavas

As discussed above, the extraction of melt at the top of the compaction pockets at *stages 1-3* may explain the origin of the melt of classified group 1a, IIa and IIb, respectively. This process in correlation with the horizontal orientation of maximum extension ($\vec{\sigma}_3$) presented in our tomography section, allows us to explain the group Ia in Central Anatolia and NW Iran, group IIa parallel to the Zagros Suture (Kurdistan lavas) and Alborz (e.g. Damavand volcano), and group IIb exposed in the East Anatolia, the Lesser Caucasus and the CEIM (Figs. 3.1 and 3.3b).

In as much as we believe in the model developed above, we cannot exclude the possibility that the lithosphere is delaminated and replaced by a compaction pocket (Fig. 3.16d) in some areas below the TIP. Recently, it has been pointed out that three conditions are required to delaminate the lithosphere (Francois *et al.*, 2014; Rigo *et al.*, 2015): (i) a negatively buoyant lithosphere, (ii) high deformation and stress rates of the lithosphere linked to regional tectonics and (iii) a viscous decoupling of the crust from the underlying lithospheric mantle. All the TIP is characterized by high deformation and stress rates (Fig. 3.3b see Masson *et al.*, 2014). Moreover, their crust is anomalously thick inferring that its base is either partially molten (700-800 °C) or has a low viscosity due to a temperature close to the solidus of the lower crust (~600 °C) (e.g. Sodoudi *et al.*, 2009; Özacar *et al.*, 2010; Mohammadi *et al.*, 2013; Skobeltsyn *et al.*, 2014; Bavali *et al.*, 2016; Motavalli *et al.*, 2016; Zabelina *et al.*, 2016).

3.7.4.1 Application of the model to the generation of the lavas shallower than 4 GPa

3.7.2.1.1 East Anatolia

In a contrasting view to the Central Iranian crust, in East Anatolia around the Suphan volcano, the high velocity anomaly at 100-200 km depth may be directly linked to a dripping of the East Anatolia lithosphere (Skobeltsyn *et al.*, 2014). Henceforth, we may hypothesize that mantle material currently present above this high velocity anomaly comes from the surrounding “Compaction pockets” (numbers 3 and 6- 11 in Fig. 3.3b). Based on the main geochemical features of Suphan lavas, it has been suggested that their parental magmas were generated by partial melting (0.7- 5 %) of a source consisting of various degree of mixing between asthenospheric and lithospheric mantle components (e.g. Özdemir *et al.*, 2014). In fact, this hybrid nature of the sources as well as the mildly alkaline to calc-alkaline affinity of those lavas could be simply explained by a “hybrid Compaction pocket material” located at lithospheric depth (Fig. 3.16d). This agrees with the more general model of Salters & Shimizu (1988) proposing that a shallow mantle reservoir, i.e. some specific areas of the continental lithospheric mantle, could also lead to geochemical characteristics similar to those observed in subduction-related magmatism (i.e. volcanic arcs). Because similar melts from the Kars plateau and South Armenia (lesser Caucasus) were extracted from the mantle to feed the Suphan volcano, it is normal that the lavas from the latter display similar calc-alkaline affinity as well as significant OIB-like geochemical patterns. In fact, all these regions represent “hybrid lithospheric depth-seated Compaction pocket material”. In addition, such component could explain the various isotopic ranges of depleted to enriched mantle sources mentioned for group IIb lavas.

3.7.2.1.2 The Lesser Caucasus and Central Zagros

It is important to note that tomographic maps of the crust down to 60 km depth across a large region enclosing the Lesser and Great Caucasus highlight the presence of low velocity conduits below each volcano. In between volcanic regions, the crust is thin and the lithosphere is extremely cold (e.g. Zabelina *et al.*, 2016) suggesting that the lithosphere located between volcanoes initiates a drip into the underlying mantle. Similar lithospheric dripping could be observed in the Bavali *et al.* (2016) tomography cross-section and connect the Sabalan and Sahand volcanoes. In the Central Zagros Suture, the same processes may be invoked, because the low seismic velocity anomaly occurs from 50 km (the base of the crust) down to 100 km (Alinaghi *et al.*, 2007) and lies above the compaction pocket 24 (Fig. 3.3b).

These observations are coherent with Pang *et al.* (2016)'s interpretation linking the source of the adakites from this region to the partial melting of the lower crust, whereas the alkaline lavas associated to those adakites (see Omrani *et al.*, 2008) may reflect the partial melting of a mantle source. Such complicated sources, corresponding to partial melting of heterogeneous mantle with/without a role of the lower crust, was also suggested for parental calc-alkaline melts, with or without adakitic affinity, of lavas from the Sahand and Sabalan volcanoes and the Lesser Caucasus (e.g. Ghalamghash *et al.*, 2016; Pang *et al.*, 2016).

3.7.2.1.3 The Cenozoic magmatism in the NW Iran, the Alborz and the CEIM.

Because the lithosphere constructed by the hybrid lithospheric depth-seated compaction pocket consists of large amounts of metasomatized mantle, it must be irreversibly buoyant. Regardless of the thermal conditions and of the thickness of the overlying crust, the mantle lithosphere is dynamically stable, i.e. it cannot be delaminated. As an example, a tomography profile and Bourger anomalies across Alborz indicate the presence of a low velocity anomaly

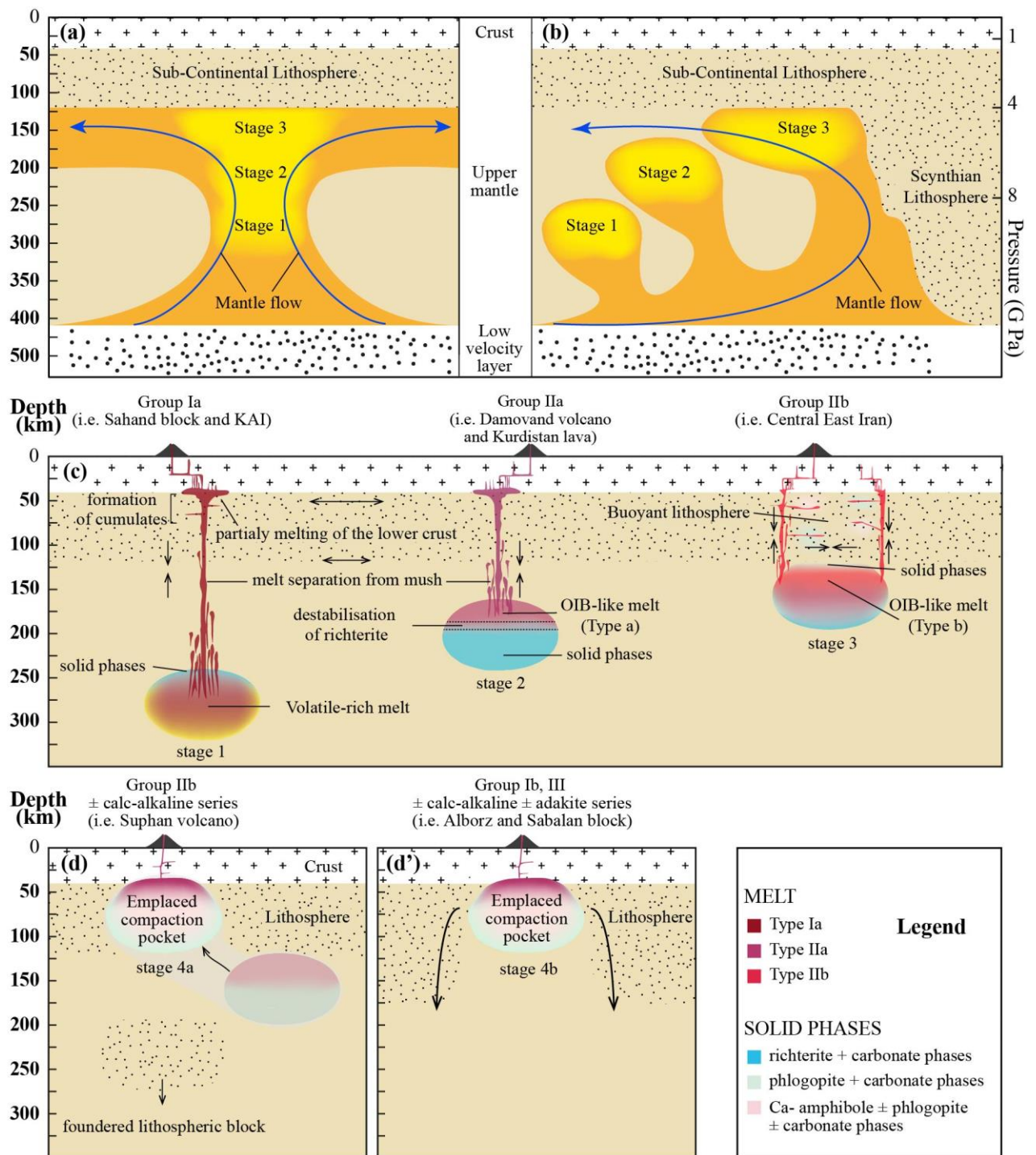


Figure 3.16. (a and b) Schematic cartoons proposed for the development and ascent evolution of compaction pockets from low velocity layer at the top of the MTZ: in case a, the upper mantle is motionless (Fig. 3.2); in case b, the low velocity layer and the overlying mantle moves North with the BMW (Fig. 3.4a). In the first case, sets of synchronous diapirs, with a 100 km horizontal size, develop, whereas in the last case, the northern diapirs develop before the southern ones. At 240 depth (8 GPa), a compaction pocket form inside the diapirs, because of precipitation of the interstitial volatile-rich melt as hydrated-carbonated phases (*stage 1*), when a compaction pocket rise at 195 km depth (6.5 GPa, *stage 2*), hydrated-carbonated phases destabilise and finally at shallower depth than 150 km (*stage 3*) Fig. 3.16 (continued) hydrous melting occur. During *stage 1*, 2 and 3 the accumulation

of melt inside the compaction pockets lead to the drastic increase of the effective pressure at their top, to the hydrofracturation of the surrounding mantle and the generation of the swarms of dykes. Consequently, it is deduced that during the first stage, the melt extracted from the compaction pockets has similar composition to those of the lamproitic melt in the KAI and Sahand block, such melt can form cumulate at shallower depths (Fig. c, *stage 1*). During the second stage, the extracted melt is similar to OIB-like melt (group IIa) of the Damavand Volcano and Kurdistan Lava. Finally, during stage 3, melting of fertile peridotite lead to form OIB-like melt (group IIb, Fig. c). When, a lithosphere block is foundering, the compaction pocket, located next to it, can flow inside the space liberated by the lithosphere detachment (Fig. d). Alternatively, the compaction pocket can induce a delamination of the overlying lithosphere, which results in its upward intrusion and of the dripping of the lithosphere on both sides of the compaction pockets (Fig. d'). Melts involved during both processes can lead to form melt with signature of calc-alkaline \pm adakitic affinity.

located from the base of the crust (~50 km depth) down to 100 km depth (e.g. Sodoudi *et al.*, 2009). Except for the Damavand volcano, the main magmatic activities in Alborz are restricted to Eocene time (i.e. Karaj formation), strongly suggesting that the low velocity anomaly relates to melt-free materials. Similarly in the Sabalan block, high K calc-alkaline to alkaline magmatism (group Ib) occurred mainly during Eocene to Oligo-Miocene (Babakhani *et al.*, 1990) and incidentally during late Cretaceous (e.g. Aghazadeh *et al.*, 2015). As we indicate in the geochemistry section, group Ib and Ic lavas, in term of alkalinity, are intermediate between ultrapotassic group Ia and OIB-like group II lavas, while their isotopic ratios are mainly close to those of the OIB-like lavas (Fig. 3.9). Previous studies proposed a phlogopite-bearing or an enriched mantle source located at lithospheric or asthenospheric depths, respectively (e.g. Pang *et al.*, 2013; Aghazadeh *et al.*, 2015). Many experimental studies focused on the melting of phlogopite-bearing peridotite, at relatively low pressure (from ~1 up to 1.5 GPa), and showed that the produced melts have intermediate to mafic silica saturated and oversaturated compositions (Hirschmann *et al.*, 1998, Conceicao & Green, 2004; Condamine & Médard, 2014). On the other hand, the most primary lavas of groups Ib and Ic are potassium-rich and silica-undersaturated. Melting experiments performed at higher pressure (i.e. 3GPa) indicated that around 1200-1250 °C the produced melt is foiditic to trachybasaltic in composition, silica

under-saturated, potassium rich (~ 6 wt.%) and has TiO₂ content similar to that of OIB-like melts (~ 2.5-3 wt.%) (Condamine *et al.*, 2016). The group Ic lavas display similar TiO₂ content (1.6- 3.8 wt.%) to that OIB melts, while the group Ib differs by its lower TiO₂ content (< 1.5 wt.%). However, if melting of the phlogopite-bearing peridotite occurred in the garnet-stability field and melts produced there eventually interacted with lithospheric shallow melts, the chemical compositions of Ib group may be explained. In addition, we suggest that the sources of group Ib lavas are also hybrid compaction pocket material located at lithospheric depths. In fact the TIP Eocene magmatism always displays a typical transient signature between high K calc-alkaline and alkaline signatures (“subduction-influenced” pattern) with a dominant tendency of calc-alkaline affinity for group III (i.e. the Alborz) to a dominant alkaline affinity for group Ib (i.e. the Sabalan block). As mentioned before, crystallization of HFSE bearing-minerals (e.g. amphibole and phlogopite) can lead to similar geochemical features to those observed for arc-derived lavas. However, those minerals could also form through reaction processes between fluids and/or alkali rich melts with the lithospheric upper mantle (see for example Sweeney & Ulmer, 1993; Coltorti *et al.*, 2004; Grant *et al.*, 2014). The last scenarios or combination of multi-extracted melts at lithospheric depth could likely explain the transient calc-alkaline and alkaline signature of group III and group Ib lavas.

Below the CEIM, the presence of a low velocity anomaly (Fig. 3.5) and the absence of a recent magmatic activity may indicate that the lithosphere is buoyant, melt-free and not able to delaminate. In addition, the crustal thickness and geothermal heat flow are normal (Motavalli *et al.*, 2016). These are good arguments to discard the hypothesis of delamination of the lithosphere, which explains why the top of the compaction pocket below CEIM is restricted to ~120 km depth. Such observations are also in agreement with the restriction of the main magmatic activity of the CEIM from Early to Late Cenozoic time.

3.8 CONCLUSION

There is a consensus to consider that the C-O-H carrying phases transported by subduction slabs play a major role in metasomatizing both the mantle wedge and the BMW. Because of the positive buoyancy of the hydrated and carbonated mantle in the MTZ, diapirs may develop and carry these elements into the overlying olivine stability field where, due to the incompatible behaviour of volatiles, melts produced by low degree of decompression melting of the mantle are enriched in volatiles. As these volatile-rich melts form a connected network at extremely low concentrations, a compaction process is quite instantaneously initiated and leads to the formation of melt-rich pockets. This can cause the low velocity areas imaged by seismic tomography and which we call compaction pockets by reference to their shape.

The model that we assemble here reproduces satisfactorily the formation of such compaction pockets $\sim 160 \times 80$ km in size, if we consider that mantle viscosity is not sensitive to low amounts of inter-granular melt (~ 1 % in volume) and if the volatile-rich melts themselves have a very low viscosity (allowing them to segregate easily from the matrix). In that framework, the development of compaction pockets requires an upward obstruction to melt percolation that would result from the precipitation of hydrated/carbonated phases. As long as the melt concentration in the compaction pockets remains low, the effective pressure is small. When melt concentration increases, the effective pressure rises at their top, controlled by the weight of the connected melt column integrated over the compaction pockets height. Because of the large size of these compaction pockets and the large density contrast between the volatile-rich melts and the surrounding mantle, this effective pressure reaches a few 100 MPa, triggering melt extraction by brittle processes such as dyking.

Such a model may apply to any problem associated to the migration of volatiles-rich melts, for instance in the mantle wedge below an active subduction. In the present study we apply it the migration of the volatile-rich melts through the upper mantle below the TIP. Based on large scale tomographic models and reflectors data, we propose that volatile-rich diapirs generate at the top of the MTZ in an area about 600 km wide located between the Great Caucasus and the Zagros-Bitlis Sutures. The analysis of tomographic models down to 300 km depth leads to the identification of various compaction pockets underlying the Turkish-Iranian lithosphere. According to our model, the development of the compaction pockets starts with the crystallization of richterite and carbonates between 8 and 6.5 GPa and at ~1300°C. Such conditions fix a strong constraint on mantle temperature below the TIP, i.e. ~200°C below the average adiabatic temperature below a normal oceanic plate. Such a condition is consistent with long living subduction processes (~200 Ma) which cool the upper mantle beneath the TIP and eventually lead to a sufficient temperature drop to maintain the continents thermal stability. Besides, according to our model, the geochemical fingerprints of group IIa lavas are evidence of the presence of residual hydrated/carbonated phases in the mantle source corresponding to high pressure and low temperature (e.g. richterite, 8-6 GPa and 1300 °C).

Finally, we show that the magmatic provinces from the TIP systematically occur where the lithosphere is in horizontal extension and above/or at the border of, a compaction pocket. Several geochemical characteristics indicate that their mantle sources are metasomatised. In addition, part of the classified lavas are subduction influenced, and others have an OIB like chemical signature. The distribution of these lavas as well as those of the compaction pockets indicate that this variety of magmatic mantle sources is consistent with the development of dykes swarms during the ascent of the compaction pockets. We conclude that “subduction influenced” pattern of exotic ultrapotassic melts in group Ia lavas indicates the presence of a deep-seated mantle source (related to recycled sediments). In contrast, the sodic alkaline lavas

group IIa and IIb with “OIB-like” patterns represent extracted melts via two series of dykes that developed during partial melting at ~195 km and at ~ 135 km depth, respectively. The combination of geophysical observations and lavas geochemical signatures implies that the emplacement of compaction pockets at shallow lithospheric depths and their interaction with the crust, may also generate alkaline melts with “subduction influenced” patterns and or calc-alkaline affinity (e.g. adakites). This is coherent with the main geochemical features of the most voluminous lavas (group Ib and III) from the TIP.

Chapter IV: Conclusions & perspectives

4.1 CONCLUSION

The results of our study highlight the importance of the MTZ in which a large volume of recycled materials accumulate during the various phases of subduction and delamination that affected the Turkish-Iranian Plateau (TIP). This study, based on a multidisciplinary approach (petrology-geochemistry-geology-geophysics-modeling-experimentation), leads to a model accounting for the diversity of the TIP magmatism. A commonly accepted idea is that, in the seismic tomographic models the red zones (low velocity) represent hot zones. Our study evidences that beneath the lithosphere ~100 km size elliptic structures exhibit a velocity contrast, up to 8%, with the ambient mantle. These structures, which we call compaction pockets, are specific to the TIP. In our work, we provide strong arguments to show that compaction pockets result from the accumulation of a few percent of volatile-rich melts, which according to the pressure and temperature conditions, may lead to the precipitation of hydrous-carbonated minerals (richterite, phlogopite, Ca-amphibole, magnesite and dolomite). The presence of these minerals and/or melts in the compaction pockets are the only valuable explanation to their huge seismic velocity contrast with the surrounding mantle. Besides, the crystallization of these minerals requires a temperature 200°C lower than that of the adiabat. These compaction pockets gradually rise and finally at three critical depths (250 km, 195 km and 135 km) generate swarms of dykes, which may be the sources of the different phases of magmatic activities observed at the TIP during the last 80 Ma.

Clearly, the fact that the mantle is abnormally cold beneath continents bordered by subduction zones, which have operated during an orogeny is unavoidable. This idea was defended by Rabinowicz et al. (1980), but was subsequently abandoned because this model assumed that most of the material transported by the subduction plates stores in the MTZ.

During almost forty years the dominant paradigm has been that subduction plates go directly into the lower mantle. Thanks to seismic tomography, we know today that this idea is wrong in at least 80% of cases, especially around East Asia and beneath the west coast of the USA. This results from the following individual or combined effects: (i) the spinel-perovskite endothermic phase change, (ii) the depletion of the mantle below the crust of the subducting slab, (iii) the inversion of the density contrast of eclogite with the surrounding mantle across the spinel-perovskite transition and (iv) finally, the collision of a lower mantle plume with a MTZ cold horizon essentially due to the ponding of subducted oceanic slabs and/or delaminated fragments of continental lithosphere. Actually, all these effects apply below the TIP and are evidenced by the particular cold MTZ horizon occurring below the compaction pockets. We thus propose that, below the TIP, the mantle flow remains confined within the upper mantle. Consequently, during at least the Cimmerian orogeny (~200 Ma), the various lithospheric fragments ponded in the MTZ may continuously cool the upper mantle by about 200°C. In the MTZ, the differentiation of the various lithospheric block and the formation of harzburgitic horizons enriched in CO₂ and H₂O floating at the top of the MTZ take several 10 Ma (Motoki *et al.*, 2015). Besides, the development of diapirs enriched in CO₂ and H₂O should take also about 10 Ma to: (i) separate from the MTZ; (ii) cross the asthenosphere, and (iii) collide with the base of the sub-continental lithosphere (Houseman *et al.*, 1997). Consequently, the development of compaction pockets, their transport and their collision with the sub-continental lithosphere are only possible when the orogenic system is at a pivotal period during which the differentiation of the subducted materials makes the upper part of the MTZ diapirically unstable.

Below the TIP, the melt from the compaction pockets reach the surface through three different paths. First, when the compaction pocket lies below a ~100-120 km thick lithosphere, horizontally stretched on both sides orthogonal to a major fault or suture (e.g. Central Anatolia see Fig 3.2, and Caucasus Fig.3.4, respectively), a narrow vertical conduit (≤ 100 km at the base

of the lithosphere and < 40 km wide at the base of the crust) is initiated, and brings melts from the compaction pocket up to the surface. In these regions, the resulting lava flows and volcanoes mainly consist of asthenosphere derived-melts, OIB-type II. Eventually, between two paralleled vertical melt conduits, this process favours the dripping of the overlying lithosphere (e.g. Caucasus Fig 3.4). When the dripping is completed, space is released and the compaction pocket could rise up to the Moho. Then, a high topography is generated in relationship with both the delamination of the lithosphere and the intrusion of the low-density compaction pocket, (e.g. Central Zagros). Finally, those processes lead to mantle derived-melts accumulation at the base of the crust coexisting with lower crustal-derived melts (adakites). The case of Sabalan may be linked to the one of Central Zagros. Tomographic data indicates that the crust and lithosphere is there anomalously slow. Meanwhile, there is no evidence for a compaction pocket lying below the Sabalan lithosphere (Fig 3.3b). Actually, the nearest compaction pocket lies ~200 km to the South-East below the Sahand block. The main magmatic activity of the Sabalan block is restricted to the Eocene but the Plio-Quaternary Sabalan volcano. It is striking to note that the the magmatism in both Sabalan and Sahand blocks are similar: they have a wide range in composition with alkaline, calc-alkaline and adakite affinities. Except for alkaline magmatism, linked to melt extracted when the compaction pocket is located below the lithosphere, we suggest that the calc-alkaline magmatism is linked to melts produced when the compaction pocket intrudes the lithosphere. Finally, the latter could react (mixing) with crust-derived melts leading to the adakite signatures observed in both calc-alkaline and alkaline rocks.

The second type of path for the migration of the metasomatic melts occurs in the Alborz. Unlike previous cases, the stress field is there highly compressive and the crust is particularly thick (55 km). It implies that the temperature at the Moho reaches 800°C, a value high enough for the lower crust to be plastic (Motavalli *et al.*, 2016). Accordingly, all the conditions required for the delamination of the lithosphere are met. Below the Damavand volcano, due to the

proximity of sub-lithospheric compaction pockets to the North-West and to the South-East (compaction pockets number 14-15-16, Fig 3.3b), melt extracted from these compaction pockets may flow and then pond below the crust. Finally, the relative high amplitude of the extensional stress on the horizontal direction at the border of the compaction pocket (number 14) implies that the $(\vec{\sigma}_1, \vec{\sigma}_2)$ plane is vertical there and thus that the melt accumulated below the crust may directly reach the surface. The young magmatism from the Damavand volcano mainly consists in mantle-derived melts, OIB-type I. Interestingly there is no adakite signature. The joint section going from Western part of Alborz to the Zagros Suture clearly shows that the Arabian plate underthrust the Iranian plateau along the Main Zagros Suture (Motavalli *et al.*, 2011). This is consistent with the fact that the lithosphere below Alborz delaminates from North to South towards the Zagros. This is an alternative to the model proposed by Francois *et al.* (2015). The latter develop the concept of the delamination of the Iranian plateau from the South to the North and resulting from the crustal thickening related to the Arabian-Iranian continental collision along the Zagros Suture. It should be noted that the magmatism of western Alborz is strictly Eocene in age (e.g. Karaj formation). The Southwards migration of the compaction pockets (~200 km) from Sabalan to Sahand, considered above, may also apply to the Kurdistan compaction pocket (number 13, Fig. 3.3b). Accordingly, it is likely that, during Eocene, the Kurdistan compaction pocket was very close to Alborz. It justifies that melt provided by the Kurdistan compaction pocket may have pond inside the lower part of the thick crust of Alborz or even inside the asthenosphere replacing the lithosphere after delamination. We note that the volcanism of West Alborz has heterogeneous compositions, mainly calc-alkaline with less alkaline asthenosphere-derived melts. Therefore, it represents heterogeneous mantle sources emplaced at normal lithosphere depths (e.g. solidus of amphibole rich pyrolite plus 5 % dolomite at 2 GPa is 1100 °C; Wallace & Green, 1988). That indicate that the ponding of melt effectively occurred inside the asthenosphere, i.e. several km below the Moho.

In East Anatolia, the path that allows melt to reach the surface strongly differs from that of the other studied regions. Actually, the occurrence of a several hundred km wide high velocity anomaly lying between 100 to 200 km depth leads many authors to state that the lithosphere is delaminated. The delamination is interpreted as the results of the collision between Arabian and Eurasian plates (Keskin, 2005), or simply, as suggested in the present study, by the fact that (i) the crust is anomalously thick and ii) the lithosphere is strongly stretched on the NW-SE direction. Whatever the cause, the delamination is the only reasonable explanation for the high topography of East Anatolia. Besides, low extension NW-SE “en-echelon” faults characterise the region. The main volcanoes seem to be associated to the “en-echelon” faults. From these observations, we may deduce that melts of the >120 km-deep compaction pockets, which surrounds the delaminated zone, flows below the crust and eventually reach the surface forming the various volcanoes scattered through the region. This may explain why the melts mainly have asthenosphere derived-melt sources (OIB-type II).

We observed that, two compaction pockets which underlies the Central Iran lithosphere are not associated with volcanism. This results from the fact that the Arabian plate simultaneously (i) horizontally compress and (ii) vertically stretches the Iranian lithosphere ($\vec{\sigma}_1$ is horizontal and $\vec{\sigma}_3$ is vertically oriented). Both features imply that the melt along the lithosphere-asthenosphere boundary ponds forming sills. This observation is very important because it suggests that sub-lithospheric compaction pockets compressed during collision of two plates may eventually underplate and solidify. Finally, when both systems cool, the lithosphere may have a ~200 km thickness and be cold and buoyant. Such structure may be similar to that associated to cratons.

Are other examples on Earth where this succession of events is still active? It is possible that below the Basin and Range (West coast of USA), Massif Central (France) or Eifel (Germany) some hydrated diapirs detach from the MTZ. Future work may lead to decipher new

opportunities to observe the emplacement of such diapirs. Sincerely, the probability to find new locations where such successions of events and features occur is low. Meanwhile, we believe that there are many regions where the collisions of the compaction pocket with the lithosphere happened long time ago. Therefore, the lithospheric fingerprints of compaction pockets emplaced during old orogeny/s may be still accessible. For instance, the Pan-African lithosphere below the Hoggar has been destabilized after the Alpine orogeny (Fourel *et al.*, 2013; Milelli *et al.*, 2012). Actually, this destabilisation triggered an active alkaline magmatism. In the future, we want to show that this volcanism may result from the destabilisation of the 200 km thick lithosphere resulting from the subcontinental solidification of a compaction pocket encased during the Pan African orogeny. Actually, many authors suggest that there is a mantle plume below the Hoggar. Such explanation is not realistic, because the tomographic models show that the plume is evanescent at a depth greater than 300 km (Begg *et al.*, 2009).

Our work therefore introduces a new concept: a low velocity structure occurring within the mantle is not necessarily related to a hot convective plume. More generally, it should now be admitted that seismic tomography gives a picture of the chemical heterogeneity of the mantle in addition to its thermal structure. We believe that we are on the verge of a revolution in understanding the role of the mantle petrology, which results from the coupled study of convection and chemical differentiation. Our model of magmatism originating from an "anomalously cold" upper mantle may be an alternative hypothesis to a magmatism coming from a warm (or "normal" sub-oceanic zones, subduction zones, mantle plumes, etc.).

We demonstrate that an anomalously cold upper mantle favour the stability of hydrated and carbonated phases down to high pressure (e.g. 8-6.5 GPa at ~1300 °C). Accordingly, in this cold mantle environment, three critical depths (e.g. 240 km, 195 km, and 135 km) correspond to the stability limits of hydrated/carbonated phases. In fact, at these three critical depths, the mineral precipitation at the top of the compaction pockets leads to a dramatic increase of the

effective pressure and to the melt extraction via dyke swarms. We classify the alkaline lavas into three groups (I, II and III). The geochemical patterns of group I and II are linked to mantle sources located in the asthenosphere. The geochemical characteristics of those lavas require metasomatized mantle similar to those of the compaction pockets. For example, group Ia lavas, represent the most extreme exotic melt of the TIP. They are ultrapotassic, characterized by low $^{143}\text{Nd}/^{144}\text{Nd}$, and varied $^{87}\text{Sr}/^{86}\text{Sr}$, which resemble that of lamproites. Generally, the origin of exotic lamproitic like melts is linked to an extremely depleted mantle with a contribution of continental like components. At ~240 km to 195 km depth inside a compaction pocket, a lamproite like melt in equilibrium with harzburgite-like (depleted) mantle is produced which likely represents Group Ia lavas. Eventually, when the top of compaction pocket crosses the stability field of those hydrated and carbonated phases (i.e. shallower than 195 km depth), the partial melting of an enriched richterite-carbonate bearing mantle produces a melt in equilibrium with those minerals as a residual source. The geochemical patterns of OIB-type lavas (IIa) corresponds to this source. When the top of the compaction pocket arrives at $\leq \sim 155$ km depth, non hydrated-carbonated phases are stable and at this stage the melts results from partial melting of the mantle enriched by volatiles (H_2O and CO_2) and correspond to OIB type IIb lavas. At ~135 km, phlogopite + carbonate form and the interstitial melts are consumed. Finally, at shallow depth when the hydrated phases, i.e. phlogopite or amphibole, partially melt, the melts have similar compositions than asthenosphere derived alkaline potassic (group Ic) lavas or shallow lithospheric depth calc-alkaline (group III) lavas, respectively. In the chapter 3, we show that the characteristics of the alkaline melts of the TIP is consistent with this classification.

In the TIP, the study of the origin of the alkaline rocks is mainly based on whole rock geochemistry, whereas less attention is paid to early-crystallized minerals. In chapter 2, we not only focused on whole rocks chemistry, but also we detail the mineral chemistry to see how

magmatic history is recorded by complex zoning. In the Salavat Range, upper Eocene alkaline rocks out crops as lavas (HM- and LM-lavas) or intrusions and more rarely as calc-alkaline lavas (Ps-rocks). HM and LM-lavas consist of clinopyroxene as macro crystals with complex zoning. Based on physico-chemical properties, the zoning patterns of clinopyroxenes divide into type I, II, III and IV. The main parameter used to classify patterns is whether they included a colorless zone (high Mg#), i.e. Type I and II, and or a green colored zone (low Mg#), i.e. type III, in the core or rim of the crystal. Whereas in Type IV the colorless zone is absent. Moreover, the trace element concentrations of the colorless and green zones are in equilibrium with the depleted and enriched melts, respectively. The simple correlation of the modal abundance of the crystal with colorless zones has a direct impact on the bulk rock geochemistry. Lavas with colorless zones: (i) are ultrapotassic ii) are depleted in term of trace elements iii) have low $^{143}\text{Nd}/^{144}\text{Nd}$ (i.e. types I and II), whereas lavas lacking colorless zones i) are sodic ii) are enriched in term of trace elements iii) high $^{143}\text{Nd}/^{144}\text{Nd}$ (i.e. types III and IV). Trace element patterns of the melt in equilibrium with green colored zones (types III and IV) are similar to those of the pillow lavas (with absence of colorless zone, i.e. of type IV) and also are similar to those of the OIB -type lavas (IIB) of the plateau. Whereas lavas with high mode of colorless zones have similar trace element patterns to those of the cumulative xenoliths of the TIP. Interestingly, the cumulative xenoliths frequently occurring in the group Ia lavas from the TIP are interpreted as high pressure crystalized ultrapotassic melts (e.g. lamproite or kamafugite) near the Moho or even deeper. Moreover, the HM and LM-lavas with green colored (types III and IV) or colorless zones (types I and II) have bulk rocks isotopic ratios of OIB-type (group IIB) and ultrapotassic-type (group Ia), respectively.

The simultaneous occurrence of colorless and green zones in clinopyroxenes from the rocks from the Salavat Range indicate the contact of a group Ia melt mush with group IIB melt while ascending up to the surface. According to our model the swarm of stage I dykes form

while the top of the compaction pocket reaches a depth of 250 km, while type IIb ones develop when the compaction pocket eventually collides the lithosphere, i.e. when stage III dykes develop. According to our compaction model, the time interval separating the development of stage I and stage III dyke swarms is of about 0.3 Ma: i.e. dykes of type I must have ponded in a hot horizon, at most 0.3 Ma before the triggering of type III dykes. In order to prevent the complete crystallization of type Ia melts, the temperature in the ponding horizon must be greater than about 1000°C (e.g. Eggler & Wendlandt, 1979; Eggler, 1989). Around the Sabaland and Sahan regions: (i) the crust is ~40 km to 55 km thick, (ii) the Moho temperature ranges between 700°C and 800°C and (iii) the lithosphere is less than 120 km thick, i.e. this last condition implies that the temperature gradient through the whole lithosphere exceeds 10°C/km (Motavalli *et al.*, 2016). Therefore, the ponding horizon may stand at a depth of about 70 km: i.e. it may lie close to the spinel-garnet interface. Assuming that, at the time of formation of the stage I dyke swarms, the overlying lithosphere was not tectonically stressed, the density jump at the spinel-garnet interface may by itself lead to a vertical stretching of the lithosphere at that depth ($\vec{\sigma}_3$ is vertically oriented) and thus also to the ponding of the type Ia melts (Rigo *et al.*, 2015). Finally, ~0.3 Ma later, when the compaction pocket collided the overlying lithosphere, the vertical uplift induced by that compaction pockets led to the rotation of $\vec{\sigma}_3$ to the horizontal. This may explain that dykes transporting stage III (type IIb) melts quite instantaneously mix with and bring close to the surface, partly crystallized patches of stage I melts ponded and slowly partly crystallized, 0.3 Ma years earlier at about 70 km depth. Finally, in the particular case where the lower part of the crust was locally partially molten, a mixing of the crustal melt with the mantle-derived melts, transported by the stage III dyke, may explain the formation of the adakites found in the Salavat range, i.e. hornblende andesites.

BIBLIOGRAPHY

- Ackerman, L., Špaček, P., Magna, T., Ulrych, J., Svojtka, M., Hegner, E. & Balogh, K. (2013). Alkaline and carbonate-rich melt metasomatism and melting of subcontinental lithospheric mantle: evidence from mantle xenoliths, NE Bavaria, Bohemian Massif. *Journal of Petrology* **54**, 2597-2633.
- Adamia, S., Zakariadze, G., Chkhotua, T., Sadradze, N., Tsereteli, N., Chabukiani, A. & Gventsdze, A. (2011). Geology of the Caucasus: a review. *Turkish Journal of Earth Sciences* **20**, 489-544.
- Adamia, S.A., Lordkipanidze, M.B. & Zakariadze, G.S. (1977). Evolution of an active continental margin as exemplified by the Alpine history of the Caucasus: *Tectonophysics* **40**, 183-199.
- Adiyaman, Ö., Chorowicz, J., Arnaud, O.N., Gündoğdu, M.N. & Gourgaud, A. (2001). Late Cenozoic tectonics and volcanism along the North Anatolian Fault: new structural and geochemical data. *Tectonophysics* **338**, 135-165.
- Aftabi, A. & Atapour, H. (2000). Regional Aspects of Shoshonitic Volcanism in Iran, *Episodes* **23**, 119-125.
- Agard, P., Omrani, J., Jolivet, L. & Mouthereau, F. (2005). Convergence history across Zagros (Iran): constraints from collisional and earlier deformation. *International Journal of Earth Sciences* **94**, 401-419.
- Agard, P., Omrani, J., Jolivet, L., Whitechurch, H., Vrielynck, B., Spakman, W. & Wortel, R. (2011). Zagros orogeny: a subduction-dominated process. *Geological Magazine* **148**, 692-725.
- Aghanabati, A. (1986). Geological map of the Middle East. *Geological Survey of Iran*.
- Aghazadeh, M., Castro, A., Omran, N. R., Emami, M. H., Moinvaziri, H. & Badrzadeh, Z. (2010). The gabbro (shoshonitic)-monzonite-granodiorite association of Khankandi pluton, Alborz Mountains, NW Iran. *Journal of Asian Earth Sciences* **38**, 199-219.
- Aghazadeh, M., Prelević, D., Badrzadeh, Z., Braschi, E., van den Bogaard, P. & Conticelli, S. (2015). Geochemistry, Sr-Nd-Pb isotopes and geochronology of amphibole- and mica-bearing lamprophyres in northwestern Iran: Implications for mantle wedge heterogeneity in a palaeo-subduction zone. *Lithos* **216**, 352-369.
- Ahmadian, J., Sarjoughian, F., Lentz, D., Esna-ashari, A., Murata, M. & Ozawa, H. (2016). Eocene K-rich adakitic rocks in the Central Iran: Implications for evaluating its Cu - Au - Mo metallogenic potential. *Ore Geology Reviews* **72**, 323-342.

- Ahmadzadeh, G., Jahangiri, A., Lentz, D. & Mojtahedi, M. (2010). Petrogenesis of Plio-Quaternary post-collisional ultrapotassic volcanism in NW of Marand, NW Iran. *Journal of Asian Earth Sciences* **39**, 37-50.
- Ajirlu, M. S. & Moazzen, M. (2014). Role of the Allahyarlu ophiolite in the tectonic evolution of NW Iran and adjacent areas (Late Carboniferous—Recent). *Central European Geology* **57**, 363-383.
- Akinin, V. V., Sobolev, A. V., Ntaflou, T. & Richter, W. (2005). Clinopyroxene megacrysts from Enmelen melanephelinitic volcanoes (Chukchi Peninsula, Russia): application to composition and evolution of mantle melts. *Contributions to Mineralogy and Petrology* **150**, 85-101.
- Aktuğ, B., Parmaksız, E., Kurt, M., Lenk, O., Kılıçoğlu, A., Gürdal, M. A. & Özdemir, S. (2013). Deformation of Central Anatolia: GPS implications. *Journal of Geodynamics* **67**, 78-96.
- Alavi, M. (1994). Tectonics of Zagros Orogenic belt of Iran, new data and interpretation. *Tectonophysics* **229**, 211-238.
- Alberti, A. A., Comin-Chiaramonti, P., Di Battistini, G., Nicoletti, M., Petrucciani, C. & Sinigoi, S. (1976). Geochronology of the Eastern Azerbaijan volcanic plateau (North-west Iran). *Rend. Soc. Ital. Mineral. Petrol* **32**, 579-589.
- Alberti, A. A., Comin-Chiaramonti, P., Sinigoi, S., Nicoletti, M. & Petrucciani, C. (1980). Neogene and Quaternary volcanism in Eastern Azerbaijan (Iran): some K-Ar age determinations and geodynamic implications. *Geologische Rundschau* **69**, 216-225.
- Alinaghi, A., Koulakov, I. & Thybo, H. (2007). Seismic tomographic imaging of P - and S - waves velocity perturbations in the upper mantle beneath Iran, *Geophysical Journal International* **169**, 1089-1102.
- Allen, M. B., Kheirkhah, M., Neill, I., Emami, M. H. & McLeod, C. L. (2013). Generation of arc and within-plate chemical signatures in collision zone magmatism: Quaternary lavas from Kurdistan Province, Iran. *Journal of Petrology* **54**, 887-911.
- Alonso-Perez, R., Müntener, O. & Ulmer, P. (2009). Igneous garnet and amphibole fractionation in the roots of island arcs: experimental constraints on andesitic liquids. *Contributions to Mineralogy and Petrology* **157**, 541.
- Amidi, S.M., Emami, M.H. & Michel, R. (1984). Alkaline character of Eocene volcanism in the middle part of Iran and its geodynamic situation. *Geologische Rundschau* **73**, 917-932.
- Anderson, D. L. (2006). Speculations on the nature and cause of mantle heterogeneity. *Tectonophysics* **416**, 7-22.

- Arjmandzadeh, R., Karimpour, M. H., Mazaheri, S. A., Santos, J. F., Medina, J. M. & Homam, S. M. (2011). Two-sided asymmetric subduction; implications for tectonomagmatic and metallogenic evolution of the Lut Block, eastern Iran. *Journal of Asian Earth Sciences* **41**, 283-296.
- Ashrafi, N. (2009). Mineralogy, petrology, and geochemistry of foid-syenites of East Azarbaijan, NW Iran. *Ph.D. Thesis, Geology Department, University of Tabriz, Iran, 190p.*
- Ashrafi, N., Jahangiri, A. and Haseb, N. (2014). Investigation on the chemistry of amphibole and clinopyroxene in alkaline intrusive bodies of Bozghush, Kaleibar and Razgah, NW Iran. *Iranian Journal. Crystal. Miner* **22**, 381–392.
- Asiabanha, A. & Foden, J. (2012). Post-collisional transition from an extensional volcano-sedimentary basin to a continental arc in the Alborz Ranges, N-Iran. *Lithos* **148**, 98-111.
- Austermann, J. & Iaffaldano, G. (2013). The role of the Zagros orogeny in slowing down Arabia-Eurasia convergence since ~ 5 Ma, 32(Ma), *Tectonics* **32**; 351-363.
- Austermann, J. & Iaffaldano, G. (2013). The role of the Zagros orogeny in slowing down Arabia-Eurasia convergence since~ 5 Ma. *Tectonics* **32**, 351-363.
- Avanzinelli, R., Lustrino, M., Mattei, M., Melluso, L. & Conticelli, S. (2009). Potassic and ultrapotassic magmatism in the circum-Tyrrhenian region: significance of carbonated pelitic vs. pelitic sediment recycling at destructive plate margins. *Lithos* **113**, 213-227.
- Aydin, F., Karsli, O. & Chen, B. (2008). Petrogenesis of the Neogene alkaline volcanics with implications for post-collisional lithospheric thinning of the Eastern Pontides, NE Turkey. *Lithos* **104**, 249-266.
- Aydin, F., Schmitt, A. K., Siebel, W., Sönmez, M., Ersoy, Y., Lermi, A. & Duncan, R. (2014). Quaternary bimodal volcanism in the Niğde Volcanic Complex (Cappadocia, central Anatolia, Turkey): age, petrogenesis and geodynamic implications. *Contributions to Mineralogy and Petrology* **168**, 1078.
- Azizi, H., Asahara, Y. & Tsuboi, M. (2014). Chemie der Erde The role of heterogenetic mantle in the genesis of adakites northeast of Sanandaj, northwestern Iran. *Chemie Der Erde - Geochemistry* **74**, 87-97.
- Babakhani, A. R., Lesquyer, J. L. & Rico, R. (1990). Geological map of Ahar quadrangle (scale 1: 250,000). *Geological Survey of Iran, Tehran, Iran.*
- Barrat, J. A., Keller, F., Amossé, J., Taylor, R. N., Nesbitt, R. W. & Hirata, T. (1996). Determination of rare earth elements in sixteen silicate reference samples by ICP-MS

- after Tm addition and ion exchange separation. *Geostandards and Geoanalytical Research* **20**, 133-139.
- Barth, M. G., McDonough, W. F. & Rudnick, R. L. (2000). Tracking the budget of Nb and Ta in the continental crust. *Chemical Geology* **165**, 197-213.
- Barton, M. & van Bergen, M. J. (1981). Green clinopyroxenes and associated phases in a potassium-rich lava from the Leucite Hills, Wyoming. *Contributions to Mineralogy and Petrology* **77**, 101-114.
- Barton, M., Varekamp, J. C. & Van Bergen, M. J. (1982). Complex zoning of clinopyroxenes in the lavas of Vulcini, Latium, Italy: evidence for magma mixing. *Journal of Volcanology and Geothermal Research* **14**, 361-388.
- Bavali, K., Motaghi, K., Sobouti, F., Ghods, A., Abbasi, M., Priestley, K. & Rezaeian, M. (2016). Lithospheric structure beneath NW Iran using regional and teleseismic travel-time tomography. *Physics of the Earth and Planetary Interiors* **253**, 97-107.
- Becker, M. & Roex, A. P. L. (2006). Geochemistry of South African on-and off-craton, Group I and Group II kimberlites: petrogenesis and source region evolution. *Journal of Petrology* **47**, 673-703.
- Begg, G. C., Griffin, W. L., Natapov, L. M., O'Reilly, S. Y., Grand, S. P., O'Neill, C. J., & Bowden, P. (2009). The lithospheric architecture of Africa: Seismic tomography, mantle petrology, and tectonic evolution. *Geosphere* **5**, 23-50.
- Bektas, O. (1984). Dogu Pontidlerde Üst Kretase yaşlı shoshonitic volkanizma ve Jeotektonik önemi. *Karadeniz Technical University Bulletin of Earth Sciences* **3**, 53-62.
- Belov, A. A., Somin, M. L. & Adamiya, S. A. (1978). Precambrian and Paleozoic of the Caucasus (brief synthesis). *Jahrbuch der Geologischen* **121**, 155-175.
- Berberian, F. & Berberian, M. (1981). Tectono-plutonic episodes in Iran. Zagros Hindu Kush Himalaya Geodynamic Evolution, *American Geophysical Union & Geological Society of America*, Washington, 5-32.
- Berberian, M. & King, G. C. P. (1981). Towards a paleogeography and tectonic evolution of Iran. *Canadian journal of earth sciences* **18**, 210-265.
- Bercovici, D. & Karato, S. I. (2003). Whole-mantle convection and the transition-zone water filter. *Nature* **425**, 39-44.
- Berra, F. & Angiolini, L. (2014). The evolution of the Tethys region throughout the Phanerozoic: A brief tectonic reconstruction, in L. Marlow, C. Kendall and L. Yose, eds., *Petroleum systems of the Tethyan region: AAPG Memoir* **106**, 1-27.

- Beydokhti, R. M., Karimpour, M. H., Mazaheri, S. A., Santos, J. F. & Klötzli, U. (2015). U-Pb zircon geochronology, Sr-Nd geochemistry, petrogenesis and tectonic setting of Mahoor granitoid rocks (Lut Block, Eastern Iran). *Journal of Asian Earth Sciences* **111**, 192-205.
- Bonadiman, C., Beccaluva, L., Coltorti, M. & Siena, F. (2005). Kimberlite-like metasomatism and 'garnet signature' in spinel-peridotite xenoliths from Sal, Cape Verde Archipelago: relics of a subcontinental mantle domain within the Atlantic oceanic lithosphere?. *Journal of Petrology* **46**, 2465-2493.
- Bonin, B. (1998). Alkali-calcic and alkaline post-orogenic (PO) granite magmatism : petrologic constraints and geodynamic settings. *Lithos* **45**, 45-70.
- Bottrill, A. D., van Hunen, J. & Allen, M. B. (2012). Insight into collision zone dynamics from topography: numerical modelling results and observations. *Solid Earth* **3**, 387-399.
- Boztuğ, D., Harlavan, Y., Arehart, G. B., Satır, M. & Avcı, N. (2007). K-Ar age, whole-rock and isotope geochemistry of A-type granitoids in the Divriği-Sivas region, eastern-central Anatolia, Turkey. *Lithos* **97**, 193-218.
- Boztuğ, D., Jonckheere, R.C. (2007). Apatite fission-track data from central- Anatolian granitoids (Turkey): constraints on Neo-Tethyan closure. *Tectonics* **26**, TC3011. doi:10.1029/2006TC001988.
- Brey, G. P., Bulatov, V. K. & Giris, A. V. (2011). Melting of K-rich carbonated peridotite at 6-10GPa and the stability of K-phases in the upper mantle. *Chemical Geology* **281**, 333-342.
- Brey, G. P., Bulatov, V. K., Giris, A. V. & Lahaye, Y. (2008). Experimental melting of carbonated peridotite at 6-10 GPa. *Journal of Petrology* **49**, 797-821.
- Browning, J., Karaoglu, O., Gudmundsson, A. & Bazargan, M. (2016). Numerical modelling of triple-junction tectonics at Karlıova, Eastern Turkey, with implications for regional magma transport. *Earth and Planetary Science Letters* **452**, 157-170.
- Brunet, M. F., Granath, J. W. & Wilmsen, M. (2009). South Caspian to central Iran basins. *Geological Society, London, Special Publications* **312**, 1-6.
- Bucholz, C. E., Jagoutz, O., Schmidt, M. W., & Sambuu, O. (2014). Phlogopite-and clinopyroxene-dominated fractional crystallization of an alkaline primitive melt: petrology and mineral chemistry of the Dariv Igneous Complex, Western Mongolia. *Contributions to Mineralogy and Petrology* **167**, 994.
- Cai, Z. & Bercovici, D. (2016). Two-dimensional magmons with damage and the transition to magma-fracturing. *Physics of the Earth and Planetary Interiors* **256**, 13-25.

- Canil, D. & Scarfe, C. M. (1990). Phase relations in peridotite þ CO₂ systems to 12 GPa: implication for the origin of kimberlite and carbonate stability in the Earth's mantle. *Journal of Geophysical Research* **95**, 15805-15816.
- Carpenter, R. L., Edgar, A. D. & Thibault, Y. (2002). Origin of spongy textures in clinopyroxene and spinel from mantle xenoliths, Hessian Depression, Germany. *Mineralogy and Petrology* **74**, 149-162.
- Castro, A., Aghazadeh, M., Badrzadeh, Z. & Chichorro, M. (2013). Late Eocene-Oligocene post-collisional monzonitic intrusions from the Alborz magmatic belt, NW Iran. An example of monzonite magma generation from a metasomatized mantle source. *Lithos* **180-181**, 109-127.
- Cellai, D., Conticelli, S. & Menchetti, S. (1994). Crystal-chemistry of clinopyroxenes from potassic and ultrapotassic rocks in central Italy: implications on their genesis. *Contributions to Mineralogy and Petrology* **116**, 301-315.
- Ceuleneer, G. & Rabinowicz, M. (1993). Mantle flow and melt migration beneath oceanic ridges: models derived from observations in ophiolites. Mantle flow and melt generation at mid-ocean ridges, edited by J. P. Morgan, D. K. Blackman, and J. M. Sinton, AGU, Washington, D. C. 123-154.
- Chiaradia, M. (2009). Adakite-like magmas from fractional crystallization and melting-assimilation of mafic lower crust (Eocene Macuchi arc, Western Cordillera, Ecuador). *Chemical Geology* **265**, 468-487.
- Coltorti, M. & Grégoire, M. (2008). Metasomatism in oceanic and continental lithospheric mantle: introduction. *Geological Society, London, Special Publications* **293**, 352p.
- Coltorti, M., Beccaluva, L., Bonadiman, C., Faccini, B., Ntaflos, T. & Siena, F. (2004). Amphibole genesis via metasomatic reaction with clinopyroxene in mantle xenoliths from Victoria Land, Antarctica. *Lithos* **75**, 115-139.
- Comin-Chiaramonti, P., Meriani, S., Mosca, R. & Sinigoi, S. (1979). On the occurrence of analcime in the northeastern Azerbaijan volcanics (northwestern Iran). *Lithos* **12**, 187-198.
- Conceição, R. V. & Green, D. H. (2004). Derivation of potassic (shoshonitic) magmas by decompression melting of phlogopite + pargasite lherzolite. *Lithos* **72**, 209-229.
- Condamine, P. & Médard, E. (2014). Experimental melting of phlogopite-bearing mantle at 1 GPa: Implications for potassic magmatism. *Earth and Planetary Science Letters* **397**, 80-92.

- Condamine, P., Médard, E. & Devidal, J.-L. (2016). Experimental melting of phlogopite-peridotite in the garnet stability field. *Contributions to Mineralogy and Petrology* **171**, 95.
- Conticelli, S., Avanzinelli, R., Poli, G., Braschi, E. & Giordano, G. (2013). Shift from lamproite-like to leucititic rocks: Sr–Nd–Pb isotope data from the Monte Cimino volcanic complex vs. the Vico stratovolcano, Central Italy. *Chemical Geology* **353**, 246-266.
- Copley, A. & Jackson, J. (2006). Active tectonics of the Turkish-Iranian Plateau. *Tectonics* **25**, TC6006, doi:10.1029/2005TC001906, 2006.
- Couch, S., Sparks, R. S. J. & Carroll, M. R. (2001). Mineral disequilibrium in lavas explained by convective self-mixing in open magma chambers. *Nature* **411**, 1037-1039.
- Dalton, J. A. & Presnall, D. C. (1998). The continuum of primary carbonatitic-kimberlitic melt compositions in equilibrium with lherzolite: data from the system CaO-MgO-Al₂O₃-SiO₂-CO₂ at 6 GPa. *Journal of Petrology* **39**, 1953-1964.
- Dargahi, S., Arvin, M., Pan, Y. & Babaei, A. (2010). Lithos Petrogenesis of post-collisional A-type granitoids from the Urumieh - Dokhtar magmatic assemblage, Southwestern Kerman, Iran: Constraints on the Arabian - Eurasian continental collision. *Lithos* **115**, 190-204.
- Dasgupta, R. & Hirschmann, M. M. (2006). Melting in the Earth's deep upper mantle caused by carbon dioxide. *Nature* **440**, 659-662.
- Davidson, J. P., Morgan, D. J., Charlier, B. L. A., Harlou, R. & Hora, J. M. (2007). Microsampling and isotopic analysis of igneous rocks: implications for the study of magmatic systems. *Annu. Rev. Earth Planet. Sci.*, **35**, 273-311.
- Davidson, J., Hassanzadeh, J., Berzins, R., Stockli, D. F., Bashukooh, B., Turrin, B. & Pandamouz, A. (2004), The geology of the Damavand volcano, Alborz Mountains, northern Iran, *Geological Society of America Bulletin* **116**, 16-29.
- Davis, F. A. & Hirschmann, M. M. (2013). The effects of K₂O on the compositions of near-solidus melts of garnet peridotite at 3 GPa and the origin of basalts from enriched mantle. *Contributions to Mineralogy and Petrology* **166**, 1029-1046.
- Davis, F. A., Hirschmann, M. M. & Humayun, M. (2011). The composition of the incipient partial melt of garnet peridotite at 3GPa and the origin of OIB. *Earth and Planetary Science Letters* **308**, 380-390.

- Demouchy, S., Deloule, E., Frost, D. J. & Keppler, H. (2005). Pressure and temperature-dependence of water solubility in Fe-free wadsleyite. *American Mineralogist* **90**, 1084-1091.
- DePaolo, D. J. (1981). Trace element and isotopic effects of combined wallrock assimilation and fractional crystallization. *Earth and planetary science letters* **53**, 189-202.
- Dhnot D., Chorowicz, J., Yurur, T., Froger, J-L., Kos, O., Gondoglu, M.N. (1998). Emplacement of volcanic vents and geodynamics of Central Anatolia, Turkey. *Journal of Volcanology and Geothermal Research* **85**, 33-54.
- Di Rocco, T., Freda, C., Gaeta, M., Mollo, S. & Dallai, L. (2012). Magma chambers emplaced in carbonate substrate: petrogenesis of skarn and cumulate rocks and implications for CO₂ degassing in volcanic areas. *Journal of Petrology* **53**, 2307-2332.
- Didon, J. & Gemain, Y. M. (1976). Le Sabalan, volcan plio-quadernaire de l'Azerbaïdjan oriental (Iran): étude géologique et pétrographique de l'édifice et de son environnement régional (Doctoral dissertation, Université Scientifique et Médicale de Grenoble).
- Dirik, K. & Göncüoğlu, C. (1996). Neotectonic characteristics of central Anatolia. *Inter Geol Rev* **38**, 807-817.
- Dobosi, G. & Fodor, R. V. (1992). Magma fractionation, replenishment, and mixing as inferred from green-core clinopyroxenes in Pliocene basanite, southern Slovakia. *Lithos* **28**, 133-150.
- Dobosi, G. (1989). Clinopyroxene zoning patterns in the young alkali basalts of Hungary and their petrogenetic significance. *Contributions to Mineralogy and Petrology* **101**, 112-121.
- Doroozi, R., Vaccaro, C., Masoudi, F. & Petrini, R. (2016). Cretaceous alkaline volcanism in south Marzanabad, northern central Alborz, Iran: Geochemistry and petrogenesis. *Geoscience Frontiers* **7**, 937-951.
- Drummond, M. S., & Defant, M. J. (1990). A model for trondhjemite-tonalite-dacite genesis and crustal growth via slab melting: Archean to modern comparisons. *Journal of Geophysical Research: Solid Earth* **95**, 21503-21521.
- Duda, A. & Schmincke, H. U. (1985). Polybaric differentiation of alkali basaltic magmas: evidence from green-core clinopyroxenes (Eifel, FRG). *Contributions to Mineralogy and Petrology*, **91**, 340-353.
- Dupuy, C., Liotard, J. M. & Dostal, J. (1992). Zr/Hf fractionation in intraplate basaltic rocks: carbonate metasomatism in the mantle source. *Geochimica et Cosmochimica Acta* **56**, 2417-2423.

- Eggler, D. H. (1989). Kimberlites: How do they form?. In Kimberlites and Related Rocks (ed. J. Ross) *Blackwell* **1**, 489-504.
- Eggler, DH. & Wendlandt, RF . (1979). Experimental studies on the relationship between kimberlite magmas and the partial melting of peridotite. In: Boyd FR, Meyer HOA (eds) The mantle sample: inclusions in kimberlites and other volcanics. *Am Geophys Union, Washington DC*, 308–338.
- Emami, M. H. (1992). Explanatory text of Sarab, Geological Quadrangle Map 1:100000, No. 5565, Geological Survey of Iran, Tehran (in Persian).
- Enggist, A., Chu, L. & Luth, R. W. (2012). Phase relations of phlogopite with magnesite from 4 to 8 GPa. *Contributions to Mineralogy and Petrology* **163**, 467-481.
- Esmaeily, D. (2005). Petrology of the Jurassic Shah-Kuh granite (eastern Iran), with reference to tin mineralization. *Journal of Asian Earth Sciences* **25**, 961-980.
- Eyuboglu, Y., Santosh, M., Yi, K., Bektaş, O. & Kwon, S. (2012). Discovery of Miocene adakitic dacite from the Eastern Pontides Belt and revised geodynamic model for the late Cenozoic evolution of the Eastern Mediterranean region. *Lithos* **146-147**, 218-232.
- Faccenna, C., Bellier, O., Martinod, J., Piromallo, C. & Regard, V. (2006). Slab detachment beneath eastern Anatolia: A possible cause for the formation of the North Anatolian fault. *Earth and Planetary Science Letters* **242**, 85-97.
- Faul, U. H. (1997). Permeability of partially molten upper mantle rocks from experiments and percolation theory. *Journal of Geophysical Research* **102**, 10299-10311.
- Fichtner, A., Saygin, E., Taymaz, T., Cupillard, P., Capdeville, Y. & Trampert, J. (2013). The deep structure of the North Anatolian fault zone. *Earth and Planetary Science Letters* **373**, 109-117.
- Fitton, J.G & Upton, B.G.J. (1987). Alkaline igneous rocks. *Geological Society, London, Special Publications* **30**, 544.
- Foley, S. & Peccerillo, A. (1992). Potassic and ultrapotassic magmas and their origin. *Lithos* **28**, 181-185.
- Foley, S. (1992). Vein-plus-wall-rock melting mechanisms in the lithosphere and the origin of potassic alkaline magmas. *Lithos* **28**, 435-453.
- Foley, S. F. (1994). Geochemical and experimental studies of the origin of ultrapotassic igneous rocks. *Neues Jahrbuch für Mineralogie, Abhandlungen* **167**, 1-55.

- Foley, S.F., Venturelli, G., Green, D.H. & Toscani, L., (1987). The ultrapotassic rocks: characteristics, classification, and constraints for petrogenetic models. *Earth Science Reviews* **24**, 81-134.
- Förster, M. W., Prelević, D., Schmück, H. R., Buhre, S., Veter, M., Mertz-Kraus, R., & Jacob, D. E. (2016). Melting and dynamic metasomatism of mixed harzburgite+ glimmerite mantle source: Implications for the genesis of orogenic potassic magmas. *Chemical Geology* **455**, 182-191.
- Fotohi, M. (1973). *A comprehensive review of geology and oil possibilities in Moghan area. National Iranian Oil Company* (No. 348). Geological report.
- Fourel, L., Milelli, L., Jaupart, C. & Limare, A. (2013). Generation of continental rifts, basins, and swells by lithosphere instabilities. *Journal of Geophysical Research: Solid Earth* **118**, 3080-3100.
- Francois T., Burov, E., Agard, P. & Meyer, B. (2014). Buildup of a dynamically supported orogenic plateau: Numerical modeling of the Zagros/Central Iran case study *Geochemistry, Geophysics, Geosystems* **15**, 1632-2654.
- Frezzotti, M. L. & Touret, J. L. (2014). CO₂, carbonate-rich melts, and brines in the mantle. *Geoscience Frontiers* **5**, 697-710.
- Fritschle, T., Prelević, D., Foley, S. F., & Jacob, D. E. (2013). Petrological characterization of the mantle source of Mediterranean lamproites: Indications from major and trace elements of phlogopite. *Chemical Geology* **353**, 267-279.
- Fukao, Y., Widiyantoro, S. & Obayashi, M. (2001). Stagnant slabs in the upper and lower mantle transition region. *Reviews of Geophysics* **39**, 291-324.
- Fumagalli, P., Zanchetta, S. & Poli, S. (2009). Alkali in phlogopite and amphibole and their effects on phase relations in metasomatized peridotites: A high-pressure study. *Contributions to Mineralogy and Petrology* **158**, 723-737.
- Gao, Y., Hou, Z., Kamber, B. S., Wei, R., Meng, X. & Zhao, R. (2007). Lamproitic Rocks from a Continental Collision Zone : Evidence for Recycling of Subducted Tethyan Oceanic Sediments in the Mantle Beneath Southern Tibet, *Journal of Petrology* **48**, 729-752.
- Gerya, T. V., Connolly, J. A., Yuen, D. A., Górczyk, W., & Capel, A. M. (2006). Seismic implications of mantle wedge plumes. *Physics of the Earth and Planetary Interiors* **156**, 59-74.

- Ghalamghash, J., Mousavi, S. Z., Hassanzadeh, J. & Schmitt, A. K. (2016). Geology, zircon geochronology, and petrogenesis of Sabalan volcano (northwestern Iran). *Journal of Volcanology and Geothermal Research* **327**, 192-207.
- Ghasemi, A. & Talbot, C.J. (2006). A new tectonic scenario from the Sanandaj-Sirjan Zone (Iran). *Journal of Asian Earth Sciences* **26**, 683-693.
- Ghorbani, M. R. & Bezenjani, R. N. (2011). Slab partial melts from the metasomatizing agent to adakite, Tafresh Eocene volcanic rocks, Iran. *Island Arc*, **20**, 188-202.
- Ghorbani, M. R., Graham, I. T. & Ghaderi, M. (2014). Oligocene-Miocene geodynamic evolution of the central part of Urumieh-Dokhtar Arc of Iran. *International Geology Review* **56**, 1039-1050.
- Ghosh, D. B., Bajgain, S. K., Mookherjee, M. & Karki, B. B. (2017). Carbon-bearing silicate melt at deep mantle conditions. *Scientific Reports* **7**, 1-8.
- Ghosh, S., Litasov, K. & Ohtani, E. (2014). Phase relations and melting of carbonated peridotite between 10 and 20 GPa: A proxy for alkali- and CO₂-rich silicate melts in the deep mantle. *Contributions to Mineralogy and Petrology* **167**, 1-23.
- Ghosh, S., Ohtani, E., Litasov, K. D. & Terasaki, H. (2009). Solidus of carbonated peridotite from 10 to 20 GPa and origin of magnesiocarbonatite melt in the Earth's deep mantle. *Chemical Geology* **262**, 17-28.
- Girnis, A. V., Bulatov, V. K. & Brey, G. P. (2011). Formation of primary kimberlite melts- Constraints from experiments at 6-12GPa and variable CO₂/H₂O. *Lithos* **127**, 401-413.
- Gogus, O. H. & R. N. Pysklywec (2008). Near-surface diagnostics of dripping or delaminating lithosphere, *Journal of Geophysical Research*. **113**, B11404, doi:10.1029/2007JB005123.
- Gögüs, O.H., Pysklywec, R.N., Corbi, F. & Faccenna, C. (2011). The surface tectonics of mantle lithosphere delamination following ocean lithosphere subduction: insights from physical-scaled analogue experiments. *Geochemistry, Geophysics, Geosystems* **12**, Q05004. <http://dx.doi.org/10.1029/2010GC003430>.
- Grant, T. B., Milke, R. & Wunder, B. (2014). Experimental reactions between olivine and orthopyroxene with phonolite melt: implications for the origins of hydrous amphibole+ phlogopite+ diopside bearing metasomatic veins. *Contributions to Mineralogy and Petrology* **168**, 1073.
- Grassi, D., Schmidt, M. W. & Günther, D. (2012). Element partitioning during carbonated pelite melting at 8 , 13 and 22 GPa and the sediment signature in the EM mantle components. *Earth and Planetary Science Letters* **327-328**, 84-96.

- Green, D. H. (2015). Experimental petrology of peridotites, including effects of water and carbon on melting in the Earth's upper mantle. *Physics and Chemistry of Minerals* **42**, 95-122.
- Green, D. H., Hibberson, W. O., Kovács, I. & Rosenthal, A. (2010). Water and its influence on the lithosphere-asthenosphere boundary. *Nature* **467**, 448-451.
- Green, H. W., Chen, W. P., & Brudzinski, M. R. (2010). Seismic evidence of negligible water carried below 400-km depth in subducting lithosphere. *Nature* **467**, 828-831.
- Green, T. H. & Pearson, N. J. (1987). An experimental study of Nb and Ta partitioning between Ti-rich minerals and silicate liquids at high pressure and temperature. *Geochimica et Cosmochimica Acta* **51**, 55-62.
- Grégoire, M., Bell, D. & Le Roex, A. (2002). Trace element geochemistry of phlogopite-rich mafic mantle xenoliths: their classification and their relationship to phlogopite-bearing peridotites and kimberlites revisited. *Contributions to Mineralogy and Petrology* **142**, 603-625.
- Grégoire, M., Bell, D. R. & Le Roex, A. P. (2003). Garnet lherzolites from the Kaapvaal Craton (South Africa): trace element evidence for a metasomatic history. *Journal of Petrology* **44**, 629-657.
- Grégoire, M., Rabinowicz, M. & Janse, A. J. A. (2006). Mantle mush compaction: A key to understand the mechanisms of concentration of kimberlite melts and initiation of swarms of kimberlite dykes. *Journal of Petrology* **47**, 631-646.
- Grützner, T., Prelević, D. & Akal, C. (2013). Geochemistry and origin of ultramafic enclaves and their basanitic host rock from Kula Volcano, Turkey. *Lithos* **180**, 58-73.
- Gülmez, F., Genç, Ş. C., Prelević, D., Tüysüz, O., Karacik, Z., Roden, M. F. & Billor, Z. (2016). Ultrapotassic Volcanism from the Waning Stage of the Neotethyan Subduction: a Key Study from the Izmir–Ankara–Erzincan Suture Belt, Central Northern Turkey. *Journal of Petrology* **57**, 561-593.
- Guo, Z., Wilson, M. & Liu, J. (2007). Post-collisional adakites in south Tibet: products of partial melting of subduction-modified lower crust. *Lithos* **96**, 205-224.
- Hassanzadeh, J. & Wernicke, B. P. (2016). The Neotethyan Sanandaj-Sirjan zone of Iran as an archetype for passive margin-arc transitions. *Tectonics* **35**, 586-621.
- Hassanzadeh, J., Stockli, D. F., Horton, B. K., Axen, G. J., Stockli, L. D., Grove, M. ... & Walker, J. D. (2008). U-Pb zircon geochronology of late Neoproterozoic–Early Cambrian granitoids in Iran: implications for paleogeography, magmatism, and exhumation history of Iranian basement. *Tectonophysics* **451**, 71-96.

- Hastie, A. R., Kerr, A. C., Pearce, J. A. & Mitchell, S. F. (2007). Classification of altered volcanic island arc rocks using immobile trace elements: development of the Th–Co discrimination diagram. *Journal of petrology* **48**, 2341-2357.
- Hawkesworth, C. J., Gallagher, K., Hergt, J. M. & McDermott, F. (1993). Mantle and slab contributions in arc magmas. *Annual Review of Earth and Planetary Sciences* **21**, 175-204.
- Herzberg, C. & Ratteron, P., Zhang, J. (2000). New experimental observations on the anhydrous solidus for peridotite KLB-1. *Geochemistry, Geophysics, Geosystems* **1**. doi:10.1029/2000GC000089
- Hessami, K. & Jamali, F. (2006). Explanatory notes to the map of major active faults of Iran. *Journal of Seismology and Earthquake Engineering* **8**, 1-11.
- Hirschmann, M. M. (2000). Mantle solidus: Experimental constraints and the effects of peridotite composition. *Geochemistry, Geophysics, Geosystems* **1**. doi.org/10.1029/2000GC000070.
- Hirschmann, M. M. (2006). Water, melting, and the deep Earth H₂O cycle. *Annual Review of Earth and Planetary Sciences*. **34**, 629-653.
- Hirschmann, M. M. (2010). Partial melt in the oceanic low velocity zone. *Physics of the Earth and Planetary Interiors* **179**, 60-71.
- Hirschmann, M. M. H., Aker, M. B. B. & Tolper, E. M. S. (1998). The effect of alkalis on the silica content of mantle-derived melts **62**, 883-902.
- Hirschmann, M. M., Kogiso, T., Baker, M. B. & Stolper, E. M. (2003). Alkalic magmas generated by partial melting of garnet pyroxenite. *Geology* **31**, 481-484.
- Hofmann, A.W. (1988). Chemical differentiation of the Earth: the relationship between mantle, continental crust, and oceanic crust. *Earth and Planetary Science Letters* **90**, 297-314.
- Hole, M. J., Saunders, A. D., Rogers, G. & Sykes, M. A. (1994). The relationship between alkaline magmatism, lithospheric extension and slab window formation along continental destructive plate margins. *Geological Society, London, Special Publications* **81**, 265-285.
- Houseman, G. A. & Molnar, P. (1997). Gravitational (Rayleigh-Taylor) instability of a layer with non-linear viscosity and convective thinning of continental lithosphere. *Geophysical Journal International* **128**, 125-150.
- Ionov, D. A. & Hofmann, A. W. (1995). Nb-Ta-rich mantle amphiboles and micas: implications for subduction-related metasomatic trace element fractionation. *Earth and Planetary Science Letters* **131**, 341-356.

- Ionov, D. A., Bodinier, J. L., Mukasa, S. B. & Zanetti, A. (2002). Mechanisms and sources of mantle metasomatism: major and trace element conditions of peridotite xenoliths from Spitzbergen in the context of numerical modelling. *Journal of Petrology* **43**, 2219-2259.
- Ionov, D. A., Dupuy, C., O'Reilly, S. Y., Kopylova, M. G. & Genshaft, Y. S. (1993). Carbonated peridotite xenoliths from Spitzbergen: implications for trace element signature of mantle carbonate metasomatism. *Earth and Planetary Science Letters*, **119**, 283-297.
- Irvine, T. N. J. & Baragar, W. R. A. F. (1971). A guide to the chemical classification of the common volcanic rocks. *Canadian journal of earth sciences* **8**, 523-548.
- Jackson, M. G. & Dasgupta, R. (2008). Compositions of HIMU, EM1, and EM2 from global trends between radiogenic isotopes and major elements in ocean island basalts. *Earth and Planetary Science Letters* **276**, 175-186.
- Jafarzadeh, M., Harami, R. M., Friis, H., Amini, A., Mahboubi, A. & Lenaz, D. (2014). Provenance of the Oligocene–Miocene Zivah Formation, NW Iran, assessed using heavy mineral assemblage and detrital clinopyroxene and detrital apatite analyses. *Journal of African Earth Sciences* **89**, 56-71.
- Jahangiri, A. (2007). Post-collisional Miocene adakitic volcanism in NW Iran : Geochemical and geodynamic implications, *Journal of Asian Earth Sciences* **30**, 433-447.
- Jankovics, M. É., Taracsák, Z., Dobosi, G., Embey-Isztin, A., Batki, A., Harangi, S. & Hauzenberger, C. A. (2016). Clinopyroxene with diverse origins in alkaline basalts from the western Pannonian Basin: Implications from trace element characteristics. *Lithos* **262**, 120-134.
- Jolivet, L., Faccenna, C. & Piromallo, C. (2009). From mantle to crust: Stretching the Mediterranean. *Earth and Planetary Science Letters* **285**, 198-209.
- Jolivet, L., Faccenna, C., Huet, B., Labrousse, L., Le Pourhiet, L., Lacombe, O. & Philippon, M. (2013). Aegean tectonics: Strain localisation, slab tearing and trench retreat. *Tectonophysics* **597**, 1-33.
- Kameyama, M. & Nishioka, R. (2012). Generation of ascending flows in the Big Mantle Wedge (BMW) beneath northeast Asia induced by retreat and stagnation of subducted slab. *Geophysical Research Letters* **39**, L10309, doi:[10.1029/2012GL051678](https://doi.org/10.1029/2012GL051678).
- Karaoğlu, Ö., Browning, J., Bazargan, M. & Gudmundsson, A. (2016). Numerical modelling of triple-junction tectonics at Karlıova, Eastern Turkey, with implications for regional magma transport. *Earth and Planetary Science Letters* **452**, 157-170.

- Karato, S. I. & Wu, P. (1993). Rheology of the upper mantle: a synthesis. *Science* **260**, 771-778.
- Karato, S.I., (2011). Water distribution across the mantle transition zone and its implications for global material circulation. *Earth and Planetary Science Letters* **301**, 413-423.
- Kargaranbafghi, F. & Neubauer, F. (2015). Lithospheric thinning associated with formation of a metamorphic core complex and subsequent formation of the Iranian plateau. *GSA Today* **25**, 4-8.
- Karsli, O., Caran, Ş., Dokuz, A., Çoban, H., Chen, B. & Kandemir, R. (2012a). A-type granitoids from the Eastern Pontides, NE Turkey: records for generation of hybrid A-type rocks in a subduction-related environment. *Tectonophysics* **530**, 208-224.
- Karsli, O., Dokuz, A., Uysal, İ., Aydın, F., Kandemir, R. & Wijbrans, J. (2010). Generation of the Early Cenozoic adakitic volcanism by partial melting of mafic lower crust, Eastern Turkey: implications for crustal thickening to delamination. *Lithos* **114**, 109-120.
- Karsli, O., Dokuz, A., Uysal, Ý., Ketenci, M., Chen, B. & Kandemir, R. (2012b). Deciphering the shoshonitic monzonites with I-type characteristic, the Sisdağı pluton, NE Turkey: magmatic response to continental lithospheric thinning. *Journal of Asian Earth Sciences* **51**, 45-62.
- Karsli, O., Ketenci, M., Uysal, İ., Dokuz, A., Aydın, F., Chen, B. & Wijbrans, J. (2011). Adakite-like granitoid porphyries in the Eastern Pontides, NE Turkey: potential parental melts and geodynamic implications. *Lithos* **127**, 354-372.
- Katsura, T., Yoneda, A., Yamazaki, D., Yoshino, T. & Ito, E. (2010). Adiabatic temperature profile in the mantle. *Physics of the Earth and Planetary Interiors* **183**, 212-218.
- Kavanagh, J. L. & Sparks, R. S. J. (2009). Temperature changes in ascending kimberlite magma. *Earth and Planetary Science Letters* **286**, 404-413.
- Kelemen, P. B., Hirth, G., Shimizu, N., Spiegelman, M. & Dick, H. J. (1997). A review of melt migration processes in the adiabatically upwelling mantle beneath oceanic spreading ridges. *Philosophical Transactions of the Royal Society of London A: Mathematical, Physical and Engineering Sciences* **355**, 283-318.
- Kelemen, P. B., Shimizu, N. & Dunn, T. (1993). Relative depletion of niobium in some arc magmas and the continental crust: partitioning of K, Nb, La and Ce during melt/rock reaction in the upper mantle. *Earth and Planetary Science Letters* **120**, 111-134.
- Keller, T., & Katz, R. F. (2016), The Role of Volatiles in Reactive Melt Transport in the Asthenosphere, *Journal of Petrology* **57**, 1073-1108.

- Keller, T., Katz, R. F. & Hirschmann, M. M. (2017). Volatiles beneath mid-ocean ridges: Deep melting, channelised transport, focusing, and metasomatism. *Earth and Planetary Science Letters* **464**, 55-68.
- Keller, T., May, D.A. & Kaus, B.J. (2013). Numerical modelling of magma dynamics coupled to tectonic deformation of lithosphere and crust. *Geophysical Journal International* **195**, 1406-1442.
- Keshav, S. & Gudfinnsson, G. H. (2010). Experimentally dictated stability of carbonated oceanic crust to moderately great depths in the Earth: Results from the solidus determination in the system CaO-MgO-Al₂O₃-SiO₂-CO₂. *Journal of Geophysical Research: Solid Earth* **115**, B05205, doi:10.1029/2009JB006457.
- Keskin, M. (2005). Domal uplift and volcanism in a collision zone without a mantle plume: Evidence from Eastern Anatolia. 2005-06-20). <http://www.mantleplumes.org/Anatolia.html>.
- Keskin, M., Genç, Ş. C. & Tüysüz, O. (2008). Petrology and geochemistry of post-collisional Middle Eocene volcanic units in North-Central Turkey: evidence for magma generation by slab breakoff following the closure of the Northern Neotethys Ocean. *Lithos* **104**, 267-305.
- Khalaji, A. A., Esmaily, D., Valizadeh, M. V. & Rahimpour-Bonab, H. (2007). Petrology and geochemistry of the granitoid complex of Boroujerd, Sanandaj-Sirjan Zone, Western Iran. *Journal of Asian Earth Sciences* **29**, 859-877.
- Khalatbari Jafari, M., Babaie, H. A. & Moslempour, M. E. (2016). Mid-ocean-ridge to suprasubduction geochemical transition in the hypabyssal and extrusive sequences of major Upper Cretaceous ophiolites of Iran. *Geological Society of America Special Papers* **525**, SPE525-07.
- Khazan, Y. & Fialko, Y. (2005). Why do kimberlites from different provinces have similar trace element patterns?. *Geochemistry, Geophysics, Geosystems*, **6**.
- Kheirkhah, M., Neill, I. & Allen, M. B. (2015). Petrogenesis of OIB-like basaltic volcanic rocks in a continental collision zone: Late Cenozoic magmatism of Eastern Iran. *Journal of Asian Earth Sciences* **106**, 19-33.
- Khezerlou, A. A., Amel, N., Gregoire, M., Moayyed, M. & Jahangiri, A. (2017). Geochemistry and mineral chemistry of pyroxenite xenoliths and host volcanic alkaline rocks from north west of Marand (NW Iran). *Mineralogy and Petrology* doi, 10.1007/s00710-017-0502-6.

- Kind, R., Eken, T., Tilmann, F., Sodoudi, F., Taymaz, T., Bulut, F. & Schneider, F. (2015). Thickness of the lithosphere beneath Turkey and surroundings from S-receiver functions. *Solid Earth* **6**, 971.
- Klemme, S., Prowatke, S., Hametner, K. & Gunther, D. (2005). Partitioning of trace elements between rutile and silicate melts: implications for subduction zones. *Geochimica et Cosmochimica Acta* **69**, 2361-2371.
- Komabayashi, T. & Omori, S. (2006). Internally consistent thermodynamic data set for dense hydrous magnesium silicates up to 35 GPa, 1600 C: implications for water circulation in the Earth's deep mantle. *Physics of the Earth and Planetary Interiors* **156**, 89-107.
- Konzett, J. & Ulmer, P. (1999). The stability of hydrous potassic phases in lherzolitic mantle—an experimental study to 9.5 GPa in simplified and natural bulk compositions. *Journal of Petrology* **40**, 629-652.
- Konzett, J., Sweeney, R.J., Thompson, A.B. & Ulmer, P. (1997). Potassium amphibole stability in the upper mantle: an experimental study in a peralkaline KNCMASH system to 8.5 GPa. *Journal of Petrology* **38**, 537-568.
- Köprübas, N. & Kirmaci, M. Z. (2014). Chemie der Erde Mineral chemical constraints on the petrogenesis of mafic and g volcanoes , intermediate volcanic rocks from the Erciyes and Hasanda ~ Central Turkey, *Chemie der Erde* **74**, 585-600.
- Koulakov, I., Zabelina, I., Amanatashvili, I. & Meskhia, V. (2012). Nature of orogenesis and volcanism in the Caucasus region based on results of regional tomography. *Solid Earth* **3**, 327.
- Kuritani, T., Kimura, J. I., Ohtani, E., Miyamoto, H. & Furuyama, K. (2013). Transition zone origin of potassic basalts from Wudalianchi volcano, northeast China. *Lithos* **156**, 1-12.
- Larrea, P., França, Z., Lago, M., Widom, E., Galé, C. & Ubide, T. (2012). Magmatic processes and the role of antecrysts in the genesis of Corvo Island (Azores Archipelago, Portugal). *Journal of Petrology* **54**, 769-793.
- Le Bas, M. J., Maitre, R. W., Streckeisen, A. & Zanettin, B. (1986). A chemical classification of volcanic rocks based on the total alkali-silica diagram. *Journal of petrology* **27**, 745-750.
- Le Maitre, R. W. (2002) Igneous rocks: a classification and glossary of terms: recommendations of the International Union of Geological Sciences Subcommittee on the Systematics of Igneous Rocks. *Cambridge University Press*.
- Le Maitre, R. W. B., Dudek, P., Keller, A., Lameyre, J., Le Bas, J., Sabine, M. J. ... & Zanettin, A. R. (1989). A classification of igneous rocks and glossary of terms:

Recommendations of the International Union of Geological Sciences, Subcommittee on the Systematics of Igneous Rocks (No. 552.3 CLA). International Union of Geological Sciences.

- Le Roex, A. P., Bell, D. R. & Davis, P. (2003). Petrogenesis of group I kimberlites from Kimberley, South Africa: evidence from bulk-rock geochemistry. *Journal of Petrology*, **44**, 2261-2286.
- Leake, B. E., Woolley, A. R., Arps, C. E., Birch, W. D., Gilbert, M. C., Grice, J. D. ... & Linthout, K. (1997). Nomenclature of amphiboles: report of the subcommittee on amphiboles of the international mineralogical association commission on new minerals and mineral names. *Mineralogical magazine* **61**, 295-321.
- Lescuyer, J. L., Riuo, R. & Babakhani, A. (1978). Report of Ahar geological map, scale 1/250000. Geological Survey of Iran.
- Liotard, J.M., Dautria, J.M., Bisch, D., Condomines, J., Mehdizadeh, H. & Ritz, J.F. (2008). Origin of the absarokite-banakite association of the Damavand volcano (Iran): trace elements and Sr, Nd, Pb isotope constraints. *International Journal of Earth Sciences* **97**, 89-102.
- Litasov, K. D., Shatskiy, A. F., Pal'yanov, Y. N., Sokol, A. G., Katsura, T. & Ohtani, E. (2009). Hydrogen incorporation into forsterite in $Mg_2SiO_4-K_2Mg(CO_3)_2-H_2O$ and $Mg_2SiO_4-H_2O-C$ at 7.5-14.0 GPa. *Russian Geology and Geophysics* **50**, 1129-1138.
- Litasov, K. D., Shatskiy, A. N. T. O. N. & Ohtani, E. (2013). Earth's mantle melting in the presence of C-O-H-bearing fluid. *Physics and Chemistry of the Deep Earth*, **no number**, 38-65.
- Longerich, H. P., Jackson, S. E. & Gunther, D. (1997). Laser ablation inductively coupled plasma mass spectrometric transient signal data acquisition and analyte concentration calculation (vol 11, pg 899, 1996). *Journal of Analytical Atomic Spectrometry* **12**, 391-391.
- Lotfi, M. (1976). Geological and petrological studies of north-northeast of Miyane. MSc thesis, University of Tehran, Tehran, Iran (in Persian).
- Luhr, J. F. & Kyser, T. K. (1989). Primary igneous analcime: The Colima minettes. *American Mineralogist* **74**, 216-223.
- Lustrino, M. & Wilson, M. (2007). The circum-Mediterranean anorogenic Cenozoic igneous province. *Earth-Science Reviews* **81**, 1-65.
- Lustrino, M., Agostini, S., Chalal, Y., Fedele, L., Stagno, V., Colombi, F., & Bouguerra, A. (2016). Exotic lamproites or normal ultrapotassic rocks? The Late Miocene volcanic

- rocks from Kef Hahouner, NE Algeria, in the frame of the circum-Mediterranean lamproites. *Journal of Volcanology and Geothermal Research* **327**, 539-553.
- Lustrino, M., Duggen, S. & Rosenberg, C. L. (2011). The Central-Western Mediterranean: anomalous igneous activity in an anomalous collisional tectonic setting. *Earth-Science Reviews* **104**, 1-40.
- Lustrino, M., Keskin, M., Mattioli, M., Lebedev, V. A., Chugaev, A., Sharkov, E. & Kavak, O. (2010). Early activity of the largest Cenozoic shield volcano in the circum-Mediterranean area: Mt. Karacadağ, SE Turkey. *European Journal of Mineralogy* **22**, 343-362.
- Maaløe, S. & Scheie, S. M. (1982). The permeability controlled accumulation of primary magma. *Contributions to Mineralogy and Petrology* **81**, 350-357.
- Mallik, A., & Dasgupta, R. (2014). Effect of variable CO₂ on eclogite-derived andesite and lherzolite reaction at 3 GPa—Implications for mantle source characteristics of alkalic ocean island basalts. *Geochemistry, Geophysics, Geosystems* **15**, 1533-1557.
- Martin, H. (1999). Adakitic magmas: modern analogues of Archaean granitoids. *Lithos* **46**, 411-429.
- Masson, F., Lehujeur, M., Ziegler, Y. & Doubre, C. (2014). Strain rate tensor in Iran from a new GPS velocity field. *Geophysical Journal International*, **197**, 10-21.
- McBirney, A. & Murase, T. (1984). Rheological properties of magmas. *Annual Review of Earth and Planetary Sciences* **12**, 337-357.
- McDonough, W. F. (1990). Constraints on the composition of the continental lithospheric mantle. *Earth and Planetary Science Letters* **101**, 1-18.
- McKenzie, D. (1984). The generation and compaction of partially molten rock. *Journal of Petrology* **25**, 713-765.
- McKenzie, D. (1985). The extraction of magma from the crust and mantle. *Earth and Planetary Science Letters* **74**, 81-91.
- McKenzie, D. (1989). Some remarks on the movement of small melt fractions in the mantle. *Earth and Planetary Science Letters* **95**, 53-72.
- McKenzie, D. A. N., & O'Nions, R. K. (1991). Partial melt distributions from inversion of rare earth element concentrations. *Journal of Petrology* **32**, 1021-1091.

- McQuarrie, N. & van Hinsbergen, D. J. (2013). Retrodeforming the Arabia-Eurasia collision zone: Age of collision versus magnitude of continental subduction. *Geology* **41**, 315-318.
- McQuarrie, N., Stock, J. M., Verdel, C. & Wernicke, B. P. (2003). Cenozoic evolution of Neotethys and implications for the causes of plate motions, *Geophysical Research Letters* **30**, 30-33.
- Mei, S., Bai, W., Hiraga, T., & Kohlstedt, D. L. (2002). Influence of melt on the creep behavior of olivine-basalt aggregates under hydrous conditions. *Earth and Planetary Science Letters*, **201**, 491-507.
- Meijers, M. J. M., Smith, B., Kirscher, U., Mensink, M., Sosson, M., Rolland, Y. & Müller, C. (2015). Tectonophysics A paleolatitude reconstruction of the South Armenian Block (Lesser Caucasus) for the Late Cretaceous : Constraints on the Tethyan realm n Platform. *Tectonophysics* **644-645**, 197-219.
- Melchiorre, M., Vergés, J., Fernández, M., Coltorti, M., Torne, M. & Casciello, E. (2017). Evidence for mantle heterogeneities in the westernmost Mediterranean from a statistical approach to volcanic petrology. *Lithos*, **276**, 62-74.
- Middlemost, E. A. (1994). Naming materials in the magma/igneous rock system. *Earth-Science Reviews* **37**, 215-224.
- Milelli, L., Fourel, L. & Jaupart, C. (2012). A lithospheric instability origin for the Cameroon Volcanic Line. *Earth and Planetary Science Letters*, **335**, 80-87.
- Minarik, W. G. & Watson, E. B. (1995). Interconnectivity of carbonate melt at low melt fraction. *Earth and Planetary Science Letters* **133**, 423-437.
- Mirnejad, H., & Bell, K. (2006). Origin and source evolution of the Leucite Hills lamproites: evidence from Sr–Nd–Pb–O isotopic compositions. *Journal of Petrology* **47**, 2463-2489.
- Mirnejad, H., Hassanzadeh, J., Cousens, B. L. & Taylor, B. E. (2010). Geochemical evidence for deep mantle melting and lithospheric delamination as the origin of the inland Damavand volcanic rocks of northern Iran. *Journal of Volcanology and Geothermal Research* **198**, 288-296.
- Mitchell, R. H. & Bergman, S. C. (1991). Petrology of lamproites. *New York: Plenum*, 295-35.
- Mitchell, R. H. (1995). Kimberlites, Orangeites, and Related Rocks. *New York: Plenum*, 410.
- Mitchell, R. H. (2004). Experimental studies at 5-12 GPa of the Ondermatjie hypabyssal kimberlite. *Lithos* **76**, 551-564.

- Mohammadi, E., Sodoudi, F., Kind, R. & Rezapour, M. (2013). Tectonophysics Presence of a layered lithosphere beneath the Zagros collision zone. *Tectonophysics* **608**, 366-375.
- Morgan, W.J. (1971). Convection plumes in the lower mantle. *Nature* **230**, 42-43.
- Morimoto, N. (1988). Nomenclature of pyroxenes. *Mineralogy and Petrology* **39**, 55-76.
- Morishita, T., Ishida, Y., Arai, S. & Shirasaka, M. (2005). Determination of Multiple Trace Element Compositions in Thin (> 30 μm) Layers of NIST SRM 614 and 616 Using Laser Ablation-Inductively Coupled Plasma-Mass Spectrometry (LA-ICP-MS). *Geostandards and Geoanalytical Research*, **29**, 107-122.
- Moritz, R., Rezeau, H., Ovtcharova, M., Tayan, R., Melkonyan, R., Hovakimyan, S. & Putlitz, B. (2016). Long-lived, stationary magmatism and pulsed porphyry systems during Tethyan subduction to post-collision evolution in the southernmost Lesser Caucasus, Armenia and Nakhitchevan. *Gondwana Research* **37**, 465-503.
- Morra, G., Yuen, D. A., King, S. D., Lee, S. M. & Stein, S. (Eds.). (2015). Subduction Dynamics: *From Mantle Flow to Mega Disasters*, John Wiley & Sons, **211**.
- Motaghi, K., Tatar, M., Priestley, K., Romanelli, F., Doglioni, C. & Panza, G.F. (2015). The deep structure of the Iranian Plateau. *Gondwana Research* **28**, 407-418.
- Motavalli-Anbaran, S. H., M., Zeyen, H. & Brunet, M. F. (2011). Crustal and lithospheric structure of the Alborz Mountains, Iran, and surrounding areas from integrated geophysical modeling, *Tectonic* **30**, 1-16.
- Motavalli-Anbaran, S. H., Zeyen, H. & Jamasb, A. (2016). 3D crustal and lithospheric model of the Arabia-Eurasia collision zone. *Journal of Asian Earth Sciences* **122**, 158-167.
- Motoki, M. H. & Ballmer, M. D. (2015). Intraplate volcanism due to convective instability of stagnant slabs in the Mantle Transition Zone. *Geochemistry, Geophysics, Geosystems*, **16**, 538-551.
- Muravyeva, N. S., Belyatsky, B. V., Senin, V. G. & Ivanov, A. V. (2014). Sr–Nd–Pb isotope systematics and clinopyroxene-host disequilibrium in ultra-potassic magmas from Toro-Ankole and Virunga, East-African Rift: Implications for magma mixing and source heterogeneity. *Lithos*, **210**, 260-277.
- Murphy, D. T., Collerson, K. D. & Kamber, B. S. (2002). Lamproites from Gaussberg, Antarctica: possible transition zone melts of Archaean subducted sediments. *Journal of Petrology* **43**, 981-1001.
- Myhill, R., Frost, D. J. & Novella, D. (2017). Hydrous melting and partitioning in and above the mantle transition zone: Insights from water-rich MgO - SiO₂ - H₂O experiments. *Geochimica et Cosmochimica Acta* **200**, 408-421.

- Nabatian, G., Ghaderi, M., Neubauer, F., Honarmand, M., Liu, X., Dong, Y., ... & Bernroider, M. (2014). Petrogenesis of Tarom high-potassic granitoids in the Alborz–Azarbaijan belt, Iran: Geochemical, U–Pb zircon and Sr–Nd–Pb isotopic constraints. *Lithos* **184**, 324-345.
- Nafi Toksöz, M., Van der Hilst, R. D., Sun, Y. & Zhang, H. (2010). Seismic tomography of the Arabian-Eurasian collision zone and surrounding areas. *Monitoring Research Review* **no number**, 504-513
- Neill, I., Meliksetian, K., Allen, M. B., Navasardyan, G. & Kuiper, K. (2015). Petrogenesis of mafic collision zone magmatism : The Armenian sector of the Turkish - Iranian Plateau. *Chemical Geology* **403**, 24-41.
- Niu, Y., Wilson, M., Humphreys, E. R. & O'hara, M. J. (2011). The origin of intra-plate ocean island basalts (OIB): the lid effect and its geodynamic implications. *Journal of Petrology* **52**, 1443-1468.
- Novella, D. & Frost, D. J. (2014). The Composition of Hydrous Partial Melts of Garnet Peridotite at 6 GPa: Implications for the Origin of Group II Kimberlites. *Journal of Petrology* **55**, 2097-2124.
- O'Brien, H. E., Irving, A. J., McCallum, I. S. & Thirlwall, M. F. (1995). Strontium, neodymium, and lead isotopic evidence for the interaction of post-suhduction asthenospheric potassic mafic magmas of the Highwood Mountains, Montana, USA, with ancient Wyoming craton lithospheric mantle. *Geochimica et Cosmochimica Acta* **59**, 4539-4556.
- Ohtani, E. & Zhao, D. (2009). The role of water in the deep upper mantle and transition zone: dehydration of stagnant slabs and its effects on the big mantle wedge. *Russian Geology and Geophysics* **50**, 1073-1078.
- Ohtani, E., Litasov, K., Hosoya, T., Kubo, T. & Kondo, T. (2004). Water transport into the deep mantle and formation of a hydrous transition zone. *Physics of the Earth and Planetary Interiors* **143**, 255-269.
- Omrani, J., Agard, P., Whitechurch, H., Benoit, M., Prouteau, G. & Jolivet, L. (2008). Arc-magmatism and subduction history beneath the Zagros Mountains, Iran: a new report of adakites and geodynamic consequences. *Lithos* **106**, 380-398.
- Orejana, D., Villaseca, C. & Paterson, B. A. (2007). Geochemistry of mafic phenocrysts from alkaline lamprophyres of the Spanish Central System: implications on crystal fractionation, magma mixing and xenoliths entrapment within deep magma chambers. *European Journal of Mineralogy* **19**, 817-832.

- Özacar, A. A., Gilbert, H. & Zandt, G. (2008). Upper mantle discontinuity structure beneath East Anatolian Plateau (Turkey) from receiver functions. *Earth and Planetary Science Letters* **269**, 427-435.
- Özacar, A. A., Zandt, G., Gilbert, H. & Beck, S. L. (2010). Seismic images of crustal variations beneath the East Anatolian Plateau (Turkey) from teleseismic receiver functions. *Geological Society, London, Special Publications* **340**, 485-496.
- Özdemir, Y. & Güleç, N. (2014). Geological and geochemical evolution of the Quaternary Süphan stratovolcano, eastern Anatolia, Turkey: evidence for the Lithosphere-Asthenosphere interaction in post-collisional volcanism. *Journal of Petrology* **55**, 37-62.
- Özdemir, Y. (2016). Geochemistry of tholeiitic to alkaline lavas from the east of Lake Van (Turkey): Implications for a late Cretaceous mature supra-subduction zone environment. *Journal of African Earth Sciences* **120**, 77-88.
- Özdemir, Y., Karaoğlu, Ö., Tolluoğlu, A. Ü. & Güleç, N. (2006). Volcanostratigraphy and petrogenesis of the Nemrut stratovolcano (East Anatolian High Plateau): the most recent post-collisional volcanism in Turkey. *Chemical Geology* **226**, 189-211.
- Pang, K. N., Chung, S. L., Zarrinkoub, M. H., Li, X. H., Lee, H. Y., Lin, T. H. & Chiu, H. Y. (2016). New age and geochemical constraints on the origin of Quaternary adakite-like lavas in the Arabia–Eurasia collision zone. *Lithos* **264**, 348-359.
- Pang, K., Chung, S., Hossein, M. & Mahdi, M. (2013). Lithos Eocene - Oligocene post-collisional magmatism in the Lut - Sistan region , eastern Iran : Magma genesis and tectonic implications. *Lithos* **180-181**, 234-251.
- Pang, K., Chung, S., Hossein, M., Li, X., Lee, H., Lin, T. & Chiu, H. (2016). Lithos New age and geochemical constraints on the origin of Quaternary adakite-like lavas in the Arabia - Eurasia collision zone. *Lithos* **264**, 348-359.
- Pang, K.-N., Chung, S.-L., Zarrinkoub, M.H., Lin, Y.-C., Lee, H.-Y., Lo, C.-H., Khatib, M.M., (2013). Iranian ultrapotassic volcanism at ~11 Ma signifies the initiation of post-collision magmatism in the Arabia-Eurasiacollision zone. *TerraNova* **25**, 405-413.
- Pearce, J.A., Bender, J.F., De Long, S.E., Kidd, W.S.F., Low, P.J., Gner, Y., Saroglu, F., Yilmaz, Y., Moorbath, S. & Mitchell, J.G. (1990). Genesis of collision volcanism in Eastern Anatolia, Turkey. *Journal of Volcanology and Geothermal Research* **44**, 189-229.
- Pearson, D. G., Brenker, F. E., Nestola, F., McNeill, J., Nasdala, L., Hutchison, M. T. & Vekemans, B. (2014). Hydrous mantle transition zone indicated by ringwoodite included within diamond. *Nature* **507**, 221-224.

- Peccerillo, A. & Martinotti, G. (2006). The Western Mediterranean lamproitic magmatism: origin and geodynamic significance. *Terra Nova* **18**, 109-117.
- Peccerillo, A. & Taylor, S. R. (1976). Geochemistry of Eocene calc-alkaline volcanic rocks from the Kastamonu area, northern Turkey. *Contributions to mineralogy and petrology* **58**, 63-81.
- Persikov, E. S., Bukhtiyarov, P. G., & Sokol, A. G. (2017). Viscosity of hydrous kimberlite and basaltic melts at high pressures. *Russian Geology and Geophysics* **58**, 1093-1100.
- Pfänder, J. A., Münker, C., Stracke, A. & Mezger, K. (2007). Nb/Ta and Zr/Hf in ocean island basalts—implications for crust-mantle differentiation and the fate of Niobium. *Earth and Planetary Science Letters* **254**, 158-172.
- Phipps Morgan, J. (2001). Thermodynamics of pressure release melting of a veined plum pudding mantle. *Geochemistry, Geophysics, Geosystems* **2**.
doi.org/10.1029/2000GC000049
- Pilet, S., Baker, M. B. & Stolper, E. M. (2008). Metasomatized lithosphere and the origin of alkaline lavas. *Science* **320**, 916-919.
- Pilet, S., Hernandez, J. & Villemant, B. (2002). Evidence for high silicic melt circulation and metasomatic events in the mantle beneath alkaline provinces: the Na–Fe-augitic green-core pyroxenes in the Tertiary alkali basalts of the Cantal massif (French Massif Central). *Mineralogy and Petrology* **76**, 39-62.
- Pin, C. & Zalduegui, J. S. (1997). Sequential separation of light rare-earth elements, thorium and uranium by miniaturized extraction chromatography: application to isotopic analyses of silicate rocks. *Analytica Chimica Acta* **339**, 79-89.
- Piomallo, C. & Morelli, A. (2003). P wave tomography of the mantle under the Alpine-Mediterranean area. *Journal of Geophysical Research*: **108**. doi:[10.1029/2002JB001757](https://doi.org/10.1029/2002JB001757).
- Plank, T. & Langmuir, C.H. (1998) The chemical composition of subducting sediment and its consequences for the crust and mantle. *Chemical geology* **145**, 325-394.
- Platevoet, B., Elitok, Ö., Guillou, H., Bardintzeff, J. M., Yagmurlu, F., Nomade, S. & Özgür, N. (2014). Petrology of Quaternary volcanic rocks and related plutonic xenoliths from Gölcük volcano, Isparta Angle, Turkey: Origin and evolution of the high-K alkaline series. *Journal of Asian Earth Sciences* **92**, 53-76.
- Powell, R. (1984). Inversion of the assimilation and fractional crystallization (AFC) equations; characterization of contaminants from isotope and trace element relationships in volcanic suites. *Journal of the Geological Society* **141**, 447-452.

- Prelević, D., Foley, S. F., Romer, R. & Conticelli S. (2008). Mediterranean Tertiary lamproites derived from multiple source components in postcollisional geodynamics. *Geochimica et Cosmochimica Acta* **72**, 2125-2156.
- Prelević, D. & Foley, S. F. (2007). Accretion of arc-oceanic lithospheric mantle in the Mediterranean: evidence from extremely high-Mg olivines and Cr-rich spinel inclusions in lamproites. *Earth and Planetary Science Letters* **256**, 120-135.
- Prelević, D., Akal, C. & Foley, S. F. (2008). Orogenic vs anorogenic lamproites in a single volcanic province: mediterranean-type lamproites from Turkey. In *IOP Conference Series: Earth and Environmental Science* (Vol. 2, No. 1, p. 012024).
- Prelević, D., Akal, C., Romer, R. L., Mertz-Kraus, R. & Helvaci, C. (2015). Magmatic response to slab tearing: Constraints from the afyon alkaline volcanic complex, Western Turkey. *Journal of Petrology* **56**, 527-562.
- Prelević, D., Foley, S. F., Cvetković, V. & Romer, R. L. (2004). Origin of minette by mixing of lamproite and dacite magmas in Veliki Majdan, Serbia. *Journal of Petrology* **45**, 759-792.
- Prelević, D., Stracke, A., Foley, S. F., Romer, R. L. & Conticelli, S. (2010). Hf isotope compositions of Mediterranean lamproites : Mixing of melts from asthenosphere and crustally contaminated mantle lithosphere, *Lithos* **119**, 297-312.
- Qian, Q. & Hermann, J. (2013). Partial melting of lower crust at 10–15 kbar: constraints on adakite and TTG formation. *Contributions to Mineralogy and Petrology* **165**, 1195-1224.
- Rabinowicz, M. & Ceuleneer, G. (2005). The effect of sloped isotherms on melt migration in the shallow mantle: a physical and numerical model based on observations in the Oman ophiolite. *Earth and Planetary Science Letters* **229**, 231-246.
- Rabinowicz, M. & Toplis, M. J. (2009). Melt segregation in the lower part of the partially molten mantle zone beneath an oceanic spreading centre: Numerical modelling of the combined effects of shear segregation and compaction. *Journal of Petrology* **50**, 1071-1106.
- Rabinowicz, M., Genthon, P., Ceuleneer, G. & Hillairret, M. (2001). Compaction in a mantle mush with high melt concentrations and the generation of magma chambers. *Earth and Planetary Science Letters* **188**, 313-328.
- Rabinowicz, M., Lago, B. & Froidevaux, C. (1980). Thermal transfer between the continental asthenosphere and the oceanic subducting lithosphere: its effect on subcontinental convection. *Journal of Geophysical Research: Solid Earth* **85**, 1839-1853.

- Rabinowicz, M., Ricard, Y., & Grégoire, M. (2002). Compaction in a mantle with a very small melt concentration: Implications for the generation of carbonatitic and carbonate-bearing high alkaline mafic melt impregnations. *Earth and Planetary Science Letters*, **203**, 205-220.
- Rajabi, S. A. R., Orabi, G. H. T. & Rai, S. H. A. (2014). Oligocene crustal xenolith-bearing alkaline basalt from Jandaq area (Central Iran): implications for magma genesis and crustal nature, *Island Arc* **23**, 125-141.
- Rapp, R. P., Irifune, T., Shimizu, N., Nishiyama, N., Norman, M. D. & Inoue, T. (2008). Subduction recycling of continental sediments and the origin of geochemically enriched reservoirs in the deep mantle. *Earth and Planetary Science Letters* **271**, 14-23.
- Rhodes, J. M., Dungan, M. A., Blanchard, D. P., & Long, P. E. (1979). Magma mixing at mid-ocean ridges: evidence from basalts drilled near 22 N on the Mid-Atlantic Ridge. *Tectonophysics* **55**, 35-61.
- Rigo, A., Adam, C., Grégoire, M., Gerbault, M., Meyer, R., Rabinowicz, M. & Bonvalot, S. (2015). Insights for the melt migration, the volcanic activity and the ultrafast lithosphere delamination related to the Yellowstone plume (Western USA). *Geophysical Journal International* **203**, 1274-1301.
- Rock, N.M.S. (1991). Lamprophyres. Blackie and Son, *Glasgow*, 285.
- Rohrbach, A. & Schmidt, M. W. (2011). Redox freezing and melting in the Earth's deep mantle resulting from carbon-iron redox coupling. *Nature* **472**, 209-212.
- Rolland, Y., Perincek, D., Kaymakci, N., Sosson, M., Barrier, E. & Avagyan, A. (2012). Evidence for ~80-75 Ma subduction jump during Anatolide-Tauride-Armenian block accretion and ~48 Ma Arabia-Eurasia collision in Lesser Caucasus-East Anatolia. *Journal of Geodynamics* **56-57**, 76-85.
- Rubin, A. M. (1993). Tensile fracture of rocks at high confining pressure: implications for dike propagation. *Journal of Geophysical Research* **98**, 15919-15935.
- Rudnick, R. L. & Gao, S. (2003). Composition of the Continental Crust. In: Holland, H., D. & Turekian, K., K. (eds.) *Treatise on Geochemistry. Oxford: Pergamon* **3**, 1-64
- Saadat, S. & Stern, C. R. (2012). Petrochemistry of a xenolith-bearing Neogene alkali olivine basalt from northeastern Iran. *Journal of Volcanology and Geothermal Research* **225-226**, 13-29.
- Saadat, S., Karimpour, M. H. & Stern, C. (2010). Petrochemical Characteristics of Neogene and Quaternary Alkali Olivine Basalts from the Western Margin of the Lut Block , Eastern Iran **2**, 87-106.

- Saadat, S., Stern, C. R. & Moradian, A. (2014). Petrochemistry of ultrapotassic tephrites and associated cognate plutonic xenoliths with carbonatite affinities from the late Quaternary Qa'le Hasan Ali maars, central Iran. *Journal of Asian Earth Sciences* **89**, 108-122.
- Safonova, I., Maruyama, S. & Litasov, K. (2015). Generation of hydrous-carbonated plumes in the mantle transition zone linked to tectonic erosion and subduction. *Tectonophysics* **662**, 454-471.
- Salters, V. J. M. & Shimizu, N. (1988). World-wide occurrence of HFSE-depleted mantle. *Geochimica et Cosmochimica Acta* **52**, 2177-2182.
- Saunders, A. D., Norry, M. J. & Tarney, J. (1988). Origin of MORB and chemically-depleted mantle reservoirs: trace element constraints. *Journal of Petrology* **1**, 415-445.
- Scott, D. R. & Stevenson, D. J. (1984). Magma solitons. *Geophysical Research Letters* **11**, 1161-1164.
- Semiz, B., Çoban, H., Roden, M. F., Özpınar, Y., Flower, M. F. & McGregor, H. (2012). Mineral composition in cognate inclusions in Late Miocene-Early Pliocene potassic lamprophyres with affinities to lamproites from the Denizli region, Western Anatolia, Turkey: implications for uppermost mantle processes in a back-arc setting. *Lithos* **134**, 253-272.
- Şengör A.M.C , Ozeren S., Genc, T. & Zor E (2003). East Anatolian high plateau as a mantle-supported , north-south shortened domal structure, *Geophysical research letters* **30**, 2-5.
- Şengör, A. M. C. & Kidd, W. S .F. (1979).The post-collisional tectonics of the Turkish-Iranian Plateau and a comparison with Tibet, *Tectonophysics* **55**, 361-376.
- Şengör, A.M.C. & Yilmaz, Y. (1981). Tethyan evolution of Turkey: a plate tectonic approach. *Tectonophysics* **75**, 181-24.
- Shafaii Moghadam, H., Ghorbani, G., Khedr, M. Z., Fazlnia, N., Chiaradia, M., Eyuboglu, Y. ... & Arai, S. (2014). Late Miocene K-rich volcanism in the Eslamieh Peninsula (Saray), NW Iran: implications for geodynamic evolution of the Turkish-Iranian High Plateau. *Gondwana Research* **26**, 1028-1050.
- Shahzeidi, M., Moayyed, M., Murata, M., Yui, T. F., Arai, S., Chen, F. ... & Ahmadian, J. (2017). Late Ediacaran crustal thickening in Iran: Geochemical and isotopic constraints from the~ 550 Ma Mishu granitoids (northwest Iran). *International Geology Review* **59**, 793-811.
- Shaw, C. S. & Eyzaguirre, J. (2000). Origin of megacrysts in the mafic alkaline lavas of the West Eifel volcanic field, Germany. *Lithos* **50**, 75-95.

- Shaw, C. S. (2004). The temporal evolution of three magmatic systems in the West Eifel volcanic field, Germany. *Journal of Volcanology and Geothermal Research* **131**, 213-240.
- Shaw, C. S., Heidelbach, F. & Dingwell, D. B. (2006). The origin of reaction textures in mantle peridotite xenoliths from Sal Island, Cape Verde: the case for “metasomatism” by the host lava. *Contributions to Mineralogy and Petrology* **151**, 681.
- Sheppard, S. & Taylor, W. R. (1992). Barium-and LREE-rich, olivine-mica-lamprophyres with affinities to lamproites, Mt. Bundey, Northern Territory, Australia. *Lithos* **28**, 303-325.
- Shorttle, O., Maclennan, J. & Lambart, S. (2014). Quantifying lithological variability in the mantle. *Earth and Planetary Science Letters* **395**, 24-40.
- Skobeltsyn, G., Mellors, R., Gök, R., Türkelli, N., Yetirmishli, G. & Sandvol, E. (2014). Upper mantle S wave velocity structure of the East Anatolian-Caucasus region. *Tectonics* **33**, 207-221.
- Sodoudi, F., Yuan, X., Kind, R., Heit, B. & Sadidkhouy, A. (2009). Evidence for a missing crustal root and a thin lithosphere beneath the Central Alborz by receiver function studies. *Geophysical Journal International* **177**, 733-742.
- Sokol, A. G. & Kruk, A. N. (2015). Conditions of kimberlite magma generation: experimental constraints. *Russian Geology and Geophysics* **56**, 245-259.
- Sokol, A. G., Kruk, A. N., Palyanov, Y. N. & Sobolev, N. V. (2017). Stability of phlogopite in ultrapotassic kimberlite-like systems at 5.5–7.5 GPa. *Contributions to Mineralogy and Petrology* **172**, 21.
- Sosson, M., Rolland, Y., Müller, C., Danelian, T., Melkonyan, R., Kekelia, S., Adamia, S., Babazadeh, V., Kangarli, T., Avagyan, A., Galoyan, G. & Mosar, J. (2010). Subductions, obduction and collision in the Lesser Caucasus (Armenia, Azerbaijan, Georgia), new insights. *Geological Society, London, Special Publications* **340**, 329-352.
- Sparks, R. S. J., Brooker, R. A., Field, M., Kavanagh, J., Schumacher, J. C., Walter, M. J., & White, J. (2009). The nature of erupting kimberlite melts. *Lithos*, **112**, 429-438.
- Spera, F. J. (1984). Carbon dioxide in petrogenesis III: role of volatiles in the ascent of alkaline magma with special reference to xenolithbearing mafic lavas. *Contributions to Mineralogy and Petrology* **88**, 217-232.
- Spera, F. J. (1987). Dynamics of translithospheric migration of metasomatic fluid and alkaline magma. In: Menzies, M. & Hawkesworth, C. J. (eds) *Mantle Metasomatism*. London: Academic Press, 1-19.

- Stampfli, G. M., Hochard, C., V  rard, C. & Wilhem, C. (2013). The formation of Pangea, *Tectonophysics* **593**, 1-19.
- Stampfli, G.M. (2000). Tethyan oceans. In: Bozkurt, E., Winchester, J.A., Piper, J.D.A. (Eds.), *Tectonics and Magmatism in Turkey and Surrounding Area. Geological Society of London, Special Publication* **173**, 163-185.
- Stepanov, A. S., Campbell, I., Rapp, R. P., Lowczak, J. & Korsakov, A. V. (2017). Discussion: "Xenoliths in ultrapotassic volcanic rocks in the Lhasa block: direct evidence for crust–mantle mixing and metamorphism in the deep crust" by Wang et al. 2016 (*Contributions to Mineralogy and Petrology*) 171: 62. *Contributions to Mineralogy and Petrology* **172**, 19.
- St  cklin, J. (1968). Structural history and tectonics of Iran, a review: *American Association of Petroleum Geologists Bulletin* **52**, 1229-1258.
- Streckeisen, A. (1979). Classification and Nomenclature of Volcanic Rocks, Lamprophyres, Carbonatites, and Melilitic Rocks: Recommendation and Suggestion of the IUGS, Subcommittee on the Systematic of Igneous Rock. *Geology* **4**, 331-335.
- Su, B. X., Chung, S. L., Zarrinkoub, M. H., Pang, K. N., Chen, L., Ji, W. Q. & Khatib, M. M. (2014). Composition and structure of the lithospheric mantle beneath NE Iran: constraints from mantle xenoliths. *Lithos* **202**, 267-282.
- Sun, S. S. & McDonough, W. S. (1989). Chemical and isotopic systematics of oceanic basalts: implications for mantle composition and processes. *Geological Society, London, Special Publications* **42**, 313-345.
- Sweeney, R. J., Thompson, A. B., & Ulmer, P. (1993). Phase relations of a natural MARID composition and implications for MARID genesis, lithospheric melting and mantle metasomatism. *Contributions to Mineralogy and Petrology* **115**, 225-241.
- Tappe, S. (2004). Mesozoic mafic alkaline magmatism of southern Scandinavia. *Contributions to Mineralogy and Petrology* **148**, 312-334.
- Tappe, S., Smart, K. A., Stracke, A., Romer, R. L., Prelevi  c, D. & van den Bogaard, P. (2016). Melt evolution beneath a rifted craton edge: ⁴⁰Ar/³⁹Ar geochronology and Sr–Nd–Hf–Pb isotope systematics of primitive alkaline basalts and lamprophyres from the SW Baltic Shield. *Geochimica et Cosmochimica Acta* **173**, 1-36.
- Temel, A., G  ndođdu, M.N., Gourgaud, A. & Le Pennec, J.L. (1998). Ignimbrites of Cappadocia (Central Anatolia, Turkey): petrology and geochemistry. *Journal of Volcanology and Geothermal Research* **85**, 447-471.

- Tiepolo, M., Bottazzi, P., Foley, S. F., Oberti, R., Vannucci, R. & Zanetti, A. (2001). Fractionation of Nb and Ta from Zr and Hf at mantle depths: the role of titanian pargasite and kaersutite. *Journal of Petrology* **42**, 221-232.
- Toprak, V., Savascin, Y., Gulec, N. & Tankut, A. (1996). Structure of Galatean province. *Int. Geol.Rev* **38**, 747-758.
- Torabi, G. (2011). Middle Eocene Volcanic Shoshonites from Western Margin of Central East Iranian Microcontinent (CEIM), a Mark of Previously Subducted CEIM Confining Oceanic Crust, *Petrology (in farsi)* **19**, 675-689.
- Torabi, G., Arai, S. & Abbasi, H. (2014). Eocene continental dyke swarm from Central Iran (Khur area). *Petrology (in farsi)* **2**, 617-632.
- Torabi, G., Bölgesi, Ş. Q., & Eyaleti, B. Y. (2009). Subduction-related Eocene Shoshonites from the Cenozoic Urumieh-Dokhtar Magmatic Arc (Qaleh-Khargooshi Area , Western Yazd Province , Iran), *Turkish Journal of Earth Sciences* **18**, 583-613.
- Trønnes, R. G. (2002). Stability range and decomposition of potassic richterite and phlogopite end members at 5-15 GPa. *Mineralogy and Petrology* **74**, 129-148.
- Tumiati, S., Fumagalli, P., Tiraboschi, C. & Poli, S. (2013). An Experimental Study on COH-bearing Peridotite up to 3.2 GPa and Implications for Crust- Mantle Recycling, *Journal of Petrology* **54**, 453-479.
- Turcotte, D. L. & Schubert, G. (2014). *Geodynamics*. Cambridge University Press.
- Ubide, T., Galé, C., Larrea, P., Arranz, E. & Lago, M. (2014). Antecrysts and their effect on rock compositions: the Cretaceous lamprophyre suite in the Catalonian Coastal Ranges (NE Spain). *Lithos* **206**, 214-233.
- Ulmer, P. & Sweeney, R. J. (2002). Generation and differentiation of group II kimberlites: constraints from a high-pressure experimental study to 10 GPa. *Geochimica et Cosmochimica Acta* **66**, 2139-2153.
- Ulmer, P. (2001). Partial melting in the mantle wedge-the role of H₂O in the genesis of mantle-derived 'arc-related' magmas. *Physics of the Earth and Planetary Interiors* **127**, 215-232.
- Van den Berg, A. P., Yuen, D. A., Beebe, G. L. & Christiansen, M. D. (2010). The dynamical impact of electronic thermal conductivity on deep mantle convection of exosolar planets. *Physics of the Earth and Planetary Interiors* **178**, 136-154.
- van der Meijde, M., Marone, F., Giardini, D. & van der Lee, S. (2003). Seismic evidence for water deep in Earth's upper mantle. *Science* **300**, 1556-1558.

- Verdel, C., Wernicke, B. P., Hassanzadeh, J. & Guest, B. (2011). A Paleogene extensional arc flare-up in Iran. *Tectonics* **30**, 1-20.
- Verdel, C., Wernicke, B. P., Ramezani, J., Hassanzadeh, J., Renne, P. R. & Spell, T. L. (2007). Geology and thermochronology of Tertiary Cordilleran-style metamorphic core complexes in the Saghand region of central Iran, *Geological Society of America Bulletin* **119**, 961-977.
- Vincent, S. J., Allen, M. B., Ismail-zadeh, A. D., Foland, K. A. & Simmons, M. D. (2005). Insights from the Talysh of Azerbaijan into the Paleogene evolution of the South Caspian region, *Geological Society of America Bulletin* **11/12**, 1513-1533.
- Wagner, C. & Velde, D. (1986). The mineralogy of K-richterite-bearing lamproites. *American Mineralogist* **71**, 17-37.
- Walker, R. T., Gans, P., Allen, M. B., Jackson, J., Khatib, M., Marsh, N. & Zarrinkoub, M. (2009). Late Cenozoic volcanism and rates of active faulting in eastern Iran, *Geophysical Journal International* **177**, 783-805.
- Wallace, M. E. & Green, D. H. (1988). An experimental determination of primary carbonatite magma composition. *Nature* **335**, 343-346.
- Wang, X. C., Wilde, S. A., Xu, B. & Pang, C. J. (2016). Origin of arc-like continental basalts: Implications for deep-Earth fluid cycling and tectonic discrimination. *Lithos* **261**, 5-45.
- Wang, Y., Foley, S. F., & Prelević, D. (2017). Potassium-rich magmatism from a phlogopite-free source. *Geology* **45**, 467-470.
- Wass, S. Y. (1979). Multiple origins of clinopyroxenes in alkali basaltic rocks. *Lithos* **12**, 115-132.
- Waters, F. G. (1987). A suggested origin of MARID xenoliths in kimberlites by high pressure crystallization of an ultrapotassic rock such as lamproite. *Contributions to Mineralogy and Petrology* **95**, 523-533.
- Wei, X., Xu, Y. G., Luo, Z. Y., Zhao, J. X. & Feng, Y. X. (2015). Composition of the Tarim mantle plume: Constraints from clinopyroxene antecrysts in the early Permian Xiaohaizi dykes, NW China. *Lithos* **230**, 69-81.
- Weis, D. & Demaiffe, D. (1985). A depleted mantle source for kimberlites from Zaire: Nd, Sr and Pb isotopic evidence. *Earth and planetary science letters* **73**, 269-277.
- Wiggins, C. & Spiegelman, M. (1995). Magma migration and magmatic solitary waves in 3-D. *Geophysical Research Letters* **22**, 1289-1292.

- Willbold, M. & Stracke, A. (2006). Trace element composition of mantle end-members: Implications for recycling of oceanic and upper and lower continental crust, *Geochemistry, Geophysics, Geosystems* **7**, 1-30.
- Willm, C. H., Brasseur, R., Revoo, G., Marchand, J., Rochet, J. & Hindermeier, J. (1961). *Geological report number 235 on Moghan area. IFP mission in Azerbaijan, National Iranian Oil Company* (No. 235). Geological report.
- Wilson, M. & Bianchini, G. (1999). Tertiary-Quaternary magmatism within the Mediterranean and surrounding regions. in ‘‘The Mediterranean Basins: Tertiary Extension Within the Alpine Orogen’’, B. Durand, L. Jolivet, F. Horvath, M. Seranne, eds. *Geological Society Special Publication* **156**, 141-168.
- Wilson, M. (1989). *Igneous Petrogenesis: a Global Tectonic Approach*. Chapman & Hall, London, 466.
- Wilson, M., Tankut, A. & Guleg, N. (1997). Tertiary volcanism of the Galatia province, north-west Central, *Lithos* **42**, 105-121.
- Woolley, A. R., Bergman, S. C., Edgar, A. D., Le Bas, M. J., Mitchell, R. H., Rock, N. M. & Scott Smith, B. H. (1996). Classification of lamprophyres, lamproites, kimberlites, and the kalsilitic, melilitic, and leucitic rocks. *Canadian Mineralogist* **34**, 175-186.
- Woolley, A. R., Bergman, S. C., Edgar, A. D., Le Bas, M. J., Mitchell, R. H., Rock, N. M. & Smith, B. H. S. (1996). Classification of lamprophyres, lamproites, kimberlites, and the kalsilitic, melilitic, and leucitic rocks. *The Canadian Mineralogist* **34**, 175-186.
- Wyllie, P. J. (1980). The origin of kimberlite. *Journal of Geophysical Research: Solid Earth* **85**, 6902-6910.
- Yılmaz, A., Adamia, S., Chabukiani, A., Chkhotua, T., Erdogan, K., Tuzcu, S. & Karabiyikoglu, M. (2000). Structural Correlation of the Southern Transcaucasus (Georgia)-Eastern Pontides (Turkey). In: *Geological Society, London, Special Publications* **173**, 171-182.
- Zabelina, I., Koulakov, I., Amanatashvili, I., El Khrepy, S. & Al-Arifi, N. (2016). Seismic structure of the crust and uppermost mantle beneath Caucasus based on regional earthquake tomography. *Journal of Asian Earth Sciences* **119**, 87-99.
- Zhao, D., Y. Tian, J. Lei, L. Liu, and S. Zheng (2009). Seismic image and origin of the Changbai intraplate volcano in East Asia: Role of big mantle wedge above the stagnant Pacific slab, *Physics of the Earth and Planetary Interiors* **173**, 197-206.

- Zhu, Y. & Ogasawara, Y. (2004). Clinopyroxene phenocrysts (with green salite cores) in trachybasalts: implications for two magma chambers under the Kokchetav UHP massif, North Kazakhstan. *Journal of Asian Earth Sciences* **22**, 517-527.
- Zindler, A. & Hart, S., (1986). Chemical geodynamics. *Annual Review of Earth and Planetary Science Letters* **14**, 493-571.

Appendix

Table 1. Representative composition of clinopyroxene of alkaline rocks from the Salavat Range.

Rock type	host lava (Ha)	host lava (Ha)	host lava (Ha)	host lava (Ha)	pillow lava (Hb)	pillow lava (Hb)
Sample	M-118	M-118	M-116	M-116	M-128	M-128
Number of analysis and zone	78 (High Mg#)	64 (Low Mg#)	7 (cr)	5 (rm)	15 (cr)	24 (rm)
Type of zoning			<i>IV</i>	<i>IV</i>	<i>IV</i>	<i>IV</i>
SiO ₂	50,71	49,06	50,64	49,02	48,95	49,17
TiO ₂	0,56	0,83	0,67	0,96	0,79	0,72
Al ₂ O ₃	3,32	5,23	3,78	5,00	4,76	4,64
FeO	7,43	8,03	6,45	7,90	6,12	5,95
MnO	0,20	0,16	0,13	0,16	0,40	0,37
MgO	14,68	13,51	14,43	13,44	13,73	13,89
CaO	22,69	22,75	23,14	22,71	22,67	22,77
Na ₂ O	0,28	0,31	0,26	0,29	0,38	0,39
K ₂ O	0,00	0,00	0,01	0,02	0,01	0,01
Cr ₂ O ₃	0,03	0,05	0,27	0,14	0,01	0,01
Total	99,90	99,93	99,82	99,66	99,68	99,79
Structural formula (on 6-oxygene basis)						
Si	1,88	1,82	1,87	1,82	1,82	1,83
Al (iv)	0,12	0,18	0,13	0,18	0,18	0,17
Al (vi)	0,02	0,05	0,04	0,04	0,03	0,03
Fe ²⁺	0,12	0,12	0,11	0,12	0,11	0,10
Fe ³⁺	0,11	0,13	0,09	0,12	0,13	0,13
Mg ^I	0,73	0,68	0,74	0,68	0,76	0,77
Ti	0,02	0,02	0,02	0,03	0,02	0,02
Cr	0,00	0,00	0,01	0,00	0,00	0,00
Na	0,02	0,02	0,02	0,02	0,03	0,03
Ca	0,90	0,90	0,92	0,91	0,91	0,91
Mg	0,07	0,07	0,06	0,07		
Wo	51,30	53,24	52,02	53,17	50,93	50,95
En	41,91	39,90	41,63	39,71	42,92	43,23
Fs	6,79	6,85	6,35	7,12	6,15	5,83
Mg#	0,76	0,73	0,79	0,73	0,76	0,77

Table 1 (continued).

Rock type	pillow lava (Hb)	pillow lava (H analcime beari)	analcime beari	tephrite dyke	tephrite dyke	
Sample	M-47	M-47	M-22	M-22	M-84	M-84
Number of analysis and zone	15	16	5 (cr)	5 (rm)	15 (colorless cr)	11 (bright band)
Type of zoning			<i>IV</i>	<i>IV</i>	<i>II</i>	<i>II</i>
SiO ₂	50,17	49,83	47,20	45,74	53,11	52,52
TiO ₂	0,62	0,72	1,43	1,53	0,31	0,51
Al ₂ O ₃	4,19	4,81	6,94	8,21	2,04	3,12
FeO	7,11	7,19	7,34	7,53	4,71	5,97
MnO	0,21	0,28	0,40	0,52	0,13	0,13
MgO	14,02	13,71	11,24	10,60	15,93	14,90
CaO	23,30	22,99	23,04	22,43	23,27	21,97
Na ₂ O	0,31	0,42	0,65	0,65	0,42	0,68
K ₂ O	0,01	0,01	0,01	0,00	0,00	0,01
Cr ₂ O ₃	0,01	0,02	0,01	0,01	0,59	0,52
Total	99,98	100,19	101,23	100,81	100,51	100,34
Structural formula (on 6-oxyge						
Si	1,85	1,84	1,75	1,71	1,94	1,92
Al (iv)	0,15	0,16	0,25	0,29	0,06	0,08
Al (vi)	0,04	0,05	0,06	0,07	0,02	0,06
Fe ²⁺	0,11	0,11	0,15	0,15	0,08	0,11
Fe ³⁺	0,11	0,12	0,16	0,18	0,06	0,07
Mg ^I	0,73	0,71	0,62	0,59	0,81	0,73
Ti	0,02	0,02	0,04	0,04	0,01	0,01
Cr	0,00	0,00	0,00	0,00	0,02	0,02
Na	0,02	0,03	0,05	0,05	0,03	0,05
Ca	0,92	0,91	0,92	0,90	0,91	0,86
Mg	0,05	0,05			0,06	0,08
Wo	52,63	52,60	54,38	54,67	50,56	50,53
En	41,28	41,10	36,91	35,98	44,94	42,79
Fs	6,08	6,30	8,72	9,34	4,50	6,67
Mg [#]	0,77	0,76	0,67	0,64	0,85	0,80

Table 1 (continued).

Rock type	tephrite dyke	tephrite dyke	tephrite dyke	tephrite dyke	tephrite dyke	tephrite dyke
Sample	M-84	ch006	ch006	M-88	M-84	M-84
Number of analysis and zone	22 (rm)	28 (colorless cr)	22 (rm)	5 (colorless cr)	26 (colorless cr)	24 (rm)
Type of zoning	<i>II</i>	<i>I</i>	<i>I</i>	<i>I</i>	<i>I</i>	<i>I</i>
SiO ₂	49,75	51,00	48,68	51,91	51,43	49,53
TiO ₂	0,75	0,43	0,83	0,35	0,40	0,68
Al ₂ O ₃	4,14	2,62	4,79	2,40	1,89	3,54
FeO	8,34	6,59	8,86	5,44	6,20	7,90
MnO	0,25	0,19	0,24	0,11	0,14	0,25
MgO	13,38	14,79	12,80	15,34	15,17	13,73
CaO	22,84	23,61	22,79	24,04	23,47	22,94
Na ₂ O	0,41	0,34	0,45	0,24	0,21	0,32
K ₂ O	0,00	0,00	0,01	0,01	0,00	0,00
Cr ₂ O ₃	0,02	0,04	0,01	0,17	0,05	0,01
Total	99,87	99,60	99,45	100,05	98,97	98,88
Structural formula (on 6-oxyge						
Si	1,85	1,89	1,82	1,91	1,91	1,86
Al (iv)	0,15	0,11	0,18	0,09	0,09	0,14
Al (vi)	0,03	0,00	0,03	0,01	0,00	0,01
Fe ²⁺	0,13	0,08	0,12	0,08	0,10	0,11
Fe ³⁺	0,13	0,12	0,16	0,09	0,09	0,13
Mg ¹	0,69	0,78	0,67	0,81	0,80	0,72
Ti	0,02	0,01	0,02	0,01	0,01	0,02
Cr	0,00	0,00	0,00	0,01	0,00	0,00
Na	0,03	0,02	0,03	0,02	0,02	0,02
Ca	0,91	0,94	0,91	0,95	0,94	0,92
Mg	0,05	0,03	0,05	0,03	0,04	0,05
Wo	52,63	52,07	53,68	51,69	51,05	52,53
En	39,81	43,44	39,22	44,11	43,50	41,00
Fs	7,56	4,49	7,10	4,20	5,45	6,47
Mg#	0,73	0,79	0,71	0,83	0,81	0,74

Table 1 (continued).

Rock type	tephrite dyke	tephrite dyke	tephrite dyke	tephrite dyke	tephrite dyke	tephrite dyke	tephrite dyke
Sample	M-65	M-65	M-84	M-84	ch006	ch006	M-65
Number of analysis and zone	20 (colorless cr)	5 (rm)	102 (osc, cr)	67 (osc, rm)	122 (osc, cr)	81 (osc, rm)	5 (osc, cr)
Type of zoning	<i>I</i>	<i>I</i>	<i>IV</i>	<i>IV</i>	<i>IV</i>	<i>IV</i>	<i>IV</i>
SiO ₂	52,15	49,09	49,47	48,18	49,66	50,06	48,80
TiO ₂	0,36	0,93	0,72	0,97	0,76	0,68	0,92
Al ₂ O ₃	2,70	5,59	3,89	5,04	4,45	4,00	6,01
FeO	5,80	7,18	7,61	8,84	8,59	8,16	6,79
MnO	0,12	0,16	0,19	0,23	0,26	0,23	0,19
MgO	16,10	13,39	13,82	12,86	12,97	13,33	13,37
CaO	23,71	23,12	23,46	22,86	22,40	22,81	23,24
Na ₂ O	0,07	0,28	0,32	0,40	0,47	0,39	0,25
K ₂ O	0,01	0,00	0,00	0,01	0,07	0,00	0,01
Cr ₂ O ₃	0,18	0,02	0,01	0,01	0,01	0,02	0,03
Total	101,31	101,46	99,48	99,39	99,63	99,67	101,52
Structural formula (on 6-oxyge							
Si	1,89	1,80	1,84	1,80	1,85	1,86	1,79
Al (iv)	0,10	0,20	0,16	0,20	0,15	0,14	0,21
Al (vi)	0,01	0,05	0,01	0,03	0,05	0,04	0,05
Fe ²⁺	0,10	0,14	0,09	0,10	0,16	0,15	0,13
Fe ³⁺	0,07	0,12	0,15	0,17	0,11	0,10	0,13
Mg ^I	0,87	0,73	0,73	0,67	0,66	0,69	0,73
Ti	0,01	0,03	0,02	0,03	0,02	0,02	0,03
Cr	0,01	0,00	0,00	0,00	0,00	0,00	0,00
Na	0,00	0,02	0,02	0,03	0,03	0,03	0,02
Ca	0,92	0,91	0,94	0,92	0,90	0,91	0,91
Mg			0,04	0,05	0,06	0,05	
Wo	48,80	51,03	53,36	54,22	52,29	52,13	51,54
En	46,08	41,10	41,68	39,63	38,62	39,22	41,21
Fs	5,12	7,87	4,95	6,15	9,09	8,65	7,25
Mg#	0,84	0,74	0,76	0,71	0,71	0,73	0,74

Table 1 (continued).

Rock type	tephrite dyke	tephrite dyke	tephrite dyke	tephrite dyke	tephrite dyke	tephrite dyke	lamprophyre
Sample	M-65	M-79	M-84b	M-84	ch006	M-88	M-112
Number of analysis and zone	5 (osc, rm)	733 (osc)	49 (osc)	18 (mes)	18 (mes)	88 (mes)	80 (colorless cr)
Type of zoning	<i>IV</i>	<i>IV</i>	<i>IV</i>				<i>I</i>
SiO ₂	49,09	50,28	50,61	48,89	50,08	45,56	52,97
TiO ₂	0,93	0,66	0,61	0,89	0,75	1,56	0,22
Al ₂ O ₃	5,59	4,43	3,09	4,33	3,50	7,59	1,82
FeO	7,18	7,20	7,62	9,15	8,81	10,33	3,95
MnO	0,16	0,23	0,23	0,29	0,29	0,25	0,09
MgO	13,39	13,89	14,00	12,69	13,11	10,57	16,18
CaO	23,12	23,01	23,16	22,04	22,20	22,55	24,37
Na ₂ O	0,28	0,35	0,33	0,46	0,44	0,46	0,18
K ₂ O	0,00	0,01	0,00	0,02	0,02	0,06	0,00
Cr ₂ O ₃	0,02	0,02	0,01	0,01	0,02	0,01	0,12
Total	101,46	101,07	99,66	98,77	99,23	98,98	99,90
Structural formula (on 6-oxyge							
Si	1,80	1,85	1,88	1,84	1,88	1,73	1,94
Al (iv)	0,20	0,15	0,12	0,16	0,12	0,27	0,06
Al (vi)	0,05	0,04	0,02	0,04	0,03	0,07	0,02
Fe ²⁺	0,14	0,14	0,13	0,16	0,18	0,14	0,07
Fe ³⁺	0,12	0,10	0,11	0,13	0,10	0,19	0,05
Mg ^I	0,73	0,76	0,72	0,65	0,67	0,56	0,85
Ti	0,03	0,02	0,02	0,03	0,02	0,04	0,01
Cr	0,00	0,00	0,00	0,00	0,00	0,00	0,00
Na	0,02	0,02	0,02	0,03	0,03	0,03	0,01
Ca	0,91	0,91	0,92	0,89	0,89	0,92	0,96
Mg			0,05	0,07	0,07	0,04	0,03
Wo	51,03	50,14	52,25	52,37	51,41	56,99	50,89
En	41,10	42,04	40,73	38,04	38,21	34,62	45,45
Fs	7,87	7,82	7,02	9,59	10,38	8,38	3,66
Mg#	0,74	0,75	0,75	0,69	0,70	0,63	0,88

Table 1 (continued).

Rock type	lamprophyre	lamprophyre	lamprophyre	lamprophyre	lamprophyre	lamprophyre	lamprophyre
Sample	M-112	M-113	M-113	M-73	M-73	M-113	M-113
Number of analysis and zone	116 (rim)	22 (colorless cr)	28 (rm)	108 (osc, cr)	74 (osc, rm)	11 (osc)	31 (osc, rm)
Type of zoning	<i>I</i>	<i>I</i>	<i>I</i>	<i>IV</i>	<i>IV</i>	<i>IV</i>	<i>IV</i>
SiO ₂	49,55	54,27	51,05	50,49	50,16	51,01	50,51
TiO ₂	0,55	0,18	0,52	0,52	0,55	0,46	0,52
Al ₂ O ₃	4,01	1,15	3,66	3,54	4,18	3,38	3,57
FeO	7,70	4,14	6,81	6,93	7,29	7,03	7,04
MnO	0,17	0,12	0,14	0,17	0,18	0,26	0,27
MgO	13,47	15,90	14,26	14,36	13,71	13,98	14,01
CaO	23,45	24,82	23,88	23,20	23,55	23,04	22,92
Na ₂ O	0,30	0,23	0,20	0,28	0,30	0,42	0,38
K ₂ O	0,00	0,00	0,00	0,00	0,01	0,00	0,03
Cr ₂ O ₃	0,02	0,23	0,01	0,05	0,04	0,03	0,08
Total	99,23	101,06	100,55	99,54	99,96	99,60	99,33
Structural formula (on 6-oxyge							
Si	1,85	1,97	1,88	1,87	1,86	1,89	1,88
Al (iv)	0,15	0,03	0,12	0,13	0,14	0,11	0,12
Al (vi)	0,03	0,02	0,04	0,03	0,04	0,04	0,04
Fe ²⁺	0,11	0,10	0,12	0,11	0,11	0,13	0,12
Fe ³⁺	0,13	0,02	0,09	0,10	0,12	0,08	0,10
Mg ¹	0,72	0,84	0,74	0,74	0,72	0,73	0,73
Ti	0,02	0,00	0,01	0,01	0,02	0,01	0,01
Cr	0,00	0,01	0,00	0,00	0,00	0,00	0,00
Na	0,02	0,02	0,01	0,02	0,02	0,03	0,03
Ca	0,94	0,96	0,94	0,92	0,93	0,92	0,91
Mg	0,03	0,02	0,04	0,05	0,04	0,05	0,05
Wo	53,14	50,50	52,19	52,15	53,24	51,55	51,86
En	40,44	44,15	41,10	41,61	40,49	40,88	41,29
Fs	6,43	5,35	6,71	6,25	6,27	7,57	6,85
Mg#	0,75	0,87	0,78	0,77	0,76	0,77	0,77

Table 1 (continued).

Rock type	lamprophyre	lamprophyre	lamprophyre	lamprophyre	lamprophyre	lamprophyre	lamprophyre
Sample	M-113	M-113	M-114	M-114	M-113	M-113	M-113
Number of analysis and zone	17 (green)	9 (green rm)	12 (green rm)	9 (colorless cr)	8 (green cr)	7 (colorless rm)	4 (green cr)
Type of zoning			<i>I</i>	<i>I</i>	<i>III</i>	<i>III</i>	<i>III</i>
SiO ₂	47,93	49,87	50,02	51,86	49,01	48,47	47,44
TiO ₂	0,63	0,60	0,59	0,30	0,66	0,79	0,91
Al ₂ O ₃	5,02	4,20	3,76	2,57	4,77	5,26	6,54
FeO	10,91	7,28	8,52	6,30	8,02	7,75	9,77
MnO	0,49	0,18	0,38	0,19	0,17	0,19	0,35
MgO	10,42	13,61	12,43	14,28	12,94	12,95	10,86
CaO	23,47	23,45	23,26	24,10	23,44	23,50	23,37
Na ₂ O	0,41	0,23	0,55	0,32	0,31	0,24	0,35
K ₂ O	0,01	0,01	0,01	0,01	0,01	0,02	0,02
Cr ₂ O ₃	0,01	0,01	0,01	0,02	0,01	0,00	0,01
Total	99,32	99,46	99,58	99,98	99,37	99,17	99,63
Structural formula (on 6-oxyge							
Si	1,82	1,86	1,87	1,92	1,83	1,81	1,79
Al (iv)	0,18	0,14	0,13	0,08	0,17	0,19	0,21
Al (vi)	0,04	0,04	0,04	0,03	0,04	0,05	0,08
Fe ²⁺	0,20	0,13	0,15	0,12	0,12	0,11	0,17
Fe ³⁺	0,15	0,10	0,11	0,07	0,13	0,13	0,14
Mg ^I	0,59	0,71	0,68	0,77	0,69	0,69	0,59
Ti	0,02	0,02	0,02	0,01	0,02	0,02	0,03
Cr	0,00	0,00	0,00	0,00	0,00	0,00	0,00
Na	0,03	0,02	0,04	0,02	0,02	0,02	0,03
Ca	0,95	0,94	0,93	0,95	0,94	0,94	0,94
Mg	0,00	0,04	0,02	0,02	0,03	0,03	0,02
Wo	54,83	52,66	52,93	51,72	53,72	54,27	55,42
En	33,74	40,15	38,33	41,63	39,33	39,55	34,51
Fs	11,43	7,18	8,74	6,65	6,96	6,18	10,07
Mg [#]	0,63	0,76	0,72	0,80	0,73	0,74	0,66

Table 1 (continued).

Rock type	lamprophyre	lamprophyre	lamprophyre	lamprophyre	lamprophyre	lamprophyre
Sample	M-113	M-71	M-71	M-71	M-114	M-114
Number of analysis and zone	5 (colorless rm)	6 (colorless cr)	6 (green middle)	4 (green rm)	21 (green cr)	14 (colorless rm)
Type of zoning		<i>I</i>	<i>III</i>		<i>III</i>	<i>III</i>
SiO ₂	46,84	50,46	47,63	48,82	51,41	53,44
TiO ₂	1,05	0,43	0,85	0,61	0,34	0,16
Al ₂ O ₃	6,88	3,26	5,15	4,72	2,60	1,16
FeO	8,40	6,07	9,56	7,81	7,97	3,19
MnO	0,20	0,12	0,19	0,16	0,44	0,09
MgO	11,94	14,67	12,45	13,30	13,57	16,89
CaO	23,70	23,73	22,44	23,71	22,91	24,17
Na ₂ O	0,27	0,21	0,35	0,26	0,50	0,18
K ₂ O	0,01	0,02	0,00	0,02	0,05	0,00
Cr ₂ O ₃	0,01	0,36	0,01	0,02	0,02	0,51
Total	99,33	99,35	98,67	99,49	99,81	99,79
Structural formula (on 6-oxyge						
Si	1,76	1,87	1,80	1,82	1,91	1,95
Al (iv)	0,24	0,13	0,20	0,18	0,09	0,05
Al (vi)	0,06	0,02	0,03	0,03	0,03	0,00
Fe ²⁺	0,09	0,07	0,13	0,09	0,15	0,04
Fe ³⁺	0,17	0,12	0,17	0,15	0,09	0,05
Mg ^I	0,65	0,77	0,64	0,71	0,72	0,88
Ti	0,03	0,01	0,02	0,02	0,01	0,00
Cr	0,00	0,01	0,00	0,00	0,00	0,01
Na	0,02	0,01	0,03	0,02	0,04	0,01
Ca	0,95	0,94	0,91	0,95	0,91	0,95
Mg	0,02	0,04	0,06	0,03	0,04	0,04
Wo	56,40	52,69	53,98	54,19	51,14	50,58
En	38,28	43,24	38,12	40,71	40,16	47,14
Fs	5,32	4,07	7,90	5,10	8,70	2,28
Mg [#]	0,71	0,80	0,68	0,75	0,74	0,90

Table 1 (continued).

Rock type	lamprophyre	lamprophyre	lamprophyre	gabbro	monzogabbro	alk-felds syenite
Sample	M-112	M-71	M-113	M-95	M-95	M-97
Number of analysis and zone	8 (mes)	6 (mes)	11 (mes)	21 (rm)	6 (cr)	4
Type of zoning						
SiO ₂	48,71	50,41	48,42	51,36	50,07	50,64
TiO ₂	0,77	0,49	0,86	0,99	1,17	0,92
Al ₂ O ₃	5,04	3,65	5,47	3,25	4,64	3,57
FeO	8,62	6,63	8,01	8,11	8,71	7,45
MnO	0,19	0,14	0,23	0,25	0,24	0,24
MgO	12,60	14,10	12,80	14,14	13,80	14,98
CaO	23,25	23,62	23,28	21,61	21,32	21,87
Na ₂ O	0,35	0,21	0,30	0,44	0,43	0,34
K ₂ O	0,00	0,01	0,02	0,01	0,00	0,01
Cr ₂ O ₃	0,03	0,12	0,00	0,07	0,08	0,13
Total	99,56	99,38	99,46	100,23	100,50	101,00
Structural formula (on 6-oxyge						
Si	1,82	1,87	1,81	1,90	1,85	1,86
Al (iv)	0,18	0,13	0,19	0,10	0,15	0,14
Al (vi)	0,04	0,03	0,05	0,04	0,05	0,01
Fe ²⁺	0,13	0,11	0,11	0,19	0,17	0,15
Fe ³⁺	0,14	0,09	0,14	0,06	0,09	0,10
Mg ¹	0,66	0,74	0,68	0,68	0,64	0,82
Ti	0,02	0,01	0,02	0,03	0,03	0,03
Cr	0,00	0,00	0,00	0,00	0,00	0,00
Na	0,03	0,01	0,02	0,03	0,03	0,02
Ca	0,93	0,94	0,93	0,86	0,84	0,86
Mg	0,04	0,04	0,04	0,10	0,12	
Wo	53,98	52,36	54,23	49,80	50,81	47,05
En	38,52	41,28	39,24	39,30	38,70	44,83
Fs	7,50	6,36	6,53	10,90	10,48	8,12
Mg#	0,71	0,78	0,73	0,73	0,70	0,77

Table 2. Average mineral chemistry of feldspars from lavas and intrusions of this study.

N= number of analyses in average

Rock type	kersantite	kersantite	minette	kersantite	kersantite	kersantite	tephrite
Sample	M-71	M-159	M-112	M-113	M-114	M-114	choo6
N	3	3	8	46	19	7	6
Na ₂ O	4,20	1,32	4,28	1,74	1,37	4,50	5,02
Al ₂ O ₃	18,95	33,41	19,58	32,67	24,75	20,88	28,45
SiO ₂	65,47	45,80	64,43	47,25	48,01	63,12	52,56
K ₂ O	10,04	0,10	9,52	0,14	0,22	9,04	1,24
CaO	0,66	17,78	1,03	17,09	18,48	0,93	11,41
MnO	0,02	0,00	0,01	0,01	0,07	0,03	0,01
FeO	0,53	0,61	0,41	0,60	2,67	0,90	0,73
Cr ₂ O ₃	0,03	0,00	0,01	0,01	0,01	0,01	0,01
NiO	0,01	0,00	0,01	0,01	0,03	0,01	0,01
MgO	0,01	0,00	0,04	0,04	3,80	0,16	0,06
TiO ₂	0,06	0,02	0,08	0,02	0,23	0,11	0,06
Total	99,95	99,05	99,55	99,58	99,64	99,69	99,56
An	3,24	87,65	5,14	83,75	86,50	4,82	53,48
Ab	37,58	11,77	38,52	15,46	12,19	39,69	40,14
Or	59,18	0,58	56,34	0,79	1,31	55,49	6,39

Rock type	tephrite	tephrite	tephrite	analcime bearing lavas	host lavas (ha)	monzo gabbro
Sample	M-84	M-65	M-79	M-22	M-116	M-95
N	16	12	2	3	5	11
Na ₂ O	3,83	3,18	0,85	2,76	3,46	3,68
Al ₂ O ₃	28,20	19,73	18,48	31,48	28,85	30,24
SiO ₂	53,09	64,20	65,52	49,72	51,00	51,67
K ₂ O	1,48	11,30	15,78	0,19	0,71	0,27
CaO	11,62	1,15	0,03	15,00	13,34	13,50
MnO	0,02				0,01	0,02
FeO	0,67	0,27	0,19	0,76	0,99	0,38
Cr ₂ O ₃	0,01				0,00	0,01
NiO	0,01				0,01	0,01
MgO	0,05	0,00	0,00	0,00	0,11	0,02
TiO ₂	0,05	0,03	0,06	0,01	0,05	0,07
Total	99,02	99,85	100,89	99,91	98,56	99,86
An	57,32	5,57	0,14	74,21	65,20	65,89
Ab	34,13	28,30	7,48	24,71	30,64	32,55
Or	8,55	66,13	92,38	1,08	4,16	1,56

Table 2 (continued).

Rock type	monzo gabbro	monzo gabbro	monzonite	monzonite	alk feld-syenite	hornblende andesite
Sample	M-95	M-95	M-56	M-56	M-97	M-45b
N	19	2	13	56	3	5
Na ₂ O	5,75	4,58	4,05	5,73	5,50	2,92
Al ₂ O ₃	26,58	19,40	18,34	23,32	19,33	19,08
SiO ₂	57,00	65,62	66,66	61,08	65,82	63,70
K ₂ O	0,60	9,01	10,63	2,47	8,19	11,46
CaO	9,26	0,87	0,25	6,51	0,91	0,22
MnO	0,01	0,02				
FeO	0,36	0,25	0,10	0,38	0,33	0,14
Cr ₂ O ₃	0,01	0,00				
NiO	0,01	0,01				
MgO	0,05	0,01	0,00	0,02	0,00	0,00
TiO ₂	0,12	0,15	0,00	0,01	0,07	0,01
Total	99,75	99,93	100,04	99,53	100,22	99,80
An	45,44	4,40	1,25	32,99	4,40	1,08
Ab	51,06	41,64	35,75	50,69	48,26	26,40
Or	3,50	53,97	63,01	16,33	47,25	68,37

Table 3. Average mineral chemistry of phlogopite and biotite from lavas and intrusions of this study.

rock type sample N	minette M-112 15	kersantite M-113 7	kersantite M-159 6	kersantite M-71 17	kersantite M-73b 5	kersantite M-71 8 (mes)	tephrite M-84 2 (mes)	Hb andesite M-45 2	monzonite M-56 13	syenite M-97 2
SiO ₂	38,18	37,09	37,28	36,53	35,80	36,71	35,35	35,47	37,24	37,72
TiO ₂	1,20	1,40	2,98	2,14	3,75	2,26	4,72	2,78	4,73	4,56
Al ₂ O ₃	15,02	15,25	15,06	15,80	14,98	15,19	13,08	14,93	13,93	13,18
Cr ₂ O ₃	0,31	0,04	0,07	0,01	0,02	0,08	0,01	0,00	0,02	0,05
FeO	9,81	9,32	13,47	11,76	14,08	12,06	24,61	15,73	14,01	13,92
MnO	0,05	0,07	0,22	0,11	0,23	0,14	0,48	0,42	0,25	0,40
MgO	19,65	19,92	16,63	17,51	14,98	17,35	7,56	16,43	15,86	15,96
CaO	0,05	0,03	0,04	0,11	0,06	0,04	0,04	0,18	0,23	0,02
Na ₂ O	0,60	0,43	0,48	0,52	0,61	0,53	0,62	0,22	0,34	0,56
K ₂ O	8,98	9,90	8,85	9,00	8,79	9,05	8,81	7,01	8,59	8,96
BaO	0,22	0,34		0,42	0,68	0,46		0,23		0,07
Total	93,86	94,05	95,02	93,49	93,30	93,40	95,26	93,15	95,20	95,33
Structural formulae calculated on the basis of 22 oxygens										
Si	5,64	5,53	5,54	5,48	5,46	5,53	5,58	5,40	5,54	5,62
Al	2,36	2,47	2,46	2,52	2,54	2,47	2,42	2,60	2,46	2,38
Ti	0,13	0,16	0,33	0,24	0,43	0,26	0,56	0,32	0,53	0,51
Cr	0,04	0,01	0,01	0,00	0,00	0,01	0,00	0,00	0,00	0,01
Fe ²⁺	1,21	1,16	1,67	1,48	1,80	1,52	3,25	2,01	1,74	1,73
Mn ²⁺	0,01	0,01	0,03	0,01	0,03	0,02	0,06	0,05	0,03	0,05
Mg	4,32	4,43	3,68	3,91	3,40	3,89	1,77	3,73	3,52	3,54
Ca	0,01	0,01	0,01	0,02	0,01	0,01	0,01	0,03	0,04	0,00
Na	0,17	0,12	0,14	0,15	0,18	0,15	0,19	0,06	0,10	0,16
K	1,69	1,88	1,68	1,72	1,71	1,74	1,77	1,36	1,63	1,70
cation sum	15,58	15,77	15,55	15,54	15,56	15,59	15,62	15,57	15,59	15,71
Mg#	0,78	0,79	0,68	0,72	0,65	0,72	0,35	0,64	0,66	0,67

Table 4. Average mineral chemistry of amphibole from the lamprophyres and hornblende andesites of this study.

rock type	Kersantite	kersantite	Hb andesite	Hb andesite
sample	M-114	M-113	M-67	M-45
N	31	4	2	9
SiO ₂	39,82	39,81	41,58	44,60
TiO ₂	2,20	2,12	1,49	1,39
Al ₂ O ₃	13,85	13,96	12,97	9,31
FeO	12,21	11,96	11,53	15,76
Cr ₂ O ₃	0,01	0,01	0,02	0,01
MnO	0,21	0,19	0,11	0,70
MgO	12,57	12,92	14,51	12,64
NiO	0,03		0,06	0,05
CaO	12,18	12,37	12,32	11,76
Na ₂ O	1,96	1,95	2,06	1,58
K ₂ O	1,79	1,80	1,31	1,00
BaO	0,05		0,00	0,00
F			0,21	0,34
Cl	0,02		0,03	0,03
H ₂ O*	2,00	2,01	1,96	1,89
O=F,Cl			0,09	0,15
Total	99,17	99,43	100,66	101,63
Structural formule (on 23-oxygen)				
Si	5,95	5,93	6,05	6,50
Al (iv)	2,05	2,07	1,95	1,50
Al (vi)	0,39	0,38	0,27	0,09
Ti	0,25	0,24	0,16	0,15
Cr	0,00	0,00	0,00	0,00
Fe ³⁺	0,34	0,36	0,70	0,80
Fe ²⁺	1,19	1,13	0,71	1,12
Mn	0,03	0,02	0,01	0,09
Mg	2,80	2,87	3,14	2,74
Ni	0,00	0,00	0,01	0,01
Ca	1,95	1,97	1,92	1,84
Na	0,57	0,56	0,58	0,45
K	0,34	0,34	0,24	0,19
Mg#	0,70	0,72	0,82	0,71

Table 5. Mineral chemistry of olivine from the tephrite and monzogabbro (mgb) of this study.

Rock type	tephrite	tephrite	tephrite	tephrite	tephrite	tephrite	tephrite	tephrite	tephrite
Na ₂ O	0,02	0,01	0,00	0,02	0,00	0,00	0,01	0,00	0,01
Al ₂ O ₃	0,02	0,05	0,07	0,01	0,06	0,02	0,06	0,02	0,02
SiO ₂	37,82	37,73	38,15	37,72	37,30	37,58	37,39	35,56	34,69
K ₂ O	0,01	0,01	0,00	0,01	0,00	0,00	0,01	0,02	0,02
CaO	0,18	0,34	0,16	0,29	0,34	0,40	0,44	0,53	0,41
MnO	0,61	0,68	0,58	0,66	0,64	0,74	0,80	1,26	1,45
FeO	25,00	25,85	25,25	25,55	26,41	26,98	27,42	34,10	40,07
Cr ₂ O ₃	0,04	0,01	0,04	0,00	0,00	0,01	0,00	0,00	0,03
NiO	0,22	0,13	0,21	0,13	0,05	0,08	0,02	0,03	0,00
MgO	35,34	35,15	35,60	35,10	34,11	34,05	32,79	26,60	22,77
TiO ₂	0,00	0,02	0,03	0,02	0,00	0,01	0,02	0,04	0,04
Total	99,28	99,96	100,09	99,49	98,92	99,86	98,96	98,15	99,49
Fo	71,58	70,79	71,53	71,00	69,71	69,22	68,06	58,16	50,32

Rock type	tephrite	mgb (cr)	mgb (cr)	mgb (cr)	mgb (rm)	mgb (rm)	mgb (rm)	mgb (rm)
Na ₂ O	0,03	0,00	0,01	0,00	0,00	0,00	0,02	0,00
Al ₂ O ₃	0,06	0,01	0,02	0,02	0,03	0,05	0,02	0,05
SiO ₂	37,42	39,65	39,79	39,43	38,98	39,12	39,09	38,39
K ₂ O	0,00	0,00	0,00	0,01	0,00	0,00	0,00	0,00
CaO	0,42	0,22	0,19	0,20	0,27	0,16	0,25	0,17
MnO	0,71	0,36	0,43	0,44	0,53	0,30	0,44	0,70
FeO	26,87	19,80	19,25	19,19	22,91	19,47	23,11	26,15
Cr ₂ O ₃	0,00	0,05	0,03	0,04	0,01	0,04	0,00	0,00
NiO	0,04	0,19	0,17	0,18	0,14	0,20	0,06	0,09
MgO	33,97	40,26	40,42	40,57	37,57	40,77	37,71	35,39
TiO ₂	0,03	0,00	0,02	0,02	0,02	0,01	0,01	0,02
Total	99,53	100,54	100,33	100,11	100,45	100,11	100,71	100,97
Fo	69,26	78,37	78,91	79,02	74,50	78,87	74,41	70,69

Table 6. Chemical composition of Fe-Ti oxides from tephrites and lamprophyres of this study.

	tephrite	tephrite	tephrite	tephrite	tephrite	lamprophyre	lamprophyre
SiO ₂	0,12	0,15	0,77	0,08	0,05	0,06	0,08
TiO ₂	5,8	5,8	5,92	5,95	6	4,53	4,43
Al ₂ O ₃	8,37	8,41	8,46	8,52	9,07	4,8	4,88
Cr ₂ O ₃	0,23	0,22	0,22	0,2	0,2	0,06	0,05
Fe ₂ O ₃	50,51	50,32	47,54	50,53	48,69	55,26	55,7
FeO	30,11	30,08	30,58	30,1	29,45	30,13	30,26
MnO	0,42	0,31	0,5	0,47	0,46	0,77	0,87
MgO	4,9	5,07	4,88	4,99	5,27	3,14	3,11
ZnO	0,19	0,05	0,1	0,15			
NiO	0,03		0,07	0,11		0,06	
Total	100,67	100,41	99,05	101,11	99,2	98,81	99,38

Table 7. Trace element contents (ppm) of clinopyroxene macrocrysts determined by LA-ICP-MS.

Group	Group I	Group I	Group I	Group I	Group I	Group I	Group I	Group II	Group II	Group II
Rock type	minette	minette	minette	minette	minette	Kersantite	Kersantite	tephrite	tephrite	kersantite
Rb (ppm)	<0,049	<0,091	<0,052	0,088	0,128	0,075	0,088	0,216	<0,084	0,077
Ba	0,163	0,163	<0,126	0,45	0,87	0,134	0,148	<0,125	0,144	0,38
Th	0,0085	0,017	0,0078	0,0217	0,059	0,031	0,12	0,048	0,025	0,17
U	0,0044	0,0155	0,0101	0,0087	0,0192	0,004	0,034	0,0085		0,217
Nb	0,0088	0,0121	0,0393	0,0532	0,0251	0,0113	<0,0086	0,043	0,0246	<0,0086
Ta	<0,0064	0,0095	0,0096	0,0243	0,0138	0,009	<0,0094	0,0076	<0,0065	<0,0054
La	0,69	0,97	1,12	0,81	0,94	1,95	0,92	3,46	3,57	3,07
Ce	2,36	3,28	4,17	2,72	3,05	6,84	2,68	10,7	11,67	8,46
Pb	0,105	0,2	0,144	0,148	0,159	0,16	0,151	0,23	0,17	0,454
Sr	92,98	90,28	79,92	89,29	91,17	90,34	66,62	181,39	191,42	118,29
Nd	3,02	3,32	5,09	2,84	3,34	8,14	2,53	8,6	10,93	8,73
Zr	2,03	2,18	7,82	2,56	2,56	13,58	2,74	8,37	7,97	10,01
Hf	0,121	0,136	0,39	0,14	0,13	0,84	0,145	0,44	0,44	0,471
Sm	0,91	1,05	1,72	0,8	1,03	2,68	0,79	1,84	2,53	2,65
Eu	0,299	0,342	0,55	0,307	0,316	0,82	0,296	0,47	0,67	0,768
Gd	0,91	1,23	2,08	0,75	0,97	2,95	0,92	1,45	2,05	1,92
Dy	0,68	0,89	1,52	0,65	0,58	2,54	0,74	0,83	1,38	1,75
Y	2,89	3,36	6,67	2,53	2,56	9,83	3,49	3,4	5,42	7,01
Ho	0,115	0,152	0,29	0,111	0,117	0,46	0,16	0,169	0,22	0,346
Er	0,265	0,35	0,69	0,228	0,193	1,06	0,355	0,4	0,49	0,706
Yb	0,276	0,286	0,58	0,2	0,149	0,8	0,272	0,32	0,48	0,647
Lu	0,0291	0,042	0,114	0,0356	0,0274	0,133	0,046	0,045	0,077	0,1

Group	Group III	Group III	Group III	Group III	Group III	Group III	Group IV	Group IV	Group IV	Group IV
Rock type	kersantite	kersantite	kersantite	kersantite	kersantite	kersantite	host lava (Ha)	host lava (Ha)	host lava (Ha)	host lava (Ha)
Rb (ppm)	0,057	0,217	0,08	1,54	2,64	1,168	<0,073	<0,074	<0,083	<0,079
Ba	0,13	2,89	0,134	0,96	96,27	68,89	<0,115	0,152	0,127	0,118
Th	0,197	0,185	0,202	0,66	1,11	1,053	0,067	0,115	0,149	0,037
U	0,042	0,079	0,0146	0,146	0,21	0,845	0,0105	0,0108	0,023	0,0103
Nb	0,145	0,141	0,225	0,359	0,49	1,27	0,054	0,08	0,084	0,043
Ta	0,0305	0,0197	0,067	0,083	0,077	0,0423	0,0125	<0,0092	0,0181	<0,0057
La	6,47	5,61	7,3	14,61	11,67	8,12	3,65	4,62	6,39	3,93
Ce	23,12	19,86	26,6	41,81	36,48	21,51	12,76	16,03	21,84	13,28
Pb	0,3	0,65	0,35	0,48	3,95	3,23	0,22	0,22	0,23	0,23
Sr	110,27	109,68	109,83	134,4	136,16	860,87	96,43	103,54	127,7	111,08
Nd	25,75	20,78	28,55	37,96	36,18	19,86	13,02	16,7	21,48	13,11
Zr	83,53	57,25	120,97	138,05	104,76	75,75	28,16	37,74	41,81	22,6
Hf	3,83	2,66	5,82	5,73	4,58	2,86	1,4	1,92	2,22	1,26
Sm	7,88	6,11	9,43	10,39	10,68	6,54	4,18	5,22	5,71	3,9
Eu	2,43	1,97	2,68	3,22	3,16	1,82	1,19	1,36	1,55	0,99
Gd	8,81	6,48	9,66	10,94	11,28	6,56	4,02	4,97	5,69	3,58
Dy	7,31	5,99	8,5	9,04	9,78	5,72	3,94	4,85	4,88	3,26
Y	30,66	24,96	33,77	39,36	42,3	25,42	17,92	21,66	20,71	13,84
Ho	1,42	1,05	1,54	1,75	1,83	1,104	0,74	0,9	0,95	0,61
Er	3,45	2,9	3,91	4,34	4,71	2,7	1,99	2,43	2,49	1,53
Yb	2,68	2,35	3,39	3,52	3,94	2,63	1,71	2,1	2	1,36
Lu	0,4	0,354	0,4	0,55	0,59	0,376	0,24	0,3	0,23	0,181

Table 8. Mineral chemistry of analcime and thamsomite from the lavas of this study.

	pillow lava	pillow lava	tephrite	tephrite	analcimite	lamprophyre
SiO ₂	59.64	60.08	58.38	58.33	57.05	40.05
Al ₂ O ₃	21.27	21.91	21.43	21.34	22.57	28.4
Fe ₂ O ₃	0.07	0.19	0.22	0.15	0.26	0.07
CaO	0.1	0.05	0.06	0.1	0.13	11.84
Na ₂ O	12.13	12.41	12.51	11.24	13.21	3.15
K ₂ O	0.02	0.04	0.04	0.13	0.02	0
H ₂ O	16.256	16.522	16.219	15.841	16.435	12.52
Total	93.23	94.68	92.64	91.29	93.24	83.51

Table 9. Whole-rock major (%), trace element (ppm) and isotope ratios of lavas and intrusion from the Salavat Range.

Group	HM-lavas <i>Host lava (Ha)</i>	HM-lavas <i>Host lava (Ha)</i>	HM-lavas <i>Dyke</i>	HM-lavas <i>Dyke</i>	HM-lavas <i>Dyke</i>	HM-lavas <i>Dyke</i>	HM-lavas <i>Dyke</i>	HM-lavas <i>Dyke</i>
Sample	M-116	M-118	M-71	M-73	M-112	M-113	M-115	M-119
SiO ₂ (wt.%)	42,3	46,5	47,6	46,9	46,3	44,1	50,1	48,2
TiO ₂	0,67	0,69	0,77	0,74	0,71	0,92	0,73	0,75
Al ₂ O ₃	10,35	11,5	13,5	13,25	13	15,05	15,5	13,85
Fe ₂ O ₃	9,47	8,66	10,45	9,93	9,19	12,5	9,45	9,89
MnO	0,14	0,15	0,17	0,16	0,15	0,22	0,16	0,15
MgO	10,1	7,82	7,3	6,58	7,03	6,49	5,85	6,81
CaO	11,3	11,8	9,01	8,93	10,4	10,35	5,02	8,25
Na ₂ O	1,46	2	2,3	2,43	1,62	4,18	3,92	2,8
K ₂ O	2,42	4,1	4,73	4,66	5,15	1,4	5,12	4,28
P ₂ O ₅	0,28	0,31	0,31	0,3	0,33	0,59	0,33	0,31
BaO	0,05	0,11	0,13	0,11	0,11	0,1	0,11	0,11
LOI	11,5	5,64	4,41	4,52	6,9	3,77	3,7	2,87
Total	100,24	99,39	100,76	98,59	100,96	99,76	100,03	98,38
Sc (ppm)	29,88	36,79	42,58	41,86	40,71	59,26	26,90	37,32
V	252,24	254,45	301,24	289,43	248,19	395,70	305,66	270,71
Cr	503,40	380,11	121,44	135,11	157,37	34,34	43,06	107,04
Mn	1002,75	1193,88	1378,71	1222,50	1122,17	1964,31	1198,22	1152,34
Co	37,03	34,71	34,43	33,48	35,17	37,04	25,46	31,13
Ni	196,00	146,26	25,93	28,17	55,51	15,46	19,89	23,40
Cu	86,42	96,67	110,58	124,23	104,73	156,44	86,14	109,70
Zn	52,19	68,63	72,23	64,26	67,87	105,07	65,34	62,63
Rb	60,52	74,06	109,14	90,33	106,18	24,93	85,24	87,46
Sr	593,69	298,94	617,33	780,47	609,77	756,66	494,03	642,76
Y	15,28	17,88	22,05	22,10	20,56	31,22	22,89	22,67
Zr	87,42	60,66	72,55	71,05	85,67	81,54	120,97	71,24
Nb	7,49	4,36	4,13	4,29	7,47	5,28	7,10	4,49
Mo	1,19	0,57	0,39	1,42	0,46	0,32	0,45	0,86
Sn		0,72	1,00	1,36	1,17	1,30		1,00
Cs	0,65	2,16	3,21	1,86	0,75	3,56	7,05	1,16
Ba	431,46	959,58	1155,97	996,44	931,10	927,39	909,17	939,65
La	18,82	19,41	22,38	21,82	24,68	30,07	18,32	22,29
Ce	37,51	39,14	43,25	42,49	47,05	58,17	35,65	43,10
Pr	4,63	4,87	5,34	5,36	5,90	7,41	4,40	5,43
Nd	18,87	19,50	22,32	22,44	24,20	31,32	18,76	21,83
Sm	3,68	4,02	4,98	4,87	4,86	7,47	4,26	4,79
Eu	0,96	1,17	1,44	1,39	1,35	2,17	1,06	1,27
Gd	3,10	3,85	4,77	4,60	4,65	7,08	3,98	4,60
Tb	0,44	0,54	0,70	0,69	0,66	0,96	0,65	0,69
Dy	2,57	3,19	3,85	3,85	3,62	5,42	3,85	3,78
Ho	0,52	0,62	0,74	0,74	0,72	1,02	0,79	0,77
Er	1,41	1,65	2,05	2,06	1,91	2,79	2,16	1,99
Yb	1,29	1,49	1,83	1,84	1,72	2,39	2,06	1,99
Lu	0,19	0,21	0,28	0,27	0,26	0,36	0,34	0,28
Hf	1,95	1,60	1,81	1,88	2,21	2,09	2,66	1,97
Ta	0,33	0,21	0,25	0,30	0,43	0,26	0,40	0,23
W	1,23	0,44	0,37	2,06	0,32	1,07	2,32	0,91
Pb	7,37	8,35	15,94	14,25	17,06	21,00	7,39	15,03
Th	4,20	4,46	5,30	5,81	5,34	7,59	5,72	5,94
U	1,16	1,25	1,49	1,54	1,54	1,71	1,80	1,81
Eu/Eu*	0,86	0,91	0,90	0,90	0,87	0,91	0,78	0,83
La/Yb	14,60	13,02	12,21	11,87	14,37	12,58	8,88	11,18
¹⁴³ Nd/ ¹⁴⁴ Nd	n.a	0,512668	0,51268		0,512622	0,51275		
⁸⁷ Sr/ ⁸⁶ Sr	0,705401	0,706323	0,705429		0,706156	0,704921		

Table 9 (continued).

Group	HM-lavas <i>lava</i>	HM-lavas <i>lava</i>	HM-lavas <i>lava</i>	HM-lavas <i>lava</i>	HM-lavas <i>lava</i>	HM-lavas <i>dyke</i>	HM-lavas <i>dyke</i>	HM-lavas <i>dyke</i>	HM-lavas <i>dyke</i>
Sample	M-134	M-144	M-59	M-145	M-155	CH006B	M-74	M-80	M-82
SiO ₂ (wt.%)	53,4	48,5	49,1	51,8	48,6	47,9	45,9	45,9	47,6
TiO ₂	0,52	0,96	0,63	0,7	0,86	0,84	0,72	0,76	0,8
Al ₂ O ₃	15,1	17,15	15,4	15,5	15,15	14,85	13,35	14	14,6
Fe ₂ O ₃	7,02	11	8,42	9,19	11,25	10,7	9,92	10,1	10,6
MnO	0,13	0,19	0,17	0,12	0,19	0,18	0,17	0,17	0,18
MgO	3,73	5,47	5,43	5,78	5,37	5,36	5,98	5,61	5,8
CaO	5,06	9,3	6,38	6,07	8,78	8,9	9,09	10,15	10,35
Na ₂ O	3,27	2,69	3,32	3,04	2,67	2,56	3,69	1,9	2,4
K ₂ O	4,7	2,73	5,04	4,26	5,05	4,92	2,94	4,47	4,31
P ₂ O ₅	0,24	0,39	0,36	0,33	0,58	0,57	0,53	0,51	0,57
BaO	0,14	0,1	0,11	0,11	0,13	0,17	0,15	0,14	0,15
LOI	4,85	1,7	3,7	3,84	2,05	2,5	4,47	3,63	3,35
Total	98,19	100,3	98,15	100,83	100,81	99,57	97,1	97,5	100,86
Sc (ppm)	19,93	33,39	25,20	26,20	28,64	29,75	29,39	29,62	29,03
V	189,51	332,63	252,13	240,34	331,62	326,86	377,44	303,55	286,96
Cr	32,07	24,44	66,45	31,31	29,21	53,61	44,67	67,63	45,95
Mn	1011,22	1444,37	1383,14	910,69	1338,52	1215,30	1295,37	1391,62	1361,04
Co	20,23	31,36	24,09	23,42	30,63	29,68	30,46	33,00	32,32
Ni	17,45	18,01	18,37	21,94	20,65	22,39	21,05	23,00	21,72
Cu	78,06	151,48	104,37	88,91	114,90	101,44	500,67	125,99	123,39
Zn	62,60	88,12	77,75	57,60	82,98	77,58	77,56	90,40	87,31
Rb	96,82	62,86	103,32	74,08	107,52	86,90	80,02	93,64	77,84
Sr	450,08	678,06	1080,63	470,91	1001,25	1038,59	1112,46	1074,39	1099,70
Y	20,93	22,43	24,47	21,01	25,20	24,44	23,66	25,00	24,58
Zr	99,06	85,37	97,30	84,89	159,86	147,15	131,02	115,98	113,38
Nb	4,77	6,33	6,28	4,80	13,25	11,93	8,10	9,61	9,71
Mo	0,90	0,56	0,80	1,02	2,40	1,87	0,74	0,80	0,87
Sn	0,99	1,32	1,26	1,07				1,46	1,44
Cs	0,64	2,70	3,09	0,44	1,92	2,85	3,02	1,71	2,96
Ba	1239,99	875,89	1031,39	911,53	1046,12	1083,86	1303,68	1309,59	1285,80
La	20,40	33,72	31,01	18,10	33,10	30,67	30,32	33,46	32,92
Ce	38,22	60,96	56,95	35,27	64,18	60,00	59,28	64,50	62,77
Pr	4,46	7,06	6,77	4,23	7,91	7,38	7,28	7,85	7,55
Nd	17,75	28,02	27,03	17,70	32,39	30,50	30,40	32,09	31,45
Sm	3,92	5,99	5,42	4,07	6,75	6,38	6,41	6,92	6,60
Eu	1,12	1,72	1,50	1,16	1,69	1,54	1,54	1,90	1,90
Gd	3,89	5,26	5,24	3,81	5,45	5,45	5,45	6,57	6,13
Tb	0,57	0,75	0,73	0,59	0,81	0,81	0,77	0,85	0,83
Dy	3,44	4,01	4,07	3,47	4,34	4,08	4,16	4,54	4,38
Ho	0,70	0,77	0,81	0,70	0,84	0,82	0,78	0,87	0,85
Er	1,98	2,12	2,23	2,06	2,19	2,12	2,08	2,15	2,31
Yb	1,98	1,86	2,22	1,96	2,01	1,94	1,86	2,01	1,99
Lu	0,31	0,27	0,36	0,29	0,32	0,30	0,28	0,29	0,30
Hf	2,32	2,16	2,19	2,19	3,44	3,13	2,82	2,83	2,61
Ta	0,29	0,41	0,36	0,32	0,76	0,59	0,43	0,53	0,52
W	2,08	0,42	0,84	1,88	5,04	2,45	0,90	1,07	0,78
Pb	23,69	29,60	30,22	12,04	14,29	12,66	16,80	25,73	24,55
Th	7,24	10,80	7,69	5,53	8,44	7,54	8,14	8,23	7,92
U	2,35	2,87	2,27	1,66	2,46	2,22	2,10	2,24	2,36
Eu/Eu*	0,88	0,94	0,86	0,90	0,85	0,80	0,80	0,86	0,91
La/Yb	10,29	18,14	13,94	9,22	16,50	15,78	16,30	16,65	16,52
¹⁴³ Nd/ ¹⁴⁴ Nd						0,512662		0,512684	
⁸⁷ Sr/ ⁸⁶ Sr						0,705255		0,705238	

Table 9 (continued).

Group	HM-lavas <i>dyke</i>	HM-lavas <i>dyke</i>	HM-lavas <i>dyke</i>	HM-lavas <i>dyke</i>	HM-lavas <i>lava</i>	HM-lavas <i>lava</i>	HM-lavas <i>lava</i>	LM-Lavas <i>Host pillow lav</i>
Sample	M-84	M-85	M-86	M-88	M-60	M-62	M-63	M-47
SiO ₂ (wt.%)	48,4	47,1	47,2	46,6	51,7	51,2	49,4	48
TiO ₂	0,89	0,78	0,78	0,78	0,96	0,81	0,93	0,66
Al ₂ O ₃	15,2	14,3	14,65	14,65	16,3	15,75	17,15	16,9
Fe ₂ O ₃	9,83	10,25	10,4	10,65	9,89	8,57	9,48	7,7
MnO	0,16	0,18	0,18	0,18	0,12	0,21	0,17	0,18
MgO	4,34	5,72	5,83	6,15	3,36	3,43	4,32	4,37
CaO	8,45	10,05	10	9,93	7,8	7,49	7,22	6,45
Na ₂ O	3,01	2,19	2,28	2,89	2,6	2,88	3,14	2,77
K ₂ O	4,6	4,33	4,51	3,97	4,63	2,79	3,4	5,01
P ₂ O ₅	0,45	0,54	0,56	0,56	0,5	0,31	0,39	0,55
BaO	0,15	0,14	0,15	0,15	0,12	0,09	0,1	0,21
LOI	1,93	3,42	3,09	3,53	2,15	5,9	3,44	5,68
Total	97,49	99,11	99,77	100,13	100,24	99,75	99,2	98,65
Sc (ppm)	26,10	37,79	28,81	33,17	27,29	22,04	20,33	13,27
V	270,06	279,60	283,82	275,44	292,45	206,09	244,67	279,25
Cr	27,38	57,40	62,01	76,32	13,84	23,07	16,35	14,05
Mn	1315,54	1454,53	1366,92	1367,14	980,21	1524,11	1259,12	1300,58
Co	29,41	31,75	32,25	34,33	20,71	17,82	24,52	20,54
Ni	13,40	21,65	22,06	22,53	7,20	11,82	12,84	6,97
Cu	123,58	121,51	123,37	154,47	52,66	30,59	70,81	111,38
Zn	87,90	87,22	84,82	83,89	100,30	115,32	89,05	82,19
Rb	103,08	91,35	83,85	57,82	118,21	66,83	76,43	89,77
Sr	1088,91	1171,68	1089,74	1157,76	920,78	2988,27	1081,24	1609,59
Y	28,69	27,86	24,24	20,46	35,11	29,89	22,27	21,96
Zr	147,54	121,16	112,08	98,14	171,00	103,82	91,94	95,40
Nb	12,73	9,08	8,97	8,31	17,74	11,62	8,16	5,67
Mo	1,86	0,89	1,01	0,71	1,32	1,10	0,83	0,40
Sn	1,90	1,41	1,57	1,16	1,51	2,00	0,88	
Cs	4,73	1,98	3,53	1,31	1,10	1,34	0,82	2,00
Ba	1316,20	1327,67	1237,46	1273,68	1119,73	788,75	811,29	1634,04
La	35,75	33,33	32,01	32,82	48,54	35,58	26,64	26,02
Ce	68,90	64,02	61,38	59,45	82,37	73,32	51,32	47,72
Pr	8,21	7,97	7,52	7,21	10,00	9,18	6,17	5,83
Nd	32,61	32,63	31,45	28,44	39,51	38,44	25,24	23,65
Sm	7,12	7,10	6,84	5,94	7,88	8,33	5,10	4,85
Eu	1,84	1,95	1,81	1,62	2,32	2,20	1,58	1,20
Gd	6,57	6,50	6,03	5,26	7,97	7,19	4,81	4,39
Tb	0,91	0,85	0,79	0,71	1,09	1,01	0,71	0,63
Dy	5,05	4,73	4,22	3,72	5,89	5,38	3,71	3,48
Ho	0,99	0,88	0,81	0,72	1,17	1,03	0,73	0,71
Er	2,63	2,39	2,19	1,83	3,06	2,81	2,07	1,99
Yb	2,49	2,11	1,90	1,63	2,89	2,51	1,89	1,90
Lu	0,34	0,31	0,28	0,24	0,41	0,38	0,29	0,30
Hf	3,36	2,99	2,70	2,11	4,07	2,89	2,27	1,74
Ta	0,72	0,55	0,54	0,46	1,02	0,63	0,49	0,25
W	1,82	0,98	0,36	0,89	1,18	0,52	0,28	0,95
Pb	25,12	25,01	23,99	28,09	25,42	22,79	13,82	15,61
Th	9,96	9,50	7,71	9,13	10,46	7,53	3,88	6,74
U	2,87	2,38	2,14	2,68	2,09	2,15	1,21	1,85
Eu/Eu*	0,82	0,88	0,86	0,89	0,89	0,87	0,98	0,80
La/Yb	14,35	15,82	16,81	20,13	16,78	14,19	14,08	13,69
¹⁴³ Nd/ ¹⁴⁴ Nd	0,512601							0,512804
⁸⁷ Sr/ ⁸⁶ Sr	0,705561							0,704725

Table 9 (continued).

Group	LM-Lavas <i>Host pillow lav</i>	LM-Lavas <i>Host pillow lav</i>	LM-Lavas <i>Host pillow lav</i>	LM-Lavas <i>Host pillow lav</i>	LM-Lavas <i>Breccia/lava</i>	LM-Lavas <i>Breccia/lava</i>	LM-Lavas <i>Breccia/lava</i>	LM-Lavas <i>Breccia/lava</i>	LM-Lavas <i>Breccia/lava</i>
Sample	M-48	M-48B	M-127	M-128	M-10	M-11	M-14	M-15	M-19A
SiO ₂ (wt.%)	48,4	48,4	48,4	49,4	48,9	54,3	47,8	50	50,8
TiO ₂	0,66	0,68	0,67	0,68	0,86	0,51	0,5	0,54	0,62
Al ₂ O ₃	17,4	17	17,2	17,8	17,15	21,1	19,1	19,75	20,2
Fe ₂ O ₃	7,56	7,92	7,86	7,83	7,58	3,27	4,37	4,17	4,88
MnO	0,19	0,19	0,19	0,2	0,19	0,21	0,12	0,19	0,19
MgO	3,53	4,54	3,61	3,87	3,92	1,07	1,61	2,61	1,72
CaO	5,88	6,62	6,7	6,39	4,7	2,75	4,43	2,89	4,57
Na ₂ O	7,29	2,06	4,58	4,24	6,29	6,41	7,3	7,17	5,99
K ₂ O	1,25	5,88	3,69	4,23	2,32	5,76	1,84	4,52	4,94
P ₂ O ₅	0,51	0,53	0,56	0,56	0,69	0,17	0,38	0,28	0,43
BaO	0,1	0,2	0,35	0,29	0,17	0,23	0,15	0,26	0,24
LOI	8,08	4,72	4,83	4,88	6,8	4,95	9,33	8,56	5,31
Total	100,96	98,85	98,79	100,67	99,69	100,99	97,09	100,98	100,25
Sc (ppm)	14,31	15,46	14,70	14,00	11,44	0,81	2,75	3,34	5,31
V	288,54	265,71	268,76	254,45	292,55	123,28	111,42	161,89	217,31
Cr	13,73	14,94	16,20	15,43	11,82	3,32	4,85	3,62	6,29
Mn	1382,90	1522,99	1491,62	1503,42	1391,78	1545,24	865,31	1418,45	1423,40
Co	21,44	23,05	22,57	22,40	16,64	5,36	8,61	8,36	10,97
Ni	6,61	7,52	6,89	6,76	6,66	0,38	2,00	1,98	2,48
Cu	120,52	128,83	116,16	122,68	211,34	28,18	45,85	65,64	159,41
Zn	89,68	94,97	89,88	92,96	150,13	102,53	70,75	89,58	99,15
Rb	32,47	94,57	67,64	81,87	44,24	65,02	28,57	81,52	82,06
Sr	392,42	1254,01	1990,06	2191,69	1045,36	2121,78	1082,35	682,67	3038,98
Y	22,68	24,46	24,11	24,43	31,22	26,97	19,56	23,66	24,92
Zr	104,65	108,53	107,28	110,43	172,87	215,03	206,10	160,64	181,33
Nb	7,90	8,30	8,43	8,55	15,78	23,94	20,09	15,48	21,59
Mo	1,20	0,17	1,17	0,68	0,84	0,98	0,74	0,37	1,19
Sn	1,10	1,58	0,92	0,92	1,17	1,25	1,11	1,11	0,98
Cs	3,86	1,69	2,53	3,26	2,23	2,24	4,48	3,95	1,59
Ba	877,84	1747,42	3074,79	2532,71	1395,30	1978,21	1194,32	2198,64	2128,32
La	26,97	28,04	28,65	28,97	49,44	55,53	37,71	43,84	47,73
Ce	50,68	52,07	52,47	53,60	91,42	97,74	65,90	78,08	84,23
Pr	6,10	6,46	6,37	6,68	10,81	10,57	7,34	8,74	9,38
Nd	25,10	26,96	26,23	26,70	43,13	37,11	27,05	32,61	35,05
Sm	5,49	5,70	5,56	5,49	8,65	6,64	4,93	6,08	6,90
Eu	1,53	1,61	1,55	1,64	2,35	1,91	1,30	1,84	1,93
Gd	4,99	5,29	5,28	5,35	7,55	5,84	3,36	5,44	5,71
Tb	0,68	0,74	0,73	0,73	0,99	0,85	0,57	0,74	0,77
Dy	3,86	4,09	4,00	4,13	5,19	4,47	3,12	4,02	4,18
Ho	0,75	0,83	0,81	0,79	1,05	0,91	0,63	0,79	0,81
Er	2,09	2,40	2,29	2,28	2,88	2,53	1,82	2,03	2,15
Yb	2,05	2,19	2,16	2,17	2,49	2,54	1,89	2,13	2,18
Lu	0,30	0,32	0,32	0,33	0,39	0,39	0,30	0,32	0,31
Hf	2,37	2,57	2,49	2,62	3,62	4,28	3,19	3,20	3,42
Ta	0,42	0,51	0,49	0,52	0,63	1,17	1,06	0,74	0,98
W	1,49	0,30	1,31	1,14	0,48	1,30	2,48	1,64	0,78
Pb	26,42	28,00	27,34	28,14	20,63	43,32	21,69	30,94	43,00
Th	6,90	7,11	7,37	7,40	10,77	15,05	14,42	11,25	13,11
U	2,23	1,89	2,19	2,17	2,79	4,89	5,13	3,25	4,44
Eu/Eu*	0,89	0,90	0,87	0,92	0,89	0,94	0,98	0,98	0,94
La/Yb	13,18	12,81	13,24	13,32	19,85	21,83	19,96	20,55	21,93

¹⁴³Nd/¹⁴⁴Nd
⁸⁷Sr/⁸⁶Sr

0,512788
0,705143

Table 9 (continued).

Group	LM-Lavas <i>Breccia/lava</i>	LM-Lavas <i>Breccia/lava</i>	LM-Lavas <i>Breccia/lava</i>	LM-Lavas <i>Breccia/lava</i>	LM-Lavas <i>Breccia/lava</i>	LM-Lavas <i>Breccia/lava</i>	Ps-rocks <i>Hb andesite</i>	Ps-rocks <i>Hb andesite</i>	Ps-rocks <i>Hb andesite</i>
Sample	M-23	M-24	M-35Y	M-33	M-35	M-83	M-68	M-44	M-45
SiO ₂ (wt.%)	49,4	49,4	49,5	47,9	58,3	49,2	57	64,7	64,6
TiO ₂	0,67	0,56	0,65	0,85	0,61	0,75	0,43	0,4	0,4
Al ₂ O ₃	14,6	19,3	19,3	17,35	16,65	16,25	15,4	16,4	16,65
Fe ₂ O ₃	9,16	6,11	5,8	7,72	5,84	7,79	4,53	3,47	3,39
MnO	0,17	0,17	0,2	0,22	0,11	0,15	0,09	0,1	0,09
MgO	5,68	2,4	1,85	2,93	2,73	3,24	2,25	1,5	1,41
CaO	7,09	6,11	5,82	6,75	5,35	7,83	4,63	3,52	3,37
Na ₂ O	6,43	3,47	6,37	5,02	4,11	3	2,86	3,79	3,9
K ₂ O	1,19	5,78	3,25	3,56	2,94	5,36	4,78	4,07	4,31
P ₂ O ₅	0,45	0,52	0,42	0,6	0,34	0,39	0,14	0,17	0,17
BaO	0,11	0,23	0,26	0,21	0,12	0,11	0,11	0,12	0,11
LOI	4,17	5,17	4,3	4,29	3,14	5,07	6,41	2,33	1,62
Total	99,14	99,39	97,96	97,65	100,35	99,31	98,65	100,61	100,09
Sc (ppm)	112,63	6,88	7,03	13,92	10,05	19,03	11,22	5,27	3,89
V	333,48	200,37	210,08	282,13	104,99	249,97	139,11	65,40	59,79
Cr	83,50	7,55	13,32	14,35	22,49	27,46	48,73	57,74	44,71
Mn	3332,67	1296,89	1504,93	1681,35	915,05	1113,76	664,96	818,72	709,25
Co	31,00	15,82	12,86	19,17	13,38	18,99	11,51	6,23	5,43
Ni	21,50	3,26	3,21	6,06	7,99	10,55	12,72	12,05	9,67
Cu	69,52	164,77	153,86	141,44	16,71	107,09	25,57	14,90	13,21
Zn	146,13	82,80	95,60	104,20	62,52	65,99	33,46	56,00	51,21
Rb	72,80	98,75	49,12	48,67	96,16	104,20	100,02	128,66	122,31
Sr	1363,92	1791,35	2163,83	2225,75	747,47	1298,03	385,06	843,84	831,68
Y	43,16	19,83	25,61	29,83	25,70	21,93	18,24	18,70	17,41
Zr	104,46	102,35	176,51	170,70	136,91	68,50	162,65	78,25	72,46
Nb	11,03	8,71	21,85	19,87	21,38	5,65	9,69	21,79	19,65
Mo	0,43	0,35	1,87	2,53	1,20	0,60	2,15	1,05	1,04
Sn	1,75	0,92	1,21	1,65	1,30	0,80		1,48	1,04
Cs	13,77	2,65	2,49	2,38	1,16	0,61	1,29	3,25	2,84
Ba	1801,40	1976,98	2313,07	1793,02	1017,27	910,94	903,30	1051,43	923,33
La	29,96	29,09	46,42	45,51	71,28	22,57	21,27	39,50	37,23
Ce	53,04	52,08	82,36	83,84	121,80	42,46	37,07	68,38	63,78
Pr	6,53	6,09	9,36	10,10	12,68	5,38	4,16	7,29	6,85
Nd	26,67	23,52	35,42	40,70	44,97	21,95	15,94	26,34	24,69
Sm	6,03	4,61	7,22	8,05	7,57	4,66	3,22	4,52	4,71
Eu	1,74	1,40	2,02	2,29	2,07	1,31	0,74	1,40	1,32
Gd	6,36	4,32	6,24	7,65	6,49	4,59	2,75	4,20	3,85
Tb	0,95	0,56	0,81	1,03	0,83	0,68	0,47	0,56	0,53
Dy	5,73	3,32	4,45	5,39	4,60	3,67	2,83	3,10	2,69
Ho	1,20	0,63	0,86	1,03	0,84	0,76	0,61	0,62	0,56
Er	3,33	1,79	2,41	2,70	2,34	2,08	1,69	1,65	1,56
Yb	3,35	1,78	2,20	2,47	2,11	1,89	1,75	1,64	1,47
Lu	0,51	0,27	0,33	0,37	0,30	0,27	0,29	0,25	0,23
Hf	2,99	2,32	3,56	3,73	3,33	1,87	3,43	2,28	2,14
Ta	1,33	0,49	1,10	1,07	1,31	0,37	0,64	1,36	1,18
W	0,45	0,71	1,13	1,44	2,67	0,46	5,96	1,89	2,23
Pb	18,16	29,97	36,95	30,73	16,41	11,24	15,23	31,24	29,75
Th	23,10	7,69	12,03	10,71	19,90	5,58	9,41	10,48	9,83
U	1,22	2,17	3,89	2,77	4,36	1,26	3,09	2,76	2,37
Eu/Eu*	0,86	0,96	0,92	0,89	0,90	0,86	0,76	0,99	0,95
La/Yb	8,94	16,34	21,10	18,39	33,73	11,95	12,17	24,11	25,29

¹⁴³Nd/¹⁴⁴Nd
⁸⁷Sr/⁸⁶Sr

n.a
0,705667

Table 9 (continued).

Group	Ps-rocks <i>Hb andesite</i>	Ps-rocks <i>Monzodiorite</i>	Ps-rocks <i>Alk fel syenite</i>	Ps-rocks <i>Alk fel syenite</i>	Ps-rocks <i>Alk fel syenite</i>
Sample	M-46	M-56	M-53	M-55A	M-97
SiO ₂ (wt.%)	63,3	57,5	68,7	68	59,8
TiO ₂	0,4	0,61	0,18	0,25	0,41
Al ₂ O ₃	16,3	15,4	14	14,9	17,65
Fe ₂ O ₃	3,5	6,12	1,6	2,18	3,46
MnO	0,1	0,11	0,03	0,04	0,09
MgO	1,6	3,44	0,54	0,53	1,05
CaO	3,47	4,89	1,06	1,96	2,37
Na ₂ O	3,91	3,27	3,16	3,67	4,83
K ₂ O	4,19	4,45	6,44	6,18	6,52
P ₂ O ₅	0,17	0,45	0,03	0,06	0,19
BaO	0,11	0,1	0,02	0,03	0,08
LOI	1,48	2,39	1,32	1,9	2,2
Total	98,61	98,91	97,12	99,73	98,71
Sc (ppm)	4,57	14,57	2,73	2,25	4,49
V	63,49	159,71	22,44	44,72	77,39
Cr	60,03	95,11	43,28	57,41	31,03
Mn	778,27	944,16	262,80	283,74	753,73
Co	5,94	17,80	2,30	3,51	6,06
Ni	13,12	26,00	2,83	3,96	6,45
Cu	14,33	62,33	12,42	15,62	39,06
Zn	52,17	69,50	19,03	23,30	62,29
Rb	120,93	169,99	264,73	211,42	263,89
Sr	831,66	1073,38	117,46	217,55	697,53
Y	17,39	27,18	19,33	19,93	27,05
Zr	72,76	45,29	141,79	195,78	262,48
Nb	20,20	19,98	32,84	47,39	26,81
Mo	1,03	1,03	1,13	1,41	2,79
Sn	1,17	4,63	1,84		1,89
Cs	3,06	6,11	3,90	2,69	11,50
Ba	961,37	909,05	156,48	220,18	689,91
La	36,11	51,74	54,25	49,12	61,46
Ce	63,04	94,28	93,02	85,27	100,86
Pr	6,77	10,97	9,41	8,75	10,31
Nd	24,99	39,82	29,87	28,71	34,78
Sm	4,37	7,70	4,93	4,97	6,10
Eu	1,33	1,71	0,67	0,74	1,35
Gd	3,93	6,39	4,01	2,96	5,31
Tb	0,54	0,87	0,59	0,57	0,78
Dy	2,91	4,55	3,18	3,15	4,24
Ho	0,58	0,89	0,65	0,66	0,87
Er	1,58	2,36	1,88	1,83	2,44
Yb	1,48	2,19	2,02	1,90	2,47
Lu	0,23	0,28	0,28	0,31	0,38
Hf	2,05	2,56	3,14	4,19	5,22
Ta	1,19	1,47	2,64	4,06	1,83
W	1,68	3,35	3,94	9,93	5,75
Pb	30,52	26,29	28,94	18,28	46,09
Th	9,98	16,59	33,11	27,58	29,72
U	2,68	2,52	5,00	4,30	7,40
Eu/Eu*	0,98	0,75	0,46	0,59	0,73
La/Yb	24,43	23,66	26,83	25,83	24,85
¹⁴³ Nd/ ¹⁴⁴ Nd	0,512566	0,512542		0,512552	0,512604
⁸⁷ Sr/ ⁸⁶ Sr	0,705588	0,705389		0,706732	0,70557

Table 10. Whole-rock major (%), trace element (ppm) and isotope ratios of selected lavas from the Turkish-Iranian plateau.

Group of rock	Group Ia	Group Ia	Group Ia	Group Ia	Group Ia	Group Ia	Group Ia	Group Ia	Group Ia	Group Ia	Group Ia	Group Ia
Reference	<i>Pang et al., 2013b</i>											
Location	NW Iran											
SiO ₂	47,25	46,28	47,76	48,59	45,34	50,71	50,12	48,27	47,36	45,47	48,97	50,80
TiO ₂	1,19	1,14	1,18	1,25	1,16	1,20	1,19	1,33	1,23	1,18	1,17	1,19
Al ₂ O ₃	12,06	12,41	12,09	12,27	13,01	14,92	14,80	13,11	13,34	13,23	15,73	15,11
Fe ₂ O ₃	10,26	9,65	10,42	9,68	9,47	8,28	8,15	9,23	9,95	10,11	9,44	9,14
MnO	0,19	0,17	0,19	0,16	0,15	0,13	0,14	0,16	0,18	0,17	0,17	0,16
MgO	7,06	8,35	6,64	7,40	9,15	6,18	6,32	7,78	6,85	7,72	4,87	4,69
CaO	11,65	12,29	11,62	12,31	13,53	10,29	9,89	10,62	11,53	12,84	8,89	8,38
Na ₂ O	1,26	2,00	1,59	2,45	0,86	2,07	2,41	1,37	4,65	2,29	1,84	3,18
K ₂ O	7,38	6,20	6,82	4,36	5,96	5,36	6,16	6,72	3,23	5,47	7,96	6,31
P ₂ O ₅	1,72	1,49	1,70	1,53	1,36	0,87	0,83	1,41	1,68	1,51	0,97	1,04
Total	100	100	100	100	100	100	100	100	100	100	100	100
Cs	13	20,4	22,3	14,5	9,33	13	16,1	12,2	65,4	9,9	19,2	31,1
Rb	315	248	236	216	161	133	200	342	93,2	158	279	125
Sr	1955	1151	1614	1066	1098	1006	939	1242	1774	1185	1431	1190
Y	51,2	41	51,7	32,4	33,5	25,5	25	31,6	42,9	36,2	37,3	40,2
Zr	437	327	455	312	252	193	212	255	440	323	330	386
Nb	48,6	33,7	50,2	35,3	24,4	30,2	29,3	35,3	53,7	38	40,3	41,1
Ba	3736	2473	3792	3760	3252	2150	2072	3428	3959	3492	3764	3113
Hf	10,9	7,99	11,1	7,62	6,24	4,93	4,85	7,33	10,4	8,02	8,41	8,95
Ta	2,19	1,55	2,24	1,84	1,02	1,57	1,51	1,64	2,37	1,69	1,8	1,84
Pb	57,6	52,9	59,4	36,3	33,4	47,1	46,9	38,6	58,7	46,3	37,8	46,1
Th	30,4	30,1	31,6	15,5	19,6	12,2	12,4	18,4	32,1	25,2	28,2	26,1
U	3,32	5,15	5,4	2,46	4,36	3,12	4,84	1,65	7,79	5,95	7,05	7,29
La	93,2	87,4	94,7	55,9	72,6	37,9	35,9	56,2	79,6	72,2	73,9	77,6
Ce	192	177	197	113	144	76,8	73,9	115	162	147	148	151
Pr	24,5	21,9	24,6	13,9	17,9	9,52	9,1	14,5	20,2	18,3	18,1	18,6
Nd	96,4	85,1	97	54,2	69,8	38,2	36,7	57,4	79,4	72,4	68,8	71,2
Sm	20	16,8	20,1	11,4	14	8,1	7,8	11,8	16,4	14,9	13,7	14,4
Eu	5,23	4,18	5,25	3,21	3,98	2,68	2,57	3,58	4,61	4,08	4,07	3,98
Gd	17,8	14,8	18	10,2	12,6	7,52	7,22	10,6	14,5	13,1	12,7	12,9
Tb	2,19	1,79	2,21	1,31	1,5	0,97	0,93	1,31	1,8	1,6	1,48	1,6
Dy	10,5	8,34	10,6	6,52	7,02	4,97	4,82	6,4	8,57	7,51	7,24	7,79
Ho	1,82	1,44	1,84	1,17	1,18	0,92	0,89	1,13	1,49	1,29	1,29	1,4
Er	4,37	3,53	4,43	2,77	2,84	2,36	2,31	2,79	3,64	3,12	3,19	3,53
Tm	0,54	0,45	0,55	0,36	0,34	0,31	0,31	0,36	0,46	0,38	0,42	0,46
Yb	3,19	2,64	3,28	2,12	2,02	1,94	1,93	2,15	2,77	2,25	2,53	2,78
Lu	0,45	0,38	0,46	0,3	0,28	0,28	0,28	0,31	0,39	0,32	0,36	0,4
¹⁴³ Nd/ ¹⁴⁴ Nd				0,512469			0,512472	0,512471				
⁸⁷ Sr/ ⁸⁶ Sr				0,707793			0,707689	0,707784				
Ce/Pb	3,33	3,35	3,32	3,11	4,31	1,63	1,58	2,98	2,76	3,17	3,92	3,28
Sr/Y	38,18	28,07	31,22	32,90	32,78	39,45	37,56	39,30	41,35	32,73	38,36	29,60
Sm/Yb	6,27	6,36	6,13	5,38	6,93	4,18	4,04	5,49	5,92	6,62	5,42	5,18
Nb/U	14,64	6,54	9,30	14,35	5,60	9,68	6,05	21,39	6,89	6,39	5,72	5,64
Gd/Yb	5,58	5,61	5,49	4,81	6,24	3,88	3,74	4,93	5,23	5,82	5,02	4,64
La/Sm	4,66	5,20	4,71	4,90	5,19	4,68	4,60	4,76	4,85	4,85	5,39	5,39
Zr/Hf	40,09	40,93	40,99	40,94	40,38	39,15	43,71	34,79	42,31	40,27	39,24	43,13
Nb/Ta	22,19	21,74	22,41	19,18	23,92	19,24	19,40	21,52	22,66	22,49	22,39	22,34
Rb/Sr	0,16	0,22	0,15	0,20	0,15	0,13	0,21	0,28	0,05	0,13	0,19	0,11
Ba/Rb	11,86	9,97	16,07	17,41	20,20	16,17	10,36	10,02	42,48	22,10	13,49	24,90
Dy/Yb	3,29	3,16	3,23	3,08	3,48	2,56	2,50	2,98	3,09	3,34	2,86	2,80
Th/Nb	0,63	0,89	0,63	0,44	0,80	0,40	0,42	0,52	0,60	0,66	0,70	0,64
Ti/Eu	1359,95	1641,13	1342,89	2327,03	1742,47	2679,85	2770,98	2229,79	1601,45	1737,68	1728,16	1791,16
(La/Yb) _n	20,96	23,75	20,71	18,91	25,78	14,01	13,34	18,75	20,61	23,02	20,95	20,02
(Sm/Yb) _n	6,97	7,07	6,81	5,97	7,70	4,64	4,49	6,10	6,58	7,36	6,02	5,76
Nb/La	0,52	0,39	0,53	0,63	0,34	0,80	0,82	0,63	0,67	0,53	0,55	0,53
Hf/Sm	0,55	0,48	0,55	0,67	0,45	0,61	0,62	0,62	0,63	0,54	0,61	0,62
Ba/Th	122,89	82,16	120,00	242,58	165,92	176,23	167,10	186,30	123,33	138,57	133,48	119,27
K ₂ O+Na ₂ O+CaO	20,28	20,49	20,02	19,13	20,35	17,71	18,45	18,71	19,41	20,60	18,68	17,87
SiO ₂ +Al ₂ O ₃	59,31	58,69	59,85	60,87	58,36	65,63	64,92	61,38	60,70	58,70	64,70	65,91
CaO/Al ₂ O ₃	0,97	0,99	0,96	1,00	1,04	0,69	0,67	0,81	0,86	0,97	0,56	0,55
Na ₂ O+K ₂ O	8,64	8,20	8,41	6,81	6,82	7,43	8,57	8,09	7,88	7,77	9,79	9,49

Table 10 (continued).

Group of rock Reference Location	Group Ia <i>Shafaii Moghadam et al., 2014</i> NW Iran	Group Ia	Group Ia	Group Ia	Group Ia	Group Ia	Group Ia	Group Ia	Group Ia	Group Ia	Group Ia	Group Ia
SiO ₂	53,07	54,93	48,49	48,48	48,64	48,65	48,13	47,81	47,28	47,54	50,50	
TiO ₂	1,00	0,91	1,18	1,28	1,24	1,25	1,17	1,15	1,30	1,24	1,22	
Al ₂ O ₃	12,84	13,42	14,48	14,07	12,48	12,40	11,00	10,92	11,34	14,39	13,03	
Fe ₂ O ₃	7,52	6,97	9,48	10,18	9,11	9,18	8,78	8,58	9,37	10,50	9,61	
MnO	0,14	0,11	0,16	0,19	0,16	0,16	0,16	0,14	0,16	0,18	0,16	
MgO	6,74	6,62	6,19	5,91	7,81	7,81	10,02	10,16	8,60	6,14	5,62	
CaO	9,03	7,17	10,46	11,39	12,63	12,59	12,70	12,51	11,52	11,07	9,95	
Na ₂ O	3,47	2,51	3,89	4,31	3,67	4,11	1,12	1,13	2,29	3,79	2,85	
K ₂ O	5,13	6,45	4,29	2,82	2,89	2,47	5,50	6,21	6,43	3,90	5,79	
P ₂ O ₅	1,06	0,90	1,39	1,36	1,38	1,39	1,44	1,37	1,72	1,24	1,26	
Total	100	100	100	100	100	100	100	100	100	100	100	
Cs	77,3	107,3	18,1	12	9,4	11,5	14,8	10,4	17,8	5,7	20,5	
Rb	206,2	160,6	223,6	50,2	57,8	37,5	424,6	185,7	279,4	49,5	73,6	
Sr	1177,8	1017,7	901,4	1249,6	1195,1	1222,6	1001,8	968,6	1520,2	1671,4	1204,7	
Y	25,2	22	30,6	35,1	35,5	36,8	27,5	27,2	31,7	33,2	31,8	
Zr	282,8	314,9	305,9	275,7	242	266,5	279,3	255,4	341,1	253,4	250,6	
Nb	32,9	44,8	34,1	29	25,6	27,8	28,6	26,2	34,3	36	34,3	
Ba	2704	2250	3701	3189	3797	3703	2863	2778	3746	4410	4240	
Hf	7,8	9,9	9	7,7	8,4	8,5	8,1	8,2	10,2	7,7	9	
Ta	1,9	2,6	1,7	1,3	1,4	1,2	1,7	1,2	1,6	1,6	3,1	
Pb												
Th	33,3	40,9	32,3	21,6	20,7	21,4	23	23,7	25,2	32,1	19,8	
U	6,8	5,5	2,7	2,4	1,5	1,4	5,7	4,8	8,5	9	4,2	
La	55,3	48,1	81,4	76,2	65,7	68,1	65,3	62,8	84,3	102,7	62,8	
Ce	114,3	105,2	159,6	151,9	138,9	138,8	133,9	128,7	171,5	181,5	127	
Pr	13,95	13,25	18,16	17,31	16,38	16,7	16	15,49	19,99	19,27	15,68	
Nd	53,8	53,8	71,2	64,1	64,4	68,5	63,5	61,9	84	68,5	61,1	
Sm	11,07	10,97	12,96	12,77	12,77	13,87	12,19	12	15,65	12,96	12,07	
Eu	2,41	2,21	2,94	2,93	2,97	3	2,63	2,62	3,58	3,15	2,89	
Gd	8,04	7,48	10,5	10,84	11,47	11,14	10,09	9,3	11,92	10,92	10,27	
Tb	1,05	0,95	1,34	1,43	1,55	1,54	1,24	1,17	1,5	1,44	1,36	
Dy	4,59	4,54	6,54	7,2	7,96	7,25	6,12	5,57	6,76	6,94	5,95	
Ho	0,83	0,77	1,06	1,25	1,19	1,2	0,97	0,84	1,08	1,21	1,14	
Er	2,16	2	2,55	3,06	2,99	2,89	2,32	2,43	2,77	2,89	2,96	
Tm	0,29	0,28	0,37	0,39	0,4	0,38	0,33	0,3	0,36	0,42	0,32	
Yb	1,88	1,83	2,36	2,59	2,4	2,14	1,93	1,92	2,28	2,39	2,56	
Lu	0,26	0,28	0,3	0,33	0,32	0,34	0,26	0,25	0,31	0,37	0,27	
¹⁴³ Nd/ ¹⁴⁴ Nd					0,512475			0,512449		0,512518		
⁸⁷ Sr/ ⁸⁶ Sr					0,707866			0,707968		0,706618		
Ce/Pb												
Sr/Y	46,74	46,26	29,46	35,60	33,66	33,22	36,43	35,61	47,96	50,34	37,88	
Sm/Yb	5,89	5,99	5,49	4,93	5,32	6,48	6,32	6,25	6,86	5,42	4,71	
Nb/U	4,84	8,15	12,63	12,08	17,07	19,86	5,02	5,46	4,04	4,00	8,17	
Gd/Yb	4,28	4,09	4,45	4,19	4,78	5,21	5,23	4,84	5,23	4,57	4,01	
La/Sm	5,00	4,38	6,28	5,97	5,14	4,91	5,36	5,23	5,39	7,92	5,20	
Zr/Hf	36,26	31,81	33,99	35,81	28,81	31,35	34,48	31,15	33,44	32,91	27,84	
Nb/Ta	17,32	17,23	20,06	22,31	18,29	23,17	16,82	21,83	21,44	22,50	11,06	
Rb/Sr	0,18	0,16	0,25	0,04	0,05	0,03	0,42	0,19	0,18	0,03	0,06	
Ba/Rb	13,11	14,01	16,55	63,53	65,69	98,75	6,74	14,96	13,41	89,09	57,61	
Dy/Yb	2,44	2,48	2,77	2,78	3,32	3,39	3,17	2,90	2,96	2,90	2,32	
Th/Nb	1,01	0,91	0,95	0,74	0,81	0,77	0,80	0,90	0,73	0,89	0,58	
Ti/Eu	2487,08	2474,28	2409,05	2628,42	2506,60	2499,26	2658,87	2636,34	2172,09	2366,78	2525,01	
(La/Yb) _n	21,10	18,85	24,74	21,10	19,64	22,83	24,27	23,46	26,52	30,82	17,60	
(Sm/Yb) _n	6,54	6,66	6,10	5,48	5,91	7,20	7,02	6,94	7,63	6,03	5,24	
Nb/La	0,59	0,93	0,42	0,38	0,39	0,41	0,44	0,42	0,41	0,35	0,55	
Hf/Sm	0,70	0,90	0,69	0,60	0,66	0,61	0,66	0,68	0,65	0,59	0,75	
Ba/Th	81,20	55,01	114,58	147,64	183,43	173,04	124,48	117,22	148,65	137,38	214,14	
K ₂ O+Na ₂ O+CaO	17,63	16,13	18,63	18,53	19,19	19,17	19,32	19,85	20,24	18,76	18,59	
SiO ₂ +Al ₂ O ₃	65,91	68,36	62,97	62,55	61,12	61,05	59,12	58,74	58,62	61,93	63,54	
CaO/Al ₂ O ₃	0,70	0,53	0,72	0,81	1,01	1,02	1,15	1,15	1,02	0,77	0,76	
Na ₂ O+K ₂ O	8,60	8,96	8,17	7,13	6,56	6,58	6,62	7,34	8,72	7,69	8,65	

Table 10 (continued).

Group of rock Reference Location	Group Ia	Group Ia	Group Ia	Group Ia	Group Ia	Group Ia	Group Ia	Group Ia	Group Ia	Group Ia	Group Ia	Group Ia	Group Ia
" "	" "	" "	" "	" "	" "	" "	" "	" "	" "	" "	Moayed et al., 2008	" "	" "
" "	" "	" "	" "	" "	" "	" "	" "	" "	" "	" "	NW Iran	" "	" "
SiO ₂	54,30	55,12	49,21	49,42	47,80	47,16	50,14	45,40	45,14	49,01		49,84	49,17
TiO ₂	0,81	0,83	1,10	1,31	1,29	1,28	1,07	1,26	1,25	1,18		1,27	1,15
Al ₂ O ₃	17,35	17,14	14,02	13,10	13,05	13,03	14,66	13,34	14,27	13,12		13,91	13,10
Fe ₂ O ₃	7,48	7,25	9,27	9,58	9,30	8,86	9,55	10,20	10,33	9,49		9,21	9,19
MnO	0,16	0,16	0,17	0,17	0,16	0,15	0,17	0,18	0,17	0,16		0,15	0,16
MgO	2,57	2,73	7,76	7,21	7,43	8,14	6,20	8,01	7,20	6,32		4,39	6,34
CaO	6,57	6,11	11,64	11,85	12,43	11,60	9,68	12,92	11,74	12,10		11,09	12,10
Na ₂ O	3,60	3,44	4,60	4,05	1,30	2,87	4,24	1,43	2,26	0,74		1,21	0,72
K ₂ O	6,58	6,72	1,42	2,38	5,80	5,61	3,27	6,04	6,29	6,60		7,61	6,71
P ₂ O ₅	0,57	0,50	0,81	0,93	1,44	1,30	1,03	1,22	1,35	1,27		1,31	1,35
Total	100	100	100	100	100	100	100	100	100	100		100	100
Cs	5,8	2,8	31,8	32,1	5,6	7,8	9	8,8	10,2				
Rb	122,6	128,9	32,3	42,3	122,1	70,2	82,8	184,5	185,8	192		186	188
Sr	1672,5	1558,6	1481,8	1302	1275	953,2	1073,9	1094	1152,1	742		910	752
Y	36,8	39,9	32,8	34,9	35,8	29,5	34,1	31,4	33,5	28		30	28
Zr	353,1	395,6	256,8	262,2	314,7	291,8	285,9	283	302,9	260		298	294
Nb	33,7	42	23,1	23,9	34,7	32,6	26,9	26,6	32,8	34		32	35
Ba	3084	2957	2896	2606	3903	3216	2976	3298	3807	1981		3560	1978
Hf	8,4	10	7,7	8,4	7,9	7,2	7,7	7,9	8,5	9		10	9
Ta	3	2,9	1,9	2	2,5	1,9	2,1	1,7	1,9	1,86		1,99	1,98
Pb										38		36	32
Th	41,9	42,5	20,7	23,6	20,3	20,8	20	16,9	19,9	21		17	20
U	11,1	12	6	7,6	6,6	5,3	6	3,7	5,5	2		3	2
La	112,4	107	68,4	70,3	59,9	62,8	58,2	55,6	61,3	82		66	85
Ce	195,1	193,3	133,4	142,5	115,3	125	116,8	108,4	123,3	142		112	148
Pr	22,19	22,56	16,64	18,57	14,99	14,74	14,11	13,58	15,02				
Nd	76,4	79,1	66,9	69,3	56,3	59,6	51,7	55,2	60,4	79		64	78
Sm	13,08	13,59	12	13,56	12,1	10,01	10,79	11,52	11,79				
Eu	3	3,1	2,78	3,04	2,8	2,6	2,34	2,69	2,59				
Gd	9,97	11,09	9,86	11,23	10,56	8,78	9,72	9,53	10,49				
Tb	1,33	1,42	1,32	1,45	1,41	1,2	1,29	1,29	1,41				
Dy	7,01	7,03	7,13	7,9	7,39	5,77	7,34	6,33	6,88				
Ho	1,11	1,34	1,16	1,36	1,18	0,98	1,16	1,1	1,12				
Er	3,05	3,7	2,73	3,4	2,91	2,52	2,83	2,5	2,9				
Tm	0,46	0,53	0,38	0,4	0,41	0,34	0,4	0,36	0,39				
Yb	3,13	3,58	2,73	2,82	2,49	1,89	3,05	2,12	2,25	3,64		2,67	3,68
Lu	0,4	0,46	0,36	0,35	0,3	0,28	0,33	0,27	0,32				
143Nd/144Nd		0,512495			0,512451					0,512506			
87Sr/86Sr		0,707809			0,708074					0,707635			
Ce/Pb										3,74		3,11	4,63
Sr/Y	45,45	39,06	45,18	37,31	35,61	32,31	31,49	34,84	34,39	26,50		30,33	26,86
Sm/Yb	4,18	3,80	4,40	4,81	4,86	5,30	3,54	5,43	5,24	0,00		0,00	0,00
Nb/U	3,04	3,50	3,85	3,14	5,26	6,15	4,48	7,19	5,96	17,00		10,67	17,50
Gd/Yb	3,19	3,10	3,61	3,98	4,24	4,65	3,19	4,50	4,66	0,00		0,00	0,00
La/Sm	8,59	7,87	5,70	5,18	4,95	6,27	5,39	4,83	5,20				
Zr/Hf	42,04	39,56	33,35	31,21	39,84	40,53	37,13	35,82	35,64	28,89		29,80	32,67
Nb/Ta	11,23	14,48	12,16	11,95	13,88	17,16	12,81	15,65	17,26	18,28		16,08	17,68
Rb/Sr	0,07	0,08	0,02	0,03	0,10	0,07	0,08	0,17	0,16	0,26		0,20	0,25
Ba/Rb	25,15	22,94	89,66	61,61	31,97	45,81	35,94	17,88	20,49	10,32		19,14	10,52
Dy/Yb	2,24	1,96	2,61	2,80	2,97	3,05	2,41	2,99	3,06	0,00		0,00	0,00
Th/Nb	1,24	1,01	0,90	0,99	0,59	0,64	0,74	0,64	0,61	0,62		0,53	0,57
Ti/Eu	1620,52	1604,82	2369,79	2576,00	2752,98	2960,72	2737,13	2804,22	2894,87				
(La/Yb) _n	25,76	21,44	17,97	17,88	17,26	23,83	13,69	18,81	19,54	16,16		17,73	16,57
(Sm/Yb) _n	4,64	4,22	4,88	5,34	5,40	5,88	3,93	6,04	5,82	0,00		0,00	0,00
Nb/La	0,30	0,39	0,34	0,34	0,58	0,52	0,46	0,48	0,54	0,41		0,48	0,41
Hf/Sm	0,64	0,74	0,64	0,62	0,65	0,72	0,71	0,69	0,72				
Ba/Th	73,60	69,58	139,90	110,42	192,27	154,62	148,80	195,15	191,31	94,33		209,41	98,90
K ₂ O+Na ₂ O+CaO	16,75	16,27	17,67	18,29	19,53	20,07	17,19	20,40	20,29	19,44		19,91	19,53
SiO ₂ +Al ₂ O ₃	71,65	72,26	63,23	62,52	60,86	60,18	64,80	58,74	59,41	62,13		63,75	62,27
CaO/Al ₂ O ₃	0,38	0,36	0,83	0,90	0,95	0,89	0,66	0,97	0,82	0,92		0,80	0,92
Na ₂ O+K ₂ O	10,18	10,16	6,02	6,44	7,09	8,47	7,51	7,48	8,55	7,34		8,82	7,43

Table 10 (continued).

Group of rock Reference	Group Ia	Group Ia	Group Ia	Group Ia	Group Ia	Group Ia	Group Ia	Group Ia	Group Ia	Group Ia	Group Ia	Group Ia	Group Ia
Location	" "	" "	Aghazadeh et al., 2015 NW Iran	" "	" "	" "	" "	" "	" "	" "	" "	" "	" "
SiO ₂	48,84	48,22	47,76	47,20	45,81	47,69	47,09	47,63	49,00	48,44	48,74	49,03	
TiO ₂	1,08	1,24	1,75	1,69	1,77	1,65	1,78	1,65	1,18	1,31	1,33	1,30	
Al ₂ O ₃	12,96	12,66	14,59	14,35	13,46	14,15	13,96	13,69	9,55	13,77	14,54	14,67	
Fe ₂ O ₃	9,67	10,40	12,38	12,44	12,48	11,84	12,78	11,88	8,95	10,66	10,82	10,73	
MnO	0,18	0,28	0,21	0,21	0,22	0,20	0,25	0,21	0,15	0,19	0,18	0,19	
MgO	5,29	6,69	5,89	6,72	7,29	6,91	7,83	7,43	10,87	5,54	4,39	4,45	
CaO	11,94	11,22	9,48	9,37	11,62	9,80	8,63	9,59	12,51	9,61	9,39	9,18	
Na ₂ O	2,88	1,11	2,76	3,19	2,82	2,83	2,77	2,55	1,23	0,72	1,33	0,88	
K ₂ O	5,96	6,65	4,30	4,01	3,72	4,17	4,10	4,61	4,72	8,29	7,94	8,26	
P ₂ O ₅	1,21	1,55	0,87	0,83	0,80	0,75	0,82	0,75	1,86	1,47	1,33	1,31	
Total	100	100	100	100	100	100	100	100	100	100	100	100	
Cs			1,8	7,5	6,1	9,1	3,4	5,3	8,7	9,3	27	19	
Rb	212	154	81	80	82	82	69	96	111	183	169	169	
Sr	882	841	1233	841	545	1169	585	934	880	1490	1380	1250	
Y	36	25	32	32	28	30	30	31	22,8	36,4	33,8	35	
Zr	284	218	169	166	140	170	156	170	220	480	440	450	
Nb	27	30	14	13	12	14	13	14	27	38	34	38	
Ba	2810	2828	1639	1350	1191	1458	1230	1675	3020	3230	3270	3030	
Hf	10	8	4	4	4	4	4	4	6	10	9	11	
Ta	2,08	1,96	0,7	0,8	0,6	0,7	0,6	0,7	1,4	1,9	1,7	1,9	
Pb	28	29	24	69	51	32	53	86	32	25	49	49	
Th	19	29	12,8	14,6	9,5	14,9	11,3	15,2	13,3	37	32,2	36,7	
U	3	8	5,3	4,3	3,8	5	2,5	4,5	3,5	10,8	10,1	11	
La	78	52	51,7	51,7	40,1	48,1	42,4	50,9	40,6	84,9	75	86,9	
Ce	132	112	96,2	101	81,6	94,8	85,2	98,2	80,6	172	150	175	
Pr			11,3	12,1	10,1	11,4	10,6	11,9	10,2	20,6	17,9	21,2	
Nd	83	43	44,7	50	40,5	45,7	43,3	47	42	80,4	69	80,7	
Sm			9,2	10,1	8,9	9,4	9,1	9,8	8,7	14,8	12,6	14,8	
Eu			2,32	2,53	2,23	2,33	2,3	2,44	1,94	3,16	2,73	3,05	
Gd			7,42	8,44	7,48	7,66	7,55	7,75	6,9	10,6	9,48	10,4	
Tb			1,07	1,1	1,01	1,05	1,02	1,08	0,94	1,44	1,28	1,42	
Dy			5,36	6,16	5,37	5,74	5,55	5,92	4,72	7,51	6,87	7,24	
Ho			0,98	1,14	0,99	0,96	0,97	1,02	0,81	1,32	1,22	1,29	
Er			2,51	2,81	2,45	2,63	2,42	2,81	2,05	3,22	3,11	3,17	
Tm			0,33	0,36	0,33	0,32	0,32	0,37	0,23	0,43	0,38	0,41	
Yb	3,59	3,72	2	2,2	1,9	2,1	1,9	2,2	1,5	2,5	2,4	2,6	
Lu			0,25	0,26	0,23	0,22	0,2	0,24	0,21	0,34	0,33	0,34	
143Nd/144Nd			0,512564	0,512582	0,512573	0,51258	0,51257	0,512567	0,512463	0,51247	0,512466	0,512463	
87Sr/86Sr			0,70738	0,707408	0,707367	0,707393	0,70737	0,707402	0,707559	0,70754	0,707603	0,707545	
Ce/Pb	4,71	3,86	4,01	1,46	1,60	2,96	1,61	1,14	2,52	6,88	3,06	3,57	
Sr/Y	24,50	33,64	38,53	26,28	19,46	38,97	19,50	30,13	38,60	40,93	40,83	35,71	
Sm/Yb	0,00	0,00	4,60	4,59	4,68	4,48	4,79	4,45	5,80	5,92	5,25	5,69	
Nb/U	9,00	3,75	2,64	3,02	3,16	2,80	5,20	3,11	7,71	3,52	3,37	3,45	
Gd/Yb	0,00	0,00	3,71	3,84	3,94	3,65	3,97	3,52	4,60	4,24	3,95	4,00	
La/Sm			5,62	5,12	4,51	5,12	4,66	5,19	4,67	5,74	5,95	5,87	
Zr/Hf	28,40	27,25	42,25	41,50	35,00	42,50	39,00	42,50	36,67	48,00	48,89	40,91	
Nb/Ta	12,98	15,31	20,00	16,25	20,00	20,00	21,67	20,00	19,29	20,00	20,00	20,00	
Rb/Sr	0,24	0,18	0,07	0,10	0,15	0,07	0,12	0,10	0,13	0,12	0,12	0,14	
Ba/Rb	13,25	18,36	20,23	16,88	14,52	17,78	17,83	17,45	27,21	17,65	19,35	17,93	
Dy/Yb	0,00	0,00	2,68	2,80	2,83	2,73	2,92	2,69	3,15	3,00	2,86	2,78	
Th/Nb	0,70	0,97	0,91	1,12	0,79	1,06	0,87	1,09	0,49	0,97	0,95	0,97	
Ti/Eu			4513,45	4005,18	4756,91	4234,40	4637,23	4066,34	3642,68	2493,71	2925,73	2560,00	
(La/Yb) _n	15,58	10,03	18,54	16,86	15,14	16,43	16,01	16,60	19,41	24,36	22,42	23,97	
(Sm/Yb) _n	0,00	0,00	5,11	5,10	5,20	4,97	5,32	4,95	6,44	6,58	5,83	6,32	
Nb/La	0,35	0,58	0,27	0,25	0,30	0,29	0,31	0,28	0,67	0,45	0,45	0,44	
Hf/Sm			0,43	0,40	0,45	0,43	0,44	0,41	0,69	0,68	0,71	0,74	
Ba/Th	147,89	97,52	128,05	92,47	125,37	97,85	108,85	110,20	227,07	87,30	101,55	82,56	
K ₂ O+Na ₂ O+CaO	20,78	18,97	16,55	16,56	18,16	16,80	15,50	16,75	18,45	18,63	18,66	18,32	
SiO ₂ +Al ₂ O ₃	61,80	60,87	62,35	61,55	59,27	61,84	61,04	61,32	58,55	62,20	63,28	63,70	
CaO/Al ₂ O ₃	0,92	0,89	0,65	0,65	0,86	0,69	0,62	0,70	1,31	0,70	0,65	0,63	
Na ₂ O+K ₂ O	8,84	7,75	7,06	7,20	6,55	7,00	6,87	7,16	5,95	9,01	9,27	9,14	

Table 10 (continued).

Group of rock	Group Ia	Group Ia	Group Ia	Group Ia	Group Ia	Group Ia	Group Ia	Group Ia	Group Ia	Group Ia	Group Ia	Group Ia
Reference	" "	Prelević et al., 2014	" "	" "	" "	" "	" "	" "	" "	" "	" "	" "
Location	" "	KAI-Anatolia	" "	" "	" "	" "	" "	" "	" "	" "	" "	" "
SiO ₂	48,22	50,60	48,24	47,10	47,64	47,74	47,97	48,28	48,31	48,22	48,39	48,00
TiO ₂	1,33	1,49	1,34	1,31	1,32	1,08	1,05	1,09	1,09	1,07	1,03	1,06
Al ₂ O ₃	13,98	17,38	17,40	16,91	16,97	18,57	18,43	18,59	18,58	18,43	18,46	18,30
Fe ₂ O ₃	10,78	8,67	7,47	7,35	7,48	6,74	6,69	6,79	6,81	6,80	6,72	6,73
MnO	0,19	0,18	0,14	0,14	0,15	0,12	0,12	0,12	0,13	0,12	0,13	0,13
MgO	5,29	2,06	3,05	3,82	2,70	1,67	1,78	2,44	1,92	2,26	1,88	1,95
CaO	9,48	6,63	9,90	9,81	11,14	10,09	10,11	7,70	8,45	9,58	10,41	9,22
Na ₂ O	0,64	2,69	1,94	2,61	3,16	2,07	1,74	2,34	2,07	1,36	2,06	2,13
K ₂ O	8,60	10,02	10,00	10,44	8,92	11,62	11,84	12,38	12,37	11,82	10,60	12,17
P ₂ O ₅	1,48	0,29	0,53	0,51	0,52	0,29	0,27	0,28	0,28	0,33	0,32	0,32
Total	100	100	100	100	100	100	100	100	100	100	100	100
Cs	7,9		13,39	10,15	10,61	10,09	10,74	60,60	29,07	11,15	44,29	10,55
Rb	196		492,15	357,59	440,07	293,78	285,39	1381,32	924,41	351,25	1411,51	319,74
Sr	1540		2153,55	2535,91	3636,14	3081,80	3422,10	2436,12	3155,34	4176,38	3665,96	3086,55
Y	37,1		27,27	28,34	31,18	23,50	24,34	23,10	23,07	22,79	20,47	23,20
Zr	460		633,10	682,00	722,80	516,65	530,96	525,62	498,57	495,85	442,20	493,27
Nb	38		38,01	39,95	45,13	38,63	37,47	35,92	34,73	34,02	33,47	37,10
Ba	3110		8818,32	6171,00	6272,26	4583,71	4491,94	9229,03	7090,94	4655,93	9800,94	4874,32
Hf	7		14,96	16,15	16,75	11,77	12,45	12,30	11,67	11,53	10,52	11,70
Ta	1,9		2,27	2,43	2,70	2,14	2,12	1,94	1,86	1,81	1,91	2,16
Pb	54		121,48	38,24	105,61	29,78	89,95	66,94	76,53	71,67	37,99	79,32
Th	37		55,97	56,27	65,87	56,52	55,43	47,16	48,05	47,05	46,88	55,78
U	11,2		16,87	18,31	20,27	18,57	14,66	16,08	16,06	15,06	15,43	15,24
La	89,8		122,24	121,96	136,85	103,29	97,82	89,59	89,03	90,01	85,91	100,57
Ce	179		208,17	216,90	239,42	182,76	173,58	154,79	151,64	158,42	155,00	179,81
Pr	21,9		23,08	23,69	26,38	20,69	19,64	17,58	17,16	17,88	17,42	20,42
Nd	83,8		84,82	87,09	96,31	76,89	73,72	65,98	65,24	67,44	65,47	76,33
Sm	14,6		13,96	14,22	15,72	12,47	12,18	11,00	11,13	11,22	10,73	12,36
Eu	3,26		3,43	3,50	3,91	3,18	3,12	3,04	2,89	2,77	2,92	3,05
Gd	10,9		9,12	9,25	10,28	8,46	8,31	7,63	7,62	7,59	6,78	8,00
Tb	1,49		1,06	1,14	1,21	0,94	0,96	0,89	0,84	0,88	0,82	0,93
Dy	7,83		5,68	5,92	6,51	4,96	5,12	4,77	4,73	4,64	4,18	4,98
Ho	1,36		0,99	1,01	1,08	0,86	0,88	0,82	0,81	0,83	0,75	0,86
Er	3,2		2,51	2,58	2,88	2,21	2,35	2,27	2,11	2,16	1,89	2,26
Tm	0,41		0,36	0,36	0,40	0,32	0,33	0,32	0,32	0,30	0,25	0,31
Yb	2,5		2,24	2,33	2,57	1,98	2,12	2,06	1,97	1,89	1,80	1,98
Lu	0,36		0,32	0,32	0,36	0,30	0,30	0,29	0,29	0,29	0,24	0,28
143Nd/144Nd	0,512472				0,512534							
87Sr/86Sr	0,707522				0,705666							
Ce/Pb	3,31		1,71	5,67	2,27	6,14	1,93	2,31	1,98	2,21	4,08	2,27
Sr/Y	41,51		78,96	89,48	116,62	131,16	140,58	105,46	136,79	183,25	179,06	133,06
Sm/Yb	5,84		6,22	6,09	6,11	6,30	5,75	5,34	5,65	5,94	5,95	6,25
Nb/U	3,39		2,25	2,18	2,23	2,08	2,56	2,23	2,16	2,26	2,17	2,43
Gd/Yb	4,36		4,06	3,96	4,00	4,27	3,92	3,70	3,87	4,01	3,76	4,05
La/Sm	6,15		8,76	8,58	8,70	8,28	8,03	8,14	8,00	8,02	8,01	8,14
Zr/Hf	65,71		42,32	42,22	43,14	43,88	42,64	42,73	42,73	43,00	42,03	42,15
Nb/Ta	20,00		16,72	16,46	16,73	18,05	17,65	18,48	18,64	18,79	17,55	17,18
Rb/Sr	0,13		0,23	0,14	0,12	0,10	0,08	0,57	0,29	0,08	0,39	0,10
Ba/Rb	15,87		17,92	17,26	14,25	15,60	15,74	6,68	7,67	13,26	6,94	15,24
Dy/Yb	3,13		2,53	2,54	2,53	2,51	2,42	2,32	2,40	2,46	2,32	2,52
Th/Nb	0,97		1,47	1,41	1,46	1,46	1,48	1,31	1,38	1,38	1,40	1,50
Ti/Eu	2452,51		2345,18	2238,08	2018,34	2027,78	2023,74	2154,75	2261,67	2309,74	2111,76	2087,92
(La/Yb) _n	25,77		39,08	37,49	38,15	37,42	33,10	31,20	32,42	34,16	34,17	36,50
(Sm/Yb) _n	6,49		6,91	6,77	6,79	7,00	6,38	5,93	6,28	6,60	6,61	6,95
Nb/La	0,42		0,31	0,33	0,33	0,37	0,38	0,40	0,39	0,38	0,39	0,37
Hf/Sm	0,48		1,07	1,14	1,07	0,94	1,02	1,12	1,05	1,03	0,98	0,95
Ba/Th	84,05		157,55	109,67	95,22	81,10	81,04	195,71	147,57	98,96	209,05	87,38
K ₂ O+Na ₂ O+CaO	18,72	19,34	21,84	22,87	23,22	23,79	23,68	22,42	22,89	22,77	23,07	23,51
SiO ₂ +Al ₂ O ₃	62,20	67,98	65,64	64,01	64,61	66,32	66,41	66,87	66,89	66,65	66,85	66,29
CaO/Al ₂ O ₃	0,68	0,38	0,57	0,58	0,66	0,54	0,55	0,41	0,45	0,52	0,56	0,50
Na ₂ O+K ₂ O	9,24	12,71	11,94	13,05	12,08	13,69	13,57	14,71	14,44	13,19	12,66	14,29

Table 10 (continued).

Group of rock Reference	Group Ia	Group Ia	Group Ia	Group Ia	Group Ia	Group Ia	Group Ia	Group Ia	Group Ia	Group Ia	Group Ia	Group Ia	Group Ia
Location	" "	" "	" "	" "	" "	" "	" "	" "	" "	" "	" "	" "	" "
SiO ₂	55,13	55,94	55,95	55,84	55,00	57,21	47,13	49,09	50,17	53,30	54,11	56,14	56,39
TiO ₂	1,13	0,98	0,98	0,88	0,95	0,77	1,23	0,89	1,31	0,99	1,33	1,39	1,38
Al ₂ O ₃	10,47	17,90	18,23	19,14	17,47	20,08	16,61	18,98	14,65	17,08	10,59	11,29	11,21
Fe ₂ O ₃	12,12	6,03	5,86	5,95	6,13	5,09	7,56	6,24	8,86	6,60	8,29	6,72	6,33
MnO	1,01	0,07	0,08	0,10	0,11	0,09	0,15	0,12	0,15	0,13	0,30	0,20	0,08
MgO	3,64	3,46	3,46	2,75	3,93	1,81	2,90	2,25	4,02	4,16	5,01	5,17	5,20
CaO	4,89	6,87	6,85	6,16	6,74	5,48	11,06	7,29	10,11	8,54	9,54	7,19	7,37
Na ₂ O	1,46	4,14	4,80	4,09	3,55	3,05	2,39	1,91	1,49	3,82	1,89	1,48	1,75
K ₂ O	8,46	4,05	3,23	4,57	5,59	6,07	10,49	13,01	8,40	4,77	7,21	8,62	8,41
P ₂ O ₅	1,68	0,55	0,55	0,53	0,53	0,33	0,48	0,23	0,85	0,61	1,74	1,80	1,88
Total	100	100	100	100	100	100	100	100	100	100	100	100	100
Cs	6,90	60,64	29,56	3,75	5,21	302,82							
Rb	113,71	219,98	417,04	48,46	114,03	127,15	739,20	520,68	659,88	194,00	858,00	110,14	208
Sr	1153,08	1857,83	2144,01	2282,97	1671,99	2268,23	3271,22	2352,49	3540,05	2185,00	1195,00	974,79	1287
Y	21,24	20,54	21,32	25,94	23,18	24,43	31,23	21,75	24,94	25,00	17,00	16,38	29
Zr	313,16	272,41	338,18	465,37	446,33	398,69	740,39	498,29	595,32	379,00	422,00	242,00	456
Nb	26,27	24,61	30,24	50,90	34,61	43,75	43,82	37,32	32,80	42,00	25,00	14,59	30
Ba	1457,45	1739,34	2204,96	1983,59	2373,84	1977,51	9349,65	8155,98	5318,38	2782,00	4325,00	2196,44	3942
Hf	7,79	6,75	7,92	10,56	9,52	8,61	17,16	11,89	16,02			6,48	
Ta	1,65	1,55	1,82	2,98	2,12	2,72	2,70	1,96	2,04			0,78	
Pb	22,57	36,82	36,94	22,08	53,95	26,40	139,00	92,00	63,00	40,00	40,00	40,00	45
Th	28,48	29,28	36,56	39,52	40,73	41,44	62,04	47,49	37,17	41,30	18,60	10,09	21,6
U	9,96	6,94	10,54	8,80	11,11	6,33	19,77	14,60	5,25	10,50	1,30	2,13	4
La	88,23	107,74	125,22	144,46	124,95	133,93	132,99	85,83	92,93			28,77	
Ce	152,48	183,66	212,47	235,34	212,94	221,32	223,22	149,33	162,76			51,34	
Pr	16,61	20,03	22,41	25,31	22,16	23,12	25,10	17,10	19,26			6,13	
Nd	61,51	73,64	80,23	89,22	79,67	82,07	94,02	65,65	75,43			25,19	
Sm	9,35	11,20	12,08	12,65	11,95	11,28	15,47	10,79	12,91			5,16	
Eu	2,20	2,64	2,92	3,16	2,93	2,75	3,64	2,62	3,15			1,27	
Gd	6,43	7,61	7,87	8,23	7,71	7,12	10,24	7,22	9,17			4,39	
Tb	0,75	0,83	0,87	0,92	0,89	0,86	1,19	0,84	1,07			0,57	
Dy	4,30	4,21	4,44	5,01	4,54	4,46	6,39	4,65	5,84			3,40	
Ho	0,77	0,73	0,78	0,95	0,81	0,82	1,12	0,77	0,97			0,60	
Er	2,02	1,96	2,03	2,48	2,16	2,29	2,88	2,02	2,54			1,53	
Tm	0,28	0,26	0,28	0,34	0,32	0,34	0,42	0,29	0,34			0,22	
Yb	1,86	1,58	1,77	2,46	2,09	2,25	2,67	1,94	2,30			1,41	
Lu	0,28	0,24	0,26	0,36	0,31	0,34	0,37	0,28	0,34			0,20	
143Nd/144Nd	0,512492			0,51261		0,512515	0,512516				0,512392	0,51241	0,512491
87Sr/86Sr	0,706346			0,705559		0,706031	0,705806				0,708012	0,707958	0,707372
Ce/Pb	6,76	4,99	5,75	10,66	3,95	8,38	1,61	1,62	2,58	0,00	0,00	1,28	0,00
Sr/Y	54,29	90,46	100,56	88,02	72,14	92,85	104,75	108,16	141,92	87,40	70,29	59,52	44,38
Sm/Yb	5,03	7,08	6,83	5,14	5,71	5,02	5,80	5,56	5,60			3,65	
Nb/U	2,64	3,55	2,87	5,78	3,11	6,91	2,22	2,56	6,24	4,00	19,23	6,84	7,50
Gd/Yb	3,46	4,80	4,45	3,34	3,68	3,17	3,84	3,72	3,98			3,10	
La/Sm	9,44	9,62	10,36	11,42	10,45	11,87	8,60	7,96	7,20			5,58	
Zr/Hf	40,18	40,36	42,72	44,07	46,90	46,31	43,14	41,90	37,16			37,35	
Nb/Ta	15,92	15,88	16,61	17,08	16,35	16,10	16,23	19,02	16,10			18,73	
Rb/Sr	0,10	0,12	0,19	0,02	0,07	0,06	0,23	0,22	0,19	0,09	0,72	0,11	0,16
Ba/Rb	12,82	7,91	5,29	40,93	20,82	15,55	12,65	15,66	8,06	14,34	5,04	19,94	18,95
Dy/Yb	2,31	2,66	2,51	2,04	2,17	1,99	2,39	2,40	2,53			2,40	
Th/Nb	1,08	1,19	1,21	0,78	1,18	0,95	1,42	1,27	1,13	0,98	0,74	0,69	0,72
Ti/Eu	3073,03	2216,51	2013,44	1661,26	1936,93	1687,47	2026,90	2028,80	2481,20			6601,03	
(La/Yb) _n	34,09	48,81	50,75	42,12	42,81	42,76	35,76	31,73	28,94			14,60	
(Sm/Yb) _n	5,59	7,86	7,59	5,71	6,34	5,58	6,44	6,18	6,23			4,05	
Nb/La	0,30	0,23	0,24	0,35	0,28	0,33	0,33	0,43	0,35			0,51	
Hf/Sm	0,83	0,60	0,66	0,83	0,80	0,76	1,11	1,10	1,24			1,26	
Ba/Th	51,18	59,40	60,32	50,19	58,28	47,72	150,71	171,76	143,07	67,36	232,53	217,76	182,50
K ₂ O+Na ₂ O+CaO	14,81	15,06	14,88	14,81	15,88	14,61	23,94	22,21	20,00	17,13	18,64	17,29	17,53
SiO ₂ +Al ₂ O ₃	65,60	73,84	74,19	74,98	72,46	77,29	63,75	68,06	64,82	70,38	64,70	67,44	67,61
CaO/Al ₂ O ₃	0,47	0,38	0,38	0,32	0,39	0,27	0,67	0,38	0,69	0,50	0,90	0,64	0,66
Na ₂ O+K ₂ O	9,92	8,19	8,03	8,65	9,14	9,12	12,88	14,92	9,90	8,59	9,10	10,10	10,16

Table 10 (continued).

Group of rock Reference	Group Ia	Group Ia	Group Ia	Group Ia	Group Ia	Group Ia	Group Ia	Group Ia	Group Ia	Group Ia	Group Ib	Group Ib	Group Ib
Location	" "	" "	" "	" "	" "	" "	" "	" "	" "	" "	Aydin et al., 2008 East Pontides	" "	" "
SiO ₂	52,69	53,08	55,69	55,83	55,87	53,83	53,73	49,94	54,27		43,90	42,68	41,49
TiO ₂	1,02	1,30	1,29	1,46	1,45	1,13	1,14	1,34	1,43		1,51	1,38	1,40
Al ₂ O ₃	9,55	10,39	10,57	10,64	10,67	9,93	9,92	9,89	10,79		13,74	15,09	15,18
Fe ₂ O ₃	7,14	7,76	10,10	10,25	10,33	6,99	6,87	9,26	7,28		10,20	10,78	10,67
MnO	0,13	0,14	0,66	0,38	0,44	0,13	0,20	0,13	0,19		0,16	0,20	0,19
MgO	8,13	6,67	4,16	4,86	4,57	8,48	7,47	10,67	5,37		8,41	8,13	7,85
CaO	10,70	9,40	6,55	6,33	5,98	8,66	9,80	8,24	9,02		16,44	16,76	15,40
Na ₂ O	1,53	1,67	1,92	1,52	1,52	1,42	1,51	1,29	1,64		2,98	1,46	3,82
K ₂ O	7,62	7,84	7,00	6,94	7,43	7,93	7,78	7,70	8,31		1,16	1,95	2,48
P ₂ O ₅	1,50	1,75	2,05	1,79	1,73	1,49	1,58	1,54	1,71		1,50	1,56	1,51
Total	100	100	100	100	100	100	100	100	100		100	100	100
Cs											10,2	1,3	4
Rb	201	194	514	383	419,2	213,2	538,8	194,6	266,6		168	41,5	51,6
Sr	1253	1204	1079	1106,8	1083,1	1226,2	1230,1	1168,7	1140,7		1962	2037	6086
Y	26	24	21	26,4	26,1	23,7	22,9	25,8	25,6		21,5	27,2	27,9
Zr	449	408	434	455,9	469,5	360,8	353,3	440,5	427,9		243	222	210
Nb	29	27	27	27,9	29	22,4	21,1	26,9	26		44	41,1	48,1
Ba	4145	3399	4683	3784	3773	3428	3468	3437	3516		1303	1233	1607
Hf				12,6	12,7	9,4	9,4	11,9	11,3		5,1	5,4	3,9
Ta				1,7	1,8	1,3	1,3	1,6	1,5		2,1	2,1	2,6
Pb	48	45	42	32	32	31	32	33	30		28,6	20	24
Th	22,6	19,4	19,1	18,9	19,4	14,2	13,3	19,9	18,5		16,9	19,5	23,9
U	4,2	6,2	4,9	4,3	4,3	4	4,9	6,6	6		3,7	2,3	5,7
La				47,7	48,1	43,5	41,8	45,2	45,3		130	159,5	146,9
Ce				98,9	96,9	83,2	81	94,7	94,3		260	329,5	278,7
Pr				11,65	11,57	9,35	9,25	11,7	11,63		30,7	37,2	29,5
Nd				47,8	46,1	36,8	35,7	47,8	47,1		113	146	105,1
Sm				9,8	10,1	8,4	7,9	10,1	9,7		16,5	20,9	13,9
Eu				2,18	2,09	1,59	1,67	2,04	2,14		3,98	5,13	3,4
Gd				7,7	7,32	6,35	6,01	7,3	7,43		9,94	10,2	7,5
Tb				0,97	0,99	0,84	0,79	0,96	0,95		1,06	1,18	0,85
Dy				5,46	5,28	4,54	4,61	5,2	5,36		4,82	5,73	4,95
Ho				0,85	0,85	0,76	0,69	0,83	0,81		0,78	0,97	0,99
Er				2,73	2,55	2,3	2,17	2,51	2,61		1,98	2,45	2,64
Tm				0,3	0,3	0,27	0,27	0,32	0,33		0,25	0,32	0,34
Yb				2,12	2,03	1,86	1,81	2,04	2,13		1,53	1,95	2,34
Lu				0,31	0,29	0,27	0,25	0,3	0,29		0,23	0,28	0,45
143Nd/144Nd			0,512441	0,512417	0,512404	0,512436	0,512387	0,512445			0,512714	0,512701	
87Sr/86Sr			0,707829	0,707878	0,708135	0,708116	0,708001	0,707941			0,7052	0,705643	
Ce/Pb	0,00	0,00	0,00	3,09	3,03	2,68	2,53	2,87	3,14		9,09	16,48	11,61
Sr/Y	48,19	50,17	51,38	41,92	41,50	51,74	53,72	45,30	44,56		91,26	74,89	218,14
Sm/Yb				4,62	4,98	4,52	4,36	4,95	4,55		10,78	10,72	5,94
Nb/U	6,90	4,35	5,51	6,49	6,74	5,60	4,31	4,08	4,33		11,89	17,87	8,44
Gd/Yb				3,63	3,61	3,41	3,32	3,58	3,49		6,50	5,23	3,21
La/Sm				4,87	4,76	5,18	5,29	4,48	4,67		7,88	7,63	10,57
Zr/Hf				36,18	36,97	38,38	37,59	37,02	37,87		47,65	41,11	53,85
Nb/Ta				16,41	16,11	17,23	16,23	16,81	17,33		20,95	19,57	18,50
Rb/Sr	0,16	0,16	0,48	0,35	0,39	0,17	0,44	0,17	0,23		0,09	0,02	0,01
Ba/Rb	20,62	17,52	9,11	9,88	9,00	16,08	6,44	17,66	13,19		7,76	29,71	31,14
Dy/Yb				2,58	2,60	2,44	2,55	2,55	2,52		3,15	2,94	2,12
Th/Nb	0,78	0,72	0,71	0,68	0,67	0,63	0,63	0,74	0,71		0,38	0,47	0,50
Ti/Eu				4012,74	4159,42	4271,96	4089,83	3940,77	3992,35		2276,25	1617,23	2468,75
(La/Yb) _n				16,14	17,00	16,78	16,57	15,89	15,26		60,95	58,67	45,03
(Sm/Yb) _n				5,14	5,53	5,02	4,85	5,50	5,06		11,98	11,91	6,60
Nb/La				0,58	0,60	0,51	0,50	0,60	0,57		0,34	0,26	0,33
Hf/Sm				1,29	1,26	1,12	1,19	1,18	1,16		0,31	0,26	0,28
Ba/Th	183,41	175,21	245,18	200,21	194,48	241,41	260,75	172,71	190,05		77,10	63,23	67,24
K ₂ O+Na ₂ O+CaO	19,84	18,91	15,47	14,79	14,94	18,01	19,09	17,24	18,96		20,59	20,16	21,71
SiO ₂ +Al ₂ O ₃	62,24	63,47	66,26	66,47	66,54	63,77	63,65	59,83	65,06		57,63	57,77	56,67
CaO/Al ₂ O ₃	1,12	0,90	0,62	0,59	0,56	0,87	0,99	0,83	0,84		1,20	1,11	1,01
Na ₂ O+K ₂ O	9,14	9,51	8,92	8,47	8,96	9,35	9,30	8,99	9,94		4,14	3,41	6,31

Table 10 (continued).

Group of rock Reference	Group Ib	Group Ib	Group Ib	Group Ib	Group Ic	Group Ic	Group Ic	Group Ic	Group Ic	Group Ic	Group Ic
Location	" "	" "	" "	" "	Aghazadeh <i>et al.</i> , 2015	" "	" "	" "	" "	" "	" "
Location	" "	" "	" "	" "	NW Iran	" "	" "	" "	" "	" "	" "
SiO ₂	53,46	50,66	51,82	41,68	49,79	46,94	46,35	45,61	42,50	46,69	45,57
TiO ₂	1,05	1,04	1,22	1,19	2,56	3,14	3,30	3,14	3,81	3,39	3,09
Al ₂ O ₃	18,37	15,15	17,70	21,70	17,12	16,26	15,76	14,55	12,41	16,02	14,87
Fe ₂ O ₃	6,93	7,38	7,83	6,52	10,29	11,22	11,69	13,73	16,34	11,49	13,82
MnO	0,12	0,11	0,12	0,14	0,18	0,21	0,27	0,22	0,23	0,25	0,23
MgO	3,32	6,54	4,53	7,37	5,03	5,66	5,57	8,01	9,93	5,49	8,21
CaO	7,11	11,29	10,31	13,91	6,38	8,36	9,24	8,37	10,34	8,94	7,47
Na ₂ O	3,48	2,98	3,49	3,31	2,92	2,68	2,19	2,79	2,07	2,14	2,95
K ₂ O	5,42	4,13	2,43	3,50	4,71	4,17	4,12	2,76	1,73	4,16	2,99
P ₂ O ₅	0,73	0,71	0,55	0,68	1,02	1,37	1,49	0,84	0,66	1,43	0,79
Total	100	100	100	100	100	100	100	100	100	100	100
Cs	3,44		4,06	4,06	2,8	2,2	1,2	1	0,4	1,39	1,53
Rb	202,52	138,00	147,94	281,58	96,9	84,9	74,8	57	39,6	74,8	62,7
Sr	2848,76	2003,00	2363,06	3606,52	1120	1400	950	720	580	933	664
Y	25,81	22,00	21,09	38,30	29	32,1	32,2	25,3	23,7	35,1	28,6
Zr	309,39	318,00	225,67	1118,82	380	370	360	330	300	324	313
Nb	29,41	38,00	27,89	49,88	117	111	110	89	73	120	105
Ba	2388,62	2129,00	2016,09	6634,18	1460	1120	950	680	450	1110	852
Hf	7,54	6,69	5,74	30,15	8	7	7	7	7	7,1	7,1
Ta	1,79	2,18	1,87	3,44	7,6	7,1	7	5,9	4,9	7,7	6,6
Pb	10,34	37,00	11,21	122,13	4	3,4	4	4,5	3	8	8
Th	35,26	37,70	30,07	62,49	14,9	14,1	13,2	11,7	9,1	11,5	10,9
U	7,76	4,00	10,36	3,39	3,58	3,57	3,5	3,07	2,17	2,86	2,77
La	173,96	114,17	126,94	115,11	77,8	79,2	77	64,4	53,7	88,9	75,5
Ce	304,78	188,12	224,39	240,01	141	147	147	118	96,2	175	141
Pr	33,53	21,00	25,21	24,47	15,7	16,4	16,8	13	11	19,8	15,6
Nd	125,38	77,52	95,88	91,30	55	61,7	62,5	47,9	41,9	70,9	53
Sm	17,74	11,75	14,07	15,56	9,2	10,5	11	8,1	7,8	12,9	9,59
Eu	4,33	2,80	3,75	3,85	2,8	3,05	3,06	2,42	2,29	3,9	3,01
Gd	11,16	7,70	8,38	11,26	7,07	8,17	8,47	6,11	6,18	12,5	9,53
Tb	1,10	0,89	0,86	1,43	1,03	1,19	1,21	0,94	0,91	1,6	1,26
Dy	5,51	4,91	4,53	7,86	5,91	6,51	6,49	5,29	4,98	7,66	6,13
Ho	0,92	0,86	0,78	1,43	1,13	1,19	1,25	0,97	0,96	1,41	1,16
Er	2,26	2,19	1,92	3,80	2,76	3,04	3,08	2,5	2,41	3,53	2,82
Tm	0,30	0,32	0,28	0,54	0,4	0,41	0,41	0,34	0,33	0,44	0,37
Yb	1,81	2,08	1,75	3,77	2,3	2,5	2,4	2,1	2	2,88	2,43
Lu	0,27	0,29	0,26	0,55	0,34	0,36	0,35	0,27	0,26	0,41	0,36
¹⁴³ Nd/ ¹⁴⁴ Nd	0,512697				0,512667	0,512672	0,512669	0,512668	0,512674		
⁸⁷ Sr/ ⁸⁶ Sr	0,704349				0,705398	0,705455	0,705634	0,70479	0,70459		
Ce/Pb	29,47	5,08	20,02	1,97	35,25	43,24	36,75	26,22	32,07	21,88	17,63
Sr/Y	110,39	91,05	112,05	94,17	38,62	43,61	29,50	28,46	24,47	26,58	23,22
Sm/Yb	9,78	5,66	8,03	4,12	4,00	4,20	4,58	3,86	3,90	4,48	3,95
Nb/U	3,79	9,50	2,69	14,73	32,68	31,09	31,43	28,99	33,64	41,96	37,91
Gd/Yb	6,15	3,71	4,78	2,98	3,07	3,27	3,53	2,91	3,09	4,34	3,92
La/Sm	9,81	9,72	9,02	7,40	8,46	7,54	7,00	7,95	6,88	6,89	7,87
Zr/Hf	41,05	47,52	39,32	37,10	47,50	52,86	51,43	47,14	42,86	45,63	44,08
Nb/Ta	16,40	17,41	14,89	14,50	15,39	15,63	15,71	15,08	14,90	15,58	15,91
Rb/Sr	0,07	0,07	0,06	0,08	0,09	0,06	0,08	0,08	0,07	0,08	0,09
Ba/Rb	11,79	15,43	13,63	23,56	15,07	13,19	12,70	11,93	11,36	14,84	13,59
Dy/Yb	3,04	2,36	2,58	2,08	2,57	2,60	2,70	2,52	2,49	2,66	2,52
Th/Nb	1,20	0,99	1,08	1,25	0,13	0,13	0,12	0,13	0,12	0,10	0,10
Ti/Eu	1452,52	2226,61	1954,35	1857,54	5475,69	6170,97	6463,12	7771,97	9961,79	5216,36	6156,52
(La/Yb) _n	68,81	39,42	51,93	21,88	24,26	22,72	23,01	22,00	19,26	22,14	22,29
(Sm/Yb) _n	10,87	6,28	8,92	4,58	4,44	4,67	5,09	4,29	4,33	4,98	4,39
Nb/La	0,17	0,33	0,22	0,43	1,50	1,40	1,43	1,38	1,36	1,35	1,39
Hf/Sm	0,42	0,57	0,41	1,94	0,87	0,67	0,64	0,86	0,90	0,55	0,74
Ba/Th	67,74	56,47	67,05	106,17	97,99	79,43	71,97	58,12	49,45	96,52	78,17
K ₂ O+Na ₂ O+CaO	16,01	18,41	16,23	20,72	14,01	15,20	15,55	13,91	14,14	15,24	13,41
SiO ₂ +Al ₂ O ₃	71,84	65,81	69,52	63,38	66,91	63,20	62,12	60,17	54,91	62,70	60,45
CaO/Al ₂ O ₃	0,39	0,75	0,58	0,64	0,37	0,51	0,59	0,58	0,83	0,56	0,50
Na ₂ O+K ₂ O	8,90	7,11	5,92	6,81	7,63	6,85	6,32	5,54	3,79	6,30	5,94

Table 10 (continued).

Group of rock	Group Ila	Group Ila	Group Ila	Group Ila	Group Ila	Group Ila	Group Ila	Group Ila	Group Ila	Group Ila	Group Ila	Group Ila	
Reference	" "	" "	" "	" "	" "	" "	Boccaletti, et al., 1976	" "	" "	" "	" "	" "	
Location	" "	" "	" "	" "	" "	" "	Kurdintan province	" "	" "	" "	" "	" "	
SiO ₂	51,20	51,05	47,34	47,17	48,90	43,80		46,65	46,74	45,69	46,11	46,51	48,36
TiO ₂	1,56	1,56	1,67	2,02	1,77	2,12		2,30	2,20	2,05	2,05	1,71	2,11
Al ₂ O ₃	13,24	13,19	12,87	12,23	13,27	14,80		15,59	16,32	14,78	15,01	14,48	16,04
Fe ₂ O ₃	8,02	8,04	8,08	8,96	8,43	4,16		4,05	3,71	3,66	3,52	3,98	3,82
MnO	0,12	0,12	0,11	0,13	0,12	0,15		0,14	0,14	0,14	0,14	0,14	0,14
MgO	8,94	9,03	8,53	9,39	8,61	9,30		9,28	9,16	9,18	8,94	10,06	7,01
CaO	8,72	8,70	11,71	9,86	9,46	10,04		8,56	8,69	10,19	9,65	10,09	9,53
Na ₂ O	4,27	4,44	4,57	4,84	4,52	6,21		5,15	5,23	4,52	4,54	4,66	4,52
K ₂ O	2,84	2,79	3,41	3,30	3,37	2,17		1,75	1,28	2,77	3,03	2,87	2,92
P ₂ O ₅	1,08	1,08	1,70	2,09	1,55	1,81		0,91	0,96	1,55	1,54	1,62	1,22
Total	100	100	100	100	100	100		100	100	100	100	100	100
Cs													
Rb	55	53,9	55,5	68,6	62,4								
Sr	1182	1169	1859	1534	1676								
Y	22	21,7	23,6	26,8	26,6								
Zr	221	221	317	389	348								
Nb	48,1	47,7	50,1	59,4	48,9								
Ba	1230	1227	1561	1780	2097								
Hf	4,78	4,75	6,49	7,9	7,14								
Ta	2,66	2,66	2,61	3,15	2,63								
Pb	19,6	19,4	20,7	20,4	25,2								
Th	18,4	18,3	23,2	24,8	27,1								
U	4,14	4,12	4,08	4,22	4,51								
La	90,3	88,8	140	152	165								
Ce	171	169	268	286	301								
Pr	20,2	20,1	32,2	33,5	34,6								
Nd	73,5	72,4	117	118	121								
Sm	10,7	10,4	16,3	16	16,3								
Eu	2,68	2,61	4,02	3,89	3,95								
Gd	6,56	6,48	8,99	8,97	9,18								
Tb	0,83	0,85	1,07	1,11	1,12								
Dy	4,06	3,99	4,72	5,14	5,06								
Ho	0,74	0,71	0,79	0,89	0,9								
Er	1,68	1,69	1,66	1,92	1,96								
Tm	0,25	0,24	0,24	0,27	0,29								
Yb	1,53	1,48	1,4	1,61	1,7								
Lu	0,23	0,22	0,22	0,24	0,26								
143Nd/144Nd	0,512732		0,512679		0,512633								
87Sr/86Sr	0,705081		0,705243		0,705472								
Ce/Pb	8,72	8,71	12,95	14,02	11,94								
Sr/Y	53,73	53,87	78,77	57,24	63,01								
Sm/Yb	6,99	7,03	11,64	9,94	9,59								
Nb/U	11,62	11,58	12,28	14,08	10,84								
Gd/Yb	4,29	4,38	6,42	5,57	5,40								
La/Sm	8,44	8,54	8,59	9,50	10,12								
Zr/Hf	46,23	46,53	48,84	49,24	48,74								
Nb/Ta	18,08	17,93	19,20	18,86	18,59								
Rb/Sr	0,05	0,05	0,03	0,04	0,04								
Ba/Rb	22,36	22,76	28,13	25,95	33,61								
Dy/Yb	2,65	2,70	3,37	3,19	2,98								
Th/Nb	0,38	0,38	0,46	0,42	0,55								
Ti/Eu	3499,51	3574,97	2494,31	3106,04	2681,37								
(La/Yb) _n	42,33	43,04	71,73	67,72	69,62								
(Sm/Yb) _n	7,77	7,81	12,94	11,04	10,65								
Nb/La	0,53	0,54	0,36	0,39	0,30								
Hf/Sm	0,45	0,46	0,40	0,49	0,44								
Ba/Th	66,85	67,05	67,28	71,77	77,38								
K ₂ O+Na ₂ O+CaO	15,83	15,93	19,69	18,01	17,35	18,42	15,46	15,20	17,47	17,22	17,62	16,98	
SiO ₂ +Al ₂ O ₃	64,44	64,24	60,21	59,41	62,17	58,59	62,24	63,06	60,47	61,12	60,99	64,40	
CaO/Al ₂ O ₃	0,66	0,66	0,91	0,81	0,71	0,68	0,55	0,53	0,69	0,64	0,70	0,59	
Na ₂ O+K ₂ O	7,11	7,23	7,98	8,14	7,89	8,38	6,91	6,51	7,28	7,57	7,53	7,44	

Table 10 (continued).

Group of rock	Group IIa	Group IIa	Group IIa	Group IIa	Group IIa	Group IIa	Group IIa	Group IIa	Group IIa	Group IIa	Group IIa	Group IIa	Group IIa
Reference	"	"	"	"	"	"	"	"	"	"	"	"	"
Location	"	"	"	"	"	"	"	"	"	"	"	"	"
SiO ₂	47,77	48,45	48,34	48,94	49,08	49,37	49,71	49,71	43,33	42,85	41,98	43,09	
TiO ₂	1,91	2,21	1,95	1,86	1,80	1,80	1,80	1,73	1,73	1,76	1,68	1,71	
Al ₂ O ₃	15,10	15,88	13,64	13,60	14,12	14,11	13,55	14,24	13,10	13,33	12,87	12,90	
Fe ₂ O ₃	5,38	3,62	3,82	4,17	4,01	4,06	4,36	3,94	10,01	10,33	9,92	10,03	
MnO	0,15	0,14	0,14	0,14	0,14	0,14	0,14	0,14	0,17	0,16	0,16	0,16	
MgO	8,59	7,07	8,53	7,90	7,90	7,81	7,95	7,84	11,46	11,84	11,58	11,60	
CaO	9,57	9,28	9,05	9,42	9,24	9,16	9,35	8,84	14,27	14,72	15,41	14,05	
Na ₂ O	3,86	4,45	4,94	5,08	4,89	4,96	4,66	5,11	3,74	2,91	2,82	4,41	
K ₂ O	2,53	2,72	3,36	3,17	3,19	3,22	3,16	3,15	0,44	0,31	1,87	0,29	
P ₂ O ₅	1,10	1,22	2,16	1,95	1,76	1,89	1,73	1,65	1,75	1,78	1,72	1,76	
Total	100	100	100	100	100	100	100	100	100	100	100	100	
Cs													
Rb									24,3	236	47	38,2	
Sr									2603	1762	2457	2199	
Y									27	28,2	27,5	27,5	
Zr									219,8	222,4	214,9	217,4	
Nb									50,9	51,2	49,2	49,5	
Ba									1640	1709	1237	1144	
Hf									4,58	4,66	4,48	4,67	
Ta									2,59	2,57	2,47	2,5	
Pb									13,7	13,1	13,1	13,3	
Th									13,3	13,1	12,7	12,9	
U									2,55	2,32	2,41	2,53	
La									144,9	144,6	149	150,1	
Ce									261,9	266,3	262	269,3	
Pr									26,9	27,4	26,4	27,3	
Nd									113,4	114,6	112,1	114,2	
Sm									15,2	15,4	14,8	15,3	
Eu									3,9	4	3,8	3,9	
Gd									11,4	11,5	11,1	11,4	
Tb									1,2	1,2	1,2	1,2	
Dy									5,5	5,6	5,4	5,6	
Ho									0,9	0,9	0,9	1	
Er									2,3	2,3	2,2	2,3	
Tm									0,3	0,3	0,3	0,3	
Yb									1,9	1,9	1,9	1,9	
Lu									0,3	0,3	0,3	0,3	
143Nd/144Nd													0,512696
87Sr/86Sr													0,704435
Ce/Pb									19,12	20,33	20,00	20,25	
Sr/Y									96,41	62,48	89,35	79,96	
Sm/Yb									8,00	8,11	7,79	8,05	
Nb/U									19,96	22,07	20,41	19,57	
Gd/Yb									6,00	6,05	5,84	6,00	
La/Sm									9,53	9,39	10,07	9,81	
Zr/Hf									47,99	47,73	47,97	46,55	
Nb/Ta									19,65	19,92	19,92	19,80	
Rb/Sr									0,01	0,13	0,02	0,02	
Ba/Rb									67,49	7,24	26,32	29,95	
Dy/Yb									2,89	2,95	2,84	2,95	
Th/Nb									0,26	0,26	0,26	0,26	
Ti/Eu									2654,74	2639,45	2657,69	2630,53	
(La/Yb) n									54,70	54,59	56,25	56,67	
(Sm/Yb)n									8,89	9,01	8,65	8,95	
Nb/La									0,35	0,35	0,33	0,33	
Hf/Sm									0,30	0,30	0,30	0,31	
Ba/Th									123,31	130,46	97,40	88,68	
K ₂ O+Na ₂ O+CaO	15,96	16,45	17,35	17,68	17,32	17,34	17,18	17,09	18,46	17,94	20,10	18,74	
SiO ₂ +Al ₂ O ₃	62,86	64,33	61,98	62,54	63,20	63,48	63,26	63,95	56,43	56,18	54,85	55,99	
CaO/Al ₂ O ₃	0,63	0,58	0,66	0,69	0,65	0,65	0,69	0,62	1,09	1,10	1,20	1,09	
Na ₂ O+K ₂ O	6,39	7,17	8,30	8,26	8,08	8,18	7,83	8,25	4,19	3,22	4,69	4,69	

Table 10 (continued).

Group of rock	Group IIb	Group IIb	Group IIb	Group IIb	Group IIb	Group IIb	Group IIb	Group IIb	Group IIb	Group IIb	Group IIb	Group IIb
Reference	" "	" "	" "	" "	" "	Pearce et al., 1990	" "	" "	" "	" "	" "	" "
Location	" "	" "	" "	" "	" "	East Anatolia	" "	" "	" "	" "	" "	" "
SiO ₂	48,47	48,55	48,72	48,78	46,53	50,66	48,78	50,83	50,89	54,92	48,36	50,28
TiO ₂	1,70	1,70	1,75	1,76	2,41	2,05	3,41	2,05	1,69	1,91	2,89	2,87
Al ₂ O ₃	17,24	16,68	17,59	17,66	16,80	17,29	15,25	17,67	18,22	16,05	16,80	15,61
Fe ₂ O ₃	9,03	9,42	8,67	9,04	13,56	9,74	13,44	11,05	10,22	11,06	12,65	12,64
MnO	0,17	0,16	0,16	0,16	0,19	0,15	0,24	0,21	0,18	0,18	0,18	0,20
MgO	6,78	8,53	6,46	6,77	4,63	6,58	3,76	4,15	3,75	3,14	6,03	4,62
CaO	9,47	9,19	9,57	9,66	9,09	8,30	7,55	6,61	7,55	6,68	8,72	8,03
Na ₂ O	4,10	2,90	4,20	3,21	4,81	4,06	4,02	4,90	4,92	3,68	2,91	3,93
K ₂ O	2,48	2,35	2,33	2,44	1,46	0,85	2,19	1,56	1,82	2,00	1,02	1,32
P ₂ O ₅	0,55	0,52	0,55	0,53	0,53	0,33	1,36	0,98	0,76	0,37	0,45	0,49
Total	100	100	100	100	100	100	100	100	100	100	100	100
Cs												
Rb	53	38	41	53	28	11	53	22	35	62	22	28
Sr	727	662	703	727	579	531	584	676	619	250	397	393
Y	25	21	25	25	36	26	55	43	38	45	31	39
Zr	179	160	180	179	296	187	381	393	358	356	211	313
Nb	47	45	46	45	21	10,1	31	36	29	37	13	21
Ba	515	462	458	503	381	221	482	438	468	321	153	180
Hf						4,23					6,77	8,37
Ta						0,43					1,14	1,51
Pb					5	3	4	39	48	13	8	6
Th	9	8	10	7	6	2,07					3,65	3,95
U						0,3					1,1	0,73
La	25					18,9					23,48	28,6
Ce	49,1					52,72					62,18	77,74
Pr	5,23											
Nd	20,6					26,64					32,38	44,1
Sm	4,52					5,17					7,07	8,45
Eu	1,54					1,63					1,9	2,4
Gd	4,69											
Tb						0,69					0,87	1,13
Dy	4,28											
Ho	0,74					0,83						1,57
Er	2,1											
Tm												
Yb	2,06					2,46					3,07	4
Lu	0,35					0,41					0,45	0,61
¹⁴³ Nd/ ¹⁴⁴ Nd												
⁸⁷ Sr/ ⁸⁶ Sr						0,70389						0,70432
Ce/Pb						17,57					7,77	12,96
Sr/Y	29,08	31,52	28,12	29,08	16,08	20,42	10,62	15,72	16,29	5,56	12,81	10,08
Sm/Yb	2,19					2,10					2,30	2,11
Nb/U						33,67					11,82	28,77
Gd/Yb	2,28											
La/Sm	5,53					3,66					3,32	3,38
Zr/Hf						44,21					31,17	37,40
Nb/Ta						23,49					11,40	13,91
Rb/Sr	0,07	0,06	0,06	0,07	0,05	0,02	0,09	0,03	0,06	0,25	0,06	0,07
Ba/Rb	9,72	12,16	11,17	9,49	13,61	20,09	9,09	19,91	13,37	5,18	6,95	6,43
Dy/Yb	2,08											
Th/Nb	0,19	0,18	0,22	0,16	0,29	0,20					0,28	0,19
Ti/Eu	6602,89					7540,10					9123,50	7169,25
(La/Yb) _n	8,71					5,51					5,49	5,13
(Sm/Yb) _n	2,44					2,34					2,56	2,35
Nb/La	1,88					0,53					0,55	0,73
Hf/Sm	0,00					0,82					0,96	0,99
Ba/Th	57,22	57,75	45,80	71,86	63,50	106,76					41,92	45,57
K ₂ O+Na ₂ O+CaO	16,05	14,45	16,10	15,31	15,36	13,21	13,76	13,07	14,29	12,36	12,65	13,29
SiO ₂ +Al ₂ O ₃	65,71	65,23	66,31	66,44	63,32	67,95	64,03	68,50	69,11	70,97	65,16	65,89
CaO/Al ₂ O ₃	0,55	0,55	0,54	0,55	0,54	0,48	0,49	0,37	0,41	0,42	0,52	0,51
Na ₂ O+K ₂ O	6,58	5,26	6,53	5,65	6,27	4,91	6,21	6,45	6,74	5,68	3,93	5,26

Table 10 (continued).

Group of rock Reference Location	Group IIb	Group IIb <i>Kheirkhah et al., 2013</i> NW Iran	Group IIb	Group IIb	Group IIb	Group IIb	Group IIb	Group IIb	Group IIb	Group IIb	Group IIb	Group IIb	Group IIb
SiO ₂	52,43	50,58	50,60	50,20	52,86	54,71	55,51	54,09	50,04	49,97	49,57	49,95	
TiO ₂	1,33	1,77	1,92	1,78	1,28	1,25	1,14	1,31	1,53	2,19	2,03	1,47	
Al ₂ O ₃	18,59	17,17	17,33	17,08	16,28	16,51	16,19	16,10	16,34	17,56	17,72	15,02	
Fe ₂ O ₃	8,25	9,60	10,26	9,71	9,10	8,17	7,81	8,49	9,83	11,41	11,35	8,81	
MnO	0,13	0,15	0,16	0,15	0,14	0,13	0,13	0,14	0,16	0,17	0,18	0,12	
MgO	4,79	6,03	5,34	6,15	6,73	5,62	5,94	6,10	7,52	3,81	4,17	6,28	
CaO	8,56	8,68	8,49	9,17	8,16	7,62	7,57	8,09	8,65	7,00	7,29	12,54	
Na ₂ O	4,06	4,85	4,96	4,69	4,19	4,43	4,28	4,17	4,47	5,56	5,33	3,61	
K ₂ O	1,40	0,79	0,65	0,72	1,00	1,28	1,12	1,19	1,02	1,58	1,61	1,39	
P ₂ O ₅	0,44	0,38	0,28	0,35	0,26	0,28	0,30	0,32	0,44	0,75	0,74	0,82	
Total	100	100	100	100	100	100	100	100	100	100	100	100	
Cs	0,2				0,6					0,1	0,5	2,1	
Rb	26	11	9	11	19	31	28	29	16	20	25	9	
Sr	760	564	492	519	364	387	376	376	658	581	652	1724	
Y	21	32	31	27	25	29	23	26	31	38	38	27	
Zr	139	197	211	204	149	187	163	174	179	268	300	171	
Nb	15,5	9	8	11	10	12	11	11	15	27	27	23	
Ba	426	271	171	175	288	379	366	348	323	435	567	761	
Hf	3				3,33					5,79	5,91	3,59	
Ta	0,9				0,58					1,27	1,29	1,12	
Pb	5,4	2	4	4	5,27	6	4	9	1	9,72	10,55	13,19	
Th	6,7	7	7	6	2,97	6	9	9	7	4,67	5,65	6,72	
U	1,5				1,07					0,62	1,41	1,79	
La	30	15	15	16	16,08	20	17	19	27	37,07	39,86	54,83	
Ce	61				31,85					73,5	78,47	108,17	
Pr	6,6				4,11					9,41	9,9	13,51	
Nd	23,9	20	23	22	17,52	20	18	19	26	38,45	39,85	52,45	
Sm	4,41				3,98					7,49	7,72	8,5	
Eu	1,32				1,29					2,18	2,24	2,3	
Gd	4,28				4,45					7,14	7,14	6,39	
Tb	0,66				0,72					1,1	1,1	0,87	
Dy	3,62				4,2					6,36	6,41	4,71	
Ho	0,72				0,86					1,28	1,29	0,89	
Er	2,08				2,32					3,41	3,47	2,29	
Tm	0,29				0,36					0,54	0,55	0,34	
Yb	1,86				2,25					3,31	3,41	2,15	
Lu	0,28				0,36					0,54	0,56	0,35	
¹⁴³ Nd/ ¹⁴⁴ Nd	0,51261				0,512832					0,512708	0,51269	0,512753	
⁸⁷ Sr/ ⁸⁶ Sr	0,7053				0,704452					0,705705	0,7056	0,705008	
Ce/Pb	11,30				6,04					7,56	7,44	8,20	
Sr/Y	36,19	17,63	15,87	19,22	14,56	13,34	16,35	14,46	21,23	15,29	17,16	63,85	
Sm/Yb	2,37				1,77					2,26	2,26	3,95	
Nb/U	10,33				9,35					43,55	19,15	12,85	
Gd/Yb	2,30				1,98					2,16	2,09	2,97	
La/Sm	6,80				4,04					4,95	5,16	6,45	
Zr/Hf	46,33				44,74					46,29	50,76	47,63	
Nb/Ta	17,22				17,24					21,26	20,93	20,54	
Rb/Sr	0,03	0,02	0,02	0,02	0,05	0,08	0,07	0,08	0,02	0,03	0,04	0,01	
Ba/Rb	16,38	24,64	19,00	15,91	15,16	12,23	13,07	12,00	20,19	21,75	22,68	84,56	
Dy/Yb	1,95				1,87					1,92	1,88	2,19	
Th/Nb	0,43	0,78	0,88	0,55	0,30	0,50	0,82	0,82	0,47	0,17	0,21	0,29	
Ti/Eu	6056,88				5947,95					6022,20	5429,04	3824,20	
(La/Yb) _n	11,57				5,13					8,03	8,38	18,29	
(Sm/Yb) _n	2,63				1,97					2,51	2,52	4,39	
Nb/La	0,52	0,60	0,53	0,69	0,62	0,60	0,65	0,58	0,56	0,73	0,68	0,42	
Hf/Sm	0,68				0,84					0,77	0,77	0,42	
Ba/Th	63,58	38,71	24,43	29,17	96,97	63,17	40,67	38,67	46,14	93,15	100,35	113,24	
K ₂ O+Na ₂ O+CaO	14,02	14,33	14,10	14,57	13,35	13,33	12,97	13,45	14,14	14,13	14,24	17,53	
SiO ₂ +Al ₂ O ₃	71,02	67,74	67,94	67,28	69,13	71,22	71,71	70,19	66,38	67,53	67,30	64,97	
CaO/Al ₂ O ₃	0,46	0,51	0,49	0,54	0,50	0,46	0,47	0,50	0,53	0,40	0,41	0,84	
Na ₂ O+K ₂ O	5,47	5,64	5,61	5,40	5,19	5,71	5,40	5,36	5,50	7,13	6,95	4,99	

Table 10 (continued).

Group of rock	Group III	Group III	Group III
Reference	" "	" "	" "
Location	" "	" "	" "
SiO ₂	54,41	53,03	53,88
TiO ₂	1,10	1,16	1,00
Al ₂ O ₃	17,06	16,74	18,11
Fe ₂ O ₃	9,40	11,68	9,63
MnO	0,19	0,17	0,13
MgO	4,35	3,91	4,03
CaO	8,68	8,59	8,50
Na ₂ O	3,66	3,21	3,06
K ₂ O	0,97	1,32	1,44
P ₂ O ₅	0,19	0,20	0,22
Total	100	100	100
Cs	3,67	0,3	0,64
Rb	26,15	29,43	37,76
Sr	340	387,4	484,4
Y	24,49	24,04	24,93
Zr	99,05	84,24	99,83
Nb	5,94	4,21	4,96
Ba	228	481,4	399,8
Hf	2,52	2,46	2,48
Ta	0,48	0,33	0,37
Pb	4,02	6,77	7,64
Th	2,97	4,48	4,09
U	0,83	1,17	1,07
La	11,19	15,23	14,67
Ce	23,95	31,49	30,81
Pr	3,06	3,82	3,95
Nd	13,5	16,1	16,88
Sm	3,35	4,05	3,94
Eu	1,12	1,31	1,22
Gd	3,79	4,29	4,04
Tb	0,67	0,71	0,67
Dy	4,13	4,34	4,08
Ho	0,86	0,88	0,86
Er	2,52	2,46	2,5
Tm	0,38	0,39	0,38
Yb	2,4	2,42	2,4
Lu	0,36	0,37	0,36
¹⁴³ Nd/ ¹⁴⁴ Nd	0,51252		
⁸⁷ Sr/ ⁸⁶ Sr	0,7058		
Ce/Pb	5,96	4,65	4,03
Sr/Y	13,88	16,11	19,43
Sm/Yb	1,40	1,67	1,64
Nb/U	7,16	3,60	4,64
Gd/Yb	1,58	1,77	1,68
La/Sm	3,34	3,76	3,72
Zr/Hf	39,31	34,24	40,25
Nb/Ta	12,38	12,76	13,41
Rb/Sr	0,08	0,08	0,08
Ba/Rb	8,72	16,36	10,59
Dy/Yb	1,72	1,79	1,70
Th/Nb	0,50	1,06	0,82
Ti/Eu	5875,30	5324,52	4924,22
(La/Yb) _n	3,34	4,51	4,38
(Sm/Yb) _n	1,55	1,86	1,82
Nb/La	0,53	0,28	0,34
Hf/Sm	0,75	0,61	0,63
Ba/Th	76,77	107,46	97,75
K ₂ O+Na ₂ O+CaO			
SiO ₂ +Al ₂ O ₃			
CaO/Al ₂ O ₃	0,51	0,51	0,47
Na ₂ O+K ₂ O	4,63	4,53	4,50

Table 11. Age and location of selected igneous rocks in the Turkish-Iranian plateau.

Group	Reference	Geochemical characteristics	Age (Ma)	Longitude	Latitude	Location in the TIP
Group Ia	Aghazadeh et al., 2015	Alkaline ultrapotassic	10,98	46 32 E	38 15 N	NW Iran
Group Ia	Shafaii Moghadam et al., 2014	Alkaline ultrapotassic	10,93	45 30 E	37 53 N	NW Iran
Group Ia	Aghazadeh et al., 2015	Alkaline ultrapotassic	10,35	45 32 E	37 50 N	NW Iran
Group Ia	Shafaii Moghadam et al., 2014	Alkaline ultrapotassic	10,33	45 30 E	37 53 N	NW Iran
Group Ia	Prelević et al., 2014	Alkaline ultrapotassic	19,7			KAI-Anatolia
Group Ia	Prelević et al., 2014	Alkaline ultrapotassic	19,2			KAI-Anatolia
Group Ia	Prelević et al., 2014	Alkaline ultrapotassic	13,6			KAI-Anatolia
Group Ia	Prelević et al., 2014	Alkaline ultrapotassic	11,9			KAI-Anatolia
Group Ia	Prelević et al., 2014	Alkaline ultrapotassic	11,5			KAI-Anatolia
group Ib						
Group Ib	Boztuğ et al., 2007	Alkaline Potassic	77,4	"	"	East Central Anatolia
Group Ib	Boztuğ et al., 2007	Alkaline Potassic	77,2	38 00 E	39 50 N	East Central Anatolia
Group Ib	Boztuğ et al., 2007	Alkaline Potassic	76,6	"	"	East Central Anatolia
Group Ib	Boztuğ et al., 2007	Alkaline Potassic	75,6	"	"	East Central Anatolia
Group Ib	Boztuğ et al., 2007	Alkaline Potassic	73,7	"	"	East Central Anatolia
Group Ib	Boztuğ et al., 2007	Alkaline Potassic	73	"	"	East Central Anatolia
Group Ib	Boztuğ et al., 2007	Alkaline Potassic	72,2	"	"	East Central Anatolia
Group Ib	Boztuğ et al., 2007	Alkaline Potassic	72,1	"	"	East Central Anatolia
Group Ib	Boztuğ et al., 2007	Alkaline Potassic	71,5	"	"	East Central Anatolia
Group Ib	Boztuğ et al., 2007	Alkaline Potassic	67,9	"	"	East Central Anatolia
Group Ib	Boztuğ et al., 2007	Alkaline Potassic	67,8	"	"	East Central Anatolia
Group Ib	Boztuğ et al., 2007	Alkaline Potassic	67,6	"	"	East Central Anatolia
Group Ib	Boztuğ et al., 2007	Alkaline Potassic	65,3	"	"	East Central Anatolia
Group Ib	Boztuğ et al., 2007	Alkaline Potassic	65,2	"	"	East Central Anatolia
Group Ib	Boztuğ et al., 2007	Alkaline Potassic	62,1	"	"	East Central Anatolia
Group Ib	Aydin et al., 2008	Alkaline Potassic	5,1	39 70	41 00	East Pontides
Group Ib	Aydin et al., 2008	Alkaline Potassic	3,2	39 75	40 80	East Pontides
Group Ib	Karsli et al., 2012a	Alkaline Potassic	81,2	43	40	Kars plateau
Group Ib	Aghazadeh et al., 2010	Alkaline Potassic	28,9	47 28 52 E	38 26 34 N	NW Iran
Group Ib	Alberti et al., 1980	Alkaline Potassic	33,2	47 37 54 E	38 42 57 N	NW Iran
Group Ib	Alberti et al., 1980	Alkaline Potassic	29	47 37 54 E	38 42 57 N	NW Iran
Group Ib	Alberti et al., 1980	Alkaline Potassic	38,4	48 05 41 E	38 28 46 N	NW Iran
Group Ib	Alberti et al., 1980	Alkaline Potassic	38,4	48 03 47 E	38 29 19 N	NW Iran
Group Ib	Alberti et al., 1980	Alkaline Potassic	38,7	48 03 47 E	38 29 19 N	NW Iran
Group Ib	Alberti et al., 1980	Alkaline Potassic	39,9	48 03 47 E	38 29 19 N	NW Iran
Group Ib	Alberti et al., 1980	Alkaline Potassic	42,7	47 37 54 E	38 42 57 N	NW Iran
Group Ib	Alberti et al., 1980	Alkaline Potassic	10,5	47 43 57 E	37 57 33 N	NW Iran
Group Ib	Alberti et al., 1980	Alkaline Potassic	10,3	47 43 57 E	37 57 33 N	NW Iran
Group Ib	Alberti et al., 1980	Alkaline Potassic	9,8	47 55 E	37 93 N	NW Iran
Group Ib	Alberti et al., 1980	Alkaline Potassic	11,4	47 43 57 E	37 57 33 N	NW Iran
Group Ib	Alberti et al., 1980	Alkaline Potassic	10,7	47 43 57 E	37 57 33 N	NW Iran
Group Ib	Pang et al., 2013b	Alkaline Potassic	11,1	45 34 00 E	37 47 52 N	NW Iran
Group Ib	Pang et al., 2013b	Alkaline Potassic	11	45 29 19 E	37 45 54 N	NW Iran
Group Ib	Pang et al., 2013b	Alkaline Potassic	10,8	45 25 17 E	37 48 10 N	NW Iran
Group Ib	Pang et al., 2013b	Alkaline Potassic	10,7	45 28 10 E	37 49 38 N	NW Iran
Group Ib	Beydokhti et al., 2015	Alkaline Potassic	31,9	58 53 00 E	31 09 00 N	East Iran
Group Ib	Castro et al., 2013	Alkaline Potassic	38,2	49 11 16 E	36 18 14 N	NW Iran
Group Ib	Castro et al., 2013	Alkaline Potassic	38,7	49 08 56 E	36 19 37 N	NW Iran
Group Ib	Castro et al., 2013	Alkaline Potassic	38	49 08 56 E	36 19 35 N	NW Iran
Group Ib	Castro et al., 2013	Alkaline Potassic	24,71	47 19 25 E	38 23 24 N	NW Iran
Group Ib	Castro et al., 2013	Alkaline Potassic	23,55	47 20 10 E	38 23 17 N	NW Iran
Group Ib	Nabatian et al., 2014	High K calc alkaine-potassic	41,1	48 72 E	36 64 N	West Alborz
Group Ib	Nabatian et al., 2014	High K calc alkaine-potassic	39,7	"	"	West Alborz
Group Ib	Nabatian et al., 2014	High K calc alkaine-potassic	39	"	"	West Alborz
Group Ib	Nabatian et al., 2014	High K calc alkaine-potassic	42,56	"	"	West Alborz
Group Ib	Nabatian et al., 2014	High K calc alkaine-potassic	37,4	"	"	West Alborz
Group Ib	Nabatian et al., 2014	High K calc alkaine-potassic	42,56	"	"	West Alborz
Group Ib	Moritz et al., 2016	Alkaline Potassic	31,83	46 09 52 E	39 09 58 N	Caucasus
Group Ib	Moritz et al., 2016	Alkaline Potassic	33,49	46 13 28 E	39 06 15 N	Caucasus
Group Ib	Karsli et al., 2012b	Alkaline Potassic	41,55	40 48 E	39 00 N	Caucasus
Group Ib	Dargahi et al., 2010	Alkaline Potassic	33	56 00 E	29 52 N	SE Iran
Group Ib	Pang et al., 2013a	High K calc alkaine-potassic	39,1	59 02 34 E	32 46 39 N	East Iran
Group Ib	Pang et al., 2013a	High K calc alkaine-potassic	39,5	59 40 38 E	32 39 40 N	East Iran
Group Ib	Pang et al., 2013a	High K calc alkaine-potassic	39,4	59 13 00 E	32 42 59 N	East Iran

Table 11 (continued).

Group	Reference	Geochemical characteristics	Age (Ma)	Longitude	Latitude	Location in the TIP
Group Ib	Pang et al., 2013a	High K calc alkaine-potassic	27,7	59 49 06 E	32 33 10 N	East Iran
Group Ib	Pang et al., 2013a	High K calc alkaine-potassic	39,3	58 01 15 E	32 23 49 N	East Iran
Group Ib	Pang et al., 2013a	High K calc alkaine-potassic	37,1	59 15 41 E	32 25 26 N	East Iran
Group Ib	Pang et al., 2013a	High K calc alkaine-potassic	38,3	57 45 57 E	32 46 54 N	East Iran
Group Ib	Pang et al., 2013a	High K calc alkaine-potassic	39,1	59 01 50 E	32 25 26 N	East Iran
Group Ib	Pang et al., 2013a	High K calc alkaine-potassic	41,4	59 12 11 E	31 09 52 N	East Iran
Group Ib	Pang et al., 2013a	High K calc alkaine-potassic	46,3	59 06 15 E	31 09 45 N	East Iran
Group Ib	Pang et al., 2013a	High K calc alkaine-potassic	24,4	60 19 40 E	31 13 19 N	East Iran
Group Ib	Pang et al., 2013a	High K calc alkaine-potassic	25,5	59 29 12 E	32 38 50 N	East Iran
Group Ib	Pang et al., 2013a	High K calc alkaine-potassic	31,4	59 19 26 E	32 55 16 N	East Iran
Group Ib	Pang et al., 2013a	High K calc alkaine-potassic	31	59 19 49 E	32 57 22 N	East Iran
Group Ib	Pang et al., 2013a	High K calc alkaine-potassic	29,6	59 29 19 E	32 38 51 N	East Iran
Group Ib	Pang et al., 2013a	High K calc alkaine-potassic	27,5	59 43 16 E	32 39 25 N	East Iran
Group Ib	Pang et al., 2013a	High K calc alkaine-potassic	44,4	60 23 07 E	32 21 48 N	East Iran
Group Ib	Kananian et al., 2014	Alkaline Potassic	47	52 50 00 E	34 00 00 N	Central Iran
Group IIb	Ghorbani et al., 2014	Alkaline Potassic	34,6	50 29 15 E	34 09 55 N	Central Iran
Group Ib	Verdel et al., 2011	Alkaline Potassic	37,2	51 95 78 E	35,78 19 N	Alborz
Group Ib	Walker et al., 2009	Alklaine transitional potassic-sodic	27,5	57 31 70 E	31 22 18 N	East Iran
Group Ib	Axen et al., 2001	Alkaline	54,56	51 05 32 E	36 24 58 N	Alborz
Group Ic	Aghazadeh et al., 2015	Alklaine transitional potassic-sodic	81,4	47 20 E	38 70 N	NW Iran
Group Ic	Aistov et al., 1984	Alklaine transitional potassic-sodic	33			Central Iran
Group Ic	Aghazadeh et al., 2015	Alklaine transitional potassic-sodic	23	47 10 E	38 20 N	NW Iran
Group Ic	Aghazadeh et al., 2015	Alklaine transitional potassic-sodic	9,95	46 32 E	38 15 N	NW Iran

Table 11 (continued).

Group	Reference	Geochemical characteristics	Age (Ma)	Longitude	Latitude	Location in the TIP
Group IIa	Boccaletti, et al., 1976	Alklaine transitional sodic-potassic	0,63	47:30 E	36:11 N	Kurdintan province
Group IIa	Boccaletti, et al., 1976	Alklaine transitional sodic-potassic	0,8	"	"	Kurdintan province
Group IIa	Boccaletti, et al., 1976	Alklaine transitional sodic-potassic	0,9	"	"	Kurdintan province
Group IIa	Boccaletti, et al., 1976	Alklaine transitional sodic-potassic	1,3	"	"	Kurdintan province
Group IIa	Boccaletti, et al., 1976	Alklaine transitional sodic-potassic	0,5	"	"	Kurdintan province
Group IIa	Litord et al., 2008	Alklaine transitional sodic-potassic	1,48	52 12 E	35 94 N	Alborz
Group IIa	Litord et al., 2008	Alklaine transitional sodic-potassic	1,8	"	"	Alborz
Group IIa	Litord et al., 2008	Alklaine transitional sodic-potassic	0,8	"	"	Alborz
Group IIa	Litord et al., 2008	Alklaine transitional sodic-potassic	0,4	"	"	Alborz
Group IIa	Litord et al., 2008	Alklaine transitional sodic-potassic	0,007	"	"	Alborz
Group IIa	Litord et al., 2008	Alklaine transitional sodic-potassic	0,41	"	"	Alborz
Group IIb	Allen et al., 2011	Alkaline sodic	0,81	44 55 E	39 32 N	NW Iran
Group IIb	Allen et al., 2011	Alkaline sodic	0,48	44 52 E	39 32 N	NW Iran
Group IIb	Allen et al., 2011	Alkaline sodic	0,4	44 52 E	39 32 N	NW Iran
Group IIb	Allen et al., 2011	Alkaline sodic	0,49	42 25 E	39 40 N	NW Iran
Group IIb	Neill et al., 2015	Alkaline sodic	2,5	44 49 80 E	40 18 67 N	Caucasus
Group IIb	Neill et al., 2015	Alkaline sodic	2,4	44 38 58 E	40 17 21 N	Caucasus
Group IIb	Neill et al., 2015	Alkaline sodic	2,5	44 64 57 E	40 25 03 N	Caucasus
Group IIb	Neill et al., 2015	Alkaline sodic	2,5	44 61 39 E	40 18 73 N	Caucasus
Group IIb	Neill et al., 2015	Alkaline sodic	2,5	44 59 02 E	40 30 66 N	Caucasus
Group IIb						
Group IIb						
Group IIb						
Group IIb		Alkaline sodic				
Group IIb	Lustrino et al., 2010	Alkaline sodic	3,87	41 90 52 E	59 24 02 N	South Bitlis suture
Group IIb	Lustrino et al., 2010	Alkaline sodic	3,95	41 20 59 E	55 96 25 N	South Bitlis suture
Group IIb	Lustrino et al., 2010	Alkaline sodic	6,65	41 64 65 E	51 47 11 N	South Bitlis suture
Group IIb	Lustrino et al., 2010	Alkaline sodic	6,68	41 74 87 E	54 05 51 N	South Bitlis suture
Group IIb	Lustrino et al., 2010	Alkaline sodic	2,72	41 80 35 E	59 96 77 N	South Bitlis suture
Group IIb		Alkaline sodic	0,4	42 83 E	38 93 N	East Anatolia
Group IIb		Alkaline sodic	0,1	42 83 E	38 93 N	East Anatolia
Group IIb		Alkaline sodic				
Group IIb	Nomade et al., 2016	Alkaline sodic	2,32			Caucasus
Group IIb	Nomade et al., 2016	Alkaline sodic	1,52	44 08 E	41 37 N	Caucasus
Group IIb	Nomade et al., 2016	Alkaline sodic	1,4	44 06 E	41 38 N	Caucasus
Group IIb	Nomade et al., 2016	Alkaline sodic	1,48	43 54 E	41 39 N	Caucasus
Group IIb	Nomade et al., 2016	Alkaline sodic	2,14	"	"	Caucasus
Group IIb	Nomade et al., 2016	Alkaline sodic	2,08	"	"	Caucasus
Group IIb	Nomade et al., 2016	Alkaline sodic	2,84	"	"	Caucasus
Group IIb	Nomade et al., 2016	Alkaline sodic	2,41	"	"	Caucasus
Group IIb	Nomade et al., 2016	Alkaline sodic	2,73	"	"	Caucasus
Group IIb	Nomade et al., 2016	Alkaline sodic	1,77	44 11 E	41 18 N	Caucasus
Group IIb	Nomade et al., 2016	Alkaline sodic	1,83	44 12 E	41 18 N	Caucasus
Group IIb	Nomade et al., 2016	Alkaline sodic	2,13			Caucasus
Group IIb	Nomade et al., 2016	Alkaline sodic	1,08	43 44 E	41 32 N	Caucasus
Group IIb	Nomade et al., 2016	Alkaline sodic	0,309	43 44 E	41 29 N	Caucasus
Group IIb	Nomade et al., 2016	Alkaline sodic	0,439			Caucasus
Group IIb	Nomade et al., 2016	Alkaline sodic	0,244	43 46 E	41 31 N	Caucasus
Group IIb	Nomade et al., 2016	Alkaline sodic	0,189			Caucasus
Group IIb	Nomade et al., 2016	Alkaline sodic	0,09	43 43 E	41 39 N	Caucasus
Group IIb	Nomade et al., 2016	Alkaline sodic	0,0013	43 50 E	41 39 N	Caucasus
Group IIb	Nomade et al., 2016	Alkaline sodic	0,057	43 40 E	41 39 N	Caucasus
Group IIb	Pearce et al., 1990	Alkaline sodic	0,83	41 90 52 E	59 24 02 N	South Bitlis suture
Group IIb	Pearce et al., 1990	Alkaline sodic	0,94	41 90 52 E	59 24 02 N	South Bitlis suture
Group IIb	Pearce et al., 1990	Alkaline sodic	4,4	41 49 E	38 73 N	East Anatolia
Group IIb	Pearce et al., 1990	Alkaline sodic	6	41 49 E	38 73 N	East Anatolia
Group IIb	Pearce et al., 1990	Alkaline sodic	1,18			East Anatolia
Group IIb	Pearce et al., 1990	Alkaline sodic	0,7	42 22 E	36 62 N	East Anatolia
Group IIb	Pearce et al., 1990	Alkaline sodic	0,36	42 83 E	38 93 N	East Anatolia
Group IIb	Pearce et al., 1990	Alkaline sodic	0,23	42 83 E	38 93 N	East Anatolia
Group IIb	Pearce et al., 1990	Alkaline sodic	3,6	40 49 E	38 88 N	East Anatolia
Group IIb	Pearce et al., 1990	Alkaline sodic	2,6	40 49 E	38 88 N	East Anatolia
Group IIb	Pearce et al., 1990	Alkaline sodic	1,51			
Group IIb	Pearce et al., 1990	Alkaline sodic	1,51			
Group IIb	Pearce et al., 1990	Alkaline sodic	4,4			East Anatolia
Group IIb	Pearce et al., 1990	Alkaline sodic	6			East Anatolia
Group IIb	Pearce et al., 1990	Alkaline sodic	1,18			East Anatolia
Group IIb	Pearce et al., 1990	Alkaline sodic	3,6			Central Iran
Group IIb	Ghorbani et al., 2014	Alkaline sodic	18,2	52 29 20 E	32 57 30 N	Central Iran

Table 11 (continued).

Group	Reference	Geochemical characteristics	Age (Ma)	Longitude	Latitude	Location in the TIP
Group IIb	Ghorbani et al., 2014	Alkaline sodic	34,6			Central Iran
Group IIb	Ghorbani et al., 2014	Alkaline sodic	19,1	50 26 E	34 14 N	Central Iran
Group IIb	Ghorbani et al., 2014	Alkaline sodic	428* ka			Central Iran
Group IIb		Alkaline sodic				Central Iran
Group IIb	Yeganehfar et al., 2013	Alkaline sodic	19,7	52 53 E	32 45 N	Central Iran
Group IIb	Tankut et al., 1998	Alkaline sodic	~18-20			North Central Anatoli:
Group IIb	Varol et al., 2014	Alkaline sodic	18,8			North Central Anatoli:
Group IIb	Varol et al., 2014	Alkaline sodic	14,32			North Central Anatoli:
Group IIb	Aydin et al., 2014	Alkaline sodic	654*ka			Central Anatolia
Group IIb	Aydin et al., 2014	Alkaline sodic	224*ka			Central Anatolia
Group IIb	Aydin et al., 2014	Alkaline sodic	490*ka			Central Anatolia
Group IIb	Yeganehfar et al., 2013	Alkaline sodic	26,5	52 47 E	32 44 N	Central Iran
Group IIb	Ghorbani et al., 2014	Alkaline sodic	34,6	50 29 15 E	34 09 55 N	Central Iran
Group IIb		Alkaline sodic				
Group IIb	Verdal et al., 2011	Alkaline sodic	32,7	51 00 78 E	36 20 15 N	Alborz
Group IIb	Dorrozi et al., 2016	Alkaline sodic	? 90	~"	"	Alborz
Group IIb		Alkaline sodic				
Group IIb	Saadat et al., 2010	Alkaline sodic	2			East Iran
Group IIb	Saadat et al., 2010	Alkaline sodic	2,6			East Iran
Group IIb		Alkaline sodic				East Iran
Group IIb	Walker et al., 2009	Alkaline sodic	2,6			East Iran
Group IIb	Walker et al., 2009	Alkaline sodic	2,2			East Iran
Group IIb	Walker et al., 2009	Alkaline sodic	2,25			East Iran
Group IIb	Walker et al., 2009	Alkaline sodic	1,6			East Iran
Group IIb	Walker et al., 2009	Alkaline sodic	1,74			East Iran
Group IIb	Walker et al., 2009	Alkaline sodic	4,81			East Iran
Group IIb	Saadat et al., 2010	Alkaline sodic	15,4			East Iran
Group IIb	Saadat et al., 2010	Alkaline sodic	15,5			East Iran
		Alkaline sodic				East Iran
		Alkaline sodic				East Iran
		Alkaline sodic				East Iran
Group IIb	Saadat et al., 2010	Alkaline sodic	15,4			East Iran
Group IIb	Saadat et al., 2010	Alkaline sodic	15,5			East Iran

Table 11 (continued).

Group	Reference	Geochemical characteristics	Age (Ma)	Longitude	Latitude	Location in the TIP
Group III	Azizi et al., 2014	Calc-alkaline	10,6	47 29 E	35 28 N	Kurdistan Province
Group III	Eyuboghlu,2013	Calc-alkaline	58,1	40 33 E	40 01 N	East Pontides
Group III	Eyuboghlu,2013	Calc-alkaline	58,1	40 33 E	40 01 N	East Pontides
Group III	Eyuboghlu,2013	Calc-alkaline	56	40 33 E	40 01 N	East Pontides
Group III	Eyuboghlu,2013	Calc-alkaline	55,8	40 33 E	40 01 N	East Pontides
Group III	Eyuboghlu,2013	Calc-alkaline	42,4	40 33 E	40 01 N	East Pontides
Group III	Eyuboghlu, 2012	Calc-alkaline	8,79	39 50 E	40 30 N	East Pontides
Group III	Eyuboghlu, 2012	Calc-alkaline	7,86	39 50 E	40 30 N	East Pontides
Group III	Jahangiri, 2007	Calc-alkaline	11	45 52 E	38 80	NW Iran
Group III	Karsli et al., 2012b	Calc-alkaline	65,8	39 47 E	40 5 N	East Pontides
Group III	Karsli et al., 2012b	Calc-alkaline	53,55	39 47 E	40 5 N	East Pontides
Group III	Karsli et al., 2012b	Calc-alkaline	51,34	39 47 E	40 5 N	East Pontides
Group III	Karsli et al., 2010	Calc-alkaline	50,27	40 00 E	40 40 N	East Pontides
Group III	Karsli et al., 2010	Calc-alkaline	47,4	40 00 E	40 40 N	East Pontides
Group III	Moritz et al., 2016	Calc-alkaline	22,46	46 08 E	39 08 N	Caucasus
Group III	Moritz et al., 2016	Calc-alkaline	22,22	46 10 E	39 02 N	Caucasus
Group III	Topuz et al., 2011	Calc-alkaline	52,87	40 00 E	40 00N	
Group III	Topuz et al., 2011	Calc-alkaline	52,97	"	"	
Group III	Chiu et al., 2013	Calc-alkaline	2-0,4	47 47 E	38 20N	NW Iran
Group III	Chiu et al., 2013	Calc-alkaline	5,8	"	"	NW Iran
Group III	Chiu et al., 2013	Calc-alkaline	6,5	"	"	NW Iran
Group III	Chiu et al., 2013	Calc-alkaline	4,3	"	"	NW Iran
Group III	Chiu et al., 2013	Calc-alkaline	4,4	"	"	NW Iran
Group III	Chiu et al., 2013	Calc-alkaline	5,3	"	"	NW Iran
Group III	Chiu et al., 2013	Calc-alkaline	4,2	"	"	NW Iran
Group III	Chiu et al., 2013	Calc-alkaline	6	"	"	NW Iran
Group III		Calc-alkaline				
Group III	Yeganehfar et al., 2013	Calc-alkaline	20,55	52 43 E	32 49 N	Central Iran
Group III						
Group III	Ahmadian et al., 2016	High K calc-alkaline	52	54 10 E	33 20 N	Central Iran
Group III	Ahmadian et al., 2016	High K calc-alkaline	50,3	54 10 E	33 20 N	Central Iran
Group III	Ardjmanzadeh, et al., 2011	Calc-alkaline	33,5	68 68 E	35 11 N	East Iran
Group III	Delavari et al.,2014	Calc-alkaline	58,6	60 14 E	31 52 N	NE Iran
Group III	Shabanian et al., 2012	Calc-alkaline	18,5	58 60 E	36 81 N	NE Iran
Group III	Shabanian et al., 2012	Calc-alkaline	26,2	58 60 E	36 81 N	NE Iran
Group III	Shabanian et al., 2012	Calc-alkaline	19,5	58 60 E	36 81 N	NE Iran
Group III	Shabanian et al., 2012	Calc-alkaline	2,9	58 60 E	36 81 N	NE Iran
Group III	Ardjmanzadeh, et al., 2014	Calc-alkaline	33,3	58 50 E	32 20 N	East Iran
Group III	Ghorbani et al., 2014	Calc-alkaline	14,1	52 55 E	32 41 N	Central Iran
Group III	Ghorbani et al., 2014	Calc-alkaline	26	50 02 E	34 43 N	Central Iran
Group III	Ghorbani et al., 2014	Calc-alkaline	15,4	50 04 E	34 47 N	Central Iran
Group III	Rossetti et al., 2014	Calc-alkaline	52,4	58 00 E	36 23 N	NE Iran
Group III	Rossetti et al., 2014	Calc-alkaline	53,6	57 59 E	3624 N	NE Iran
Group III	Rossetti et al., 2014	Calc-alkaline	52,2	57 59 E	36 24 N	NE Iran
Group III	Yeganehfar et al., 2013	Calc-alkaline	18,67	52 38 E	33 00 N	Central Iran
Group III	Omran et al., 2008	Calc-alkaline	< 5Ma			Central Zagros suture
Group III	Vincent et al., 2005	High K calc-alkaline	~40 Ma			Alborz
Group III	Boztuğ & Jonckheere, 2007	High K calc-alkaline	~60 Ma			Central Anatolia
Group III	Innocenti et al., 1975	High K calc-alkaline	0,9 Ma			Central Anatolia
Group III	Boztuğ & Jonckheere, 2007	High K calc-alkaline	~29Ma			NE-Central Anatolia
Group III		High K calc-alkaline	0,78			Central Anatolia
Group III	Boztuğ & Jonckheere, 2007	High K calc-alkaline	~10-16			Central Anatolia
Group III	Boztuğ & Jonckheere, 2007	High K calc-alkaline	~40			Central Anatolia
Group III	karsli, 2007	High K calc-alkaline	43,5	39 70 E	40 00 N	East Pontides
Group III	karsli, 2007	High K calc-alkaline	44,1	39 70 E	40 00 N	East Pontides